Fabrication and Electromagnetic Properties of Metallic Nano-Helices

José Manuel Caridad Hernández

A thesis submitted to the University of Dublin, Trinity College,
in application for the degree of *Doctor of Philosophy*

School of Physics

Trinity College Dublin
2014

CONTENTS

LIST OF FIGURES

LIST OF TABLES

DECLARATION

I declare that this thesis has not been submitted as an exercise for a degree at this or any other university and it is entirely my own work.
I agree to deposit this thesis in the University's open access institutional repository or allow the Library to do so on my behalf, subject to Irish Copyright Legislation and Trinity College Library conditions of use and acknowledgment.

José M. Caridad

1. MOTIVATION AND OUTLOOK

Helically-shaped sytems are widely known in physics, biology or chemistry. Examples are some types of carbon nanotubes, DNA and collagen (double and triple helices, respectively), lipid bilayers, bacterial flagella (Salmonella and Esterichia Coli), coils of spirochetes bacteria, tendrils, etc. [1] Regarding practical applications, helices are widely studied and used at the macro- and micro-scale. They are present in custom devices to store mechanical energy (springs, helical micro-electro-mechanical systems) [2] or parts of custom photonic crystals [3,4]. Furthermore, metallic helical structures are used as antennae in a wide range of applications covering the mid-infrared, microwave and radio frequency ranges of the electromagnetic spectrum [5,6]. In addition, due to their particular shape lacking mirror symmetry, these structures are model systems to study chiral effects either in optical, magneto-optical or magneto-transport measurements [7,8].

However, the performance of the helical antennae has not been investigated into the optical frequency range yet, primarily due to the required extremely small scale. Optical (or plasmonic) antennae demand fabrication accuracies better than a few nanometers, a precision not achieved up to date in helical nano-structures made from metals. Despite the associated difficulties, the production and understanding of these kinds of metallic nano-devices are highly desirable since they represent a novel type of antenna with unprecedented magneto-electric (chiral) behaviour. Therefore, the optical (plasmonic) helical antenna is an emerging opportunity for innovative optoelectronic devices given the unique properties rising from this particular non-centrosymmetric shape.

The present thesis reports on the fabrication of a scalable production technique for nano-sized helically shaped metals (nano-coils) with a structural quality on the nanoscale far exceeding any prior art. Their fabrication accuracy allowed the observation of a localized surface-plasmon along the metallic nano-helix. This fact, together with the optical properties associated with their chiral shape determine the functionality of metallic nano-helices as antennae in the optical spectrum. In addition, the sample's chirality is manifested in the magneto-optical and magneto-resistance measurements of these samples as well.

This thesis is organized as follows:

Chapter 2 contains the relevant background necessary to understand the growth principles of so-called sculptured thin films. These structures are modifications of columnar thin films which include two- and three- dimensional shapes such as slanted columns, zigzags or helicoidal morphologies [9].

Chapter 3 presents the general framework describing the scattering of electromagnetic waves required to evaluate the optical properties of single and periodically arranged structures at the nano-scale, with emphasis on helical geometries. Information about plasmonic effects in metallic nano-structures is included in order to understand the behaviour of the helical nano-structures as antennae in the optical spectrum.
As introduced above, helices are exemplary chiral structures. A detailed background on chirality is provided in **Chapter 4**. In addition, manifestations of chirality in the optical, magneto-optical and magneto-electrical properties of chiral systems are included in this chapter as well.
Chapter 5 enumerates the different experimental techniques to fabricate metallic nano-helices, justifying the growth procedure employed in this work: glancing angle deposition. Furthermore, it describes the scanning electron microscope technique utilized to assess the nano-helix quality and structural regularity and explains the required set-ups to demonstrate the optical, magneto-optical and magneto-transport properties of these chiral nano-structures.
The main results of this thesis are compiled in **Chapter 6**. The here improved growth technique allows the fabrication of uniform and well-spaced regular helices at the nano-scale. In addition, the systematic study presented shows that the potential vast number of parameters availiable to optimize sculptured thin films [10] is considerably decreased when considering the growth of uniform free-standing metallic nano-structures.
The optical properties of arrays composed of metallic nano-helices are studied in the *far-field* for the visible and near-infrared wavelength ranges, showing that the response can be deliberately tuned by the individual nano-helix structural parameters. The existence of a longitudinal localized surface-plasmon in the metallic nano-helices is proved. The wavelength of this plasmon scales linearly with the total length of the nanostructure and primarily determines the working of the helical antenna in the optical spectrum. This scaling is in marked contrast to conventional micro- and macroscopic helical structures where the antenna operation mode scales with the length of a single turn only. The *near-field* of nano-helices made from different metals is succesfully evaluated through surface-enhanced Raman spectroscopy (SERS), showing how the different electronic structure of the growing metals affect the plasmonic *near-field* of the optical antenna.
In addition, these samples show the expected chiral behaviour in their optical, magneto-optical and magneto-trasport properties. The tuneability of these chiral properties for different wavelengths depending on the samples' structural parameters is shown for the first time in the experiments conducted in this thesis.
Finally, **Chapter 7** summarizes the main conclusions of this study, suggests further work to be carried-out and addresses the potential application of the metallic nano-helices.

2. ENGINEERING SCULPTURED THIN FILMS

Sculptured thin films are columnar nano-structured materials with anisotropic and unidirectionally varying properties that can be designed and realized in a controllable manner using physical vapour deposition (PVD) [9]. The ability to instantaneously change the growth direction of the columnar morphology through simple variations in the direction of the incoming vapour flux, leads to a wide spectrum of two- and three- dimensional columnar forms, for example zig-zags and nano-helices (see Fig. 2.1). The column diameter can range from ∼10 to 300 nm. The chemical compostion is in principle unlimited, ranging from insulators to semiconductors to metals [9]. This chapter is devoted to explain the morphology of generic columnar thin films depending on their main growth parameters. The basic knowledge here introduced provides the principles to grow actual nano-helices from different metals as further explained and demonstrated in **Sections 5.1** and **6.1**, respectively.

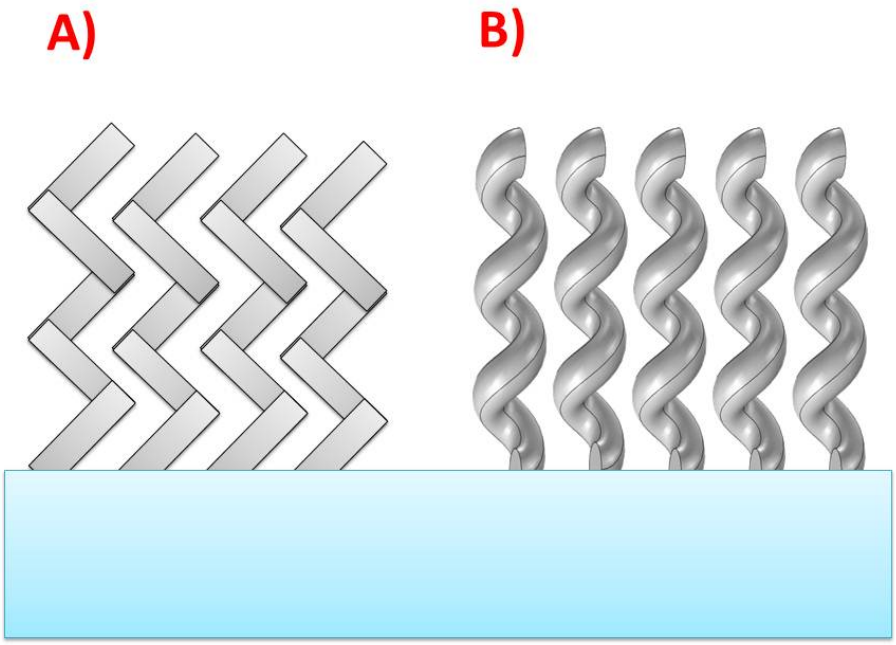

Fig. 2.1: Examples of sculptured thin films. A) Zig-zags. B) Helical structures.

2.1 Columnar thin film morphology and growth mechanics

The structure of columnar thin films deposited by physical vapour deposition (PVD) depends in general on several processing parameters such as the growth temperature T, the residual gas pressure, flux directionality, evaporated material, substrate material, substrate roughness, substrate motion and the deposition geometry [9, 11].

Evaporations are performed at room temperature and low pressure. The material in a source evaporates towards a substrate held at an angle γ to the incoming directional vapour flux and the arriving atoms settle on it to form a thin film (see Fig. 2.2A). Nucleation clusters of sizes of 1 to 3 nm in diameter initially form on the substrate. The clusters evolve into expanding and competing columns as the film thickness increases, provided that the film temperature is maintained below about a third of its melting point [9]. This results in an array of surface features and associated void network defining the different features. Columnar thin films are the direct result of self-shadowing at the length scale of the arriving adatoms (Fig. 2.2B).

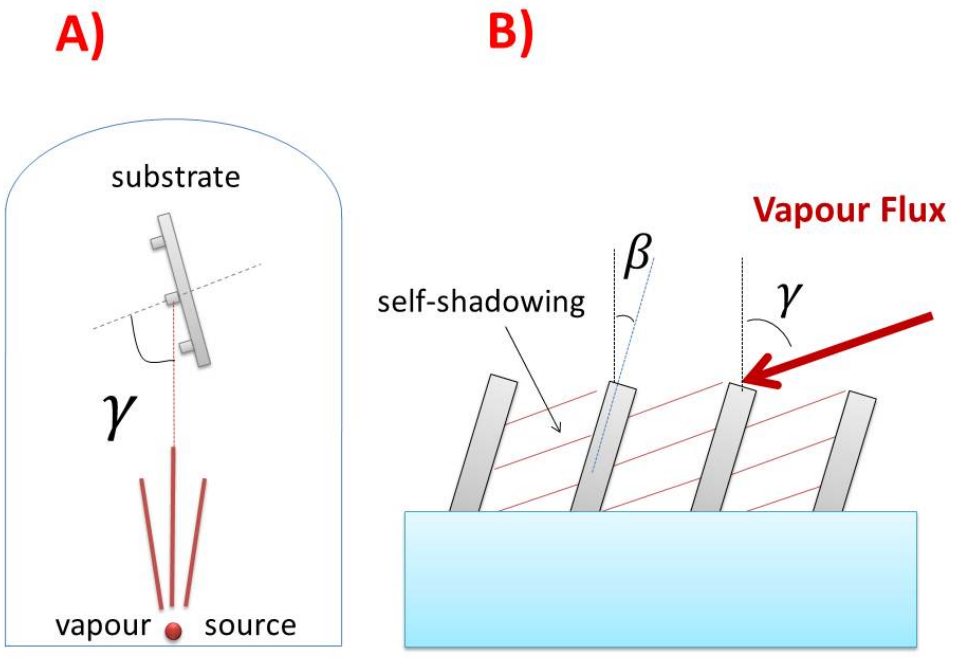

Fig. 2.2: Columnar thin-film growth mechanics. A) Vapour incidences at an angle γ with respect to the substrate normal. B) The self-shadowing mechanism between structures allows the growth of columnar films with an inclination angle β with respect to the substrate normal. β is related to γ through the relation $\beta = \gamma - \arcsin(\frac{1-\cos(\gamma)}{2})$ [12].

2.2 The Structure Zone Model

In 1969 Movchan and Demchishin developed a qualitative model describing the top-surface morphology of electron-beam evaporated films through one of the formerly enumerated processing factors: the reduced growth temperature $\frac{T}{T_m}$ [9], where T_m is the melting temperature af the evaporated material. The use of this homologous temperature is directly related to the thermally-induced surface diffusion (adatom mobility) of the materials [9]. They introduced the Structured Zone Model (SZM) in order to classify the observed morphologies in a wide range of elemental materials and compounds, from metals to oxides, from amorphous to crystalline and from low to high melting point materials [9]. Four zones can be distinguised within this model (Fig. 2.3) which cover the fundamental physical processes acting during growth: shadowing, surface diffusion, and bulk diffusion.

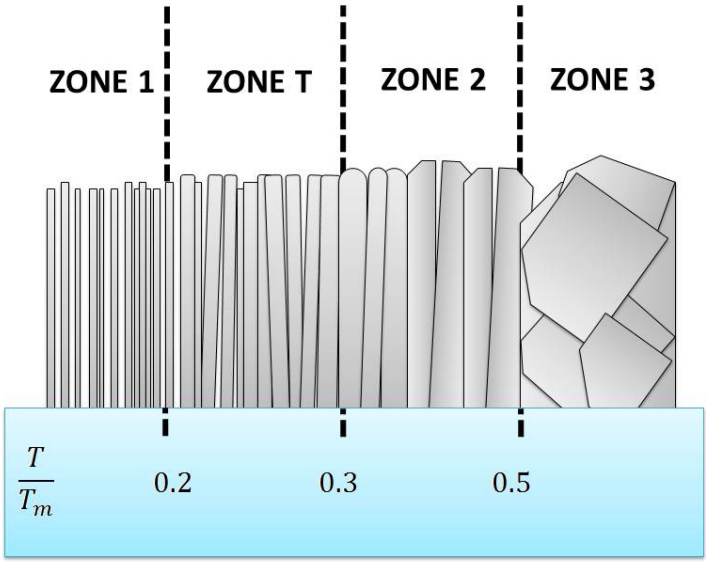

Fig. 2.3: Structured Zone Model for columnar thin films. The process variable is the reduced temperature $\frac{T}{T_m}$, where T is the growth temperature and T_m is the melting point of the growth material. Zone 1 is characterized by soft films composed by small clusters arranged in a columnar shape. Films in Zone T are harder and present larger cluster sizes than in Zone 1. When increasing the $\frac{T}{T_m}$ ratio, facets start to appear first on the surface (Zone 2) and then in the bulk (Zone 3).

Shadowing controls the film nano-structure and texture in Zone 1, characterized for having low reduced temperatures $\frac{T}{T_m} < 0.2$, i.e., low ad-atom mobilities. The film is composed of small clusters attached in a columnar shape with tapered voids between columns. Films that grow within Zone 1 are mechanically soft.
Zone T occurs for $0.2 < \frac{T}{T_m} < 0.3$ and it was added in the SZM model after Thornton expanded it to include a second processing factor: residual gas pressure during an ion

bombardment step [9]. This zone is characterized for harder columnar structures with less voids than Zone 1. The zone is still dominated by shadowing effects, however, the columns generally increase their size with their height due to the temperature rising during the growth plus an ad-atom mobility associated with energetic ion bombardment.
For higher reduced temperatures, the top surface has facets due to significant adatom mobility first on the surface (Zone 2) and then in the bulk (Zone 3). In particular, in Zone 2 ($0.3 < \frac{T}{T_m} < 0.5$), the film consist of columnar grains with defined dense grain boundaries, faceted top surfaces and increased grain width. Meanwhile, in Zone 3 ($\frac{T}{T_m} > 0.5$) the nano-structure exhibits equixed grains. Table 2.1 summarizes the main mechanisms governing the growth and the film morphology within the four zones.

Tab. 2.1: Thin film growth mechanisms

Zone	Growth mechanism	Film morphology
1: $\frac{T}{T_m} < 0.2$	Shadowing.	Columnar with voids. Small cluster size.
T: $0.2 < \frac{T}{T_m} < 0.3$	Shadowing. Ion particle energy.	Columnar. Larger cluster size.
2: $0.3 < \frac{T}{T_m} < 0.5$	Surface diffusion.	Columnar crystallites.
3: $\frac{T}{T_m} > 0.5$	Bulk diffusion.	3D grains.

3. OPTICAL PHENOMENA IN METALLIC NANO-STRUCTURES

Periodic arrays of regular nano-helices can be effectively regarded as complex electromagnetic media giving rise to novel optical and transport phenomena such as the magneto-chiral anisotropy [7, 8]. In the present chapter, the theoretical framework necessary to analyze the optical measurements is described. In particular, it comprises the two following topics: elastic and inelastic light scattering by individual nano-objects and nano-structured metamaterials and bulk and surface plasmons of metallic nano-structures.

The interaction of electromagnetic radiation with matter can be considered at different length scales, which in turn determines the appropriate theoretical approach to use [13]. Two main length scales are crucial when dealing with periodic arrays of regular particles: the separation δ between the individual elements and the characteristic length of the single objects a [14] (for example, the radius in the case of an sphere). When δ is much shorter than the wavelength λ of the incident radiation ($\lambda >> 10\delta$ [14, 15]), each particle is subjected to the incident (electric) field and secondary fields produced by scattering from multiple neighbouring particles [14, 15]. Under these conditions the system is *optically dense* and its electromagnetic response resembles that of a homogeneous, isotropic media mainly driven by the overall material properties rather than the structure of the individual elements and/or their collective arrangement. On the other hand, when the particle separation is about one order of magnitude smaller than the wavelength of the incident radiation ($\lambda \sim 10\delta$ [14, 15]), the electromagnetic field experienced by each particle is determined by the incident field and secondary fields produced just by the nearest neighbours. In this case, the electromagnetic response is essentially anisotropic and both the structure of each particle and their spatial arrangement need to be taken into account. At these wavelengths, the system behaves as a *metamaterial*, with the possibility of exhibiting novel properties not found in the material's bulk properties, such as a negative refractive index [16]. Finally, when $\lambda \lessapprox 10\delta$ [14, 15], the medium behaviour is determined by the mere summation of the *individual particle responses*. This medium is anisotropic and does not depend on the spatial arrangement of the individual nanoparticles. The aforementioned regimes are illustrated in Fig. 3.1 taking a helix as the individual particle.

The comparison between λ and the characteristic length of the individual particle a also determines both the theoretical approach to use for the *individual particle* as well as the *metamaterial* regime. Within the *individual particle* context, several exact theories

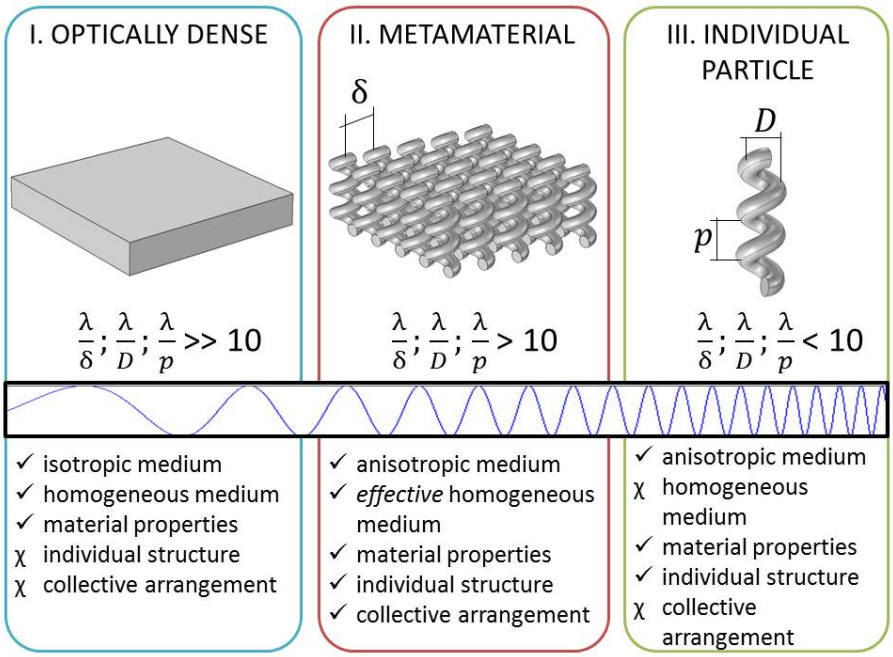

Fig. 3.1: Optical regimes of nano-structured materials with a nano-helix as individual particle. The different regimes are characterized depending on the ratios between the wavelength λ and the particle separation length δ and/or the two characteristic lengths of a helix: the pitch, p, and the diameter, D.

or numerical techniques can be used [15]. Furthermore, some approximations can be employed in special cases [15]. For example, when $\lambda >> a$ the approximation of *Rayleigh scattering* can be used [17]. This analytical model approximates the scatterer geometry as a single dipole with a polarizability which depends on the size and refractive index of the material composing the particle. In the case of $\lambda \sim a$ these approximations are no longer valid and a *field optics* approach must be used which involves solving Maxwell's equations with the specific boundary conditions of the particle [15]. Finally, when $\lambda << a$ the *geometrical optics* approach can be used assuming that the incident plane wave can be represented as a collection of independent parallel rays [15, 17].

In addition, when dealing with metallic particles, there can be a need to take into account bulk and surface plasmon effects ocurring in nano-particles made from these materials. At frequencies corresponding to the metallic particle's plasmon resonance, the optical response of the object (specially nano-sized structures) is equivalent to a strongly coupled plasma [18]. Although driven by different physics, metallic nano-particles can be regarded as the optical counterpart of radio-frequency (RF) antennas: both (macro- and nano-) devices manipulate their *near-field*[1] in a subwavelength regime, thus, surpassing the diffraction limit [19, 20].

[1] For a given λ, the *near-field* of a structure comprises distances up to 2λ away from the cited object.

3.1 Scattering of electromagnetic radiation by individual nano-particles

Amongst others, matter is composed by discrete electric charges: electrons and protons. These electric charges get accelerated and oscillate in the presence of an electromagnetic wave. Once accelerated, the charges might re-radiate electromagnetic waves (photons) in all directions, a radiative process called *scattering*. Alternatively, accelerated charges might convert the electromagnetic energy into other forms of energy such as heat, which is named *absorption* process.

Scattering mechanisms can be separated into two principal forms: elastic or inelastic. The former comprises scattered photons that have the same energy as the incident photons. Meanwhile, in the inelastic process, incident and scattered photons do not posess the same energy as a consequence of the interactions between photons and phonons, defects and/or impurities present in matter (dissipation), magnons, etc.

In general, the theoretical description of any scattering problem by a randomly shaped particle is not trivial [15]. In the case of elastic scattering, exact analytical solutions only exist for a few simple geometries such as spheres and infinite cylinders [21]. By applying certain assumptions such as homogeneous internal fields (i.e. $\lambda >> a$), approximate analytical solutions can be found for nano-structures with different geometries such as rings and disks [22, 23]. The Rayleigh-Debye theory, a generalization of the Rayleigh scattering, can be used for calculating the scattering mechanism of slightly larger samples and complex shaped composites of low refractive index ratio m with respect the surrounding medium such as finite height cylinders and rings [17,21]. This method is used in **Chapter 6**, to calculate analitically the elastic scattering response from individual nano-helices in the *far-field*.

Any of the analytically aforementioned techniques have a limited range of application due to their initial assumptions. These limitations can be partially circumvented by using computational methods. Modern numerical techniques such as discrete dipole approximation (DDA), [24], finite difference time domain (FDTD), [25] and finite element method (FEM), [25–27] allow for numerically solving Maxwell's equations to calculate the scattering from arbitrary shapes. FEM is employed in **Chapter 6** to calculate the scattering from nano-helices in the *near-* and *far-field*. This method is chosen as it enables the treatment of complex shapes (such as helices) because the imposed shape-dividing mesh is not confined to a rectangular geometry [28].

Finally, inelastic Raman scattering of probing molecules deposited on metallic nano-helices is utilized to experimentally assess the *near-field* of these latter nano-structures (*c.f.* **Chapter 6**). This indirect evaluation relies on the fact that the local *near-field* is greatly increased in metallic nano-structured substrates, which in turn enhances the Raman response of substances deposited on them [29,30]. The theory behind Raman processes will be introduced in the last part of this section.

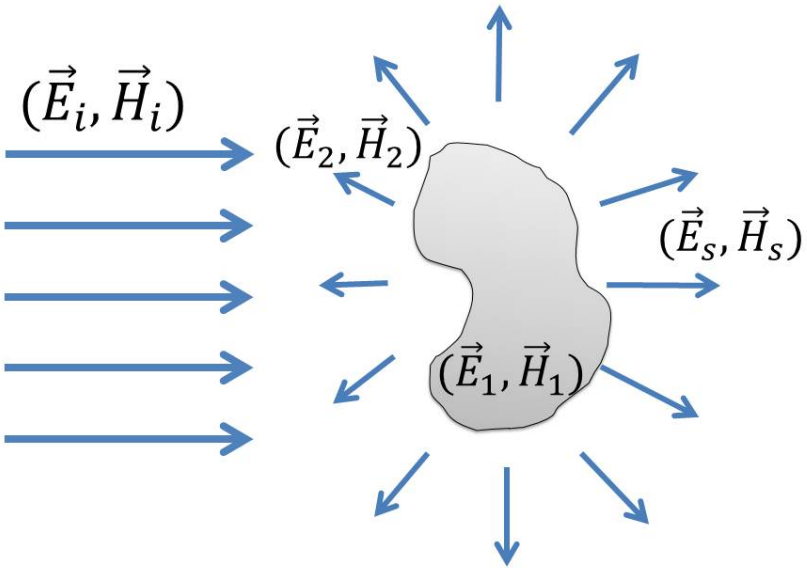

Fig. 3.2: General scattering problem. The incident electromagnetic field $(\vec{E}_i, \vec{H}_i)$, gives rise to the internal fields $\vec{E}_1$ and $\vec{H}_1$ inside the particle and the scattering fields $\vec{E}_s$ and $\vec{H}_s$. The total fields of the surrounding medium $(\vec{E}_2, \vec{H}_2)$ are composed of the incident and scattering fields.

3.1.1 General formulation of the scattering problem

In general, both the angular distribution of scattered light and the absorption by individual particles depend on the particles shape, size and the constituent material [17]. The fundamental problem when exposing a particle to an arbitrary monocromatic electromagnetic wave of amplitude ($\vec{E}_0$,$\vec{H}_0$) and frequency ω is the determination of the electromagnetic field at all points inside the particle $(\vec{E}_1, \vec{H}_1)$, as well as the calculation of the electromagnetic field within the homogeneous medium in which the particle is embedded $(\vec{E}_2, \vec{H}_2)$ (see Fig. 3.2). By considering both media to be composed of a linear, isotropic and homogeneous material, the latter field is given by a linear superposition of the incident $(\vec{E}_i, \vec{H}_i)$ and the scattered field $(\vec{E}_s, \vec{H}_s)$ [17]:

$$\vec{E}_2 = \vec{E}_i + \vec{E}_s; \qquad \vec{H}_2 = \vec{H}_i + \vec{H}_s \tag{3.1}$$

where

$$\vec{E}_i = \vec{E}_0 e^{i(\vec{k}\cdot\vec{r}-\omega t)}; \qquad \vec{H}_i = \vec{H}_0 e^{i(\vec{k}\cdot\vec{r}-\omega t)} \tag{3.2}$$

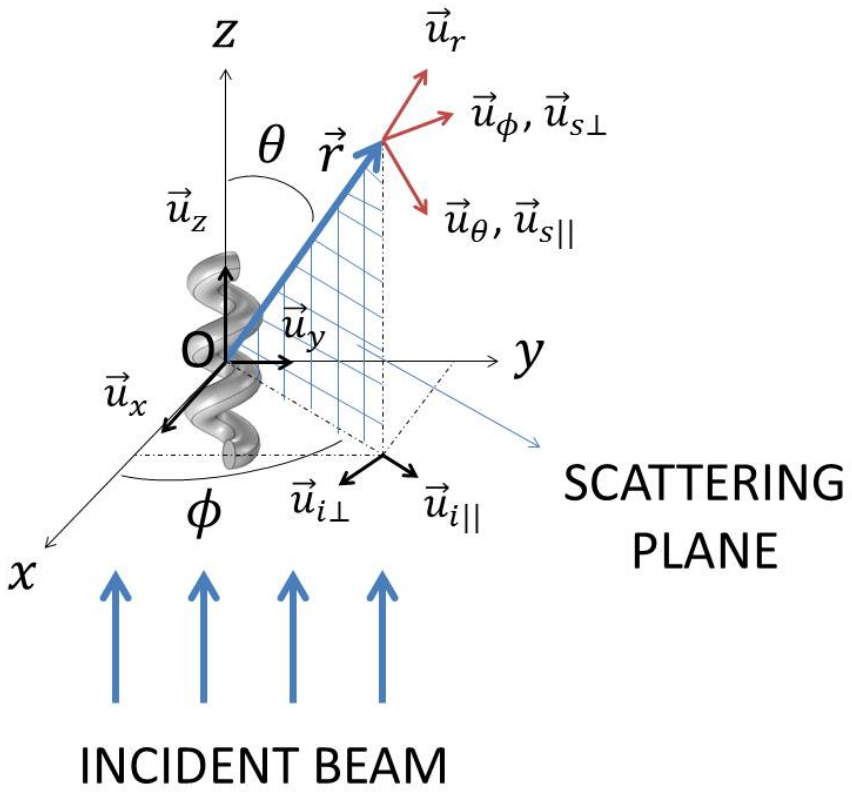

Fig. 3.3: Schematic of a single helix showing the relevant vectors and angles for the description of the scattering process.

and $\vec{k}$ is the wavevector in the surrounding medium.

Both fields $(\vec{E}_j, \vec{H}_j)$ must obey Maxwell's equations (Appendix A) at all points with continuous permitivity (ϵ_j) and permeability (μ_j), where $j = \{1, 2\}$ denotes the medium in consideration [17]. In addition, it can be proved that both electromagnetic fields $(\vec{E}_j, \vec{H}_j)$ satisfy the Helmholtz wave equation (see **Appendix A**). To fully solve the scattering problem, one needs to consider the boundary between the particle and the surrounding medium too. At this interface, in general, a sudden change in ϵ_j and μ_j occurs. Corresponding boundary conditions (Appendix A) have to be imposed at that interface, which requires continuity of the tangential components of $\vec{E}_j$ and $\vec{H}_j$ across the surface separating both media.

3.1.2 Scattering matrix from a particle with an arbitrary shape

Consider an arbitrary particle which is illuminated by a plane harmonic electromagnetic wave which propagates in the z direction (see Fig.3.3). Any point in the particle can be chosen as the origin O of a coordinate system (x, y, z) with orthonormal basis vectors $\{\vec{u}_x, \vec{u}_y, \vec{u}_z\}$. The scattering direction $\vec{u}_r$ and $\vec{u}_z$ form a so-called *scattering plane* uniquely

determined by the azimuthal angle ϕ, *i.e.* the normal vector to the plane $\vec{u}_{s\perp} \equiv \vec{u}_\phi$. Any other vector contained in the *scattering plane* is composed of the orthonormal basis vectors $\{\vec{u}_r, \vec{u}_{s\parallel} \equiv \vec{u}_\theta\}$. For convenience, the incident field $\vec{E}_i$ is separated into components parallel ($\vec{E}_{i\parallel}$) and perpendicular to the scattering plane ($\vec{E}_{i\perp}$):

$$\vec{E}_i = \vec{E}_{i\parallel} + \vec{E}_{i\perp} = E_{i\parallel}\vec{u}_{i\parallel} + E_{i\perp}\vec{u}_{i\perp} = (E_{0\parallel}\vec{u}_{i\parallel} + E_{0\perp}\vec{u}_{i\perp})e^{i(\vec{k}\cdot\vec{r}-\omega t)} \tag{3.3}$$

where $|\vec{k}| = k = \frac{2\pi n_2}{\lambda}$ is the wavenumber modulus, n_2 is the refractive index of the surrounding medium and λ is the wavelength of the radiation in a vacuum. The orthonormal basis is given by:

$$\vec{u}_{i\perp} = \sin\phi \cdot \vec{u}_x - \cos\phi \cdot \vec{u}_y \tag{3.4}$$

$$\vec{u}_{i\parallel} = \cos\phi \cdot \vec{u}_x + \sin\phi \cdot \vec{u}_y \tag{3.5}$$

At sufficiently large distances from the origin, in the *far-field* region ($\vec{k}\cdot\vec{r} >> 1$) the scattered field $\vec{E}_s$ is transverse ($\vec{u}_r \cdot \vec{E}_s \simeq 0$) and has the asymptotic form [17]:

$$\vec{E}_s = i\frac{e^{i\vec{k}\cdot\vec{r}}}{\vec{k}\cdot\vec{r}}\vec{A} \tag{3.6}$$

for $\vec{k}\cdot\vec{r} >> 1$ and $\vec{u}_r \cdot \vec{A} = 0$. $\vec{A}$ accounts for the dependence of $\vec{E}_s$ on the angles θ and ϕ.
As a consequence, the scattered field in the far-field region can be written as:

$$\vec{E}_s = E_{s\parallel}\vec{u}_{s\parallel} + E_{s\perp}\vec{u}_{s\perp} = E_{s\parallel}\vec{u}_\theta + E_{s\perp}\vec{u}_\phi \tag{3.7}$$

and it can be related to the incident field through a scattering matrix $\{S_j\}$ (j = 1,2,3,4):

$$\begin{pmatrix} E_{s\parallel} \\ E_{s\perp} \end{pmatrix} = i\frac{e^{i\vec{k}\cdot(\vec{r}-\vec{z})}}{\vec{k}\cdot\vec{r}} \begin{pmatrix} S_2 & S_3 \\ S_4 & S_1 \end{pmatrix} \begin{pmatrix} E_{\parallel i} \\ E_{\perp i} \end{pmatrix} \tag{3.8}$$

The components of the scattering electric field can be used to calculate experimentally observable quantities, for example, the irradiance. In general, by interposing different polarizers between particle and detector it is possible to obtain the Stokes parameters[2]

[2] The Stokes parameters are a set of values that describe the polarization state of electromagnetic radiation. They were defined as a convenient alternative to the description of incoherent or partially polarized radiation in terms of its total intensity, degree of polarization, and the shape parameters of the polarization ellipse.

of the light scattered by a particle [17]:

$$I_s =< E_{\parallel s}E^{\dagger}_{\parallel s} + E_{\perp s}E^{\dagger}_{\perp s} > \tag{3.9}$$

$$Q_s =< E_{\parallel s}E^{\dagger}_{\parallel s} - E_{\perp s}E^{\dagger}_{\perp s} > \tag{3.10}$$

$$U_s =< E_{\parallel s}E^{\dagger}_{\perp s} + E_{\perp s}E^{\dagger}_{\parallel s} > \tag{3.11}$$

$$V_s = i < E_{\parallel s}E^{\dagger}_{\perp s} - E_{\perp s}E^{\dagger}_{\parallel s} > \tag{3.12}$$

where the superscript † denotes transposition and complex conjugation. The relation between incident and scattered Stokes parameters is given by:

$$\begin{pmatrix} I_s \\ Q_s \\ U_s \\ V_s \end{pmatrix} = \frac{1}{k^2r^2} \begin{pmatrix} S_{11} & S_{12} & S_{13} & S_{14} \\ S_{21} & S_{22} & S_{23} & S_{24} \\ S_{31} & S_{32} & S_{33} & S_{34} \\ S_{41} & S_{42} & S_{43} & S_{44} \end{pmatrix} \begin{pmatrix} I_i \\ Q_i \\ U_i \\ V_i \end{pmatrix} \tag{3.13}$$

The different combinations between the elements of the so-called Müller matrix $\{S_{ij}\}$ (Eq. 3.13) and the elements of the scattering matrix $\{S_j\}$ (Eq. 3.8) can be found in Ref. [15, 17]. Some particular simple cases are:

- At incident unpolarized light with irradiance $(I_i, 0, 0, 0)^T$ (the superscript T denotes transposition), the Stokes parameters of the scattered light are $\frac{I_s}{I_i} = S_{11}$, $\frac{Q_s}{I_i} = S_{21}$, $\frac{U_s}{I_i} = S_{31}$ and $\frac{V_s}{I_i} = S_{41}$ (the factor $1/k^2r^2$ is ommited for simplicity). Therefore S_{11} represents the angular distribution of scattered light given unpolarized incident light. This scattered light is in general partially polarized with a degree of polarization $\sqrt{(S_{21}^2 + S_{31}^2 + S_{41}^2)/S_{11}^2}$ (*i.e.*, scattering is effectively a mechanism for polarizing light [17]).

- For right-circularly polarized light $(I_i, 0, 0, I_i)^T$, the irradiance of the scattered light is $S_{11} + S_{14}$. Meanwhile, for left-circularly polarized light $(I_i, 0, 0, -I_i)^T$, the irradiance of the scattered light is $S_{11} - S_{14}$. Therefore, S_{14} is interpreted as the difference in irradiances for left ($I_{s|L}$) and right ($I_{s|R}$) circulary polarized incoming light: $S_{14} = \frac{I_{s|R} - I_{s|L}}{2I_i}$.

- S_{12} denotes the difference in scattered irradiances for incident light polarized parallel $(I_i, I_i, 0, 0)^T$ and perpendicular $(I_i, -I_i, 0, 0)^T$ to a specific scattering plane: $S_{12} = \frac{I_{s|\parallel} - I_{s|\perp}}{2I_i}$.

- S_{13} denotes the difference in scattered irradiances for incident light polarized at an angle +45° $(I_i, 0, I_i, 0)^T$ and -45° $(I_i, 0, -I_i, 0)^T$ to a specific scattering plane : $S_{13} = \frac{I_{s|+45^\circ} - I_{s|-45^\circ}}{2I_i}$.

It should be noted that given incident light of arbitrary polarization, the light scattered by a single particle or an ensemble of **identical** particles with the same relative orientation to the incoming beam is completely polarized. Thus, in this case, the degree of polarization of the scattered light is constant, however, the type of the polarization will be modified [17]. In contrast, an ensemble of non-identical particles will depolarize any incident polarized light beam.

3.1.3 Extinction, scattering and absorption cross-sections

The knowledge of the total electromagnetic field in the *far-field* zone allows for calculating important optical characteristics of the scattering object such as the extinction, absorption and scattering cross-sections. These optical cross-sections are defined as follows [17]: the product of the scattering cross-section C_{sca} and the incident monochromatic energy flux gives the monochromatic power removed from the incident wave as a result of its scattering in all directions. Analogously, the product of the absorption cross-section, C_{abs}, and the incident monochromatic energy flux gives the total monochromatic power removed from the incident wave as a result of absorption of light by the object. Finally, the extinction cross-section, C_{ext}, is the sum of the scattering and absorption cross-sections and, when multiplied by the incident monochromatic energy flux, gives the total monochromatic power removed from the incident wave due to scattering and absorption [17].
To determine the optical cross-sections, the scatterer is surrounded by an imaginary sphere with a radius large enough to be in the *far-field* zone. Considering the surrounding medium to be nonabsorbing, the net rate into the sphere at which the electromagnetic energy crosses the surface A of the sphere is equal to the power absorbed by the particle $W^{(abs)}$. This rate is always non-negative as there are no electromagnetic sources within the sphere:

$$W^{(abs)} = -\int_A \vec{S} \cdot d\vec{A} \tag{3.14}$$

where $\vec{S} = \left[\vec{E}(\vec{r}) \times H(\vec{r})\right]$ is the Poynting vector. $W^{(abs)}$ can be written as a combination of three terms [17]:

$$W^{(abs)} = W^{(inc)} - W^{(sca)} + W^{(ext)} \tag{3.15}$$

$$W^{(inc)} = -\int_A \vec{S}^{(inc)} \cdot d\vec{A} \tag{3.16}$$

$$W^{(sca)} = \int_A \vec{S}^{(sca)} \cdot d\vec{A}. \tag{3.17}$$

$W^{(sca)}$ is the rate at which energy is scattered across the surface in the outward direction,

meanwhile $W^{(inc)}$ are the surrounding medium losses which are zero in the present case as the latter is considered to be not absorbing. $W^{(ext)}$ is the sum of the energy absorption rate and the energy scattering rate:

$$W^{(ext)} = W^{(sca)} + W^{(abs)} \tag{3.18}$$

Thus, having an incident flux $I_i = \frac{1}{2}\sqrt{\epsilon_2/\mu_2}|E_0|^2$ (irradiance), it follows:

$$C_{ext} = \frac{W^{(ext)}}{I_i} \tag{3.19}$$

$$C_{sca} = \frac{W^{(sca)}}{I_i} \tag{3.20}$$

$$C_{abs} = C_{ext} - C_{sca} \tag{3.21}$$

All cross sections are by definition positive quantities and have the dimension of an area. They depend on the direction, polarization state, and wavelength of the incident electromagnetic radiation as well as on the particle size, morphology, refractive index and orientation with respect to the reference frame. C_{ext} is not merely given by the area of the sample's geometrical projection on the detector surface G, instead, the dimensionless quantity $\frac{C_{ext}}{G}$ is commonly introduced to compare the scattering extinction efficiency depending on the scatterers shape. Analogously $\frac{C_{sca}}{G}$, $\frac{C_{abs}}{G}$ can be defined.
Finally, the quantity $\frac{dC_{sca}}{d\Omega}$ has the dimension of area and is called the differential scattering cross-section (Ω denotes a solid angle). It describes the angular distribution of the scattered light and specifies the electromagnetic power scattered into a unit solid angle in a given direction per unit of incident intensity. This implies that:

$$C_{sca} = \int_{4\pi} \frac{dC_{sca}}{d\Omega} \mathrm{d}\Omega. \tag{3.22}$$

3.1.4 Particles small compared to the wavelength: Rayleigh-Debye scattering

In the case of small particles, the self-field caused by the electric dipole moments $\vec{p}_e$ of the particles modifies the total electric field $\vec{E}$ inside ($\vec{E}_1$) and near ($\vec{E}_2$) the scatterer. A particle much smaller than the wavelength of the incident radiation can be considered to be placed in an homogeneous applied electric field $\vec{E}_i$. In this case the expression $\vec{p}_e = \overline{\overline{\alpha}}\vec{E}_i$ is applicable, where the anisotropic tensor $\overline{\overline{\alpha}}$ has the dimension of volume and defines the polarizability of the particle. If $\overline{\overline{\alpha}}$ is isotropic ($\overline{\overline{\alpha}} = \alpha$), that is, the directions of $\vec{p}_e$ and $\vec{E}_i$ always coincide, it can be shown that the scattering matrix in Eq. 3.8 simplifies to [21]:

$$\begin{pmatrix} S_2 & S_3 \\ S_4 & S_1 \end{pmatrix} = -ik^3\alpha \begin{pmatrix} \cos\theta & 0 \\ 0 & 1 \end{pmatrix} \tag{3.23}$$

where θ is the scattering angle (see Fig. 3.3). Eq. 3.23 represents the so-called *Rayleigh scattering* approximation. Rayleigh scattering is the elastic scattering of electromagnetic radiation by objects much smaller than the wavelength of the incident radiation. It approximates the particle as a single dipole radiating in all directions with a polarizability depending on the size a and refractive index of the particle relative to the surrounding medium $m = \frac{n_1}{n_2}$.
The Rayleigh theory can be generalized with the *Rayleigh-Debye* scattering formalism which can be used for slightly larger particles and composites with complex shapes [17,21] as is the case of nano-helices. Within the Rayleigh-Debye formalism, it is considered that the nano-particle is composed of non-interacting infinitesimal spheres. Under this assumption, the scattering matrix elements (Eq. 3.23) of an isotropic, homogeneous sphere ($\alpha = \frac{3(m^2-1)}{4\pi(m^2+2)}v$) are divided by its volume v and the resulting quotients are finite when the sphere radius a tends to 0 [17]:

$$s_1 = \lim_{a\to 0}\frac{S_1}{v} = \frac{-3ik^3}{4\pi}\frac{m^2-1}{m^2+2} \simeq \frac{-ik^3}{2\pi}(m-1) \tag{3.24}$$

$$s_2 = \lim_{a\to 0}\frac{S_2}{v} = \frac{-3ik^3}{4\pi}\frac{m^2-1}{m^2+2}\cos\theta \simeq \frac{-ik^3}{2\pi}(m-1)\cos\theta \tag{3.25}$$

where the approximation $\frac{m^2-1}{m^2+2} \simeq \frac{2}{3}(m-1)$ when m $\to$ 1 was used [17] (as stated below, m$\approx$1 is an actual conditon of the Rayleigh-Debye model). s_1 and s_2 can be regarded as scattering elements per unit volume. Under certain conditions discussed further below, the scattering matrix elements from a particle of arbitrary shape can be calculated by integrating Eq. 3.24 over the volume of the particle. The two heuristic conditions which limit the applicability of the Rayleigh-Debye model are [17]:

- The refractive index relative to the surrounding medium m has to be close to 1: $|m-1| << 1$. This condition limits the reflection angle of the incident wave at the interface to be small.
- Small changes of phase and amplitude of an incident wave: $2ka|m-1| << 1$, where a in this case represents any of the characteristic lengths of the particles. This assumption involves that the phase of the incident electromagnetic wave does not change considerably across the particle.

Despite these restricting conditions, it has been recently demonstrated that the theory's applicability can be considerably extended [31]. In particular, if the dimensionless quan-

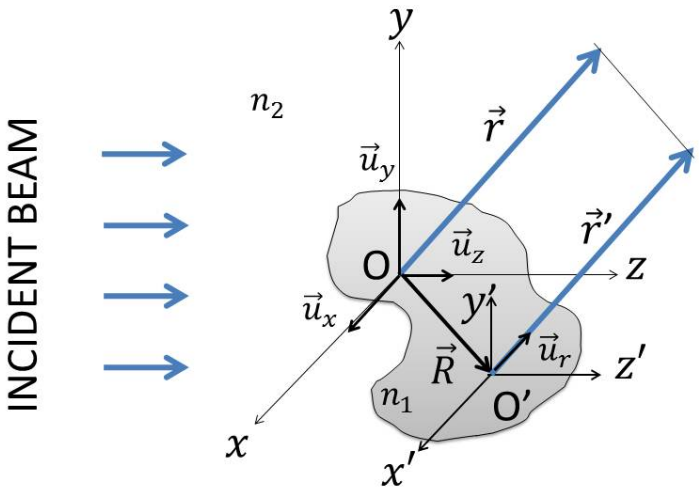

Fig. 3.4: Coordinate systems for determining the Rayleigh-Debye scattering of a particle with arbitrary shape.

tity $x_p = \frac{\pi}{\lambda}a$ is smaller than 0.4, the Rayleigh-Debye theory yields predictions within 30% of error for $|m-1| \sim 2$ or more [31].

The Rayleigh-Debye scattering formalism can be deduced from the Rayleigh scattering matrix (Eq. 3.24). Consider an arbitrary particle illuminated by a plane wave propagating in the z' direction as it is depicted in Fig. 3.4. Within the Rayleigh-Debye approximation, the contribution of a volume element Δv located at the position O' with respect to the field scattered by the particle in the direction $\vec{u}_r$ is:

$$\begin{pmatrix} \Delta E_{s\parallel} \\ \Delta E_{s\perp} \end{pmatrix} = i\frac{e^{i\vec{k}\cdot(\vec{r}'-\vec{z}')}}{\vec{k}\cdot\vec{r}'}\Delta v \begin{pmatrix} s_2 & 0 \\ 0 & s_1 \end{pmatrix} \begin{pmatrix} E'_{i\parallel} \\ E'_{i\perp} \end{pmatrix} \tag{3.26}$$

where $E'_{i\parallel} = E'_{0\parallel}e^{i\vec{k}\vec{z}'}$, $E'_{i\perp} = E'_{0\perp}e^{i\vec{k}\vec{z}'}$, and the amplitudes $E'_{0\parallel}$ and $E'_{0\perp}$ are independent of the position vector. As can be seen from Eq. 3.26, the physical basis of Rayleigh-Debye scattering is the following: each spherical volume element shows Rayleigh scattering independently of the other volume elements. The waves scattered in a given direction by all these elements interfere because of the different positions of the volume elements in space. In order to calculate the interference effects there is a need to refer the phases of all scattered waves to a common origin of coordinates O and then add them. For this, consider a rectangular coordinate system (x', y', z') which is centered at O' (see Fig. 3.4). Let $-Z$ be the z' coordinate of the origin O of a reference coordinate system

(x, y, z) parallel to (x', y', z'). Then, the incident field at O is

$$E_{0\parallel} = E'_{i\parallel}(-Z) = E'_{0\parallel} e^{-i\vec{k}\cdot\vec{Z}}, \tag{3.27}$$

$$E_{0\perp} = E'_{i\perp}(-Z) = E'_{0\perp} e^{-i\vec{k}\cdot\vec{Z}}. \tag{3.28}$$

It follows that $E'_{i\parallel} = E_{0\parallel} e^{i\vec{k}\cdot(\vec{Z}+\vec{z'})}$ and $E'_{i\perp} = E_{0\perp} e^{i\vec{k}\cdot(\vec{Z}+\vec{z'})}$. Using the relations $\vec{r'} = \vec{r} - \vec{R}$, then Eq. 3.26 becomes [17]:

$$\begin{pmatrix} \Delta E_{s\parallel} \\ \Delta E_{s\perp} \end{pmatrix} = i \frac{e^{i\vec{k}\cdot(\vec{r}-\vec{z})}}{\vec{k}\cdot\vec{r}} \Delta v e^{i\delta} \begin{pmatrix} s_2 & 0 \\ 0 & s_1 \end{pmatrix} \begin{pmatrix} E_{i\parallel} \\ E_{i\perp} \end{pmatrix} \tag{3.29}$$

with the phase difference $\delta = |\vec{k}|\vec{R}\cdot(\vec{u}_z - \vec{u}_r)$, and $E_{i\parallel} = E_{0\parallel} e^{i\vec{k}\cdot\vec{z}}$ and $E_{i\perp} = E_{0\perp} e^{i\vec{k}\cdot\vec{z}}$. Since the particle is much smaller than the distance to the point of observation, one can approximate $(\vec{k}\cdot\vec{r'})^{-1} \approx (\vec{k}\cdot\vec{r})^{-1}$. Finally, the total field $\vec{E}_s$ scattered in the direction $\vec{u}_r$ is obtained by integrating Eq. 3.29 over the particle volume v [17]:

$$\begin{pmatrix} E_{s\parallel} \\ E_{s\perp} \end{pmatrix} = i \frac{e^{i\vec{k}\cdot(\vec{r}-\vec{z})}}{\vec{k}\cdot\vec{r}} \begin{pmatrix} S_2 & 0 \\ 0 & S_1 \end{pmatrix} \begin{pmatrix} E_{i\parallel} \\ E_{i\perp} \end{pmatrix} \tag{3.30}$$

$$S_1 = -\frac{ik^3}{2\pi}(m-1)v f(\theta, \phi), \tag{3.31}$$

$$S_2 = -\frac{ik^3}{2\pi}(m-1)v f(\theta, \phi)\cos\theta. \tag{3.32}$$

Within these expressions, the form factor $f(\theta, \phi)$ depends entirely on the geometry of the scatterer and is given by:

$$f(\theta, \phi) = \frac{1}{v}\int_v e^{i\delta} dv. \tag{3.33}$$

3.1.5 Rayleigh-Debye scattering of nano-helices

As shown in Eq. 3.30, the form factor (Eq. 3.33) of the Rayleigh-Debye theory implies information on the shape of the scatterer. In order to calculate the form factor of a helical structure, it may be approximated by periodic rods and rings as depicted in Fig.3.5. Considering the proper nature of the Rayleigh-Debye formalism, this is justified as follows: as mentioned in **Section 3.1.4**, within this theory, each volume element produces scattering independently from other volume elements, with rings and rods being the elementary elements into which a helical structure can be decomposed [6]. The validity of this assumption will become apparent in the **Section 6.2** by comparison with the experimental

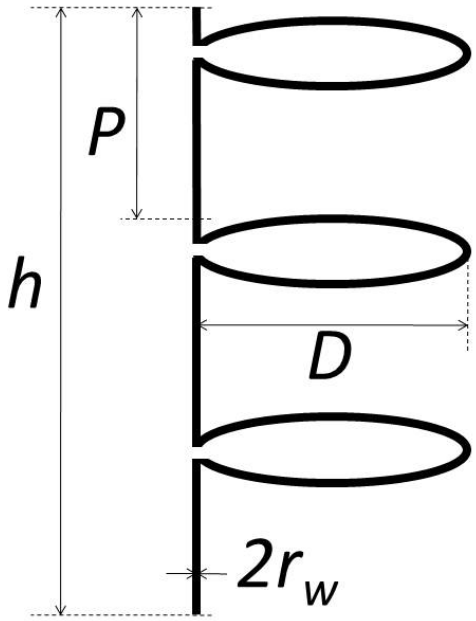

Fig. 3.5: Approximation of a helical structure based on rods and rings. h is the total height of the structure, D and p are the helical diameter and pitch, respectively, and r_w is the radius of the wire composing the rod and the ring. Note that as it is, this approximation does not reflect the chirality of the actual helical shape.

data of the specular reflection of arrays of nano-helices.

Rayleigh-Debye scattering from a rod

The form factor from a rod can be found in Ref. [17]: consider a cylinder of radius a and finite length $2l$ illuminated by a light-beam making an angle ξ with the cylinder's axis (see Fig. 3.6). The direction of the incident $\vec{u_i}$ and scattered $\vec{u_r}$ waves are specified by $\vec{u_i} = \sin\xi\vec{u_z} - \cos\xi\vec{u_x}$ and $\vec{u_r} = \sin\theta\cos\phi\vec{u_x} + \sin\theta\sin\phi\vec{u_y} + \cos\theta\vec{u_z}$. The position vector $\vec{R}$ of a point in the particle with respect to the origin O in polar coordinates (ρ, ψ, x) is given by $(x, \rho\cos\psi, \rho\sin\psi)$ in cartesian coordinates. Thus, the form factor in Eq. 3.33 for the case of a rod reads:

$$f(\theta,\phi;\xi) = \frac{1}{\pi a^2 2l}\int_{-l}^{l} e^{-ikAx}dx \int_0^a \rho d\rho \int_0^{2\pi} e^{-ik\rho(B\cos\psi + C\sin\psi)}d\psi \tag{3.34}$$

where $A = \cos\xi + \sin\theta\cos\phi$, $B = \sin\theta\sin\phi$, and $C = \cos\theta - \sin\xi$. Solving the three integrals (see Ref. [17]) we get the expression for the form factor of a finite cylinder for a given angle of incidence ξ:

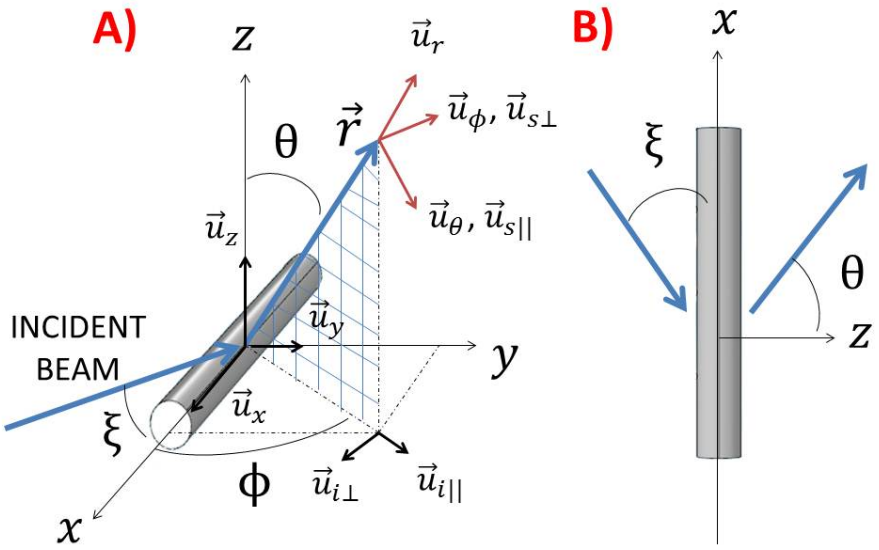

Fig. 3.6: Coordinate systems used to calculate the Rayleigh-Debye scattering for the particular case of a solid rod with circular cross-section.

$$f(\theta, \phi; \xi) = \frac{2\sin(kAl)}{kAl} \frac{J_1(xM)}{xM} \tag{3.35}$$

with $M = \sqrt{B^2 + C^2}$ and $J_1(x)$ being the Bessel function of the first kind.

Rayleigh-Debye scattering from a ring

Following a similar procedure, the form factor of a ring of radius a and cross section radius b (Fig. 3.7) can be derived as demonstrated in Ref. [32]. In this case:

$$f(\theta, \phi; \alpha, \beta) = \frac{1}{2\pi^2 b^2} \int_0^{2\pi} e^{ik\cdot(\vec{u}_i - \vec{u}_r)\vec{R}} d\phi \int e^{ik(\vec{u}_i - \vec{u}_r)\cdot(\vec{r}' - \vec{R})} dA \tag{3.36}$$

where the unit vector of the incident wave $\vec{u}_i$ and the unit vector of the scattered wave $\vec{u}_r$ are expressed in terms of the polar and azimuthal angles α and β, ϕ and θ, respectively. $\vec{R} = (a\cos\phi, a\sin\phi), 0$ is the position vector at the center of a cross-section, $\vec{r}'$ is the position vector to a point on the same cross section, $d\vec{A}$ is a surface element at the position vector $\vec{r}'$. The second integral in Eq. 3.36, gives the amplitude of the form factor of a very thin circular disc situated at $\vec{R}$ and having unit normal $\vec{u}_t$. The first integral runs over the entire torus and gives the total amplitude. After some algebra [32] the following expression can be derived for the form factor of a ring:

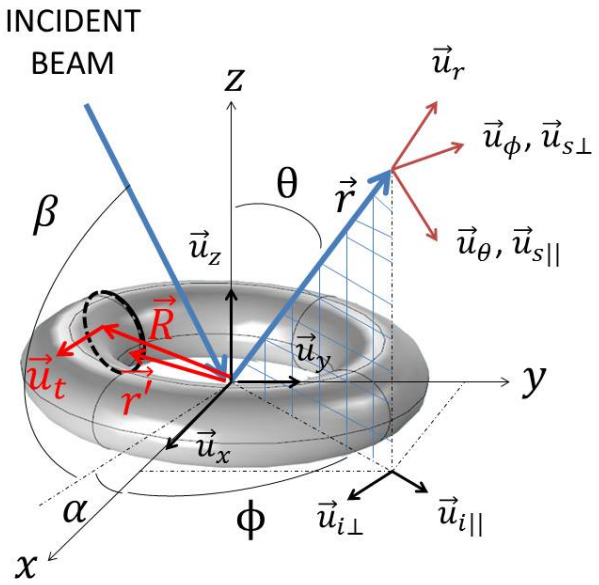

Fig. 3.7: Coordinate system used to calculate the Rayleigh-Debye scattering for the particular case of a ring with circular cross-section. The origin of the coordinate system is situated at the centre of the torus.

$$f(\theta,\phi;\alpha,\beta) = \frac{1}{2\pi^2 b^2}\sum_{n=-\infty}^{\infty} B_n A_{-n} \tag{3.37}$$

$$A_n = \frac{1}{\sqrt{2\pi}} i e^{in\psi} J_n(2\pi\rho a) \tag{3.38}$$

$$B_n = \sqrt{\frac{\pi}{2}} b^2 e^{in\psi} \times \sum_{m=0}^{\infty} \frac{(-1)^m}{m!(1+m)!}(\pi s b)^{2m} I_n^{(m)} \tag{3.39}$$

where ψ, ρ and ζ are defined through the reciprocal position vector $\vec{s}$

$$\vec{s} = \frac{\vec{u}_i - \vec{u}_r}{\lambda} = \rho\cos\psi\vec{u}_x + \rho\sin\psi\vec{u}_y + \zeta\vec{u}_z. \tag{3.40}$$

In the previous equations, n and m are bound variables (indices of summation). The integral $I_n^{(m)} = \int_0^{2\pi}(1-\cos^2\eta)^m e^{in\phi}d\phi$ and the detailed explanation on its analytical calculation can be found in Ref. [32]. Finally, η is the angle between the vector $\vec{u}_i - \vec{u}_r$ and the unit tangent $\vec{u}_t$ and is given by:

$$\vec{u}_t = \frac{\vec{t}}{|\vec{t}|} = \frac{\vec{R}}{|\vec{t}|d\phi} = -\sin\phi\vec{u}_x + \cos\phi\vec{u}_y + 0\vec{u}_z \tag{3.41}$$

$$\cos\eta = \vec{u}_s \cdot \vec{u}_t = \frac{\sin(\psi - \phi)}{\sqrt{1 + \frac{\zeta^2}{\rho^2}}} \tag{3.42}$$

with $\vec{t}$ being the tangent vector.

3.1.6 Computational Electromagnetics : The Finite Element Method

Computational Electromagnetics (CEM) is the numerical approximation to the solution of Maxwell's equations **(Appendix A**) for a particular system. [25] It comprises a number of powerful methods available, able to solve problems such as scattering field and absorption by nano-structures at different frequencies. Central to these approaches is the idea of discretizing some unknown electromagnetic property such as the surface current, the $\vec{E}$ field or the electric potential V. The process of discretization is known as meshing and entails subdividing the geometry under study into small elements. Within each element, a simple functional dependence is assumed for the spatial variation of the electromagnetic property. The accuracy of the method depends on the degree of discretization, i.e. mesh size. A vast number of different techniques and commercial codes are availiable; the Method of Moments (MoM), Finite Difference Time Domain (FDTD), Finite Element Method (FEM), and Discrete Dipole Approximation (DDA) being the most popular ones to calculate light scattering problems [24, 25, 30]. Some characteristics, strengths and limits of these methods are described in Table 3.1.

Tab. 3.1: Overview of CEM techniques.

Method	Equation type	Domain	Far-field radiation condition	Discretized property
MoM	integral	frequency	yes	surface current
FEM	differential	frequency	no	$\vec{E}$, V
FDTD	differential	time	no	$\vec{E}$, V
DDA	integral	frequency	yes	dipole moment

FEM is a well-known numerical technique for solving partial differential equations that can be applied to a variety of non trivial problems in mechanics, electromagnetism, heat transport, etc. Due to the circumstance that the mesh is not confined to a rectangular domain [28], FEM is particularly suited to study complex shapes, hence suitable for single nano-helices and arrays of them. Furthermore, another main advantage of FEM over other numerical techniques is its simplicity when handling dispersive materials. Also, it provides an adaptive mesh which size depends on the local geometry and material properties of the problem. Its main general disadvantage is the calculation of the scattered distributions

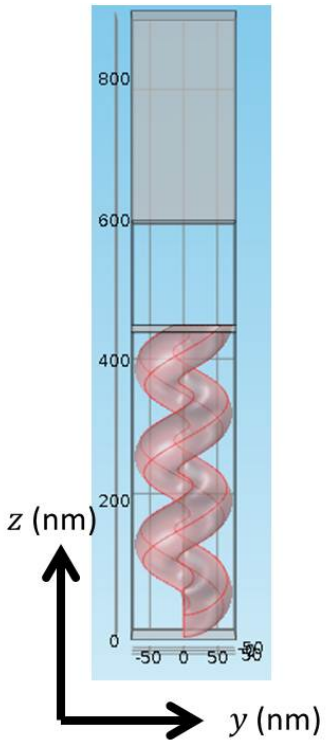

Fig. 3.8: Utilized FEM simulation cell

in the *far-field*, however, these distributions can be obtained from the FEM results using the analytical Stratton-Chu integral equation [33].
A FEM analysis of a problem consist of four basic steps [25–27]. First, the solution region is divided into a number of non-overlapping subregions or elements. Second, the governing algebraic partial differential equations (PDEs) for each element are derived provided that the potential at the vertices are known (boundary conditions). Third, all the elements are connected in the solution region. Finally, the obtained system of equations is solved using the variational approach (instead of solving directly the PDEs, one can work with an equivalent problem, an energy functional, whose minimum corresponds to the solution of the PDEs). **Appendix B** further explains and shows the implementation of these steps by solving a simple example (Poissons' equation for homogeneous media) using FEM.

Modelling the scattering from a nano-helix using COMSOL

COMSOL MULTIPHYSICS^{TM} is a commercially available FEM package. It handles most of the aforementioned FEM details, including meshing generation, equation definition and choice of the solver algorithm. What remains to the user is to define the problem geometry, material properties and boundary conditions. The multiphysics package makes it particularly suited for solving interconnected problems, for example photothermal energy conversion in plasmonic particles.

In this thesis, I used COMSOL to simulate the *near-field* intensity of the nano-helix forests and their optical cross-sections in the *far-field*. The cell used for simulating a periodic array of helices is shown in Fig. 3.8. It has the dimension of 150 nm in the x- and y-axis (which corresponds to the periodicity of the grown samples, see **Section 5.1**) and a height of 1200 nm. A perfect electric conductor, PEC, (see **Appendix A**) is used to represent the 80 nm optically thick Ag layer placed under the helices (see **Section 5.1**). Periodic boundary conditions are used to simulate an array with periodicity of 150 nm in the x- and y- directions. A perfectly matched layer, PML, boundary condition (**Appendix B**) is used to absorb the scattered field in the positive z-direction.
The optical *near-field* intensity distribution is calculated as $I = |\vec{E} \cdot \vec{E}^{\dagger}|$, where the incident light is polarized normal to the substrate in the y-direction. The simulated helix dimensions (pitch, diameter, number of turns and wire diameter) are those of the experimental nano-helices (see **Section 6.2**). In additon, the effects of absorption and scattering can be separated using the FEM method as follows. The absorbed power P_{abs} is proportional to $P_{abs} \propto \int_v |\vec{E} \cdot \vec{E}^{\dagger}| dv$, where v is the volume of the nano-helix. The specular scattered power P_{sca} can be calculated for the samples in consideration from the power of the relative field leaving the top surface above the scatterer and is given by $P_{sca} \propto \int_S (\vec{E} \times \vec{H}) d\vec{S}$, where S is the surface above the scatterer.

3.1.7 Fundamentals of Raman scattering

Raman scattering or the Raman effect is an inelastic scattering of light discovered by C.V. Raman [34] after its theoretical prediction by A. Smekal [35]. Experimentally [36], when a high intensity laser radiation is passed through a sample, photons from the laser beam excite electrons within the sample to a virtual energy state (real energy states give rise to resonant Raman processes [37]). Upon relaxation, the electrons can fall back to the state that they started from, reemitting a photon with the same energy as the exciting photon. This leads to the previously explained elastic (Rayleigh) scattering (see Fig. 3.9A). However, it is possible for the discussed electrons to relax back into an state which has different energy than the state they started in. For example, in a molecule this excited state could be some vibrational state. In this inelastic case, the original photon and the reemitted photon differ in energy by the amount which separates the initial and the excited states, which is referred to as the Raman effect. In perturbation theory, the Raman effect corresponds to the absorption and subsequent emission of a photon via an intermediate quantum state of a material, that is, is a second order process. The Raman interaction leads to two possible outcomes (see Fig. 3.9B,C):

- The sample absorbs energy and the emitted photon has a lower energy than the absorbed photon. This situation is named Stokes Raman scattering (Fig. 3.9B).
- The sample provides energy and the emitted photon has a higher energy than the

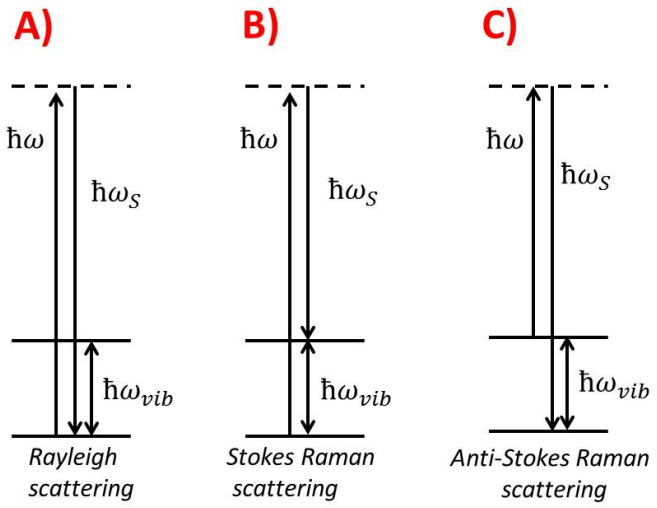

Fig. 3.9: Rayleigh and Raman scatterings. A) Rayleigh scattering: the scattered photon has an energy ($\hbar\omega_S$) equal to the energy of the excited photon ($\hbar\omega$). B) Stokes Raman scattering: the scattered photon has an energy ($\hbar\omega_S$) smaller than the energy of the exciting photon ($\hbar\omega$). The energy difference ($\hbar\omega_{vib}$) corresponds to the substraction of the energy level of an excited molecular state, here assumed to be a vibrational one, and the initial energy level of the electron. C) Anti-Stokes Raman scattering: the scattered photon has an energy bigger than the energy of the exciting photon.

absorbed photon. This situation is called anti-Stokes Raman scattering (Fig. 3.9C).

The spectrum of the scattered photons is termed the Raman spectrum. It shows the intensity of the inelastic scattered light as a function of its frequency difference to the incident photons. The position of corresponding Stokes and anti-Stokes peaks form a symmetric pattern around the incident frequency. These frequency shifts are symmetric because they correspond to the energy difference between the same upper and lower resonant states. The intensities of the pairs of features will typically be different, though. They will depend on the population of the initial state of the material. In thermodynamic equilibrium, the energetically upper state will be less populated than the lower state. Therefore, the rate of transitions from the lower to the upper state (Stokes transitions) will be higher than in the opposite direction (anti-Stokes transitions). Therefore, Stokes scattering peaks are higher in intensity than anti-Stokes scattering peaks, since the ratio of these two peaks depends on the temperature. This property can be used to determine the temperature of the sample. At this stage it should be pointed out that the Raman effect differs from the process of *fluorescence*. Although the result of both processes is in essence the same, the major difference is that the Raman effect takes place for any frequency of the incident light. In other words, a fluorescence peak is anchored at a specific frequency, whereas a Raman peak maintains a constant separation from the excitation frequency.

3.2 Nanostructured metamaterials

Metamaterials are *effectively homogeneous*[3] artificial media engineered to have electromagnetic properties that may not be found in nature and/or in the material they are made from. The tuneability of the electromagnetic properties in these complex media is achieved by tailoring the structural shape of the scattering elements, selecting their inner arrangement (spacing) and/or their growth material. In general, the propagation of electromagnetic signals in metamaterials can be affected in several ways [38] such as:

- *anisotropy*: dependency on the spatial direction;
- *chirality*: magneto-electric coupling of the system;
- *non-linearity*: emission of absorbed energy at different frequencies;
- *dispersion*: change in velocity of the electromagnetic wave depending on its wavelegth.

The problem of solving the electromagnetic response of metamaterials is the problem of solving the four *Maxwell's equations* and the *continuity equation* subjected to the corresponding boundary conditions (**Appendix A**). These five equations state the relationships between the fundamental electromagnetic quantities at a position $\vec{r}$ and time t. They are the electric field vector $\vec{E}$ [V/m], the electric flux density $\vec{D}$ [C/m^2], the magnetic field vector $\vec{H}$ [A/m], the magnetic flux density $\vec{B}$ [T], the current density $\vec{J}$ [A/m^2] and the scalar electric charge density ρ [C/m^2].
Out of the five equations mentioned, only three are independent. To obtain a solvable system, we need two more equations describing the macroscopic properties of the medium under study, the so-called *constitutive relations*. These are for example [39]:

$$\vec{D}(\vec{r},t) = \mathcal{F}\{\vec{E}(\vec{r},t), \vec{H}(\vec{r},t)\} \tag{3.43}$$

$$\vec{B}(\vec{r},t) = \mathcal{G}\{\vec{E}(\vec{r},t), \vec{H}(\vec{r},t)\} \tag{3.44}$$

where $\mathcal{F}$ and $\mathcal{G}$ are in general non-linear functions of $\vec{E}(\vec{r},t)$ and $\vec{H}(\vec{r},t)$ and represent a non-linear, spatial and temporal non-local (dispersive) system.
Determining the relationship between the flux densities $\vec{D}(\vec{r},t)$ and $\vec{B}(\vec{r},t)$ and the fields $\vec{E}(\vec{r},t)$ and $\vec{H}(\vec{r},t)$ starts with the definition of the auxiliary fields $\vec{D}(\vec{r},t)$ and $\vec{H}(\vec{r},t)$:

$$\vec{D}(\vec{r},t) = \epsilon_0 \vec{E}(\vec{r},t) + \vec{P}(\vec{r},t) \tag{3.45}$$

$$\vec{H}(\vec{r},t) = \mu_0^{-1} \vec{B}(\vec{r},t) - \vec{M}(\vec{r},t) \tag{3.46}$$

[3] For a given wavelength λ, effectively homogeneous materials are materials composed from structures whose average separation δ is much smaller than λ.

where $\vec{P}(\vec{r},t)$ is the electrical polarization field (density of permanent induced dipoles) and $\vec{M}(\vec{r},t)$ is the magnetization field (density of permanent magnetic dipole moments), which are defined in terms of microscopic bound charges and bound currents respectively. For most materials, the constitutive relations are in general not linear. Calculating the constitutive relations from first principles involves determining how $\vec{P}(\vec{r},t)$ and $\vec{M}(\vec{r},t)$ are created from a given $\vec{E}(\vec{r},t)$ and $\vec{B}(\vec{r},t)$. These relations may be empirical (based on measurements), or theoretical (based on mechanics, transport theory or other tools of condensed matter physics).

3.2.1 Linear electromagnetic metamaterials

For frequency-dependent fields acting on spatially local (non-dispersive, homogeneous) materials, the most convenient way to restructure the constitutive relations presented in Eqs. 3.43 is (see **Appendix A**):

$$\vec{D}(\vec{r},\omega) = \mathcal{F}\{\vec{E}(\vec{r},\omega),\vec{H}(\vec{r},\omega)\} \tag{3.47}$$

$$\vec{B}(\vec{r},\omega) = \mathcal{G}\{\vec{E}(\vec{r},\omega),\vec{H}(\vec{r},\omega)\} \tag{3.48}$$

Being interested only in the linear response of a medium, the functions $\mathcal{F}$ and $\mathcal{G}$ are approximated as linear operators. On this basis, the most general type of linear medium is called *bianisotropic* [38] and it is characterized by the following frequency-dependent constitutive relations:

$$\vec{D}(\vec{r},\omega) = \overline{\overline{\epsilon_{EH}}}(\vec{r},\omega)\vec{E}(\vec{r},\omega) + \overline{\overline{\xi_{EH}}}(\vec{r},\omega)\vec{H}(\vec{r},\omega) \tag{3.49}$$

$$\vec{B}(\vec{r},\omega) = \overline{\overline{\zeta_{EH}}}(\vec{r},\omega)\vec{E}(\vec{r},\omega) + \overline{\overline{\mu_{EH}}}(\vec{r},\omega)\vec{H}(\vec{r},\omega) \tag{3.50}$$

where $\overline{\overline{\epsilon_{EH}}}(\vec{r},\omega)$ is called permittivity, $\overline{\overline{\mu_{EH}}}(\vec{r},\omega)$ permeability, and $\overline{\overline{\xi_{EH}}}(\vec{r},\omega)$and $\overline{\overline{\zeta_{EH}}}(\vec{r},\omega)$ are magneto-electric parameters of the medium. All of these elements are 3 x 3 constitutive dyadics (second-rank Cartesian tensors) [39].
Bianisotropic media are systems in which each flux density ($\vec{D}(\vec{r},\omega)$, $\vec{B}(\vec{r},\omega)$) depends on both $\vec{E}(\vec{r},\omega)$ and $\vec{H}(\vec{r},\omega)$. In contrast, in *anisotropic* media, each flux-density depends only on one field, *i.e.*, the magnetoelectric dyadics are zero. *Bi-isotropic* media are systems in which each flux density ($\vec{D}(\vec{r},\omega)$,$\vec{B}(\vec{r},\omega)$) depends on $\vec{E}(\vec{r},\omega)$ and $\vec{H}(\vec{r},\omega)$, and the constitutive dyadics do not depend on the spatial direction. Finally, *isotropic* media do not depend on any particular spatial direction, and each flux density depends only on $\vec{E}(\vec{r},\omega)$ or $\vec{H}(\vec{r},\omega)$. A summary of linear bi-anisotropic media and their corresponding constitutive relations is shown in Fig. 3.10A. Furthermore, depending on the structural morphology of a medium, there exist several possible types of spatial anisotropies. All of

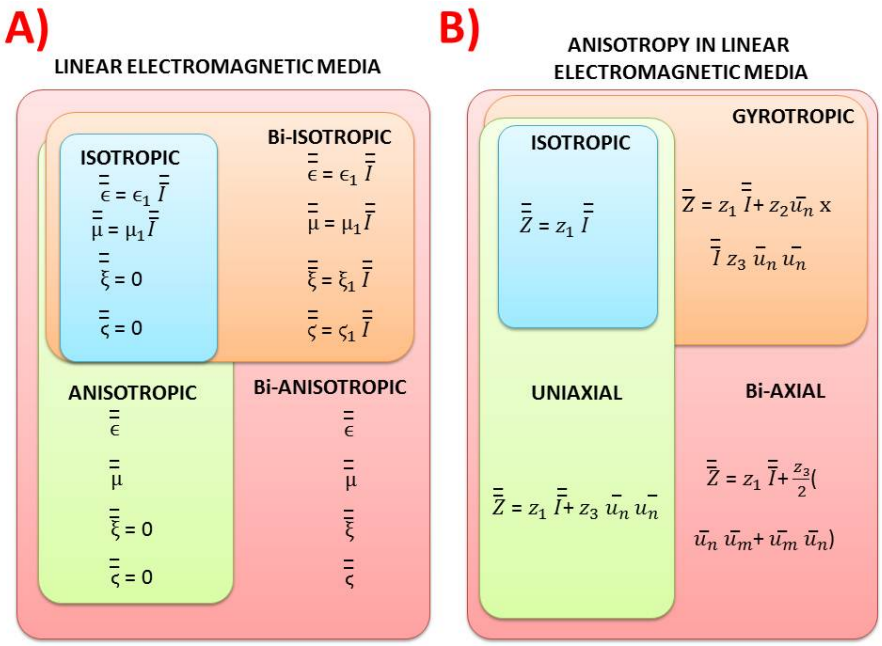

Fig. 3.10: Summary of linear bi-anisotropic media [9,38]. $\overline{\overline{I}}$ is the unit dyadic, $\vec{u}_n$ and $\vec{u}_m$ represent the main axes of the uniaxial or biaxial media and $\overline{\overline{Z}}$ accounts for the permittivity, permeability or magneto-electric dyadic of the medium. Meanwhile, z_1, z_2 and z_3 the corresponding scalar parameters of $\overline{\overline{Z}}$ following certain directions of the material.

them are characterized by certain well-known properties captured in the dyadic structure: isotropy, uniaxially, gyrotropy and biaxially are some of them as depicted in Fig. 3.10B.

The theoretical analysis of the constitutive relations dyadics can be simplified depending on the specific medium for which they are going to be calculated. Two common conditions in electromagnetic media are the Lorentz-reciprocity and/or the Losslessness. Both constraints impose symmetry conditions which symplify the constitutive dyadics calculation. The notion of reprocity is linked to the symmetry of the system with respect to the time reversal operation. In particular, for a Lorentz-reciprocal medium one finds:

$$\overline{\overline{\epsilon_{EH}}} = \overline{\overline{\epsilon_{EH}}}^{T}, \quad \overline{\overline{\mu_{EH}}} = \overline{\overline{\mu_{EH}}}^{T}, \quad \overline{\overline{\xi_{EH}}} = \overline{\overline{-\zeta_{EH}}}^{T} \tag{3.51}$$

Meanwhile, a medium is lossless when it does not absorb a significant amount of energy of a propagating electromagnetic wave per unit distance. In this case:

$$\overline{\overline{\epsilon_{EH}}} = \overline{\overline{\epsilon_{EH}}}^{\dagger}, \quad \overline{\overline{\mu_{EH}}} = \overline{\overline{\mu_{EH}}}^{\dagger}, \quad \overline{\overline{\xi_{EH}}} = \overline{\overline{\zeta_{EH}}}^{\dagger}. \tag{3.52}$$

3.2.2 Calculation of constitutive relations in metamaterials: Homogenization formalisms

As previously mentioned, a material composed of individual structures (often periodically arranged) may be characterized as an effectively homogeneous medium, when the electromagnetic wavelengths are sufficiently large in comparison with the length scales of the composite, *i.e.*, it can be considered as a metamaterial. A proper effective medium description allows to describe the averaged electromagnetic response of the metamaterial (*i.e.* its constitutive relations) by knowing the elementary constituents and their spatial distribution. This information is highly valuable when designing devices with unusual electromagnetic properties for custom applications.

Considerable advances have been achieved in the homogeneization processess of linear metamaterials. Homogeneization techniques were traditionally fully theoretical [38–40], however novel heuristic approaches have emerged, avoiding some limitations of the analytical methods [41, 42]. In more detail, on the one hand, analytical homogeneization methods are mainly restricted to the quasistatic limit or specific geometries. Nevertheless, recent theories are starting to deal with homogenization methods for spatially dispersive materials [40]. The usual scope of classical homogenization formalisms is the calculation of some 'mixing rules' which contain the effective constitutive relations as a function of the constituent materials, their structure and their fractional volumes [40]. Some of these mixing models are the Clausius-Mossotti formalism, Maxwell-Garnett formalism, the Bruggeman formalism and the Strong-Property-Fluctuation theory [38, 40]. On the other hand, heuristic homogeneization techniques are mainly performed by numerical or experimentally retrieved field averaging within the unit cell defining the metamaterial [41, 42].

In the following, the Dilute Mixtures [43] and Maxwell Garnett [43] homogeneization approaches for bianisotropic materials will be revisited. Particular solutions will be reported for the case of helical constituents arranged in bi-isotropic and uniaxial configurations.

3.2.3 Dilute Mixtures and Maxwell-Garnett formalisms

Any bottom-up approach to macroscopically model heterogeneous media start from the response of a single scattering element. First assume that the mixture (heterogeneous system) to be analyzed consists of an external isotropic medium (ϵ_2, μ_2) where bi-anisotropic inclusions ($\overline{\overline{\epsilon_1}}$, $\overline{\overline{\mu_1}}$, $\overline{\overline{\xi_1}}$, $\overline{\overline{\zeta_1}}$) are embedded according to Fig. 3.11. The coherent wavelength that penetrates the composite medium is considerably larger than the characteristic inhomogeneity measure (for example, the inclusion size) of the mixture. That is, the system is treated within the quasi-static limit[4] [43]. In addition, the system is supposed to be in the dilute regime with a small density of inclusions (< 30 %).

[4] In this context, the quasi-static limit involves a constant electric field at any point within the particle.

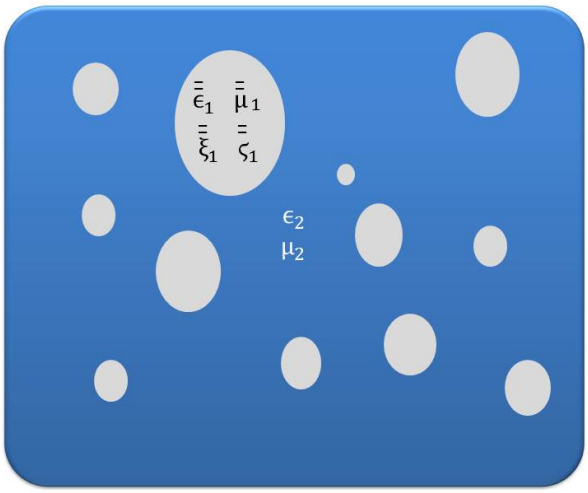

Fig. 3.11: Mixture of an external isotropic medium (ϵ_2, μ_2) with bi-anisotropic inclusions ($\overline{\overline{\epsilon_1}}$, $\overline{\overline{\mu_1}}$, $\overline{\overline{\xi_1}}$, $\overline{\overline{\zeta_1}}$).

Dilute Mixtures formalism

The problem of finding out effective bi-anisotropic parameters of a mixture requires solving the average electric, $\langle\vec{p}_e\rangle$, and magnetic, $\langle\vec{p}_m\rangle$, dipole moments in the medium. When the mixture consists of inclusions in a background matrix with zero electric and magnetic polarization, it is the magnitude and density of the dipole moments of the inclusions that determine the average polarizations of the total system. To be able to average the dipole moments, there is a need to know both, the polarizabilities of the inclusions and the local field exciting them. The effective material parameter relations for the bi-anisotropic mixture (Eq. 3.49) can be re-written as:

$$\langle\vec{d}\rangle = M_{eff} \cdot \langle\vec{f}\rangle \tag{3.53}$$

with the flux- and field-vectors:

$$\langle\vec{d}\rangle = \begin{pmatrix}\vec{D}\\ \vec{B}\end{pmatrix}, \quad \langle\vec{f}\rangle = \begin{pmatrix}\vec{E}\\ \vec{H}\end{pmatrix} \tag{3.54}$$

and the effective material dyadic

$$M_{eff} = \begin{pmatrix} \overline{\overline{\epsilon_{EH}}} & \overline{\overline{\xi_{EH}}} \\ \overline{\overline{\zeta_{EH}}} & \overline{\overline{\mu_{EH}}} \end{pmatrix} \tag{3.55}$$

which contains the 36 components (6×6 matrix) of the effective description of the entire complex medium (inclusions and background). In terms of the polarizability of an inclusion, the six-vector dipole moment (containing both $\langle \vec{p}_e \rangle$ and $\langle \vec{p}_m \rangle$) reads:

$$\langle \vec{p} \rangle = \mathcal{A} \langle \vec{f} \rangle \tag{3.56}$$

where $\mathcal{A}$ is the *bi-anisotropic* polarizability dyadic

$$\mathcal{A} = \begin{pmatrix} \overline{\overline{\alpha_{ee}}} & \overline{\overline{\alpha_{em}}} \\ \overline{\overline{\alpha_{me}}} & \overline{\overline{\alpha_{mm}}} \end{pmatrix} \tag{3.57}$$

$\overline{\overline{\alpha_{ee}}}$ and $\overline{\overline{\alpha_{mm}}}$ are the electric and magnetic polarizability dyadics, respectively; meanwhile $\overline{\overline{\alpha_{me}}}$ and $\overline{\overline{\alpha_{em}}}$ represent the two magneto-electric polarizabilities. Therefore, the mixture with bianisotropic constituents having a density $\mathcal{N}$ of such inclusions in an isotropic background environment (the latter described by the dyadic M_2) has an effective material six-dyadic in the dilute mixture formalism of [43]:

$$M_{\text{eff}} = M_2 + \mathcal{N} \cdot \mathcal{A} = \begin{pmatrix} \epsilon_2 \overline{\overline{I}} & 0 \\ 0 & \mu_2 \overline{\overline{I}} \end{pmatrix} + \mathcal{N} \begin{pmatrix} \overline{\overline{\alpha_{ee}}} & \overline{\overline{\alpha_{em}}} \\ \overline{\overline{\alpha_{me}}} & \overline{\overline{\alpha_{mm}}} \end{pmatrix}. \tag{3.58}$$

Maxwell-Garnett formalism

The approximation of the Dilute Mixture formalism can be substantially improved using the well-established Maxwell-Garnett approach. The essential novel step in the Maxwell-Garnett formalism is at the calculation of the dipole moment of a single polarizable inclusion. It is not the average field $\langle \vec{f} \rangle$ that excites the inclusion but rather the local field $\vec{f}_{\text{loc}} = \begin{pmatrix} \vec{E}_{\text{loc}} \\ \vec{H}_{\text{loc}} \end{pmatrix}$, which takes into account the effect of the averaged surrounding polarization $\langle \vec{P} \rangle = \mathcal{N} \langle \vec{p} \rangle = \mathcal{N} A \langle \vec{f}_{\text{loc}} \rangle$. Therefore, the local vector field action on a given inclusion is:

$$\langle \vec{f}_{\text{loc}} \rangle = \langle \vec{f} \rangle + \frac{M_2^{-1}}{3} \langle \vec{P} \rangle = \langle \vec{f} \rangle + \begin{pmatrix} \overline{\overline{I}}/3\epsilon_2 & 0 \\ 0 & \overline{\overline{I}}/3\mu_2 \end{pmatrix} \langle \vec{P} \rangle; \tag{3.59}$$

and the effective dyadic M_{eff} can be then expressed as:

$$M_{\text{eff}} = M_2 + M_2 \left(M_2 - \tfrac{N}{3}\mathcal{A} \right)^{-1} \mathcal{N} \cdot \mathcal{A} \tag{3.60}$$

Note that this expression returns the dilute case when $\mathcal{N} \to 0$. In detail, the three-dyadics read [43]:

$$\overline{\overline{\epsilon_{EH}}} = \epsilon_2 \overline{\overline{I}} + 3\epsilon_2 (\overline{\overline{K}}_2^{-1} - \overline{\overline{I}}) \tag{3.61}$$

$$\overline{\overline{\xi_{EH}}} = \overline{\overline{K}}_2^{-1} \cdot \mathcal{N} \overline{\overline{\alpha_{em}}} \cdot \left(\overline{\overline{I}} - \tfrac{\mathcal{N} \overline{\overline{\alpha_{mm}}}}{3\epsilon_2} \right)^{-1} \tag{3.62}$$

$$\overline{\overline{\zeta_{EH}}} = \overline{\overline{K}}_1^{-1} \cdot \mathcal{N} \overline{\overline{\alpha_{me}}} \cdot \left(\overline{\overline{I}} - \tfrac{\mathcal{N} \overline{\overline{\alpha_{ee}}}}{3\epsilon_2} \right)^{-1} \tag{3.63}$$

$$\overline{\overline{\mu_{EH}}} = \mu_2 \overline{\overline{I}} + 3\mu_2 (\overline{\overline{K}}_1^{-1} - \overline{\overline{I}}) \tag{3.64}$$

where $\overline{\overline{K}}_2$ and $\overline{\overline{K}}_1$ are determined by:

$$\overline{\overline{K}}_2 = \overline{\overline{I}} - \frac{\mathcal{N} \overline{\overline{\alpha_{ee}}}}{3\epsilon_2} - \frac{\mathcal{N} \overline{\overline{\alpha_{em}}}}{3\mu_2} \cdot \left(\overline{\overline{I}} - \tfrac{\mathcal{N} \overline{\overline{\alpha_{mm}}}}{3\mu_2} \right)^{-1} \cdot \frac{\mathcal{N} \overline{\overline{\alpha_{me}}}}{3\epsilon_2} \tag{3.65}$$

$$\overline{\overline{K}}_1 = \overline{\overline{I}} - \frac{\mathcal{N} \overline{\overline{\alpha_{mm}}}}{3\mu_2} - \frac{\mathcal{N} \overline{\overline{\alpha_{me}}}}{3\epsilon_2} \cdot \left(\overline{\overline{I}} - \tfrac{\mathcal{N} \overline{\overline{\alpha_{ee}}}}{3\epsilon_2} \right)^{-1} \cdot \frac{\mathcal{N} \overline{\overline{\alpha_{em}}}}{3\mu_2} \tag{3.66}$$

A further development in the calculation of the effective material six-dyadic M_{eff} involves the determination of the response of the individual inclusions, which is done by calculating the polarizability dyadic $\mathcal{A}$. This effect will depend on the size, shape and material of each elementary constituent[5]. However, previous to this concrete step, it is convenient to exploit symmetries of the system under study in order to simplify the expressions of M_{eff} and $\mathcal{A}$ [43]. For example, nano-helices randomly arranged would form a bi-isotropic system (Fig. 3.12A), meanwhile, a uniaxial bi-anisotropic system can be formed by the nano-helices with their axes alligned along one axis (Fig. 3.12B). In the following, these two special cases will be discussed here before the introduction of the polarizabilities of a single (nano-)helix structure.

Bi-isotropic composites.

The polarizabilities ($\overline{\overline{\alpha_{ij}}}$) in Eqs. 3.61 to 3.65 are given for a given aligned orientation of the inclusions. In the case of a random distribution, *i.e.*, a bi-isotropic medium, the dyadics are scalars:

[5] Note, that in the case of regular arrays of nano-structures $\mathcal{A}$ will be the same for all the inclusions.

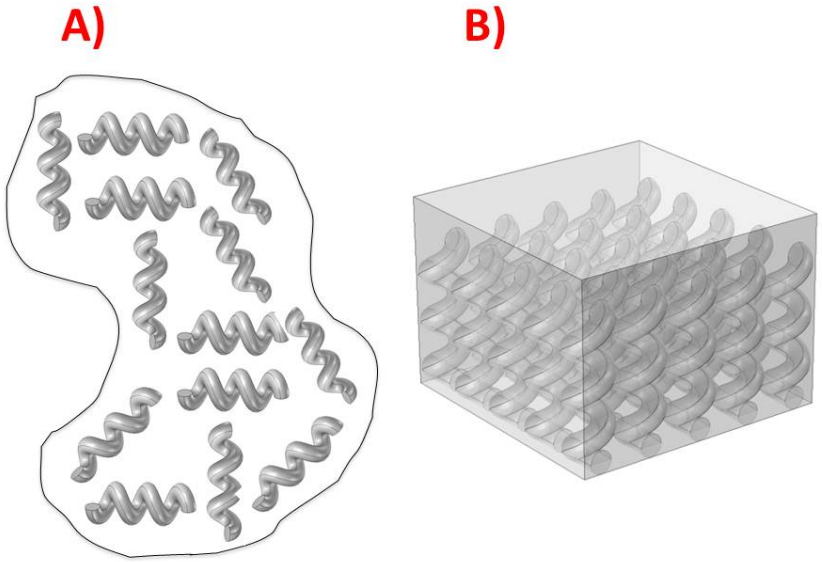

Fig. 3.12: A) Bi-isotropic and B) uniaxial bi-anisotropic systems formed by different arrangements of helical inclusions.

$$\alpha_{ij} = \frac{tr(\overline{\overline{\alpha_{ij}}})}{3} \tag{3.67}$$

where $i, j = \{m, e\}$ and $tr(\overline{\overline{\alpha_{ij}}})$ is the trace of the polarizability dyadic. In this case, the Maxwell-Garnett equations for bi-isotropic (and lossless) medium are given by [44]:

$$\epsilon_{EH} = \frac{\epsilon_2 \left(1 + \frac{2\mathcal{N}\alpha_{ee}}{3}\right)\left(1 - \frac{\mathcal{N}\alpha_{mm}}{3}\right) + 2\mathcal{N}^2 \frac{\alpha_{em}\alpha_{me}}{9}}{\left(1 - \frac{\mathcal{N}\alpha_{ee}}{3}\right)\left(1 - \frac{\mathcal{N}\alpha_{mm}}{3}\right) - \mathcal{N}^2 \frac{\alpha_{em}\alpha_{me}}{9}} \tag{3.68}$$

$$\xi_{EH} = \frac{i\mathcal{N}\alpha_{em}\sqrt{\mu_2\epsilon_2}}{\left(1 - \frac{\mathcal{N}\alpha_{ee}}{3}\right)\left(1 - \frac{\mathcal{N}\alpha_{mm}}{3}\right) - \mathcal{N}^2 \frac{\alpha_{em}\alpha_{me}}{9}} \tag{3.69}$$

$$\mu_{EH} = \frac{\mu_2 \left(1 + \frac{2\mathcal{N}\alpha_{ee}}{3}\right)\left(1 - \frac{\mathcal{N}\alpha_{mm}}{3}\right) + 2\mathcal{N}^2 \frac{\alpha_{em}\alpha_{me}}{9}}{\left(1 - \frac{\mathcal{N}\alpha_{ee}}{3}\right)\left(1 - \frac{\mathcal{N}\alpha_{mm}}{3}\right) - \mathcal{N}^2 \frac{\alpha_{em}\alpha_{me}}{9}} \tag{3.70}$$

Note, since the medium is considered as lossless, $\zeta_{EH} = -\xi_{EH}$.

Uniaxial bi-anisotropic composites.

Uniaxial chiral composites are caracterized by uniaxial constitutive relations with a symmetric cross-coupling component [43]. This means that the constitutive dyadics in Eq.

3.49 are expressed as $\overline{\overline{\mathcal{Z}}} = z_1\overline{\overline{I}}_t + z_2\vec{u}_z\vec{u}_z$, where $\overline{\overline{\mathcal{Z}}}$ stands for any of the consitutive parameter dyadics ($\overline{\overline{\epsilon_{EH}}}, \overline{\overline{\xi_{EH}}}, \overline{\overline{\mu_{EH}}}, \overline{\overline{\zeta_{EH}}}$), the unit vector $\vec{u}_z$ indicates the preferred direction in the system, $\overline{\overline{I}}_t = \overline{\overline{I}} - \vec{u}_z\vec{u}_z$ is the transverse unit dyadic, and z_1 and z_2 are material's parameters in the transversal and the preferred direction of the media. In these systems, the particles are oriented in such a way that in the transverse plane the averaged structure is isotropic. The averaged individual polarizabilities take then the form [43]:

$$\bar{\bar{\alpha}}_{ee}^{(av)} = \alpha_{ee}^{(z)}\vec{u}_z\vec{u}_z + \alpha_{ee}^{(t)}\overline{\overline{I}}_t \tag{3.71}$$

$$\bar{\bar{\alpha}}_{mm}^{(av)} = \alpha_{mm}\vec{u}_z\vec{u}_z \tag{3.72}$$

$$\bar{\bar{\alpha}}_{me}^{(av)} = \alpha_{me}\vec{u}_z\vec{u}_z \tag{3.73}$$

$$\bar{\bar{\alpha}}_{em}^{(av)} = -\alpha_{me}^{(av)} \tag{3.74}$$

The averaged scalar coefficients are related to the polarizabilities of single particles by:

$$\alpha_{ee}^{(z)} = \alpha_{ee}^{(zz)} \tag{3.75}$$

$$\alpha_{ee}^{(t)} = \frac{1}{2}\left(\alpha_{ee}^{(xx)} + \alpha_{ee}^{(yy)}\right) \tag{3.76}$$

$$\alpha_{mm}^{(z)} = \alpha_{mm}^{(zz)} \tag{3.77}$$

$$\alpha_{me} = \alpha_{me}^{(zz)} \tag{3.78}$$

The evaluation of the inverse dyadics $\bar{\bar{K}}_2^{-1}$ and $\bar{\bar{K}}_1^{-1}$ appearing in the general relations (Eqs. 3.61), leads to:

$$\bar{\bar{K}}_2^{-1} = \frac{1}{1 - \frac{\mathcal{N}\alpha_{ee}^{(t)}}{3\epsilon_2}}\overline{\overline{I}}_t + \frac{1}{D_n}\left(1 - \tfrac{\mathcal{N}\alpha_{mm}}{3\mu_2}\right)\vec{u}_z\vec{u}_z \tag{3.79}$$

$$\bar{\bar{K}}_1^{-1} = \overline{\overline{I}}_t + \frac{1}{D_n}\left(1 - \tfrac{\mathcal{N}\alpha_{ee}^{(z)}}{3\epsilon_2}\right)\vec{u}_z\vec{u}_z \tag{3.80}$$

where

$$D_n = \left(1 - \tfrac{\mathcal{N}\alpha_{ee}^{(z)}}{3\epsilon_2}\right)\left(1 - \tfrac{\mathcal{N}\alpha_{mm}}{3\mu_2}\right) + \frac{\mathcal{N}^2\alpha_{me}^2}{9\epsilon_2\mu_2}. \tag{3.81}$$

Finally, the averaged constitutive parameters for lossless uniaxial chiral media can be written now as:

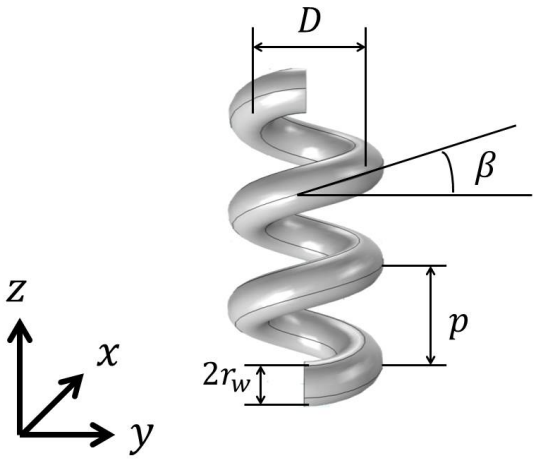

Fig. 3.13: Helix and associated structural parameters. D is the diameter of the helix, p is the pitch of the helix, r_w is the radius of its constituting wire and β is the inclination of the helix with respect to the x-y plane.

$$\overline{\overline{\epsilon_{eff}}} = \left(\epsilon_2 + \frac{\mathcal{N}\alpha_{ee}^{(t)}}{1-\frac{\mathcal{N}\alpha_{ee}^{(t)}}{3\epsilon_2}}\right)\bar{\bar{I}}_t + \left[\epsilon_2 + \frac{1}{D_n}\left(\mathcal{N}\alpha_{ee}^{(z)} - \frac{\mathcal{N}^2}{3\mu_2}(\alpha_{ee}^{(z)}\alpha_{mm} + \alpha_{me}^2)\right)\right]\vec{u}_z\vec{u}_z \quad (3.82)$$

$$\overline{\overline{\mu_{eff}}} = \mu_2\bar{\bar{I}}_t + \left[\mu_2 + \frac{1}{D_n}\left(\mathcal{N}\alpha_{mm} - \frac{\mathcal{N}^2}{3\epsilon_2}(\alpha_{ee}^{(z)}\alpha_{mm} + \alpha_{me}^2)\right)\right]\vec{u}_z\vec{u}_z \quad (3.83)$$

$$\xi_{eff} = -\zeta_{eff} = -\frac{\mathcal{N}\alpha_{me}}{D_n}\vec{u}_z\vec{u}_z. \quad (3.84)$$

3.2.4 Polarizabilities of single helical structures.

Consider a N-turn helix of diameter D, pitch p and wire radius r_w oriented along the z-axis (Fig. 3.13) and embedded in a medium with permittivity ϵ_2. Let the wire be inclined at an angle β to the transverse x-y plane. The height of the helix is then $h = 2\pi N(D/2)\tan\beta$ and the length of the wire is $L = \frac{2\pi ND}{2\cos\beta}$. An AC excitation field E_z directed along the helix' longitudinal axis will induce a voltage hE_z along the wire. The current flowing is then $I = hE_z/Z_w$, where Z_w is the wire impedance. Z_w is constant for constant β (constant inductance) [44], and the generated electric dipole moment and corresponding electric polarizability are:

$$p_e = \frac{1}{i\omega}\int I dz = \frac{Ih}{i\omega} = \frac{E_z h^2}{i\omega Z_w} \quad (3.85)$$

$$\alpha_{ee} = \frac{p_e}{\epsilon_2 E_z} = \frac{h^2}{i\omega\epsilon_2 Z_w} \quad (3.86)$$

The current flowing along the wire also produces a magnetic moment p_m and a subsequent

magneto-electric coupling (chiral polarizability) α_{me} [44]:

$$p_m = \pi N I (D/2)^2 = \frac{\pi N E_z h (D/2)^2}{Z_w} \tag{3.87}$$

$$\alpha_{me} = \frac{p_m Z_2}{E_z} = \frac{\pi N h (D/2)^2 Z_2}{Z_w} \tag{3.88}$$

where Z_1 is the impedance of the surrounding medium.

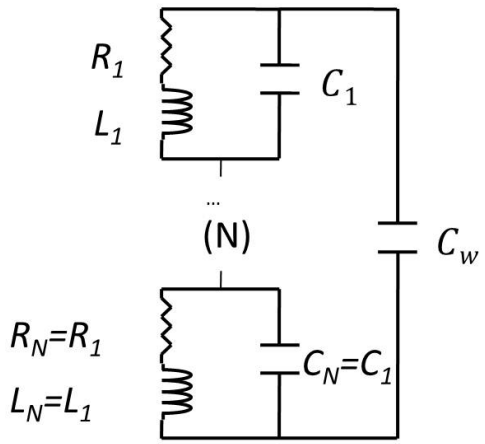

Fig. 3.14: Equivalent lumped resistor-inductor-capacitor (RLC) circuit of a N-turn helix. C_w is the existing capacitance between the tips of the helical wire. Meanwhile, R_i, L_i and C_i with $i = \{1, ..., N\}$ are the resistance, inductance and capacitance of each turn, respectively.

Next, considering a periodic magnetic excitation again directed parallel to the helix' longitudinal axis, H_z, it induces voltage and a current which are proportional to the flux enclosed [44]:

$$V = -N\pi(D/2)^2 i\omega\mu_2 H_z \tag{3.89}$$

$$I = -N\pi(D/2)^2 i\omega\mu_2 H_z / Z_w \tag{3.90}$$

The corresponding magnetic moment and magnetic polarizabilities are given by:

$$p_m = \pi N I (D/2)^2 = \frac{-N^2\pi^2(D/2)^4 i\omega\mu_2 H_z}{Z_w} \tag{3.91}$$

$$\alpha_{mm} = \frac{p_m}{H_z} = \frac{-i\omega\mu_2 N^2\pi^2(D/2)^4}{Z_w} \tag{3.92}$$

Finally, the impedance of the N-turn helix (Z_w) in the subwavelength regime, can be determined by a simple lumped RLC circuit [45, 46] as depicted in Fig. 3.14:

$$R = N\varrho\frac{l}{\pi r_w^2 - \pi(r_w - d_s)^2} \tag{3.93}$$

$$L = ND\mu_1\left[\ln\left(\tfrac{8D}{r_w}\right) - 2\right] \tag{3.94}$$

$$C = \frac{C_1}{N-1} + C_w = \frac{\pi^2 D\epsilon_2}{(N-1)\left[\ln\left(\frac{p}{2r_w} + \sqrt{(\frac{p}{2r_w})^2 - 1}\right)\right]} + \frac{2h\pi\epsilon_2}{\ln(h/r_w)} \tag{3.95}$$

where C_w is the existing capacitance between the tips of the helical wire, ϱ is the resistivity of the wire material and the skin effect depth d_s [47] is taken into account (see **Appendix A**).

3.3 Bulk and surface plasmons in metallic nano-structures

The interaction of metals with electromagnetic radiation is, to a great extent, determined by the free conduction electrons [18]. The response is described by the metal dielectric parameters, which vary considerably with frequency. In the optical range, the metal's free electron gas can support bulk and surface charge density oscillations called bulk and surface plasmons, respectively. Under specific conditions, the incident light that radiates the object couples with the surface plasmons to create self-sustaining, propagating electromagnetic waves with much shorter wavelength known as surface plasmon polaritons (SPPs) [48]. Similarly, if the electron gas is confined in two or three dimensions as in the case of subwavelength particles, the quantization of standing waves gives rise to Localized Surface Plasmon Resonances, LSPR. LSPR highly depend on the particle geometry and on the free electron density of the material under consideration [17, 30, 49, 50]. All these plasmonic resonances have distinct resonance frequencies and contribute considerably to modifying and tuning the *near-field* of the nano-structures at optical frequencies, offering *near-field* controllability within a subwavelength regime, in a clear similarity with radio-frequency (RF) antennas. [18, 20]
In this section, first the properties of bulk metals at optical frequencies are briefly described. Then, LSPR and SPPs resonances will be introduced. Finally, the analogies between RF antennas and their optical plasmonic counterparts will be discussed.

3.3.1 Metals at optical frequencies

The optical properties of metals can be described principally by the frequency-dependent complex permittivity ϵ_1 also called dielectric function or constant. This dielectric constant is mainly determined by [18]:

- Electrons moving freely within the material.
- Interband transitions taking place if the energy of the photons exceeds the interband energy difference of the metal.

The presence of an electric field, $\vec{E}$, displaces the free electrons and therefore creates associated dipole moments. With n the density of free electrons in the metal and $\vec{r}$ the electron displacement, the cumulative effect of all dipole moments results in a macroscopic polarization $\vec{P} = -ne < \vec{r} >$ which can be related to the electric field displacement $\vec{D}$ (see Eq. 3.45). Considering the metal as an isotropic medium, ϵ_1 can be expresed as [18]:

$$\epsilon_1 = 1 + \frac{|\vec{P}|}{\epsilon_0 |\vec{E}|}. \tag{3.96}$$

The displacement $\vec{r}$ (therefore $\vec{P}$) as a fuction of time t can be obtained by solving the equation of motion of the electrons under the influence of an external field.

Drude-Sommerfeld theory

The Drude-Sommerfeld model [18] considers only the effects of free electrons. In this case, $\vec{r}(t)$ can be obtained by the expression:

$$m_e \frac{\partial^2 \vec{r}}{\partial t^2} + m_e \Gamma \frac{\partial \vec{r}}{\partial t} = -e\vec{E}_0 e^{-i\omega t} \tag{3.97}$$

where e and m_e are the charge and the mass of the electrons and $\vec{E}_0$ and ω are the amplitude and frequency of the external field, respectively. The damping term Γ is given by $\Gamma = \frac{v_F}{l_f}$, where v_F is the Fermi velocity and l_f is the electron mean free path between scattering events.
Eq. 3.97 can be solved supposing that the electron displacement oscillates with the same frequency and in phase with the applied field, that is $\vec{r}(t) = \vec{r}_0 e^{-i\omega t}$ and $\vec{r}_0$ takes the following form [18]:

$$\vec{r}_0 = \frac{e\vec{E}_0}{m_e(\omega^2 + i\omega\Gamma)} \tag{3.98}$$

By inserting Eq. 3.98 into Eq. 3.96 we obtain the complex Drude-Sommerfeld dielectric function ϵ_{DS}:

$$\epsilon_{DS}(\omega) = 1 - \frac{\omega_p^2}{\omega^2 + i\Gamma\omega} = \epsilon'_{DS} + i\epsilon''_{DS} \tag{3.99}$$

$$\epsilon_{DS}(\omega) = 1 - \frac{\omega_p^2}{\omega^2 + \Gamma^2} + i\frac{\Gamma\omega_p^2}{\omega(\omega^2 + \Gamma^2)} \tag{3.100}$$

$$\tag{3.101}$$

where $\omega_p = \sqrt{\frac{ne^2}{m_e\epsilon_0}}$ is the *bulk plasma frequency*. This model gives accurate results for the optical properties of noble metals in the infrared spectra due to the absence of interband transitions in this region.

Interband transitions

High energy photons can promote electrons of lower-lying bands into the conduction band in metals, which is not considered by the Drude-Sommerfeld model. These interband transitions are present in any metal. They appear at short visible and UV wavelengths in noble metals (*e.g.* Ag, Au) or at longer wavelengths as the case of ferromagnetic metals

(*e.g.* Ni, Co) [51–53]. Classically, these transitions can be regarded as an excitation of bounded electrons. The equation of motion for a bound electron is

$$m\frac{\partial^2\vec{r}}{\partial t^2} + m\eta\frac{\partial\vec{r}}{\partial t} + \alpha\vec{r} = e\vec{E}_0 e^{-i\omega t} \tag{3.102}$$

where m is the effective mass of the bounded electrons, η is the damping constant describing radiative damping in the case of bound electrons and α is the spring constant of the potential that keeps the electron in place. Using Eq. 3.98, one can find the contribution of bound electrons to the dielectric function ϵ_{IT}:

$$\epsilon_{IT}(\omega) = 1 - \frac{\tilde{\omega}_p^2}{(\omega_0^2 - \omega^2) + i\eta\omega} = \epsilon'_{IT} + i\epsilon''_{IT} \tag{3.103}$$

$$\epsilon_{IT}(\omega) = 1 + \frac{\tilde{\omega}_p^2(\omega_0^2 - \omega^2)}{(\omega_0^2 - \omega^2)^2 + \eta^2\omega^2} + i\frac{\eta\tilde{\omega}_p^2\omega}{(\omega_0^2 - \omega^2)^2 + \eta^2\omega^2} \tag{3.104}$$

where the corresponding plasma frequency $\tilde{\omega}_p$ takes into account m, *i.e.* $\tilde{\omega}_p = \sqrt{\frac{ne^2}{m\epsilon_0}}$. In practice, permittivity models are more precise by taking into account both the free-electron ϵ_{DS} and the bound electron ϵ_{IT} contributions [18].

Due to practical and historical reasons, the complex permittivity ϵ_1 and permeablity μ_1 of any material are linked to its complex index of refraction $\tilde{n}_1$. At the same time, $\tilde{n_1}$ is composed of the optical constants such as the refractive index n_1 and the extinction coefficient k_1 which are used to describe the propagation and dissipation of electromagnetic waves in matter (see **Appendix A**). All of ϵ_1, μ_1, $\tilde{n}_1$, n_1 and k_1 are related by:

$$\tilde{n}_1 = n_1 + ik_1 = \frac{\sqrt{\epsilon_1\mu_1}}{c} = \frac{v_1}{c} \tag{3.105}$$

where c is the speed of light in vacuum and v_1 is the speed of light in the material in consideration.

Traditionally, the preferred plasmonic materials have been Au and Ag due to the low intrinsic losses through intraband and interband transitions in the VIS-NIR spectral range [18]. Nevertheless, more recently, materials like Ni, Al or Pt have generated an emerging interest due to their different electronic and magnetic properties [54, 55].

3.3.2 Localized Surface Plasmon Resonance

Localized surface plasmon resonance (LSPR) is a collective phenomenon where the confined conduction electrons oscillate coherently in response to external electromagnetic fields [17, 18]. LSPR requires zero or one dimensional confinement of the free electrons,

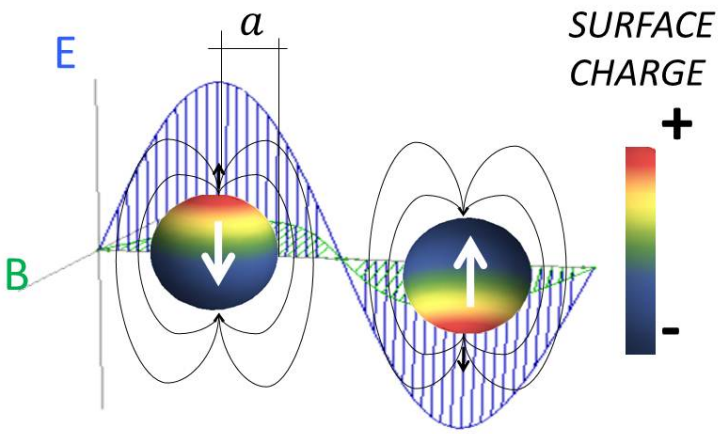

Fig. 3.15: Localized Surface Plasmon Resonance of a nano-sphere of radius a. The negative (blue) and the positive (red) free charges of the resulting dipole generates a restoring force, thus, forming a stationary plasmonic oscillation at the sphere surface.

which effectively is the case for 'small' subwavelength particles of any shape. If an electromagnetic wave in the UV-VIS-IR range is incident on a metallic nanoparticle, the electron gas gets electrically polarized at the surface. The negative and the positive charge of the resulting dipole generates a restoring force, thus forming a stationary plasmonic oscillation (see Fig. 3.15).

The effect arises not only in nano-structures made from metals [17, 30] but also in semiconductor nano-materials with considerable free carrier concentrations [49, 50]. LSPR extinction spectra depend on the nanoparticle size and shape, growth material and on the refractive index of the surrounding medium [56]. The possibility to easily manipulate the behaviour of local electromagnetic fields material- and structurally-wise makes the LSPR phenomenon interesting in terms of fundamental properties as well to be used in applications such as surface-enhanced spectroscopy [30, 57] and sensing [56]. LSPR has been investigated in structures with several different shapes, mainly focusing on simple geometries or on particles whose geometry is analogous to a RF antenna. Examples of both types of nanostructures are spheres, [17] ellipsoids, [17] disks, [54] nano-rods, [57] Bowties, [30] monopoles, [58] dipoles, [59] and Yagi-Uda nano-antennas [60].

Two important LSPR properties are the amplitude of the collective electron oscillation with respect to the driving amplitude, Q, and the width of the particle plasmon resonance, Γ. Both of them depend on the plasmonic damping, which, in a quasi-particle picture is described as population decay. In the case of localized plasmons (Fig. 3.16), this decay can

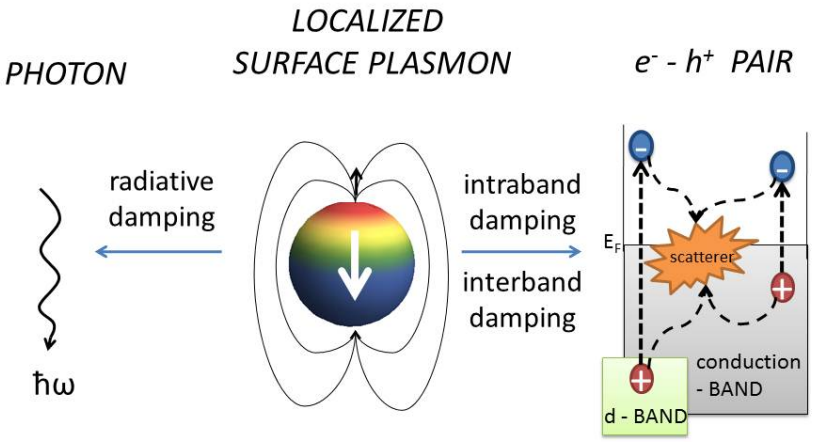

Fig. 3.16: Localized Surface Plasmon Resonance decay. The radiative damping results in the emission of a photon, meanwhile the non-radiative damping is due to dephasing of the oscillation of the collective electrons due to absorption effects (scattering with impurities, phonons, etc.)

be either radiative or non-radiative [61]. The radiative damping results in the emission of a photon (scattering field of the particle), meanwhile the non-radiative damping is due to dephasing of the oscillation of the collective electrons due to absorption effects (scattering with impurities, phonons, etc.) which ultimately dissipates the initial excitation energy as heat.

3.3.3 Surface Plasmon Polaritions

Radiating light onto a metal induces packets of electrical charges to collectively oscillate on the metal surfaces at optical frequencies (surface plasmons). At conductor-dielectric interfaces (2D confinement), these surface plasmons can couple with incoming photons creating the so called Surface Plasmons Polaritons (SPPs). Thus, SPPs are self-sustaining, propagating electromagnetic waves which are trapped at and guided along metal-dielectric interfaces. [18, 48]

The field intensity in the conductor and dielectric exponentially decreases in the direction normal to the surface. Within the interface plane, the charge distribution in the conductor propagates as a longitudinal wave along the surface (Fig. 3.17).

Since the properties of surface plasmons strongly depend on the properties of the conductor (dielectric function, surface structure) and the dielectric medium (refractive index), controlled modifications of these properties enable SPP to be potentially used for devel-

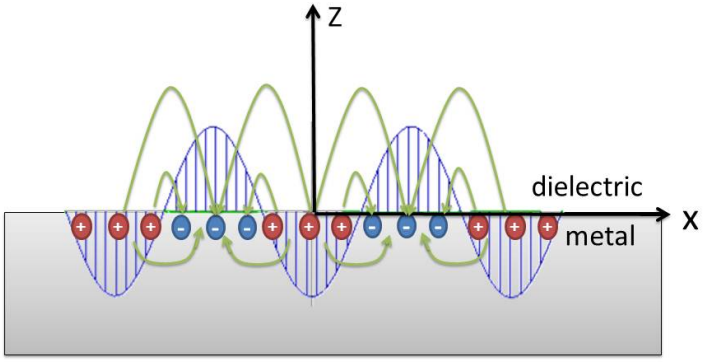

Fig. 3.17: Surface Plasmon Polariton Resonance. The incident sinusoidal electric field (blue) separates positive and negative charges on the metal surface. These charges induce an evanescent wave (green) that propagates along the interface of the metal and dielectric media, where the z-component of the electric field decays exponentially and differently in both mediums.

oping new types of photonic devices. For instance, SPPs are being explored for their potential in optics, magneto-optic data storage, microscopy and solar cells, as well as biotechnology sensors [18].

For the understanding of SPPs, it is instructive to revise the results of simple electrodynamics applied to an ideal model interface. Solving Maxwell's equation under the appropriate boundary conditions yields the SPP dispersion relations for the parallel (to the interface) $k_{\|}$ and perpendicular $k_{\perp_j}$ components of the SPP wave-vector [18]:

$$k_{\|} = k_{SP} = k_0 \sqrt{\frac{\epsilon_2 \epsilon_1}{\epsilon_2 + \epsilon_1}} \tag{3.106}$$

$$k_{\perp_j} = k_0 \sqrt{\frac{\epsilon_j^2}{\epsilon_2 + \epsilon_1}}, j = 1, 2 \tag{3.107}$$

where k_0 is the free-space wavevector and ϵ_1 and ϵ_2 are the permittivity of the metal and dielectric, respectively. The metallic medium is characterized by a general, complex frequency-dependent dielectric function $\epsilon_1(\vec{r}, \omega)$ whereas the dielectric function of the other medium ϵ_2 is assumed to be real. Waves propagating along the interface (real $k_{\|}$[6]) but bounded in the normal direction (exponential decay of k_{z_j}), can be achieved by two

[6] Taking into account the imaginary part of the dielectric funtions, $k_{\|}$ becomes complex which leads to a damped propagation within the in-plane direction.

imposed conditions on Eq. 3.106:

$$\epsilon_1 \cdot \epsilon_2 < 0 \tag{3.108}$$

$$\epsilon_1 + \epsilon_2 < 0 \tag{3.109}$$

The two expressions/conditions mean that one of the dielectric functions must be negative with an absolute value exceeding that of the other. Metals have a large negative real part of the dielectric constant along with a small imaginary part. Therefore, at the interface between a noble metal and a dielectric, SPPs modes can exist.

3.3.4 Metal nano-structures as optical antennas

Metal nanostructures can efficiently convert free propagating optical radiation to localized energy and vice-versa in the subwavelength scale [29], therefore act as the optical analogue of an antenna. Despite the similarity to their radiowave and microwave counterparts, there are crucial differences in the physical properties and scaling behaviour of optical antennas. These differences arise because of the two reasons previously explained in this section: the behaviour of metals at optical frequencies and the confinement of free electrons within the nano-structures. That is:

- metals are not perfect conductors[7] at optical frequencies, but correlated plasmas described as free electron gases (see **Section 3.3.1**). In classical antenna theory, the electromagnetic fields are restricted to the outside of an antenna. This assumption is valid at micro- and radio-frequencies, where the metals are well approximated by perfect conductors. Meanwhile, the prediction of the antenna characteristics (resonance position, absorption, scattering) in metals is more difficult in the optical range of the electromagnetic spectrum. In more detail, at optical frequencies, the skin depth of the metals is comparable to or larger than the wire diameter of the antenna.

- The antenna shape can take several forms, and their properties may be strongly shape- and material-dependent due to the previously described surface plasmon resonances (**Sections 3.3.2** and **3.3.3**). For example, LSPR can be interpreted as a strong polarization of the particle or as a huge increase of the current distribution and phase-difference, which modifies the optical antenna performance [8].

Therefore, nano-antennas exploit the diverse properties of metallic nano-structures at optical frequencies, being capable of collecting and controlling electromagnetic fields at this

[7] A perfect conductor is an ideal material with 'infinite' conductivity.

[8] Note that metallic particles that do not support LSPR or SPP should still show a antenna resonance at optical frequencies due to bulk plasmons.

scale. Apart from faster communications, further applications of these nano-antennas include nano-imaging, enhancing light-matter interactions, optical sensing, biotechnological devices, energy harvesting and radiative decay engineering [18].

4. CHIRAL SYSTEMS

Chiral systems are objects whose mirror image can not be superposed with the actual object. In other words, chiral objects break parity-reversal symmetry. A typical example of a chiral system would be human hands. Chirality-related phenomena appear in chiral media when the length characteristic of a particular transport process or the wavelength of the electromagnetic radiation is commensurated with the length which defines the chirality of the system (for example, the pitch of a helix). Regarding electronic transport, the characteristic length would be the mean free path. In the case of a ferromagnet, this quantity would be the exchange length or the spin-coherence length which are typically in the nanometer range. Moreover, optical wavelengths (near IR-Vis-UV) of the electromagnetic radiation are in the nano-meter scale, too. In consequence, chiral effects are expected to appear in both optical, magneto-optical and magneto-transport properties of the metallic nano-helices [8].
In the following sections, an introduction to chirality and common related effects in optical, magneto-optical and magneto-transport properties will be given. Furthermore, an overview of the actual samples (metallic nano-helices) as exemplary chiral systems will be provided.

4.1 Symmetry Considerations

In nature, there exist systems that can occur in two forms that are each other's 'mirror image'. These systems are called *chiral systems* (for example, DNA-strands, the sugar molecule or human hands) where the two forms of the object are named *enantiomers*. Enantiomers are *non-superposable* entities; they present identical chemical and physical properties inside an 'achiral environment', however, their response differs within a 'chiral environment'. In other words, chirality is manifested only in chiral systems subjected to a chiral combination of interactions (forces) and fluxes [62]. Pairs of enantiomers are commonly designated as 'right-' (D) and 'left-handed' (L).
Chirality can be formally defined using spatial and temporal symmetry considerations. The space reverseal (inversion) symmetry operation, represented by the parity operator $\hat{P}$, is the transformation that changes the signs of the spatial coordinates (x, y, z) $\rightarrow$ (-x, -y, -z). The time inversion symmetry operation, represented by the time operator $\hat{T}$, is the transformation that changes the sign of the temporal coordinate (t) $\rightarrow$ (-t) and can be pictorically regarded as reversing the motion of all physical entities in the system. In

this sense, chirality is exhibited by systems that possess two (enantiomeric) states which are interconnected by space inversion but not by any combination of time reversal and spatial rotations [62].

Chirality is a geometric property, *i.e.*, it is related to the shape of the chiral object. Therefore, it can be described by a geometric factor $\zeta^{L/D}$ which changes sign under $\hat{P}$ without changing sign under $\hat{T}$:

$$\begin{aligned} \hat{P}\zeta^{L/D} &= \zeta^{D/L} = -\zeta^{L/D} \\ \hat{T}\zeta^{L/D} &= \zeta^{L/D}. \end{aligned} \tag{4.1}$$

4.2 Helices as Model Chiral Systems

Mathematically, a perfect helix is defined as a three-dimensional curve of constant curvature and torsion. A helix of diameter D, and pitch, p, is defined by the following parametrisation in cartesian coordinates (see Fig. 4.1):

$$\begin{aligned} x(\theta) &= \frac{D}{2}\cos(\theta) \\ y(\theta) &= \frac{D}{2}\sin(\theta) \\ z(\theta) &= \frac{p\theta}{2\pi} \end{aligned} \tag{4.2}$$

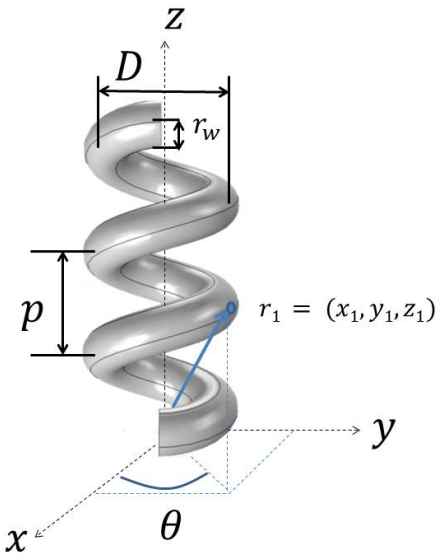

Fig. 4.1: Right-handed helix. Any point on the helix r_1 can be defined throught the diameter D, angle θ and height z. p is the pitch of the helix and r_w is the wire radius forming the helix.

Equivalently, by inverting Eqs. (4.2), D, θ, p can be expressed as:

$$\begin{aligned} \frac{D}{2} &= x^2 + y^2 \\ \theta &= \arctan(y/x) \\ p &= \frac{2\pi z}{\arctan(y/x)} \end{aligned} \tag{4.3}$$

The diameter, D, and pitch, p, of the helix are related to the curvature, κ, and torsion, τ, by:

$$\begin{aligned} \kappa &= \frac{D/2}{(D/2)^2 + \frac{p^2}{4\pi^2}}, \\ \tau &= \frac{p}{(\pi/2)(D^2 + \frac{p^2}{4\pi^2})}. \end{aligned} \tag{4.4}$$

Helices are the archetype of chiral systems. Both enantiomers (left- and right-handed helices) can be related by space inversion (parity-reversal operation) as is depicted in Fig. 4.2A .

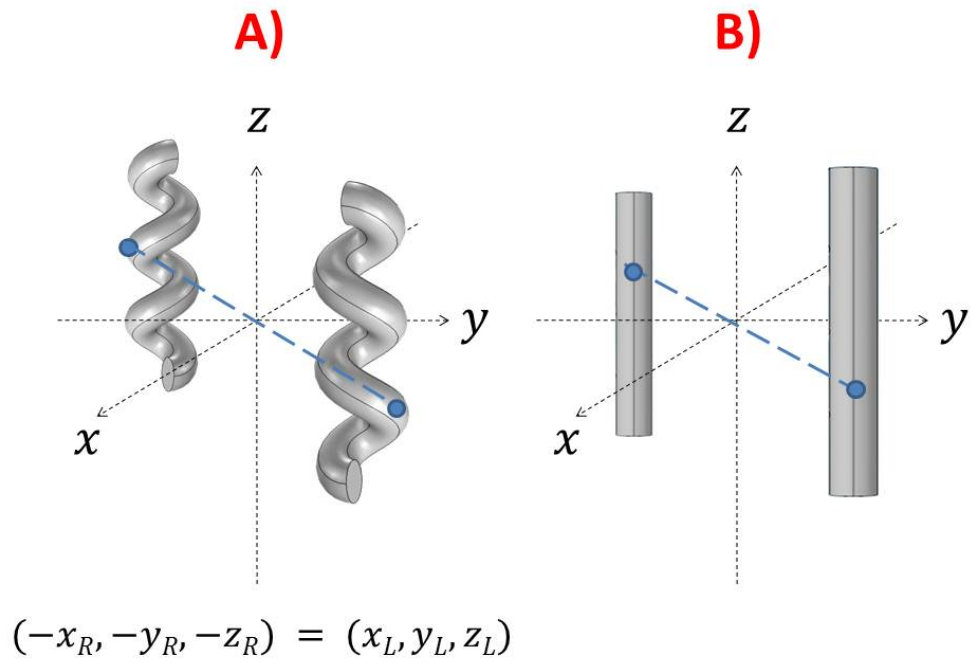

Fig. 4.2: A) A right-handed helix is converted into a left-handed helix through a parity operation and vice-versa. B) An achiral rod. Points converted by parity operation can be reached through a spatial translation as well.

By taking into account Eqs. (4.2), we can observe that the diameter D and the parameter

θ of the helix are constant after applying the parity operator $\hat{P}$. In contrast, $\hat{P}$ changes the pitch of the helix from p to -p, *i.e.*, p is a pseudoscalar quantity. A right-handed helical screw sense is characterized by a positive value of p since a positive change in θ is associated with a positive translation along the helical axis. Similarly, a left-handed screw sense is characterized by a negative value of p since a positive change in θ is now associated with a negative translation along the helical axis.

4.3 Properties of chiral systems

Chiral effects are well-known in optics. Two specific optical phenomena occur in chiral materials: the *Natural optical activity* (*NOA*) and *optical Magneto-Chiral Anisotropy* (*oMChA*). However, chirality is a general symmetry concept, therefore, chiral effects are not exclusively restricted to the optical properties of systems. The *particle-wave dualism*, suggests that physical effects existing in optics also appear in massive particles like electrons or holes [63]. This dualism would lead to the existance of a *MChA*-like effect in the magneto-transport properties of chiral systems. This phenomenon does exist indeed and is named *electrical Magneto-Chiral Anisotropy* (*eMChA*). In this subsection these main phenomena which occur in the optical, magneto-optical and magneto-transport properties of chiral systems are described.

4.3.1 Optical Activity

Natural optical activity (*NOA*) is characterized by optical rotation (*OR*) and circular dichroism (*CD*). *OR* is the ability of a chiral medium to modify the polarization plane of linearly polarized monochromatic light and is associated with the differences in the phase velocities of right and left circular polarized waves. Depending on whether the rotation is positive (clock-wise) or negative (anti-clock-wise) to the incident direction of incoming light, the optically active material is called *dextrorotatory* or *levorotatory*, respectively. *CD* is a phenomenon related with the non-vanishing difference in the attenuation (absorption) of the two circular polarized waves [62].

The two effects are illustrated separately in Fig. 4.3. Any linearly polarized light can be written as an equal combination of left-hand (*LHC*) and right-hand (*RHC*) circularly polarized light (Fig. 4.3A). In optically active materials, these two circular polarizations experience different refractive indices, n_R and n_L for *RHC* and *LHC*, respectively. After travelling the length l through the material, the two polarisations acquire a different relative phase (θ_R, θ_L), resulting in the rotation of the final polarization by the angle α

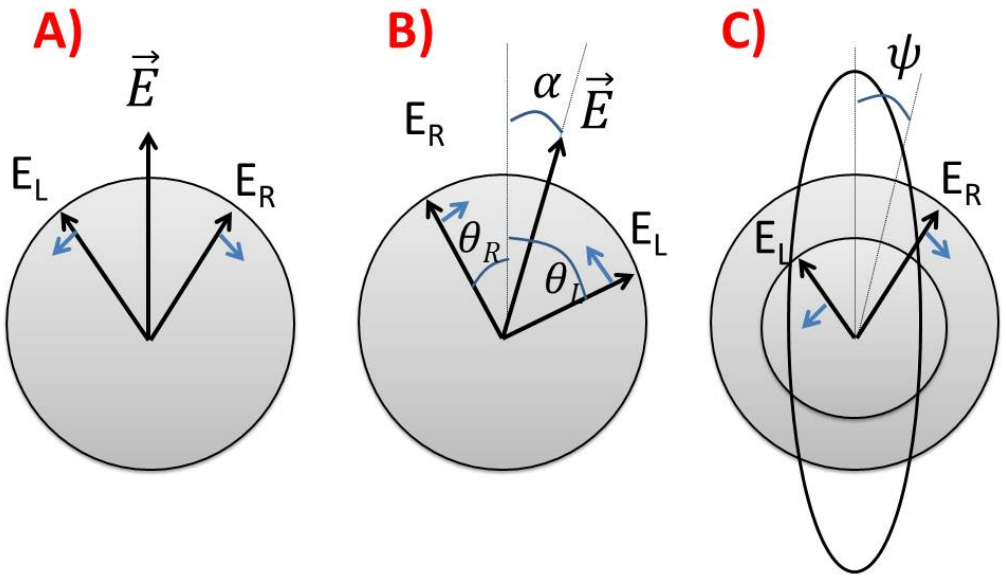

Fig. 4.3: A) The electric field $\vec{E}$ of a linear polarized radiation decomposed into coherent left- (L) and right- (R) circularly polarized components E_R and E_L, respectively. B) Rotated electric field vector at some point in the optically active medium. C) Elliptical polarization due to circular dichroism effect. Picture adapted from [62].

(see Fig. 4.3B). Therefore:

$$\theta_R = \frac{2\pi}{\lambda} n_R l$$
$$\theta_L = \frac{2\pi}{\lambda} n_L l$$
$$\alpha = \frac{1}{2}(\theta_R + \theta_L) = \frac{\pi l}{\lambda}(n_L - n_R). \tag{4.5}$$

Thus, α is proportional to $(n_L - n_R)$, called the *circular birefringence* of the medium. If, in addition, there is a difference in the absorption for *RHC* and *LHC*, the incoming linearly polarized light becomes elliptically polarized[1] as illustrated in Fig. 1C. The angle Ψ is related to the absorption difference of *RHC* and *LHC* and can be calculated as:

$$\tan(\Psi) = \frac{E_R - E_L}{E_R + E_L} \tag{4.6}$$

where E_R and E_L are the electric field amplitudes of the *RHC* and *LHC* light, respectively.

[1] Elliptically polarized light can be decomposed into coherent *RHC* and *LHC* components of different amplitude.

The quantity $\tan(\Psi)$ is known as *ellipticity*. Considering that the attenuation of the amplitude E_0 of a light beam by an absorbing medium is related to its absorption index k_1 and l by

$$E(l) = E_0 e^{-\frac{2\pi}{\lambda} k_1 l}, \tag{4.7}$$

the ellipticity can be expressed as

$$\tan(\Psi) = \frac{e^{-\frac{2\pi}{\lambda} k_{1R} l} - e^{-\frac{2\pi}{\lambda} k_{1L} l}}{e^{-\frac{2\pi}{\lambda} k_{1R} l} + e^{-\frac{2\pi}{\lambda} k_{1L} l}} = \tanh\left[\frac{\pi l}{\lambda}(k_{1L} - k_{1R})\right] \tag{4.8}$$

where k_{1R} and k_{1L} are the absorption indices for *RHC* and *LHC*, respectively. For small differences in the absorption of *RHC* and *LHC*, the ellipticity is small and can be approximated by

$$\Psi \approx \frac{\pi l (k_{1L} - k_{1R})}{\lambda} \tag{4.9}$$

that is, Ψ is proportional to $(k_{1L} - k_{1R})$, which is the *circular dichroism* of the medium. *NOA* phenomena have been observed in bio-molecules, cane sugar or crystals with corkscrew-like lattice structure such as quartz [64]. They are used in a wide range of applications to investigate organic molecules such as proteins and DNA, [65] charge-transfer transitions in chemical reactions, [66] or geometric and electronic structures of materials [67].
At this point, it is important to mention that *NOA* phenomena can be confused with the well-known *Faraday effect* [62]. The latter is a magneto-optical effect that consists of the rotation of the plane of polarization of a beam of linearly polarized electromagnetic radiation when the radiation passes through **any medium** (either chiral or achiral) parallel to the direction of an externally applied magnetic field. The physical origins of these two kinds of optical activity are completely different: *NOA* occurs because of nonlocal optical response in chiral media and is independent of the existence of a magnetic field, whereas the magnetic optical activity (*MOA*) occurs in all media because of the breaking of time-reversal symmetry by an external magnetic field.

4.3.2 Optical Magneto-Chiral Anisotropy

Optical *MChA* (*oMChA*) is an effect that establishes a link between chirality and magnetic fields [62] : in the case of optics, when light is passed through a **chiral** medium placed in an external magnetic field, the refractive index and the absorption encountered by the light differs depending on whether it travels parallel or antiparallel to the magnetic field. The associated difference in refractive index of a light beam parallel and antiparallel to the magnetic field is called *magnetochiral birefringence* [68], the difference in absorption is named *magnetochiral dichroism* [69]. *oMChA* depends on the handedness of the chiral

medium, however, it is independent of the polarization state of the light.
The propagation of light within any medium is governed by the relative dielectric tensor ϵ. For any material the magnetochiral effect can thus be deduced from an expansion of ϵ to first order in $\vec{k}$ (vector of the propagating electromagnetic wave) and $\vec{B}$ (total magnetic field) [70]:

$$\epsilon(\vec{k}, \vec{B}) = \epsilon_0 + \alpha_{NOA}^{D/L}\vec{k} + \beta_{MOA}\vec{B} + \gamma_{MChA}^{D/L}(\vec{k} \cdot \vec{B}) \tag{4.10}$$

In this expression, ϵ_0 is the zero field dielectric tensor; $\alpha_{NOA}^{D/L}$ represents the natural optical activity parameter; β_{MOA} denotes the magnetic optical activity (Faraday effect) term, and $\gamma_{MChA}^{D/L}$ constitutes the magnetochiral anisotropy parameter.
Optical *MChA* effects have been observed in the luminescence of chiral complexes [69,71], in the absorption of chiral paramagnets [68, 72] and in the photolysis of chromium oxalate complexes [73,74]. Magneto-chiral phenomena can be used to discriminate between enantiomers.

4.3.3 Electrical Magneto-Chiral Anisotropy

Electrical conductors can exist in two enantiomeric forms for several reasons: the material lattice may possess a chiral space group like tellurium, [75] or it might be composed of chiral subunits like conducting polymers [76, 77]. Ultimately, an achiral material can acquire handedness by deforming or growing it into a chiral shape, like a helix, [7] which can be regarded as a topologically induced chiral structure.
In general, the ability of an electrical conductor to carry an electrical current is reflected in the electrical conductivity tensor σ_{ij} or equivalently in the electrical resistivity tensor ρ_{ij}[2]. Both magnitudes depend on the wave vector of the moving particles $\vec{k}$ and the total magnetic field $\vec{B}$. The following expresion for the two-terminal resistance of a chiral conductor up to first order can be derived for both ballistic [63] and diffusive charge transport [7, 63]:

$$R^{D/L}(\vec{I}, \vec{B}) = R_0 \cdot [1 + \beta B^2 + \chi^{D/L}\vec{I} \cdot \vec{B} + O(I^2)]. \tag{4.11}$$

In this equation, R_0 is the resistance in absence of $\vec{B}$, β represents the usual magnetoresistance effect in all conductors and $\chi^{D/L}$ describes the *eMChA* geometric factor (*cf.* Eq. (4.1)). The average over all $\vec{k}$ of the moving particles is proportional to the current density through the conductor and therefore to the electrical current $\vec{I}$. *eMChA* of any chiral conductor is principally measured applying a magnetic field parallel or antiparallel to the linear component of the (drift) velocity of the charge carriers (see Fig. 4.4).
eMChA has already been measured for macroscopic hellically structured metallic conductors [7] and chiral single-walled carbon nanotubes [78]. It can be used to discriminate

[2] $\sigma_{ij} = \rho_{ji}^{-1}$.

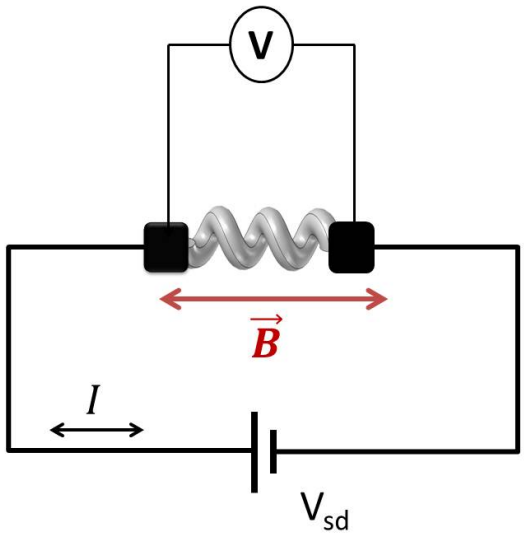

Fig. 4.4: Principal Electrical Magneto-Chiral Anisotropy measurement set-up. The helix' longitudinal axis is kept parallel (antiparallel) to the external applied magnetic field $\vec{B}$, while keeping the current I constant (Vsd is the source-drain voltage).

between the enantiomers of chiral systems (as the *oMChA*), or for direction-dependent sensing of external magnetic fields.

5. EXPERIMENTAL APPROACHES

This chapter provides a detailed description of the experimental techniques and their implementation to fabricate nano-helices and associated devices. Furthermore, it contains information on the main standard techniques used for the structural, optical and electrical characterization of the nano-helices. This includes the measurement approaches to address the magneto-chiral phenomena reflected in their magneto-optical and magneto-transport properties.

More specifically, the optical characterization of nano-helices in view of their operation as nano-sized helical antennae is undertaken via transmission and specular reflectance measurements in the *far-field*, and via Surface Enhanced Raman Spectroscopy (SERS) in the *near-field* regime. Their corresponding magneto-optical chiral properties are measured in a reflection set-up by placing the sample in an AC magnetic field produced by an electromagnet. Finally, the magneto-transport measurements are undertaken for different temperatures and magnetic fields up to 9 T using a superconductor magnet.

5.1 Fabrication of arrays of metallic nano-helices and associated nano-devices

The greatest challenge encountered when designing custom structures at the nano-scale is the ability to grow these from any kind of material on any type of substrate. Even more demanding requirements have to be fullfilled for any growth-technology to be industrially exploitable: straightforward control of shape and dimensions, high structural uniformity, fabrication into ordered arrays, process compatibility with current semiconductor integrated-circuit technologies, and large-scaling at economic cost. To date no method has been reported for 3D sculptured nanostructures which fully accomplishes these characteristics, although some of them such as Glancing Angle Deposition [79, 80] fulfill several of these requirements.
In this section, first the techniques for the growth of helical nano-structures are summarized. Then, the suitability of the chosen growing method (Glancing Angle Deposition) in the present thesis is explained. Finally, the improvements and the actual implementation of this technique are described, which allow the fabrication of nano-helices made from different metals with sub-100 nm wire thickness and helix diameter.

5.1.1 Nano-sized helical structure growth techniques - an overview

In order to fabricate nano-helices, a top-down technique and three bottom-up methods have recently emerged. These are the direct laser writing (*DLW*) in polymers [5], the self-assembly growth of nano-particles on DNA-based templates [81], the spontaneous nanowire coiling via a vapor liquid solid (*VLS*) or vapor-solid (*VS*) growth mechanism [82] and the oblique physical vapour deposition with substrate rotation (more known as Glancing Angle Deposition *GLAD*) [80], respectively.
Within the *DLW* technique, nano-helices are produced by filling by electrochemical means nano-patterned voids created in a polymer. Despite the optimal quality of the shapes and the independence of the growth material, this method has an extremely low throughput and has been demonstrated only in micro-metric helices [5].
Metallic nano-particles can be self-assembled in helical shapes on chiral nano-templates such as DNA [81]. This technique represents the state of the art regarding the smallest feature size (20 nm helical diameter). Nevertheless, the size variation produced by this approach is limited by the template geometry, and the overall structure is not electrically conducting due to the separation of the individual nano-particles.
VLS or *VS* nano-helices are synthesized by tuning properly the experimental conditions (pressure, temperature, precursors, and catalyst powders) within a chemical vapour deposition chamber. The produced samples are quite uniform, however, no accurate control over the growing parameters (helix pitch, diameter) could be demonstrated; the coils grow randomly and are dispersed on the substrate and the range of materials from which the nano-coils can be made is limited and is currently restricted to BC, SiC, ZnO, SiO and

SiO_2 [82–86]. That is, only large band-gap semiconductors and dielectrics are accesible. In addition, the nano-helices made by this method require high temperatures (above 800°) during their synthesis, which makes the technique unfavorable for current semiconductor integrated-circuit platforms [87].

GLAD is a physical vapor deposition (*PVD*) process to produce sculptured thin films (Section 2). The evaporation is performed with the substrate at a glancing angle with respect to the evaporation source and by rotating during the material deposition to produce the desired nano-structures. By using dotted patterned substrates, [88] the technique has successfully produced high-quality arrays of coiled semiconductor and insulator nanowires with a controlled pitch, diameter and helicity (left- or right-handed) [4, 88, 89]. *GLAD* nano-structure production can be undertaken on several kind of substrates at large scale [79, 80]. Furthermore, it is compatible with current semiconductor technology. However, at the current development stage, *GLAD* fails in the growth of scalable and uniform arrays of nano-structures made from high surface mobility materials, such as metals [90–94] and high-quality samples made from any material with wire and coil diameter below 100 nm [85, 93].

Tab. 5.1: Techniques for the growth of helical nano-objects

Process	Typical helical diameter (nm)	Advantages	Limitations or problems
DLW	$\sim$ 1000	Optimal quality. Array growth. Different materials.	Extremely low throughput. Feature size.
Self-assembly on DNA templates	$\sim$ 20	Feature size.	Template geometry. No electrical conduction. No array growth.
VLS-VS	$\sim$ 200	Uniformity.	Material restriction. No array growth.
GLAD	$\sim$ 40	Feature size. Different materials. Array growth. High throughput.	High surface mobility materials.

Considering the characteristics of the previous methods (summarized in Table 5.1), the advantages of *GLAD* and the challenge of surmounting the material problem made this fabrication process the most attractive for attempting the growth of metallic helical structures at the nano-scale. These are the reasons why *GLAD* is the growth technique of choice in the present study.

5.1.2 Glacing Angle Deposition

GLAD is a bottom-up fabrication approach that employs the *PVD* process at extremely oblique angles[1] on static or rotating substrates (see Fig. 5.1A). As depicted in Fig. 5.1B, due to physical shadowing at the atomic scale, a competing three-dimensional growth of incoming material-clusters starts because of the geometrically shadowed area. Given favorable conditions, such as limited adatom mobility (surface diffusion) and highly directional particle flux, the resulting thin porous film consists of well-defined nano-structures.

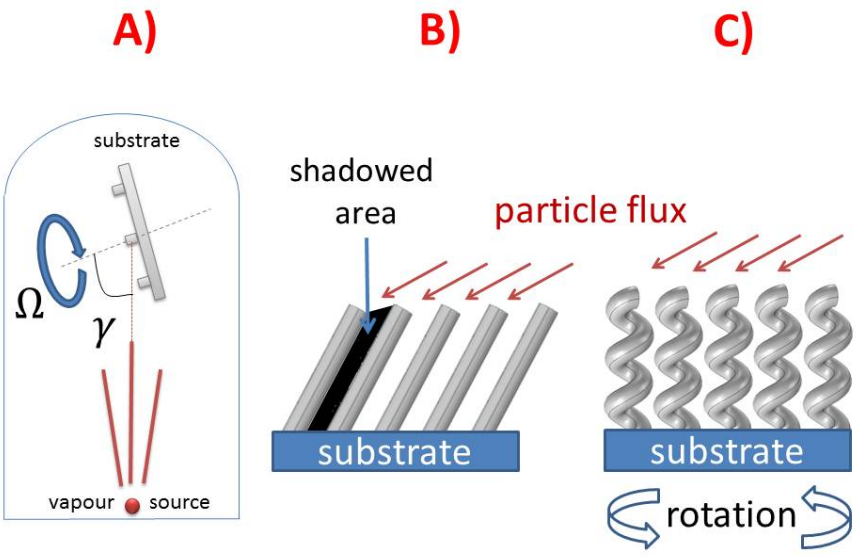

Fig. 5.1: A) *GLAD* deposition set-up, characterized by tilt-angle γ and rotational speed Ω. B) *GLAD* fabrication of slanted nano-columns. No incoming particles are deposited in the shadowed region. C) *GLAD* fabrication of nano-coils. For this, a constant tilt-angle and a homogeneous rotational speed are required.

Historically, Koning and Hellwig recognized the self-shadowing mechanism responsible for a columnar micro-structure growth during deposition at oblique angles in 1950 [9]. Young and Kowal introduced rotation around the substrate normal during deposition at tilted angles $\gamma \geq 60°$ to realize chiral polarization filters in 1959 [9]. Finally, Robbie and Brett [80] demonstrated that depositions at glacing angles $\gamma \geq 80°$ produce extremely porous thin films (densities $\leq 25\%$) and together with a controlled substrate motion, nano-structures could be fabricated.

In general, the nano-structure of films deposited by any kind of physical vapour deposition (*PVD*) depends on several processing parameters such as the growth temperature T, the residual gas pressure, evaporation material, flux directionality, substrate material,

[1] The trajectory of the incoming particle flux and the substrate-normal form typically an angle $\gamma > 80°$.

substrate roughness, substrate motion and the deposition geometry (more information in **Section 2** and Refs. [9, 11]). In the case of *GLAD*, the morphology of the structures varies depending on the deposition angles γ (tilt angle) and ϕ (azimuthal angle)[2], and the deposition flux rate r. For instance, depositions undertaken with $\gamma \geq 80°$ and $\phi = 0$ at any r produces slanted nano-columns. Vertical nano-rods are generated with a fast substrate rotation speed Ω, while growing ($\Omega >> 2\pi r/\delta$, where δ is the separation between helices). Meanwhile, nano-coils are fabricated when depositing material with constant γ, at a sufficient slow Ω ($\Omega \approx 2\pi r/\delta$) (see **Appendix C** for more details about engineering of nano-coil morphology).

Three mechanisms govern the growth of *GLAD* nano-structures: geometrical shadowing, bulk diffusion, and surface diffusion (see **Section 2** and Ref. [95]). While the geometrical shadowing depends on the incoming flux directionality, the bulk and surface (adatom) diffusion depend on the inherent properties of the material evaporated. The influence of each mechanism depends on the temperature of the nano-structures and substrate during the growth: at low temperature thin film depositions the geometrical effects dominate, whereas the diffusion effects dominate at higher deposition temperatures.

Since *GLAD* nano-structures are created due to self-shadowing effects, an extremely directional particle flux and low-adatom-mobility are crucial. The first condition is relatively easily achievable with current technology at the nano-scale (electron-beam evaporators) and/or inserting flux particle collimators. However, the second one is hard to realize in high surface-mobility materials such as metals. In general, evaporations realized by electron-beam evaporation on substrates kept at room or colder temperatures are desired for *GLAD* columnar growth[3] [9].

Problems of the state-of-the-art GLAD technique reported in literature.

High-quality uniform arrays of micro- and nano-structures made from semiconductor and insulator materials can be fabricated using *GLAD* evaporation on dot-patterned substrates[4] [4, 79, 88, 89, 96]. However, this is not sufficient to produce structures with wire diameter below 100 nm [85, 88] and/or made of high surface-mobility (adatom diffusion) materials such as metals [90–94] if the evaporation is performed at room temperature.

In general, the (adatom) diffusion length, Λ, of materials depends on the deposition rate r and the temperature T [97]. Although r is kept constant during the growth, the

[2] In this case, for a given instant of time t, the angle ϕ is given by $\phi = \Omega \cdot (t - t_0)$, where Ω is the substrate rotation speed and t_0 is the initial instant.

[3] *GLAD* nano-structures can be fabricated with other evaporation techniques such as sputtering, pulsed laser deposition or thermal evaporation; however, electron-beam evaporation is particularly favorable since the highly directional incoming atoms have very low energy ($\leq$ 1 eV), thus, it provides lower surface diffusion compared to the other methods.

[4] A dot-pattern array placed on the substrate determines initial shadowing conditions, serves as nucleation and condensation seed for the incoming particles and improves the uniformity of the sample by equally distributing the incoming flux among the nano-structures [88].

temperature rises during the evaporation, in particular in the case of high porosity films [98, 99]. Thus, Λ considerably increases during the deposition, and nano-structures made from metals are likely to get gradually thicker during the growth, eventually collapsing and/or getting deformed [90, 91, 99]. In consequence, the key to the controlled growth of regular arrays of metal nano-structures using *GLAD* is the reduction of Λ of the incoming ad-atoms. As will be shown in the following paragraphs, by 'extracting' efficiently the heat generated by the incoming atoms during the deposition step, it is possible to limit the growth temperature of the nano-structures and thus reduce Λ. This optimization step can be regarded as a proper *heat engineering* process.

GLAD Heat engineering technique.

The heat engineering step is a novel step within the *GLAD* process. It is introduced here for the first time and relies on the fast heat extraction from the nano-structures during growth. *PVD* evaporations are undertaken from medium to high vacuum conditions ($< 10^{-5}$ mbar), thus, the main way to effectively extract the heat of the incoming material is via the substrate. Some authors recently cooled down the substrate through a liquid N_2 line attached to the rotating substrate [100, 101]. This solution, appart from making the set-up much more complex and industrially more difficult to scale, leads to the formation of a strong temperature gradient between the top and bottom parts of the substrate during the growth. If the thermal conductivity of the substrate is low in comparison with the growing material (as occurs in metals deposited on common wafers used in research and industry like SiO_2), the heat extraction is not efficient and the desired nano-structures are not achieved. In fact, the only reported samples grown on Si using this method have an overall height of less than 100 nm as the sample quality considerably deteriorates with height [101].

The heat extraction problem can be better undertaken even at room temperature by introducing a *heat-management* system between the substrate and the actual nano-structure to rapidly expel the heat from the nucleated atoms from the structure to the substrate. The *heat-management* system developed in the present thesis is constituted by two thin films. The bottom layer (*heat-sink* layer) is made from a high thermal conductivity k material such as *Ag*, *Au*, etc., which enables fast heat extraction from the nano-structure array, temporal heat storage, and efficient heat transfer to the substrate underneath. The top layer (*heat-shield* layer) is made from a very-low k material such as UV photo- or poly-methyl-metacrylate (*PMMA*) resist. This resist film covers the whole substrate except the area where the nano-structures are aimed to be fabricated. Its main function is to avoid heat transfer from the areas where nano-structures are undesired to the high k layer placed below (therefore, making the *heat-management* system more efficient). Besides, as this resist layer is easy-soluble, it allows the deliberate positioning of the nano-structures on desired areas on the substrate.

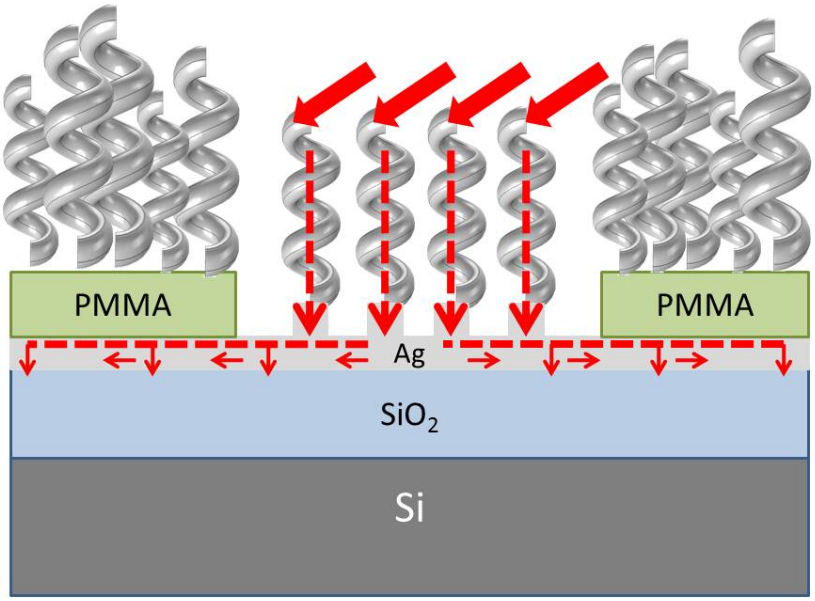

Fig. 5.2: Heat transfer management. Heat from the incoming particle flux (continuous red arrow) is transferred to the 80 nm thick *Ag* layer (large vertical dashed arrows), where it spreads (horizontal arrows). Possible heat transfer coming from irregular helices on top of the $\sim$ 200 nm *PMMA* layer is highly suppressed due to this low thermal conductivity layer, thus, improving the efficiency of the heat-management system. A 4 nm *Ge* layer is used as an adhesion layer to define *Ag* dots on SiO_2 by electron-beam lithography. The size of the areas to grow regular helices is different depending on the particular experiment to be undertaken. Overall, they vary from 100 μm to 1 mm in length and from 10 μm to 1 mm in width.

The principal heat flow is schematically depicted in Fig. 5.2. While the nano-structures are being grown on the selected area, heat is transferred to the bottom thin layer. Because this layer has high k, the heat expands rapidly through the whole thin film. As the high k layer covers the entire or large parts of the substrate surface, the acquired heat will be efficiently conducted to the substrate even in the case of having a low k substrate like SiO_2. At the same time, the low k thin film blocks the heat transmission from the incoming particles which are deposited on undesired areas. Therefore, the temperature of the nano-structures will not excessivelly rise during the growth and low-adatom mobility of the incoming atoms is achieved at any time during the deposition. Furthermore, this method makes the growth of these samples independent from any type of substrates. The efficiency of the heat management technique is demonstrated in **Section 6.1**.

5.1.3 GLAD set-up developed

Retrofittable GLAD equipment

To be able to grow *GLAD* nano-structures, a controlled substrate motion system which can be placed inside a general purpose evaporator was developed. Despite the availiability of complex and dedicated *GLAD* deposition systems [100], the adopted solution is portable, economic and produces an excellent performance as it is demonstrated in **Section 6.1**.

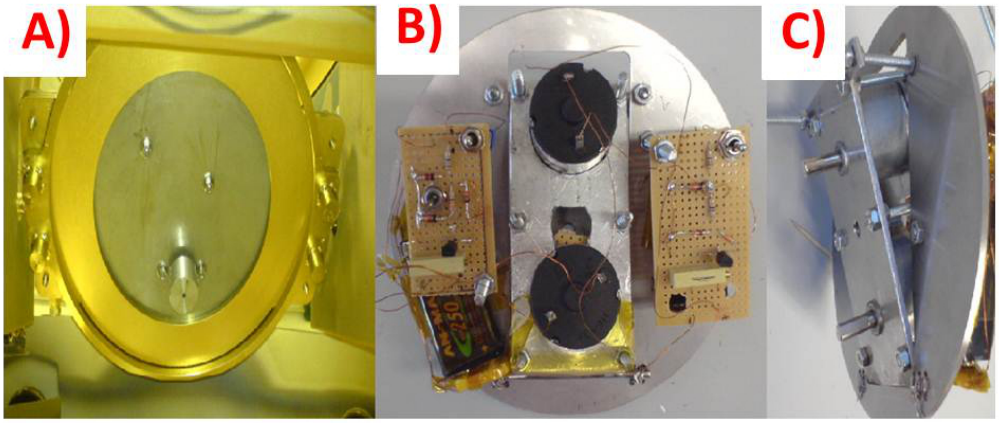

Fig. 5.3: GLAD set-up. A) Front view: rotating substrate holder inserted into the evaporator. B) Back view: two motors and electronic circuits provide two rotational speeds during the deposition. Alternatively, they enable the fabrication of both helical enantiomers (left and right helices) simultaneously. C) Side view: tilting angle control.

The developed equipment consist of electronically controlled DC motors fixed to mechanical pieces which are mounted on the 20 cm wafer holder provided by the evaporator[5] as shown in Fig. 5.3. DC motors were employed[6] rather than stepper motors as used by other groups [93, 100] to keep the best possible flux directionality when growing the nano-coils. In turn, the tuneability of the substrate rotation speed has to be done by analog electronic circuits[7]. These electronic circuits were home-built, as well.

DC motors consist of a set of coils, called an armature, inside another set of coils or a set of permanent magnets, called the stator. Applying a voltage V_m to the coils produces a torque $\hat{k}$ in the armature, resulting in rotational motion. Also, the motor torque is

[5] Samples are fabricated in a conventional evaporator machine: the Temescal FC-2000. The FC-2000 is an evaporation system which is equipped with a number of accessories designed to meet a wide range of research activities. The system basically comprises a 6-pocket EB evaporation source, a thermal evaporation source, an ion source, a substrate infrared heater and a process gas controller.

[6] DC motors provide a continuous and smooth substrate rotation.

[7] In contrast, adapting and monitoring the rotation speed of stepper motors is easily achievable by sending different pulses at different frequencies from a computer.

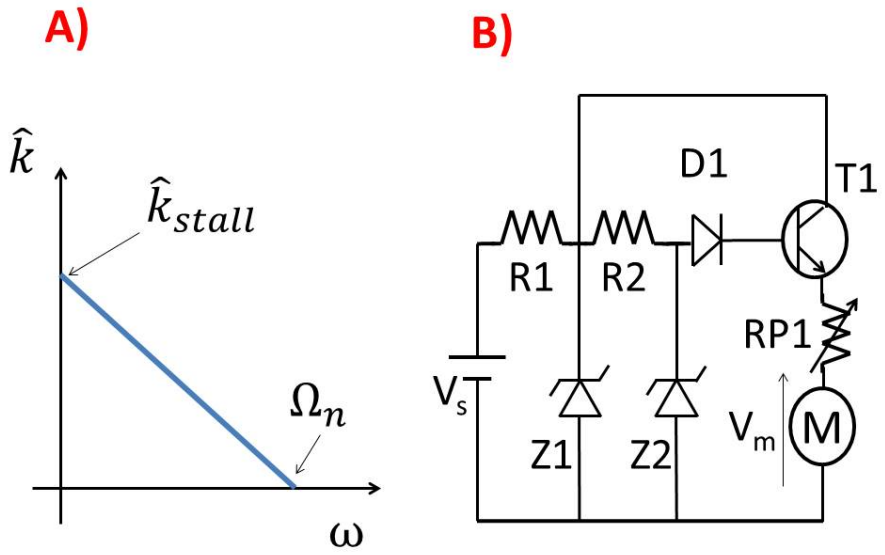

Fig. 5.4: A) Graph representing the steady-state operation of a DC motor (Eq. 5.1). B) Electronic circuit to control the rotational speed of the DC motor M. V_s is the volgate source, which is stabilized and reduced through Zener diodes *Z1*, *Z2* and resistances *R1*, *R2*. *T1* is a transistor and *RP1* is a low resistance potentiometer. *D1* is a diode which avoids any reverseal current from *T1*.

proportional to the applied current I. The operation of the motor is described by

$$\hat{k} = \hat{k}_{stall} - \Omega \cdot \hat{k}_{stall}/\Omega_n \tag{5.1}$$

where $\hat{k}_{stall}$ represents the maximum torque, without shaft rotation and Ω_n is Ω at zero load. To obtain a slow rotation Ω, $\hat{k}$ has to be close to maximum (Fig. 5.4A) . Therefore the motor needs a high current to operate at low Ω. A circuit which accomplishes these requirements is shown in Fig. 5.4B. The voltage supplied by the source V_s is stabilized and reduced through Zener diodes *Z1*, *Z2* and resistances *R1*, *R2*. Transistor *T1* is connected in common collector configuration to amplify the current at the output. A low resistance potentiometer (10 Ω) *RP1* allows the fine tuning of the voltage applied to the motor V_m. Rotation speeds obtained with this setup vary from 6 rpm down to 0.20 rpm, enough to fulfill the growth requirements.

Substrate treatment: dotted-Array and heat-management system

As previously discussed in **Section 5.1.2**, due to the high surface mobility, some modifications have to be undertaken on the substrate to obtain highly regular and uniform metallic nano-structures. First, a dot-patterned array on the substrate effectively in-

troduced regularly-spaced seeds and increases the regularity of the nano-structures [88]. Then, the insertion of the local *heat-management* system (*cf.* previous sections) reduces agglomeration and deformity. Both tasks are realized with well-known standard procedures in nano-technology:

Dot-patterned arrays are created by conventional electron-beam lithography (*EBL*). First, a thin layer of positive *PMMA* resist in anisole solution is spin-coated and baked on the substrate (Si with a 300 nm thermally grown SiO_2 layer on top). Then, the resist is exposed to an electron-beam before developing the sample into a *MIBK* and isopropanol 1:3 mixture. Afterwards, a 4 nm *Ge* and 46 nm *Ag* evaporation is carried out. The *Ge* acts as a thin adhesion layer for the creation of *Ag* nano-dots on the SiO_2. The sample is lifted-off in acetone, which removes the remaining *PMMA* layer and the undesired materials deposited on top of it. After these procedures, a regular square lattice array of ∼50 nm diameter dots is created. Fig. 5.5A shows a scanning electron microscope (*SEM*) image of such a dot-array.

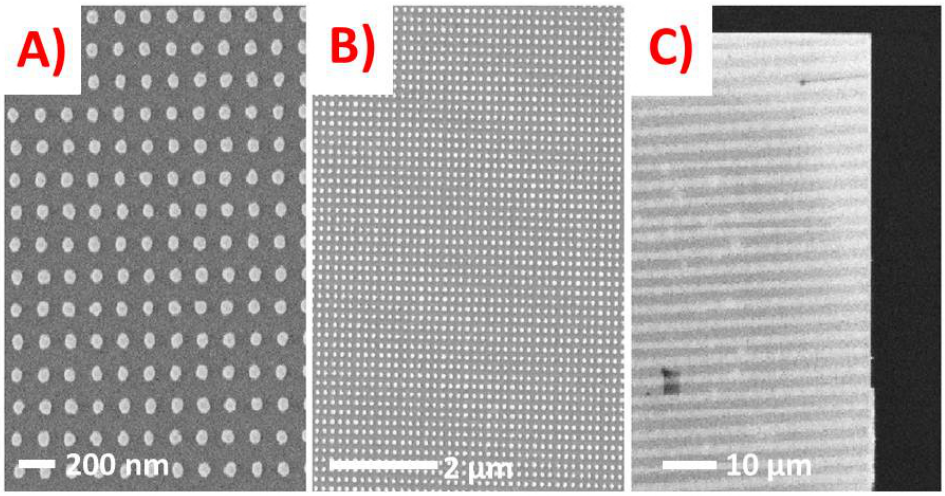

Fig. 5.5: Scanning electron microscope images of patterned SiO_2/Si substrates. A) 50 nm diameter dot array on SiO_2 made from *Ag* and a 4 nm *Ge* adhesion layer. B) Dot array after the deposition of 50 nm of *Ag* layer. C) Dot array surrounded by a ∼200 nm *PMMA* layer (black). The actual nano-dots are not visible due to the large scale of the image.

The *heat-management* system is fabricated by evaporating a ∼80 nm thick *Ag* film on the entire substrate and spin coating and baking *PMMA* resist disolved in anisole on top. Next, an exposure of the dotted area is carried out and the exposed region of the thin film succesively removed using the aforementioned mixture. This procedure completes the substrate preparation, the step before growing the nano-structures. Typical substrate sizes used were ∼4 mm × 4 mm, containing a single dot-array per substrate which size varies depending on the experiment: typically ∼1 mm × 1 mm for optical experiments

and ∼100 μm × 100 μm or smaller for the electrical measurements.

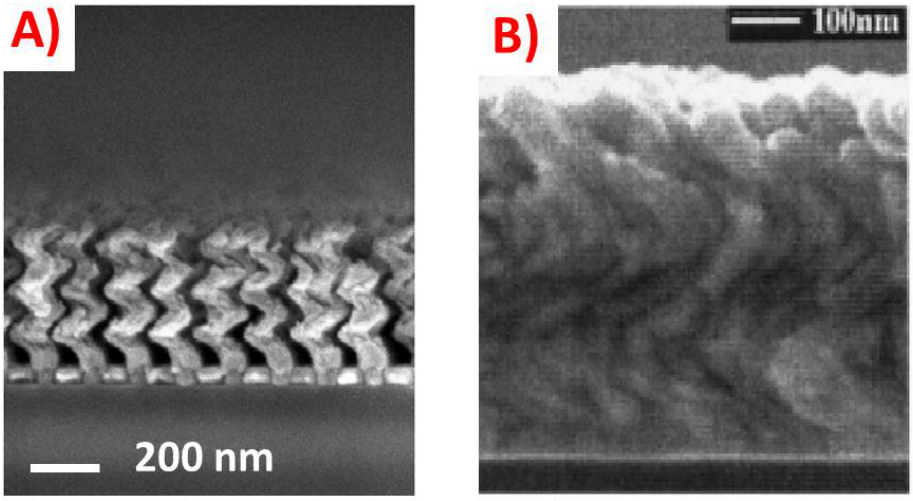

Fig. 5.6: SEM images of Ni nanohelices. A) Array made with the here proposed *heat-management* technique consisting of a thin layer of *Ag* and *PMMA*. B) Best result reported in literature [92].

Fig. 5.6A shows SEM images of nano-helix array made from *Ni* with the here proposed *heat-management* technique. Structurally well-defined and freestanding nano-helices with uniform pitch and diameter are observed with an overall height of ∼ 400 nm. There are no traces of agglomerations or collapse, proving the superiority of this growth technique over the previous state-of-the-art (Fig. 5.6B).

5.1.4 Metallic nano-helices on transparent substrates

Nano-helices might be conveniently grown on transparent substrates depending on the study or application they are going to be used for. For example, in the present thesis metallic nano-helices where grown on transparent substrates to measure their longitudinal localized plasmon in transmission and their circular dichroism (see **Section 6.2**). To optimize the growth of nano-helices in this case is not trivial. It is not possible to construct the bi-layer *Heat-management* as previously described since the *Ag* film is opaque to the light. Furthermore, the majority of transparent substrates have a low thermal conductivity below 2 $Wm^{-1}K^{-1}$ as is the case of SiO_2. This problem was solved in this study by growing the metallic nano-helices on a substrate constituted by SiO_2 and a thin layer of indium-tin-oxide (*ITO*), due to it larger thermal conductivity. Therefore, the *ITO* film acts as the *heat-sink* layer, meanwhile *PMMA* was spun on top as the *heat-shield* layer. The resulting nano-helices are less regular than those in Fig. 5.6A due to the lower thermal conductivity of *ITO* in comparison with *Ag*, however, still their quality is much better than those of Fig. 5.6B. Note that apart from being a *heat-sink* layer, *ITO* is an

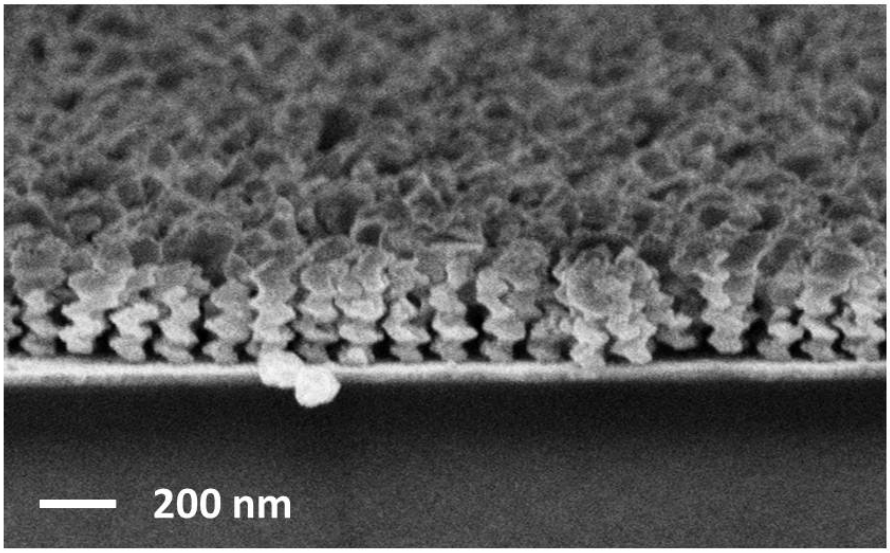

Fig. 5.7: SEM images of Ni nanohelices on a transparent substrate composed of SiO_2 and a thin film of *ITO*. Note that this image was not taken at a normal angle with respect to the helical axis.

electrically conducting compound enabling the usage of arrays of metallic nano-helices in opto-electronic applications.

5.1.5 Top-contacting of arrays of nano-helices for electrical measurements

A planar, dense cap on top of porous nano-sculptured films is sometimes desirable as it can provide encapsulation and protection for the film. If electrically conducting, it also can be used as electrode in order to undertake (magneto)-transport measurements through the array of nano-structures. This capping layer can be achieved on top of a nano-helix array by decreasing the incident flux angle towards the normal during the material deposition, causing the microstructure to evolve from porous to dense [80]. This angle decrease was done smoothly in small steps in order not to fill the porous sculptured film during the new film growth. Fig. 5.8 shows the side and top view of the generated capping layer through this first step. The tilting angle γ was decreased manually in five steps from 88° until 60° evaporating ∼40 nm of material in every step.
Afterwards, the residual porosity of the capping layer (see Fig. 5.8B) is eliminated using metallic conductive silver paint composed of large flakes (average size of >2 μm).

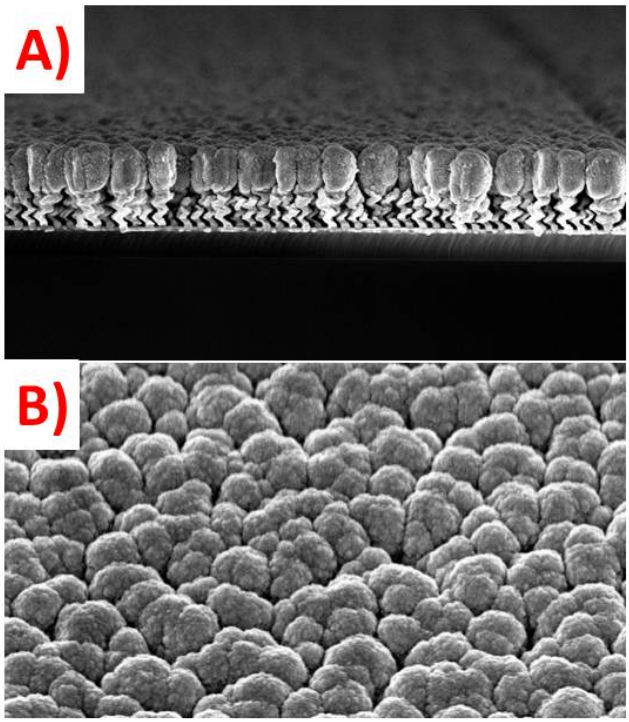

Fig. 5.8: Capping *Ni* nano-helices. A) Side view. Three-turn *Ni* nano-helices are capped by thicker *Cu* rods by decreasing smoothly the tilting angle γ. B) Top view showing the residual porosity of the *Cu* capping layer.

5.2 Structural Characterization

At the sample development stage, it is imperative to verify the structural quality of the produced nano-objects to optimize growth-conditions and assess reproducibility. This task is particularly important in complex geometries such as in the present case. Scanning electron microscopy (SEM) was utilized to examine the structure and morphology of the metallic nano-helices due to the technique's reliability and fast throughtput in comparison with alternative methods (Atomic Force Microscopy, Transmission Electron Microscopy, etc.)

5.2.1 Scanning Electron Microscopy

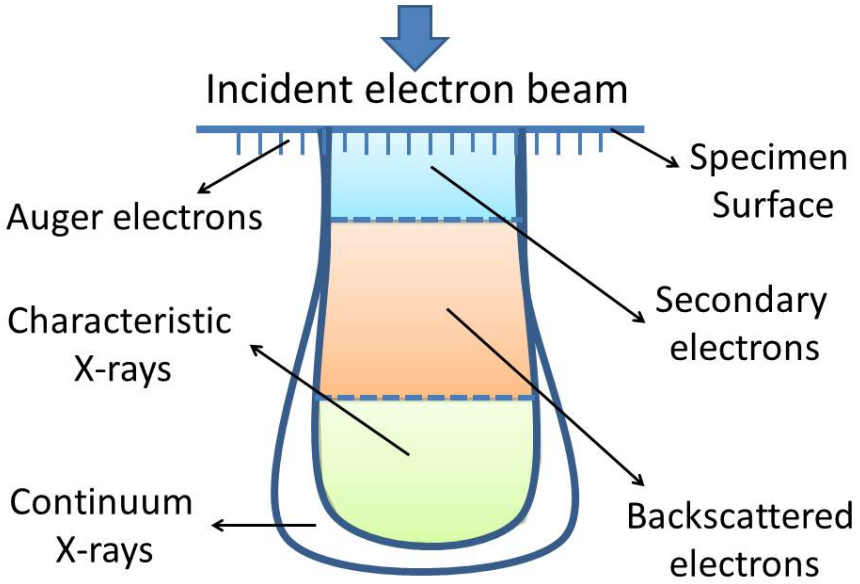

Fig. 5.9: Interaction region of electrons when carrying-out scanning electron microscopy.

An SEM is an electron microscope that produces images of a sample by scanning it with a focused beam of electrons. The electrons interact with atoms in the sample, producing various signals that can be detected and that contain information about the sample's surface topography and (chemical) composition. It is one of the most commonly used techniques for analysing structures with dimensions below the diffraction limit of light [102]. The accelerated electrons interact with the surface of the sample in a finite bulb shaped region (Fig. 5.9), the size of which depends on the incident current and acceleration voltage. Afterwards, they are either scattered, or absorbed resulting in the emission of X-rays. An image of the substrate can be reconstructed using the scattered electrons. Two types are commonly used to construct images; secondary electrons (SEs)

and backscattered electrons (BSEs).
SEs are generated by multiple inelastic scattering close to the surface of the substrate and typically have energies <50 eV. BSEs have energies >50 eV and are generated by elastic scattering further away from the sample-surface and contain depth information. The X-rays generated give information on the chemical composition of the materials. The SEs are collected either using the in-lens detector or the secondary electron detector placed outside the electron-beam column to produce an image of the sample surface. Information on the chemical composition can be gathered from the energy of the electrons and their angular distribution.
The average penetration depth r_d can be calculated following the expression $r_d = \frac{0.1E_0^{1.5}}{\rho Z}$ [103], where ρ is the material density (g/cm^3), E_0 is the accelerating voltage (KeV) and Z is the atomic number. For example, in the case of nickel r_d ≈4 nm. The maximum penetration depth can be estimated as $3 - 5r_d$ [103], being $12 - 20$ nm for Ni.
The side view of the nano-helix sample was imaged to properly visualize the helical structure and morphology. This has been achieved by building home-made stubs which allow the vertical positioning of the substrate (see Fig. 5.10).

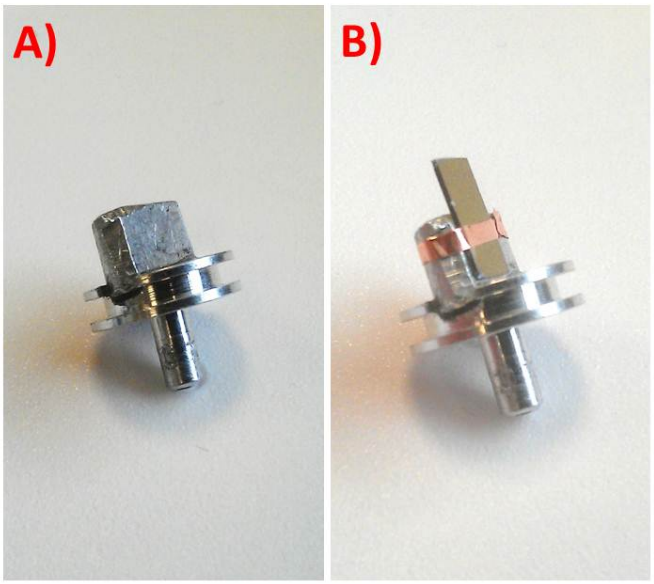

Fig. 5.10: Home-made stubs for vertical sample positioning. A) Actual stub. B) Sample attached to the stub using copper tape.

5.3 Optical characterization

5.3.1 Specular reflectance measurements

Apart from monitoring the evolution of the optical properties of nano-helices depending on their structural parameters and their collective arrangement, angle-resolved reflectance measurements are particulary useful to obtain information and discriminate the existance of surface plasmon polaritons and localized plasmon effects in nano-structures [104]. The experimental set-up to measure the unpolarized specular reflectance is shown in Fig. 5.11. These measurements were carried out my myself in collaboration with the 'A. Volta' department in the University of Pavia, in the group of Prof. V. Bellani. A commercial Fourier Transform (FT) spectrometer (Bruker IFS 66/S) was used to record the spectral response of the sample in the range from 0.25 eV to 3.1 eV (400 to 5000 nm) with a spectral resolution of 8 cm^{-1}. A Xe discharge lamp was placed in front of the entrance of the spectrometer.

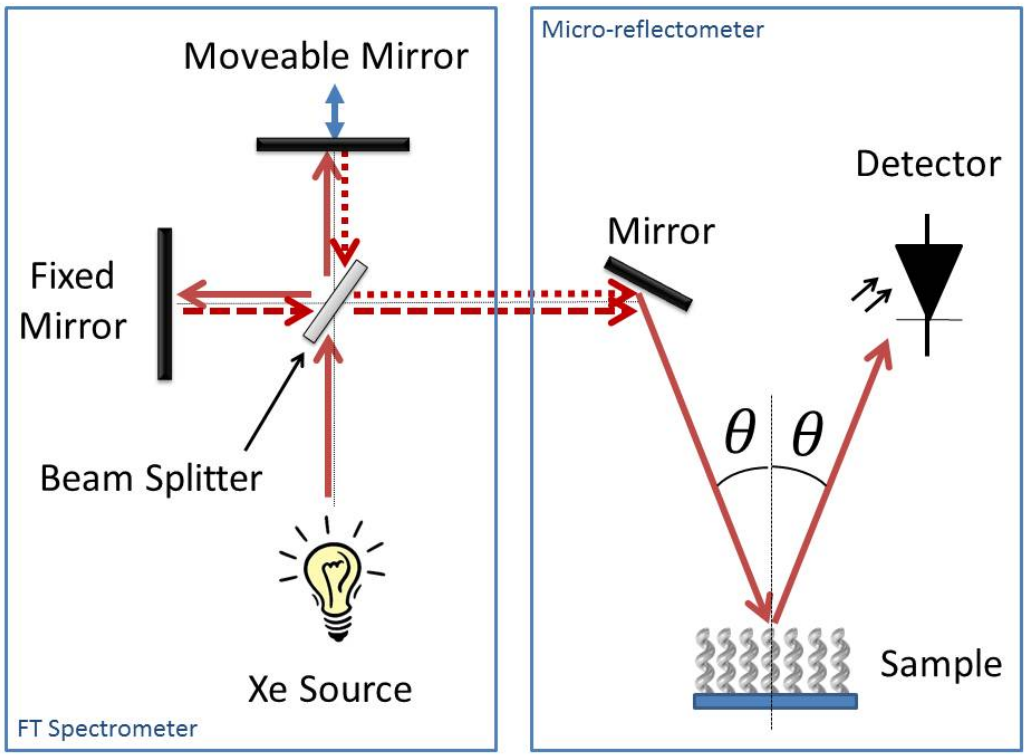

Fig. 5.11: Schematic of the set-up used to detect the reflectance spectra. A commercial FT spectrometer is coupled to a home-made micro-reflectometer. The set-up was built at the 'A. Volta' department in the University of Pavia.

The FT spectrometer was equipped with a home-made optical system as sketched in Fig. 5.11 (micro-reflectometer). The incident light coming out of the spectrometer is collimated on the sample (spot-diameter ∼500 μm). With the in-house built θ - 2θ goniometer the

incident angle was varied between 10° and 80°, with a resolution of ±1°. Two detectors were used to collect the signal: a silicon photodiode (measurement range from 400 nm to 1200 nm) and a InSb detector (measurement range from 1000 nm to 5000 nm). More details about the principles of FT spectroscopy are described in **Appendix D**.

5.3.2 Transmission measurements

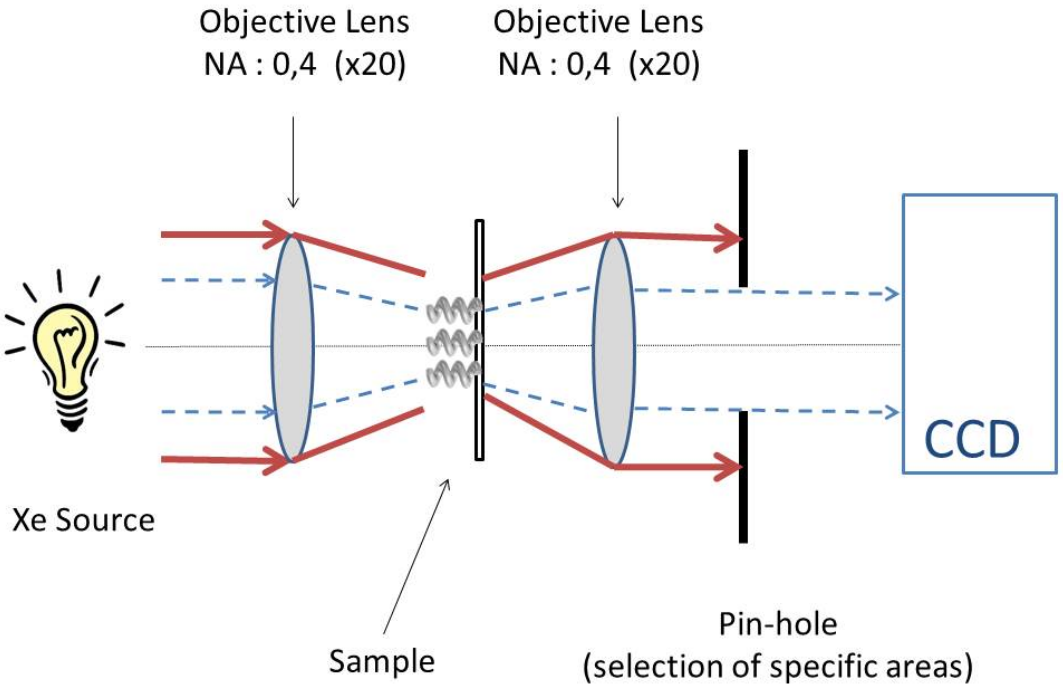

Fig. 5.12: Schematic of the set-up used to detect the transmission spectra. Xe light is focused on the sample with a ×20 microscope objective lens. A liquid N_2 cooled spectral charged-coupled device (CCD) detector[9] is used to obtain the spectral range from 400 nm to 1000 nm. A pin-hole is installed in the set-up to select the area of interest of the sample. The set-up is located in the Photonics Group laboratories, Trinity College Dublin.

Optical transmission measurements of metallic nano-helices grown on transparent substrates are suitable to evidence the evolution of the LSPR in nano-helices with a main radiative decay of the localized plasmon (as is the case of *Ag* nano-structures). In addition, the transmission measurements complement the reflectance information to corroborate and thus extract valid conclusions regarding the optical properties of metallic nano-helices. Through these measurements it is simple to obtain the extinction cross-section C_{ext} of the nano-helices, a parameter that is at a maxima at the LSPR position[10] [18].

[10] Note; that in nano-structures with mainly non-radiative plasmon damping (for example *Ni* nano-helices), the reflectance measurements are sufficient to clearly observe the LSPR since these structures

The experimental set-up to measure the unpolarized transmission spectra of small sample areas ($\sim$100 μm^2) is shown in Fig. 5.12. A commercial CCD was used to record the spectral response of the sample in the range from 0.25 eV to 1.24 eV (400 to 1000 nm). A Xe discharge lamp was used as a light source. The white light was focused on the sample through a x20 microscope objective and the areas of interest of the sample are conveniently selected with a pin-hole installed in the set-up. It should be noticed that this set-up can be conveniently tuned to measure reflectance measurements as well. In particular, it is employed in this thesis to measure the reflectance at a normal incidence $\theta = 0°$. These measurements were carried out by myself and people within the Photonics Group in the school of Physics, Trinity College Dublin, headed by Prof. John Donegan.

5.3.3 Surface-Enhanced Raman Spectroscopy

Surface enhanced Raman spectroscopy or surface enhanced Raman scattering (*SERS*) is a surface-sensitive technique that enhances Raman scattering [30] by the interaction of the investigated objects with structured metal surfaces. The enhancement factor (EF) can be as much as $\sim 10^{12}$ [30], making the technique appropriate to detect single molecules [30, 105].

Raman spectra were measured at room temperature with a Renishaw micro-Raman spectrometer using a $\times$50 objective lens (laser spot area $\sim$4 μm^2) and two excitation wavelengths: 633 nm and 785 nm. The spectral resolution of the apparatus was $\sim$2 cm^{-1}. The calibration was carried out by utilizing the Rayleigh and Si bands at 0 cm^{-1} and 521 cm^{-1}, respectively. Spectra acquisition time was of the order of few minutes keeping the power on the samples below 1 mW to avoid sample heating. A high-pass filter is installed in front of the CCD detector to shield undesired laser light. Two Raman active probing molecules were used to assess the *near-field* of metallic nano-helices: graphene and p-mercaptoaniline (pMA).

Near-field, Enhancement-Factor assessment and probing molecules

The evaluation of the enhancement factor (EF) is a paramount issue to precisely probe the *near-field* of the metallic nano-helices by $SERS$. The EF is proportional the fourth power of the magnitude of the local field enhancement F_{loc} ($EF \propto |F_{loc}|^4$) [30, 56]. It is experimentally determined by evaluating the following the expression

$$EF = \frac{I_{SERS} \cdot N_{REF}}{I_{REF} \cdot N_{SERS}} \tag{5.2}$$

which represents the ratio of the $SERS$ signal I_{SERS} to the reference Raman signal I_{REF} measured and normalized per molecule. N_{SERS} and N_{REF} are the number of molecules

posses a minimal scattering component

giving rise to the signal in the SERS and reference set-up, respectively. The estimation of the number of molecules (N_{SERS} and N_{REF}) in Eq. 5.2 entails difficulties due to several reasons such as inhomogeneous filling of voids or residual irregularities in the shape of the nano-helices under investigation. Any of these reasons will lead to EF mismatches with theoretical calculations, resulting in a generally indetermined near-field distribution around the nano-particles. This situation is particularly relevant in nano-structures with non-trivial topologies such as the arrays of nano-helices in the present study.
Graphene avoids the formerly described important source of error regarding the number of contributing molecules to the Raman signal: being a mono-atomically thin material, the condition $N_{SERS} \approx N_{REF}$ is reasonably well fulfilled. Therefore, by using graphene, a more precise assessment of the plasmonic *near-field* is possible [106]. However, graphene can not show the maximum EF that the nanohelices are capable to produce as it does not cover them entirely. For the latter purpose, the *SERS* spectra of pMA deposited around *Ag* nano-helices were measured.

Raman signature of graphene and p-mercaptoaniline

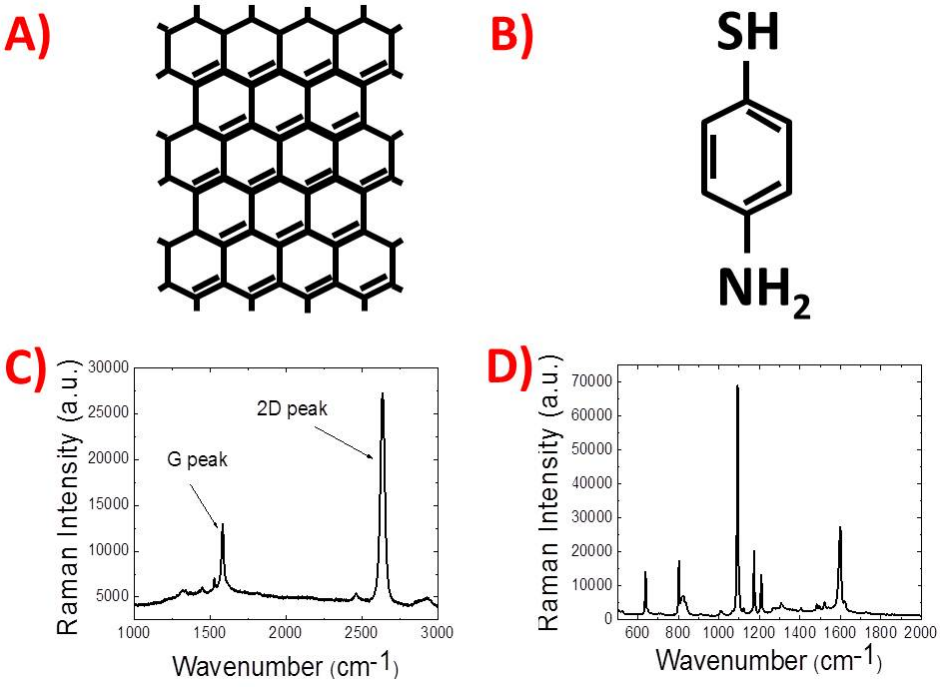

Fig. 5.13: SERS probing molecules. A) Graphene. B) p-mercaptoaniline (pMA) also named 4-aminothiophenol. C) Typical Raman spectrum of graphene. D) Typical Raman spectrum of pMA.

The two most prominent features of the Raman spectra of graphene are the so called G and 2D modes which lie around ∼1580 cm^{-1} and ∼2650 cm^{-1} [107]. They are due to bond

stretching of all pairs of sp2 atoms in rings and chains in the graphene (see Fig. 5.13A), and the symmetry-allowed second order of the breathing modes of sp2 atoms, respectively [107]. These are the two peaks used to examine the *near-field* the metallic nano-helices (see Fig. 5.13C). In contrast, pMA possesses a rather complex Raman spectrum within the range 400 cm^{-1} to -1600 cm^{-1} (see Fig. 5.13D and Ref. [30]). For consistency and comparison purposes, the peak around $\sim$1580cm^{-1} was used to evaluate the $SERS\ EF$, which is due to the bond stretching of all pairs of sp2 atoms in rings (see Fig. 5.13B). Further details on the *near-field* and $SERS\ EF$ estimation of metallic nano-helices using graphene and pMA are described in **Appendix E**.

5.4 Magneto-optical characterization

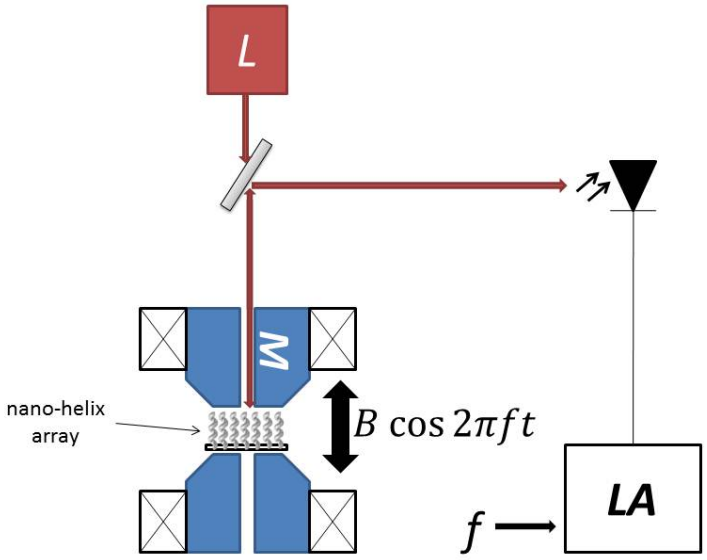

Fig. 5.14: Schematic showing the principle set-up used for the observation of MChD in reflection. The sample is shined with a monocromatic radiation produced by laser sources L. An AC magnet M, generates a magnetic field $\vec{B}$ which oscillates at a frequency f. The intensity difference of the reflectance for parallel and antiparallel $\vec{B}$ is phase-sensitively detected by a photodiode connected to a lock-in amplifier LA.

The principal experimental set-up for observing the Magneto-Chiral Dichroism (MChD) of the nano-helices in a reflection configuration is presented in Fig. 5.14. The experiments were carried-out my myself at the High Magnetic Field Laboratory in Toulouse, France, in collaboration with the group of Prof. G.J.L.A.Rikken. The sample is inserted at room-temprerature within an AC magnet (M) which oscillates at a frequency f. The typical frequencies and field-amplitudes achieved are from 5 to 20 Hz and from 0 to 1.2 T, respectively. The used light was produced by laser sources (L) with different wavelengths at 432, 533, 633 and 735 nm. The intensity difference of the reflectance ($\Delta R = R(+\vec{B}) - R(-\vec{B})$) between the two magnetic field directions is phase-sensitively detected by a lock-in amplifier (LA). The carried-out MChD detection in a reflection configuration is the first experimental realization of this kind. In this respect, it should be emphasized, too, that a reflection set-up for MChD detection is not straightforward as conventional dichroism experiments are performed in transmission. The incident photons experience an opposite direction of the magnetic field once they are reflected. Thus, one might think that the effect gets cancelled. From a photon-picture point of view, MChD can be detected in reflection as the unpolarized photons scattered from the 'chiral' voids differently depending on the magnetic field direction (parallel or antiparallel to the helical

axis). This different scattering create an imbalance in the number of photons in the detector, allowing the MChD observation in reflection.

5.5 *Magneto-electrical characterization*

The principal experimental set-up for observing the electrical Magneto-Chiral Anisotropy (eMChA) of arrays of uniaxially alligned nano-helices is presented in Fig. 5.15. The sample is inserted whithin a homogeneous magnetic field $\vec{B}$ (in this case up to 8 T) produced by a superconducting coil. This magnetic field is alligned parallel or antiparallel to the axis of the nano-helices. The resistance of the sample is measured in a standard 2-point configuration for different applied magnetic fields and current intensities $\vec{I}_{SD}$. The usage of the 2-point configuration is justified as the nano-helices are made from metal, *i.e.*, the contact resistance between the electrodes and the actual samples is ohmic. More importantly, up to second order, any contribution to the experimentally measured total magneto-resistance from the contacts must scale as $|\vec{B}|^2$ or $|\vec{I}|^2$ for symmetry reasons [108]. That is, no $\vec{I}\cdot\vec{B}$ contribution is possible from the contacts. The overall measured resistance of the nano-helix array and contacts is $\sim$4 Ω for arrays of 100 μm $\times$ 100 μm and $\sim$80 Ω for arrays of 10 μm $\times$ 10 μm. Meanwhile, the strength of the detected eMChA effect is of the order of a few mΩ. To reduce the picked-up noise in the electrical measurements the detection set-up has to be undertaken using phase-sensitive measurements in a standard 2-point set-up as shown in Fig. 5.15. This circuit measures the resistance of a sample with precision up to $\pm$10 $\mu\Omega$. Finally, the variation of the eMChA effect depending on the temperature of the sample is studied in this thesis. The latter is possible since the superconducting magnet is attached to a cryo-free refrigerator which reaches 2K as minimum cooling temperature.

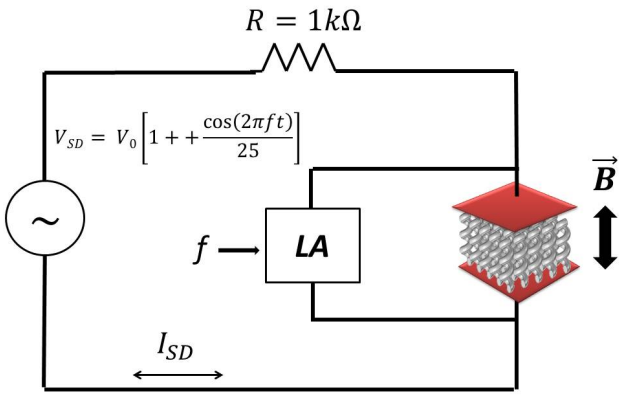

Fig. 5.15: Schematic showing the experimental set-up for measuring eMChA. The standard 2-point set-up is used in a phase-sensitive measurement technique. The source-drain voltage (V_{SD}) applied to the sample has a main DC component and a much smaller AC component at a frequency f (in this case f = 113 Hz). The resistor R is three orders of magnitude bigger than the resistance of the sample under study in order to convert the voltage-source into a current-source I_{SD} passing through the circuit. Finally, the variations of AC voltage that produced into the sample under study by I_{SD} are detected by the lock-in amplifier LA.

6. RESULTS AND DISCUSSIONS

As mentioned in **Chapter 1**, metallic helical structures are widely used in many applications covering the radio-frequency, micro-wave and mid-infrared part of the electromagnetic specturm [5, 6]. However, they have not yet been studied nor exploited in the visible spectrum due to the lack of structurally well-defined metallic helical objects at the nano-scale.

The purpose of this chapter is first to demonstrate in more detail how the fabrication method proposed in **Section 5.1** is able to successfully produce large area arrays of regularly-shaped, nano-sized, aligned and freestanding metallic nano-helices. In particular, it reports a systematic study describing key factors to optimize their growth parameters. The five metals attempted in this study are some of the most difficult materials to engineer using *GLAD* due to their high surface mobility [90–92].

The manufacturing simplicity and precision of the reported metallic helical nano-structures make these samples ideal for the identification of theoretically predicted and genuinely novel optical and chiral effects at the nano-scale [8, 18, 19]. In this respect, it is possible to demonstrate how the optical and electrical properties of the nano-helices are tuneable by the pitch, diameter and number of turns of a single helix (*cf.* **Section 6.2.1**). Furthermore, Surface-Enhanced Raman Spectroscopy is used to experimentally demonstrate the performance of these nano-antennas (*cf.* **Section 6.2.4**).

Finally, the chirality-related effects described in **Chapter 4** are demonstrated for the first time in this study *at the nano-scale* for a chiral medium composed of materials with no internal chiral structure. Thus, the reported topologically induced chirality of the structures allows the shifting of the optical activity and magneto-chiral anisotropy for different wavelengths depending on the samples' structural parameters within the optical electromagnetic spectrum. Meanwhile, the chiral magneto-trasport properties show the predicted electrical magnetochiral anisotropy [7]. These latter effects are tested in *Ni* since they are stronger in ferromagnetic metals than in diamagnetic or paramagnetic materials [70] (their permeability is higher, thus their magnetic flux $\vec{B} = \mu_0(\vec{H} + \vec{M})$ is larger).

6.1 Nano-helices made from different metals

Nano-helix arrays made from five different metals *Ni*, *Cu*, *Co*, *Al* and *Ag* have been attempted in this study. This range of selected metals in principle allows to address novel combinations of the optical, electronic and magnetic properties of these elemental metals due to their actual helical geometry at the nano-scale. The growth results achieved were satisfactory for all of the former elements with the exception of *Al*. It has to be emphasized that these are five of the most difficult materials to engineer into nano-structures using *GLAD* due to their high surface-atom mobility [90–92].
In this section, the fabricated nano-helices are presented together with a detailed comparison with growth theories [9] and previous state-of-the-art [90–94]. Furthermore, a reasoned and comprehensive study on the selection of the optimum *GLAD* parameters (see **Section 5.1**) is provided for the different metals chosen. Table 6.1 summarizes the bulk thermal and electrical properties of the referred metals which are needed for the analysis here presented.

Tab. 6.1: Main thermal and electrical properties of used metals [109, 110]

Metal	Melting point T_m [K]	Boiling point T_b [K]	Termal conductivity K [$\mathrm{Wm^{-1}K^{-1}}$]	Electrical resistivity ρ [nΩm]
Ni	1728	3186	90.9	69.3
Co	1768	3200	100	62.4
Cu	1357	2835	401	16.78
Ag	1234	2435	429	15.87
Al	933	2792	273	22.2

Since the key parameter for any *PVD* growth is the surface diffusion length Λ of the metal, Table 6.2 displays the materials' constants necessary to estimate it. This parameter depends on both, the growing temperature T and the deposition rate r and can be calculated by [97, 99]:

$$\begin{aligned} \Lambda &= \sqrt{D\tau_m} \\ D &= D_0 e^{\frac{-E_h}{k_B T}} \\ D_0 &= \frac{a_0^2}{4} f \\ \tau_m &= \frac{a_0}{r} \\ E_h &= \frac{\Delta_h}{5} \end{aligned} \tag{6.1}$$

where k_B is the Boltzmann constant and the following are parameters of the incoming atoms (material): τ_m is the mobility lifetime, D_0 is the intrinsic diffusivity, E_h is the

energy required for site hopping, f is the lattice vibration frequency, Δ_h is the activation energy for an atom to escape out of the structure, and a_0 is the atomic radius. In this work, f is calculated following the Lennard-Jones estimations of a one-dimensional chain of surface atoms of mass m and spring constant K [97, 111]: $f = \sqrt{\frac{K}{m}}$.

Tab. 6.2: Metal parameters to estimate the surface diffusion length $\Lambda(T,r)$ [97, 109, 110]

Metal	Δ_h [J]	f [s^{-1}]	a_0 [pm]
Ni	$6.64{\cdot}10^{-19}$	$5{\cdot}10^{12}$	130
Cu	$4.99{\cdot}10^{-19}$	$4.8{\cdot}10^{12}$	128
Co	$6.7{\cdot}10^{-19}$	$5{\cdot}10^{12}$	125
Ag	$4.6{\cdot}10^{-19}$	$3.7{\cdot}10^{12}$	144
Al	$4.88{\cdot}10^{-19}$	$7.3{\cdot}10^{12}$	143

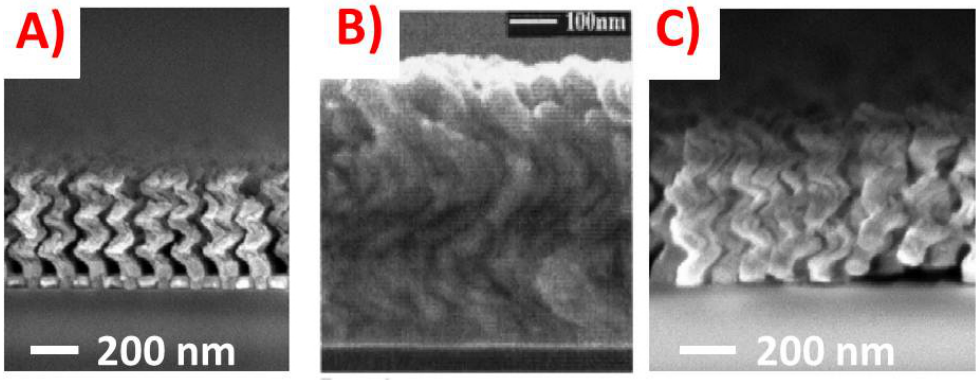

Fig. 6.1: A) *Ni* nano-helices made with pre-patterned substrate (dots) and the bi-layer *heat-management* system. B) Best result of *Ni* nano-'helices' reported in literature [92]. C) *Ni* nano-helices made on a dotted array with no *heat-management* system built on the substrate. Note that the samples shown in A) and C) were fabricated during the *same* growth process in order to emphasize the importance of the heat engineering process developed.

6.1.1 Nickel nano-helices

Fig. 6.1A shows a SEM image of a nano-helix forest made from *Ni* using the experimental technique presented in Section 5.1. The substrate rotation-speed was $\Omega \sim 0.3$ rpm, the deposition rate 1.5 nm/s, the dot-pitch $\delta = 150$ nm and the glancing angle $\theta \sim 88°$. Structurally well-defined and freestanding *Ni* nano-helices with uniform pitch and diameter are observed with an overall height of about 300 nm. There are no traces of agglomerations or collapse, proving the superiority of our procedure over the previous state-of-the-art (Figs. 6.1B,C)

The maximum temperature reached during any growth process can be estimated from the

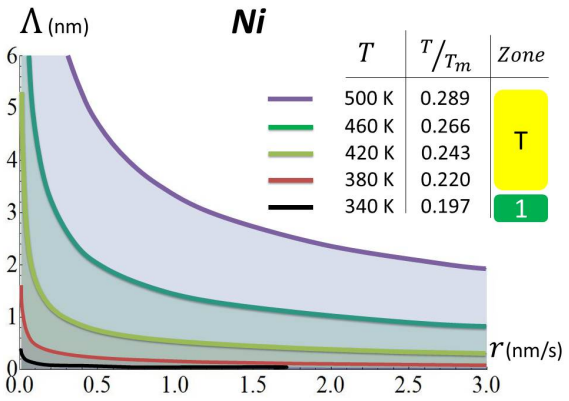

Fig. 6.2: Calculated *Ni* surface diffusion length Λ depending on the deposition rate r for a set of different temperatures. Legend shows the absolute growth temperature T, the reduced temperature T/T_m and the corresponding zone of the SZM.

appearance of the sculptured thin film using the Structured Zone Model (SZM) presented in **Chapter 2**. The uniformly structured and well-separated nano-helices in Fig. 6.1A imply that they were grown within the Zone 1 of the SZM. This gives an estimation of the maximum temperature reached during their growth of $T \sim 0.20 \cdot T_m = 350$ K. Meanwhile, the thicker and collapsed nano-helices presented in 6.1b,c suggest that they fall well into the Zone 2 of the SZM, with a temperature estimate of at least $T \sim 0.30 \cdot T_m = 520$ K. Consequently, the reduction of the growth temperature due to the here introduced *heat-management* system can be quantitatively assessed to be more than ∼170 K. In other words, the maximum surface diffusion length during growth is reduced when using the *heat-management* from ∼20 nm to less than 1 nm (both values estimated at the depostion rate of 1nm/s).

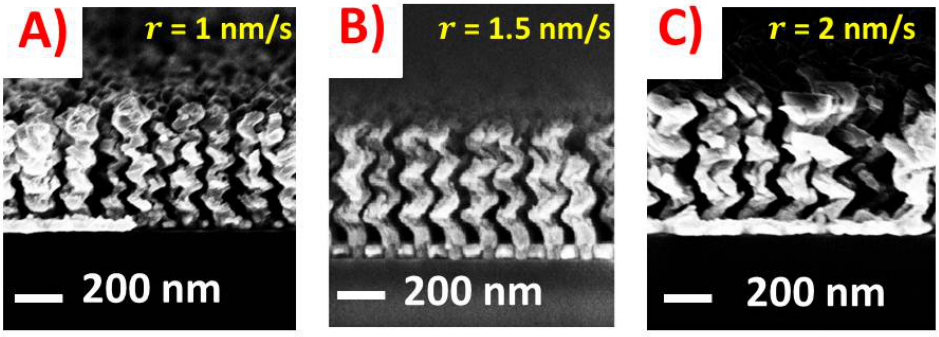

Fig. 6.3: *Ni* nano-helices for different deposition rates. A) $r = 1$ nm/s. B) $r = 1.5$ nm/s. C) $r = 2$ nm/s. The most uniform and well-separated helices are produced for $r = 1.5$ nm/s and a dot-spacing of $\delta = 150$ nm.

This result has to be related with $\Lambda(T,r)$ to gain more details on the actual growth

process. Fig. 6.2 shows the calculated $\Lambda(T, r)$ for *Ni*. It considerably increases for lower deposition rates and higher growth temperatures. Following this theoretical dependence, the higher r, the smaller Λ at any growing T, thus, the better the structure should be. However, this trend was not experimentally confirmed. An improvement in the quality of the samples between rates 1 and 1.5 nm/s is observed, but the samples become less uniform for a 2 nm/s rate (see Fig. 6.3).

These discrepancies between theory and the experimental findings are attributed to two possible causes: first, the fact that for higher rates, the particle flux is less directional and less homogeneous due to collisions within the incoming evaporated flux [112]. Second, the radiation losses from the source are higher for higher r [98]. Therefore, in the latter case the effective growth temperature of the nano-structures is higher at higher r.

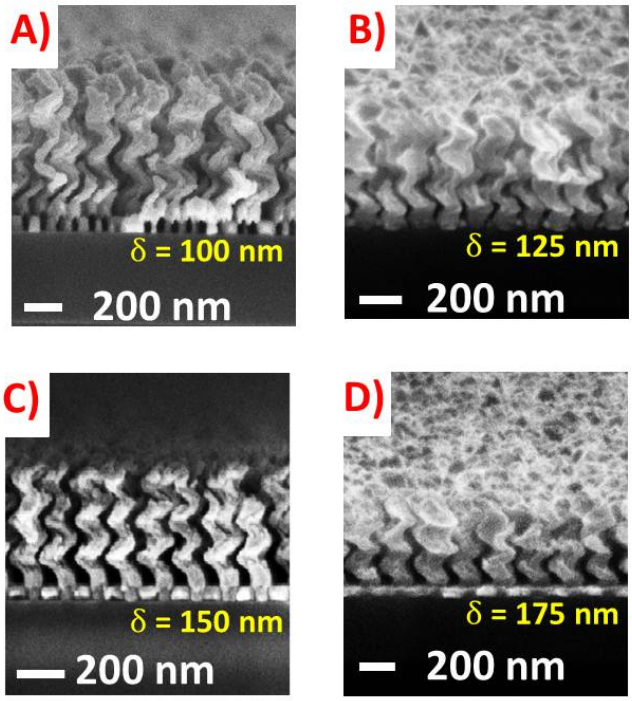

Fig. 6.4: Ni nano-helices for different dot separation. A) $\delta = 100$ nm. B) $\delta = 125$ nm. C) $\delta = 150$ nm. D) $\delta = 175$ nm. More uniform and separated nano-helices are obtained for larger δ. In addition, larger δ involves larger thickness of the wire which forms the nano-helix.

For these reasons, 1.5 nm/s was chosen as the convenient evaporation rate for *Ni* nano-helices. Once r is fixed, Ω is left as the variable parameter to change the helical pitch and diameter (**Appendix C**).

The last parameter to be fixed in the *Ni* case is the dot-pitch δ of the pre-structured substrate (**Section 5.1.2**). It was experimentally found that nano-helices are less uniform, collapsed and agglomerated for $\delta \leq 125$ nm. Meanwhile for $\delta > 175$ nm the helical wire was thicker than 100 nm in diameter. These features can be clearly observed in Fig. 6.4.

The explanation of this behaviour is the following: in metals with $\Lambda < 0.1\delta$ such as *Ni* the wire thickness is determined by shadowing between neighbouring pillars rather than by the surface diffusion length [113]. Consequently, the larger δ, the thicker the wire diameter. However, in the case of thinner wire diameters (*i.e.* smaller δ), since the ratio $\frac{\Lambda}{\delta}$ is larger, irregularities are more noticeable and relevant than for thicker wires. In the regime $\Lambda < 0.1\delta$, the processes to introduce irregularities include bifurcation (branching) of the helices and increase of the amount of material deposited onto a growing helix due to a decrease in the number of neighbours [114]. These were the reasons to choose 150 nm as the optimum value for δ for the growth of *Ni* nano-helices.

6.1.2 Cobalt nano-helices

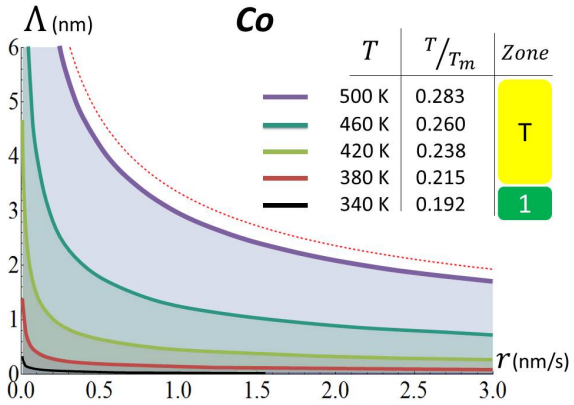

Fig. 6.5: Calculated *Co* diffusion length Λ depending on the deposition rate r for a set of different temperatures. The red dashed line shows Λ of *Ni* at 500 K for comparison purposes, demonstrating the similarity of the two materials. Legend shows the absolute growth temperature T, the reduced temperature T/T_m and the corresponding zone of the SZM.

The thermal and electrical properties of *Co* are close to those of *Ni* (see Tables 6.1 and 6.2). Therefore, the calculated $\Lambda(T, r)$ exhibits similar values (Fig. 6.5). This rensemblance suggest that the optimum growth parameters are close to the ones for *Ni* nano-helices, that is r ∼1.5 nm/s, θ ∼88° and δ ∼150 nm.

Fig. 6.6 shows freestanding *Co* nano-helices with an overall height of about 600 nm using the optimum parameters of *Ni* nano-helices. It is noticeable that the uniformity of the helical pitch and diameter is degraded at the tip of the helices from ∼500 nm onwards. This effect appears also in the *Ni* case and is likely to be due to residual non-uniform shadowing during the growth stage of the nano-structures rather than an increment of Λ due to the temperature rising during the growth of the structures. This conclusion is supported by the fact that the thickness of the helical wire does not increase progresively with the length of the structure (as occurs when Λ increases [99]) but rather a sudden structural collapse occurs at ∼500 nm height. This progressive degradation of the quality

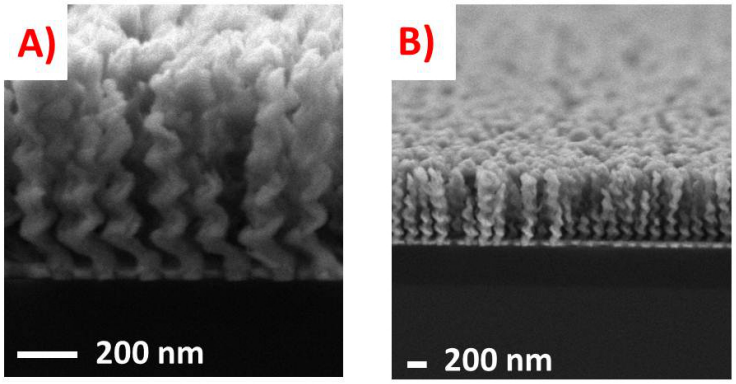

Fig. 6.6: *Co* nano-helices made with $\Omega \sim 0.3$ rpm and a pre-patterned substrate and the bi-layer *heat-management* system. Note, the few broken nano-helices are a consequence of the cleaving process of the samples prior to the SEM examination.

of the nano-structures for a given height is a general *GLAD* restriction rather than a limitation of the actual material [10].

6.1.3 Copper nano-helices

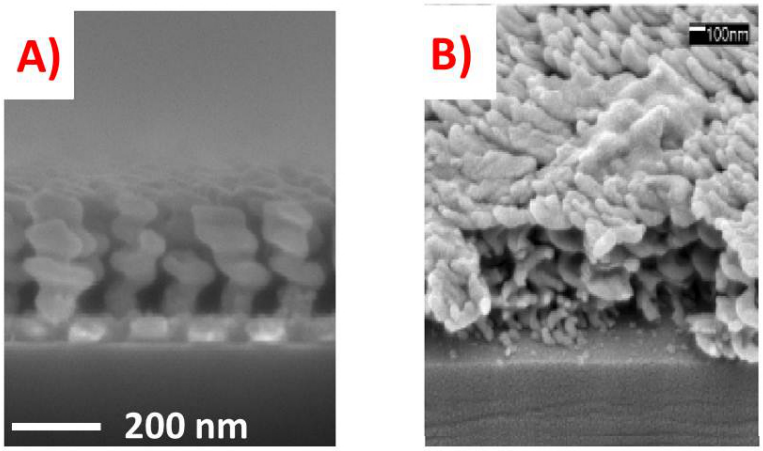

Fig. 6.7: A) *Cu* nano-helices made with $\Omega \sim 0.3$ rpm, with a pre-patterned substrate ($\delta = 150$ nm) and the bi-layer heat-management. B) *Cu* nano-'helices' reported in literature [90].

For comparison purposes, the first attempt to grow *Cu* nano-coils was carried out taking the same parameters as for *Ni* ($r \sim 1.5$ nm/s and $\theta \sim 88°$, $\delta \sim 150$ nm). The achieved results are shown in Fig. 6.7A. Despite of the lack of parameter optimization, the produced *Cu* nano-helices show superior structural quality than the reported state-of-the-art *Cu* nano-helices produced by *GLAD* (Fig. 6.7B). However, the produced *Cu* nano-helix structures appear less regular and controlled than the *Ni* and *Co* counterparts. Particularly, the wire forming a *Cu* nano-helix is found to be thicker ($\sim$ 100 nm) than for *Ni*

and *Co* ($\sim$ 70 nm). As a result, the windings seem to collapse within an individual *Cu* nano-helix. These observation indicate that the diffusion length $\Lambda(T,r)$ for *Cu* is larger than for *Ni* or *Co*, which is further underpined by the theoretical estimation of $\Lambda(T,r)$ showed in Fig. 6.8.

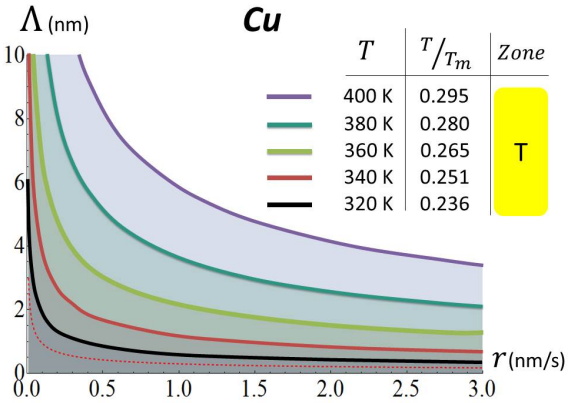

Fig. 6.8: Calculated *Cu* diffusion lengths Λ depending on the deposition rate r for a set of different temperatures. The red dashed line shows the surface diffusion length of *Ni* at 400 K for comparison. The legend shows the absolute growth temperature T, the reduced temperature T/T_m and the corresponding zone of the SZM.

From the experimental observations, the reduction of the growth temperature due to the *heat-management* system can be estimated to be around $\sim$200 K. This is justified as follows: the produced *Cu* nano-helices showed in Fig. 6.7 are grown within the Zone T of the Structured Zone Model (**Section 2.2**) because the nano-structures are well-separated but with a 'thick' wire diameter ($\sim$100 nm). Therefore, the estimatation of the maximum temperature reached during their growth is $T \sim 0.25 \cdot T_m = 340$ K. In comparison, the collapsed nano-helices presented in Fig. 6.7B suggest that they were grown well in the Zone 2 regime, with a minimum temperature estimation of $T \sim 0.4 \cdot T_m = 540$ K. The similar values of temperature reduction for *Cu* and *Ni* agrees with the fact that the heat management is equally fabricated in both cases. In terms of the maximum surface diffusion length reached during growth, for a given r of 1.5nm/s, the insertion of the heat-management system considerably reduces it from $\sim$60 nm to $\sim$1.5 nm. This small value of Λ implies that the change of this parameter (*i.e.* increase of T) during the growth does not produce deformation of the nano-helices. The latter effect is corroborated noticing that the thickness of the wire composing the helices in Fig. 6.7A stays approximately constant and does not increase along the length of the helix.

A further optimization of the fabrication of *Cu* nano-helices was attempted trying to further reduce the value of the surface diffusion length during the growth by modifying r. For this, samples were fabricated at three different deposition rates: 1 nm/s, 1.5 nm/s, and 2 nm/s (see Fig. 6.9). Interestingly, the helix quality is better for smaller r. The *Cu* nano-helices grown at $r = 1$ nm/s possess bifurcation (branching), typical of lower surface

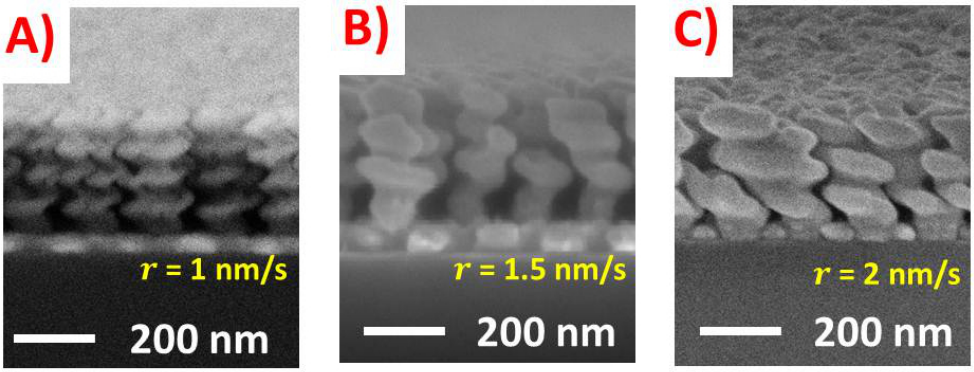

Fig. 6.9: *Cu* nano-helices for different deposition rates. A) $r = 1$ nm/s. B) $r = 1.5$ nm/s. C) $r = 2$ nm/s. The helix quality is better for smaller r, an effect which is not explained only considering $\Lambda(T,r)$.

diffusion conditions. Meanwhile for larger r the nano-structures get a thicker diameter, windings are melted within a helix and the structure gets more deformed. This behaviour is not expected from the calculation of Λ. For *Cu* at the maximum estimated growth temperature (340 K), Λ(340 K,1 nm/s) = 1.2 nm and Λ(340 K,2 nm/s) = 0.9 nm. This small surface diffusion difference would suggest that the nano-helices fabricated within this range of r should look similar, with an even better shape for higher r. However, Fig. 6.9 shows the opposite tendency. This behaviour indicates that although for all the cases the increase in growth temperature is small due to the heat-management system, the starting growing temperature is higher for higher deposition rates. This effect might be explained due to a dominant contribution the radiation losses from the source, which increase for higher r [98].

Sumarizing the two main results found during the fabrication of *Cu* nano-helices are: first, the minimal change of growth temperature during the deposition (which is related to a negligible change of Λ). Second, a better quality of nano-helices for smaller r. The first conclusion implies that the *heat-management* system works efficiently when transferring heat from the nano-structure to the substrate, keeping the nano-helices temperature close to the substrate temperature. The second demonstrates that the actual radiation losses from the source are a key mechanism in the *Cu* growth of nano-helices. Both reasonings suggest that for further optimizing the growth of this material, there is a need to cool down the substrate slightly rather than trying to improve the heat-management system (by tuning the bi-layers, etc.).

Finally, it should be noticed that the actual δ range highly depends on the selected r especially for the *Cu* case: a smaller r would allow the growth of regular structures with smaller δ than a bigger r. For example, in the case of $r = 1.5$ nm/s, a convenient δ to

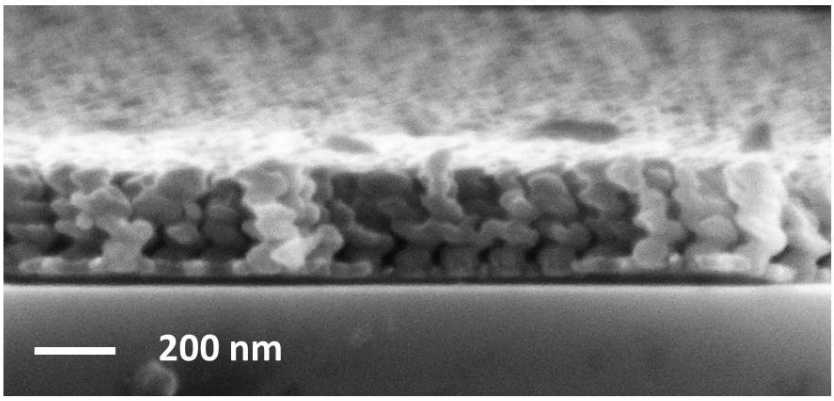

Fig. 6.10: *Cu* nano-helices for $\delta = 100$ nm and $r = 1.5$nm/s. The nano-structures have collapsed and with a less regular shape than those of Fig.6.7A.

growth *Cu* nano-helices is between 100 and 150 nm. A δ larger than that range would produce helices with a wire diameter larger than 100 nm. Meanwhile, a shorter δ would make the helices collapse (see Fig. 6.10 where $\delta = 100$ nm).

6.1.4 Aluminium nano-helices

A difficult material to be engineered by *GLAD* is *Al* due to its high surface mobility (Fig. 6.11) and low melting temperature (Table 6.2). The growth of *Al* nano-helices using different sets of parameters was attempted, and in all cases the results are similar to the ones presented in Fig. 6.12. Despite some initial coiled growth, *Al* crystallites are formed once the temperature increases minimally during the growth. The low T_m of this material places the nano-structures already at room-temperature (start of the growth) into Zone 2 of the SZM, which implies the growth of large crystal grains making it difficult to grow *Al* nano-helices of smaller and/or comparable size. The appearance of these crystals suggests that at the end of the growth the temperature rose up to at least $T \sim 0.4 \cdot T_m = 370$ K. To overcome the material difficulties when growing *Al* nano-structures there are two possible options:

- To cool the substrate down initially to ∼200 K, thus, the nano-helices would be within Zone T during the entire growth.
- To synchronize the evaporator and substrate rotation controller to grow the nano-structures discontinuously. This would avoid the growth temperature increasing by 70 K in this case.

6.1.5 Silver nano-helices

Fig. 6.13 shows an SEM image of a nano-helix forest made from *Ag*. For better comparison purposes, the growing parameters were again chosen to be those of *Ni* ($\Omega \sim 0.3$ rpm, r

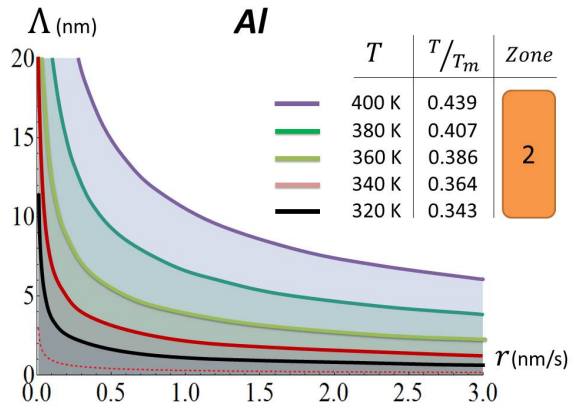

Fig. 6.11: Calculated *Al* diffusion length Λ depending on the deposition rate r for a set of different temperatures. The red dashed line shows the surface diffusion length of *Ni* at 400 K for comparison. The legend shows the absolute growth temperature T, the reduced temperature T/T_m and the corresponding zone of the SZM.

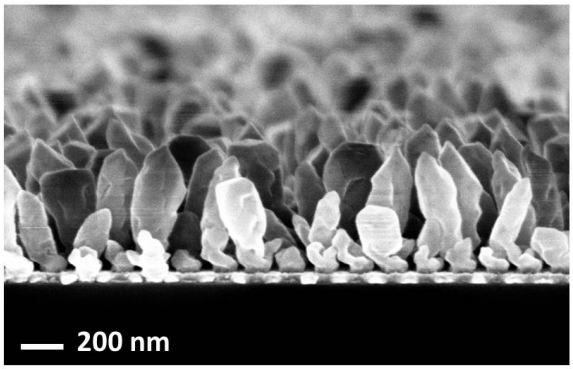

Fig. 6.12: Typical result of *Al* nano-helices with the developed *heat-management* system. Columnar crystallites are developed as a consequence of the low melting temperature T_m of this metal.

= 1.5 nm/s, θ ∼88° and δ = 150 nm). Structurally well-defined and freestanding *Ag* nano-helices are observed with an overall height of about 300 nm. There are no traces of collapse, however, the individual nano-helices are structurally less uniform than in the cases of *Ni* and *Co*. Futhermore, a weak tendency towards agglomeration is indicated by the SEM images at the top of the columnar film. The lower uniformity is expected when compared to *Ni* and *Co* at the used growth parameters (see Fig. 6.14). The mentioned structural features indicate that the nano-helices grow within the T zone. Thus, the temperature rising during growth is estimated to be $T \sim 0.25 \cdot T_m = 310$ K.
Apparently, the quality of these nano-helices is better than those made from *Cu* and *Al*. This phenomena is again due to the lower temperature achieved during the growth of *Ag*

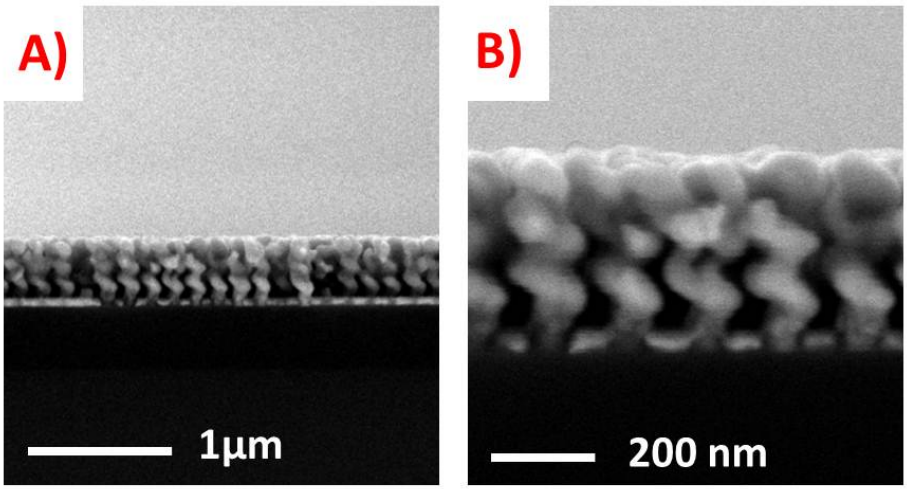

Fig. 6.13: Ag nano-helices fabricated with the bi-layer *heat-management* system using the same growth parameters as for *Ni*. A) and B) shows the same sample with different magnification.

nano-helices, that is, providing a smaller Λ in comparison to the other two metals (see Fig. 6.14). As described in the next section, the lower temperature rise in *Ag* nano-helices is perfectly correlated to the higher thermal conductivity of *Ag* compared to any other metal studied, which allows for a more efficient heat extraction to the heat-sink first, and subsequently to the substrate.

A further optimization of the fabrication of *Ag* nano-helices was attempted trying to further reduce the value of Λ during the growth by varying r. For this, samples were fabricated at three different deposition rates: 1 nm/s, 1.5 nm/s and 2 nm/s (see Fig. 6.15). Clearly, the best quality *Ag* nano-helices are produced for a depostion rate of 1.5 nm/s, minimizing both contributions which degrade the nano-helix quality: the surface diffusion length of the metal and the radiation loss from the source.

Finally, the most suitable δ to grow *Ag* nano-helices have to be larger than 100 nm since at this separation the nano-structures collapse as can be shown in Fig. 6.16, and δ has to be smaller than 150 nm if the wire thickness has to be thiner than 100 nm.

6.1.6 General remarks on the growth of metallic nano-structures via GLAD

Several conclusions can be extracted from the present study. First, *Ni* and *Co* are the easiest materials to be *GLAD* engineered followed by *Ag* and ultimately *Cu*. *Al* does not

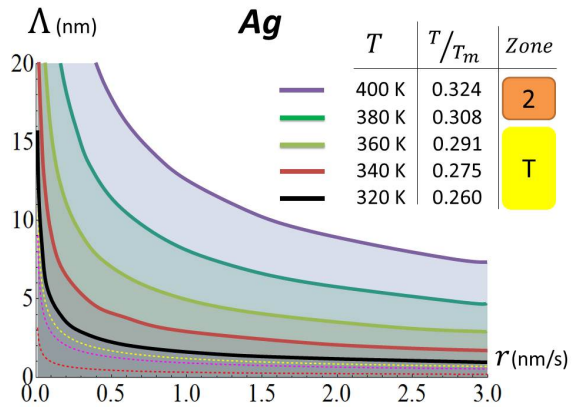

Fig. 6.14: A) Calculated *Ag* diffusion length Λ depending on the deposition rate r for a set of different temperatures. For comparison, the red, yellow and magenta dashed lines show Λ of *Ni*, *Cu* and *Ag* at 400 K, 340 K and 308 K, respectively. The legend shows the absolute growth temperature T, the reduced temperature T/T_m and the corresponding zone of the SZM.

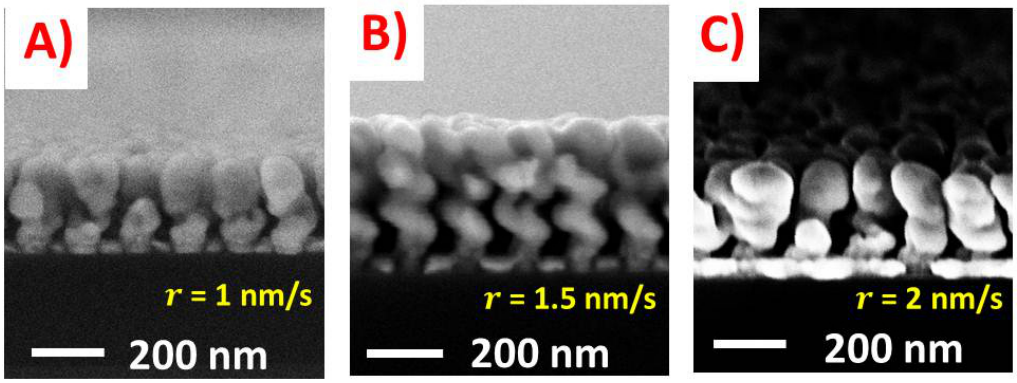

Fig. 6.15: *Ag* nano-helices for different deposition rates with $\delta = 150$ nm. A) $r = 1$ nm/s. B) $r = 1.5$ nm/s. C) $r = 2$ nm/s. The structural quality fo the helix is found to be best for $r = 1.5$ nm/s.

seem to be a good metal for undertaking room-temperature *GLAD* as it is carried-out here. This trend results from a combination of the surface diffusion length, the ratio of the growth versus the melting temperature of these materials, and the radiation losses from the source. Interestingly, these three causes are inter-dependent and amongst others rely upon one common external parameter: the growth rate r. Fig. 6.17 shows an inter-relational schematic of all of them. For a given growth temperature T, the surface diffusion length Λ decreases when increasing r since the incoming ad-atoms are trapped ('buried') faster [97]. However, in a practical implementation of *GLAD*, when increasing r in an evaporator, the radiation losses increase too, hence increasing T and subsequently Λ. These behaviours are experimentally observed in the undertaken experiments too, and therefore explain the quality of the nano-helices made from different metals when varying r.

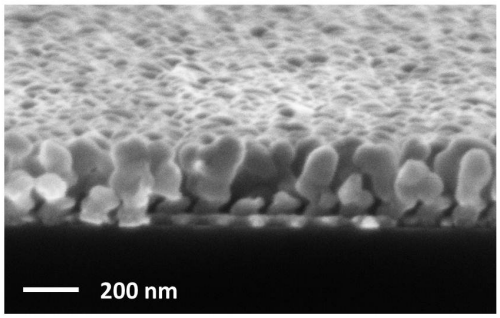

Fig. 6.16: Ag nano-helices for $\delta = 100$ nm and $r = 1.5$nm/s.

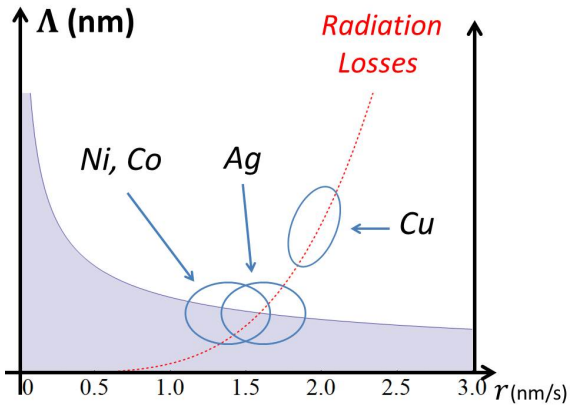

Fig. 6.17: Surface diffusion length depending on the growth-rate r. For a given T, Λ decreases when increasing r (blue line). However, in an evaporator, when r increases, the radiation losses increase, too. Thus, T and Λ increase as well. On the basis of our observations, *Ni* and *Co* grow in a regime where the radiation losses are not dominant. The latter, however, contributes more in the case of *Ag* and it is important in the *Cu* case. The red dashed line indicates the radiation losses contributions, which scale as the fourth power of T [98]. However, this dashed line is an schematic visualization of the effect, since the relation between T and r is not given.

Second, the insertion of a *heat-management* system on the substrate considerably improves the *GLAD* technique by reducing the temperature of the growing structures in-situ. This temperature reduction in this work is estimated to be ∼200 K when growing metallic nano-structures on SiO_2. In fact, the *heat-management* technique opens the possibility for growing highly uniform metallic *GLAD* nano-structures at room temperature. Therefore not only the substrate temperature, but also the efficient heat extraction (substrate thermal conductivity) is important for *GLAD* depositions.

Third, for any material, the increase of shadowing irregularities during the columnar growth degrades progressively the structural quality of the nano-structures. This behaviour was observed in *Co* and *Ni*, the materials with the lowest surface mobility mate-

rials studied in this work, after an overall height larger than ∼500 nm.
Fourth, for a given initial substrate temperature and substrate thermal conductivity, the combination of materials, separation of pre-patterned dots, deposition rate and substrate rotation speed together define a structure phase-space which determines the column morphologies produced during a *GLAD* process [10]. According to the presented results, these vast potential parameter space available for *GLAD* depositions is in fact considerably reduced when considering the growth of uniform free-standing metallic nano-structures. There are narrow useful windows to select the dot-spacing δ and the depostion rate r which depend on the surface diffusion length of the metal and the thickness of the wire forming the nano-structures. The substrate rotation speed Ω seems to be the most flexible parameter to engineer *GLAD* nano-structures.

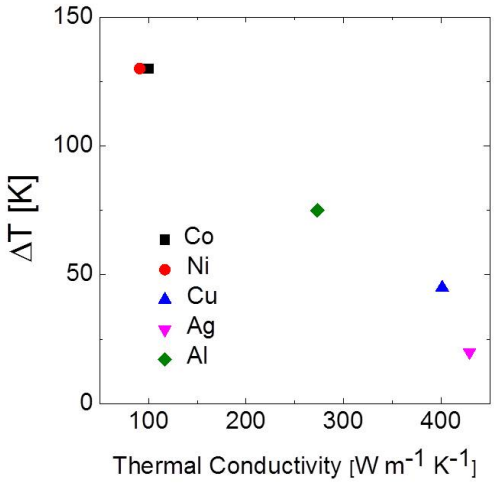

Fig. 6.18: Change of the growth temperature depending on the thermal conductivity of the selected metals.

Finally, besides the substrate temperature and substrate thermal conductivity, also the thermal conductivity of the actual metal affects the temperature rise during growth and the quality of the nano-structures. The latter effect is explicitly introduced and proven in this work. The temperature rise of nano-helices made from the selected materials was found to be ∼130 K (*Ni* and *Co*), ∼70 K (*Al*), ∼50 K (*Cu*) and ∼15 K (*Ag*). This sequence follows the same trend as the thermal bulk conductivities of these materials (Table 6.1) as depicted in Fig. 6.18. Interestingly, the structural quality of the nano-helices does not follow this trend, which is a consequence of the differing adatom surface-diffussivities of these materials at the given reduced growth temperature T/T_m.

6.2 Optical properties of metallic nano-helices

In this section, the results of the optical experiments carried-out on metallic nano-helices are presented. The experimental data acquired in both the *near-* and the *far-field* agree with the corresponding theoretical models (*cf.* **Chapter 3**), proving how the helical structure and the electronic and magnetic properties of the metals do regulate the optical response of the nano-helices. Chirality-related optical experiments are separately discussed in **Section 6.3**.

6.2.1 Far-field regime

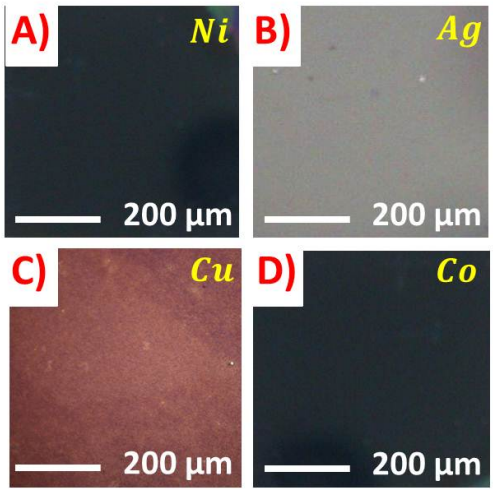

Fig. 6.19: Optical images of nano-helices made from different metals. The total length of the nano-structures is ∼850 nm. A) *Ni* nano-helices. B) *Ag* nano-helices. C) *Cu* nano-helices. D) *Co* nano-helices. The matt-black colour of *Ni* and *Co* nano-helices indicates strong visible light absorption. Meanwhile, the matt and brighter reflectance of the *Cu* and *Ag* nano-helices denotes considerable light scattering in different directions.

Fig. 6.19 shows top-view optical images of *Ni*, *Cu*, *Co* and *Ag* nano-helix arrays. The individual nano-helices have a total coiled wire length of ∼850 nm. In all four cases, the nano-structures possess a matt appearance and their reflectance is different than in their corresponding bulk state. The matt-black colour of *Ni* and *Co* nano-helix arrays indicates strong visible-light absorption. Meanwhile, the matt and higher reflectance of *Cu* and *Ag* nano-helices is symptomatic for considerable light scattering in all directions. It should be emphasized that no transmission is possible in any of these samples as the nano-helices are standing on a highly reflective 80 nm thick *Ag* film (*cf.* **Section 5.1**).
The quantitative examination of the optical properties in the *far-field* regime is focused on *Ni* and *Ag* nano-helices grown on opaque and transparent substrates. *Ni* is chosen

because it allows the combination of optical properties of plasmonic antennae with magnetic properties, providing novel multifunctional devices [55]. Meanwhile, *Ag* is the most commonly studied plasmonic material together with *Au* [115]. Two experimental approaches were used to assess the *far-field* properties of both types of metallic nano-helices based on specular-reflectance and transmission measurements (**Sections 5.3.1** and **5.3.2**, respectively). Angle-resolved reflectance measurements are particulary useful to discriminate between the existance of surface plasmon polaritons and localized plasmon effects in metallic nano-structures [104]. Meanwhile, as demonstrated in the present study, a combination of reflection and transmission measurements is suitable to distinguish the decay type (radiative or non-radiative) of localized plasmon resonances in nano-helices depending on the metal used to fabricate these structures.

Specular-reflectance

For the *Ni* samples, specular-reflectance measurements in the wavelength range from 400 nm to 5000 nm were carried out, covering the visible and the near-IR spectrum as a function of incident angle (see **Section 5.3.1**). These measurements were performed in collaboration with the group of Prof. Vittorio Bellani at the University of Pavia (Italy). Four samples (S1 to S4) with *Ni* nano-helices of different pitch and diameters (see Table 6.3) were measured. The nano-helix forest area was ∼1 mm^2 in each sample.

Tab. 6.3: Pitch p, diameter D, height h, number of turns N, and length of a single turn $l = \sqrt{(\pi D)^2 + p^2}$ of the regular-shaped and free-standing fabricated *Ni* nano-helix forests (S1 to S4). The helix wire diameter is $2r_w \approx 70$ nm in all samples. The nano-helices are grown in a square lattice with a periodicity of $\delta = 150$ nm. All four samples were grown on an opaque and highly reflective substrate.

Sample	pitch, p [nm]	diameter, D [nm]	height, h [nm]	no. turns, N	lenth one turn, l [nm]
S1 (*Ni*)	325 ± 9	169 ± 9	400 ± 20	1.23	622 ± 14
S2 (*Ni*)	130 ± 6	102 ± 6	242 ± 15	1.86	346 ± 8
S3 (*Ni*)	128 ± 9	72 ± 9	390 ± 16	3.04	260 ± 13
S4 (*Ni*)	63 ± 6	59 ± 6	234 ± 20	3.7	196 ± 7

Fig. 6.20A shows the reflectance of samples S1, S3 and S4 at almost normal incidence (10°). The *Ni* nano-helix forests generally exhibit a low reflectance, <25% for the range 1000 nm (1.24 eV) to 2500 nm (0.5 eV) and <10% for the range 400 nm (3.1 eV) to 1000 nm (1.24 eV). These values are comparable with highly efficient black-silicon samples of similar thickness produced by liquid etch [116]. Also, the metallic nano-helix forests show similar reflectance to dark metals produced by laser pulses [117], however, these ablated amorphous structures consist of micro-meter sized grains. In more detail, the reflectance of *Ni* nano-helix forests shows two main minima around 750 nm to 900 nm (Min1) and 2000 nm to 3000 nm (Min2), respectively. Their position and reflectance are

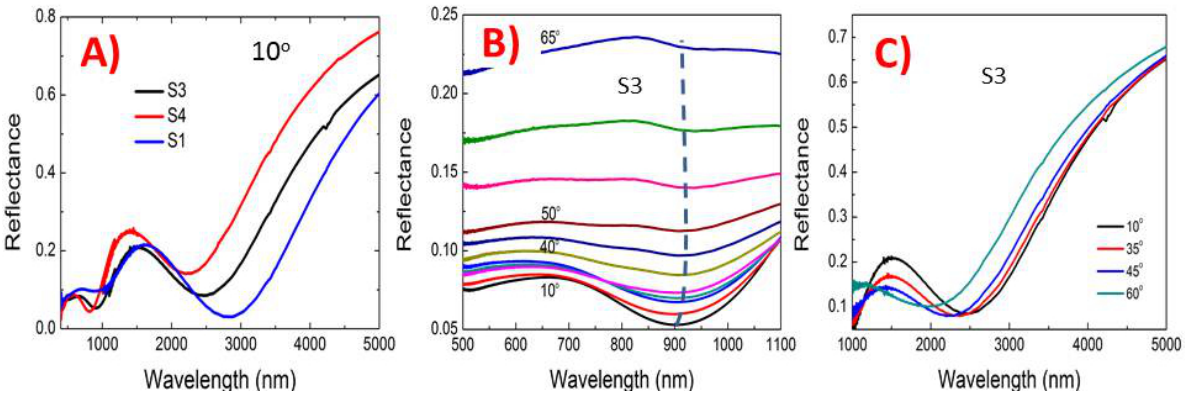

Fig. 6.20: Reflectance of *Ni* nano-helices in the range 400 nm to 5000 nm. A) Reflectance of samples S1, S3 and S4 for an incident angle $\theta = 10°$. B) Reflectance of sample S3 for different θ in the range 500 nm to 1100 nm. The dashed line is meant to be a guide to the eye showing the shifting of Min1. C) Reflectance of sample S3 for different θ in the range 1000 nm to 5000 nm.

clearly dependent on the nano-helix structural parameters and the angle of incidence θ (Figs. 6.20B,C and 6.21). When increasing θ, Min1 redshifts for samples with larger pitch and diameter with respect to the wire diameter, meanwhile it blueshifts for samples with smaller structural parameters (Fig. 6.21A). In contrast, Min2 blueshifts for all samples measured (Fig. 6.21b). The reflectance at Min1 increases when increasing θ (Fig. 6.21C). Note, that the absolute values of the reflectance depend on the height of each sample which is not exactly the same. The Min2 reflectance has a complex behavior with θ, increasing for samples with larger pitch and diameter and decreasing for samples with smaller structural parameters (Fig. 6.21D).

To properly analyze these data, one has to consider that the reflectance of each forest will depend on both the specific structure of the individual nano-helices and their overall arrangement. Typically, for a given object-array of periodicity δ (150 nm in the present case), the effective-medium description is valid when the incident wavelength $\lambda > 10\delta$ [13, 14]. That is, at $\lambda > 1500$ nm, there is no dominant contribution of the individual element response and their spatial dispersion is negligible [14]. To determine the effective-medium threshold, the Maxwell-Garnett effective-medium formalism for helical arrays and the Rayleigh-Debye scattering by single-helices at lower wavelengths are considered. Details regarding the applicability of these methods are described in **Sections 3.2.3** and **3.1.4**, respectively. Further technical details concerning the *Ni* nano-helix reflectance calculation are given in **Appendix F**.

Fig. 6.22 shows the calculated reflectance for S1, S3 and S4 at nearly normal incidence ($\theta = 10°$). The dotted lines correspond to the Rayleigh-Debye contribution, meanwhile the dashed-dotted lines represent the Maxwell-Garnett model. The matching of the calculations with the experimental data for samples S3, S4 is excellent except for wavelengths below 650 nm and a systematic small blueshift in the calculated minima. The deviations

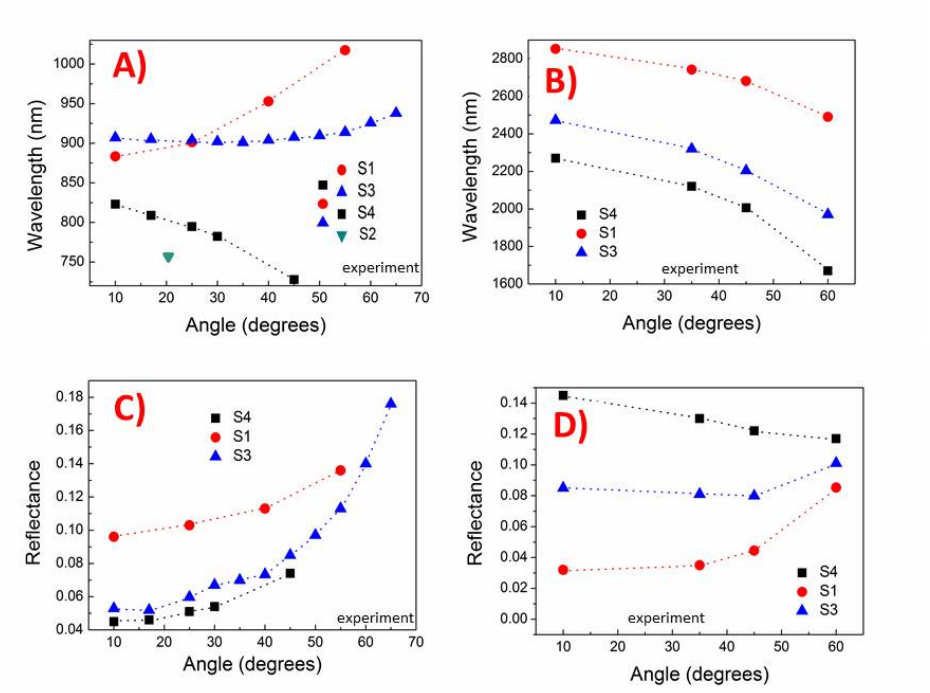

Fig. 6.21: Position and Reflectance of Min1 and Min2 in samples S1, S2, S3 and S4 depending on the incident angle θ. A) Position of Min1. B) Position of Min2. C) Reflectance of Min1. D) Reflectance of Min2.

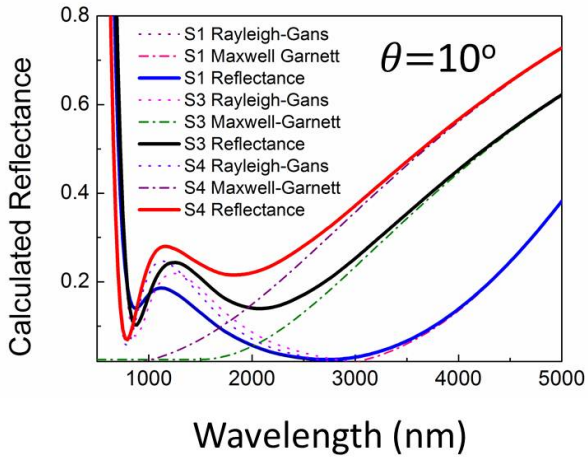

Fig. 6.22: Calculated reflectance of samples S1, S3 and S4 for $\theta = 10°$ for a wavelength range 500 nm to 5000 nm.

from the experimental data are attributed to the omission of absorption effects in the

analytical models used (see below FEM modelling of the reflectance data considering the absorption contribution). The match with sample S1 is less accurate, which agrees with the fact that the error introduced by the Rayleigh-Debye method for this sample is higher (**Appendix F**). As Fig. 6.22 demonstrates, Min2 develops at the intersection of the single nano-helix Rayleigh-Debye scattering and the Maxwell-Garnett formalism for helical arrays. That is, Min2 represents the effective-medium threshold.

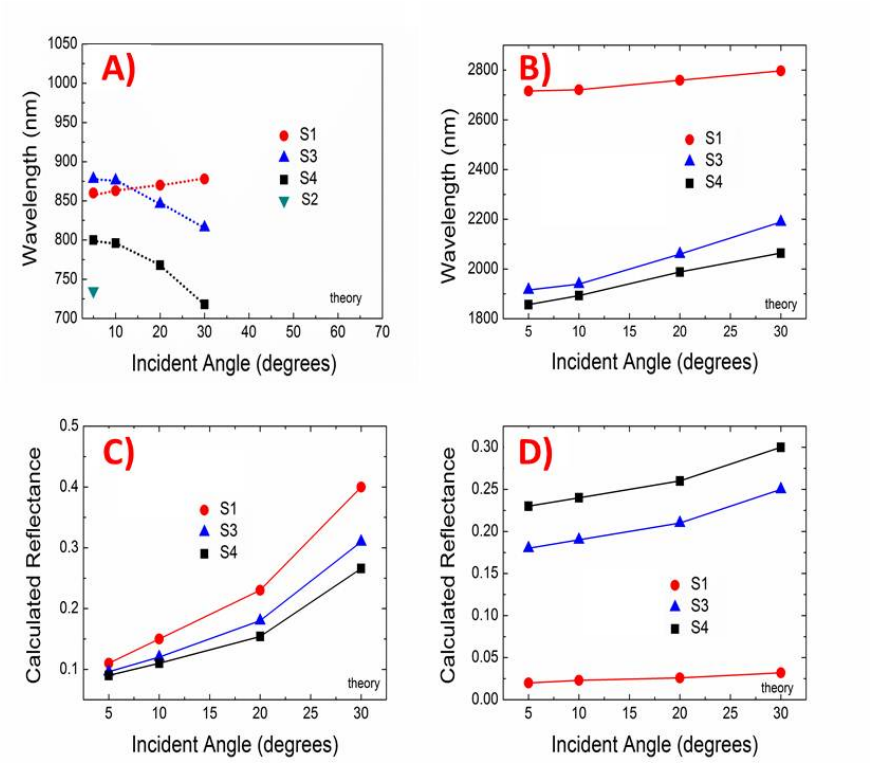

Fig. 6.23: Calculated reflectance of samples S1, S2, S3, and S4 for different incident angles θ. A) Position of Min1. B) Position of Min2. C) Reflectance of Min1. D) Reflectance of Min2.

Fig. 6.23 shows the calculated position of Min1 and Min2 and their reflectance for samples S1, S2, S3 and S4 for incident angles of 5°, 10°, 20° and 30°. As aforementioned (see also **Appendix F**), both models are no longer valid when increasing the incident angle beyond 30°. Meanwhile, for nearly normal reflectance ($\theta = 10°$), the calculated Min1 and Min2 position and relative reflectance are in very good agreement with the experimental data for the different measured nano-helix forests. This is an expected behaviour because at normal incident angle, the models used exhibit almost no limitations as discussed in **Appendix F**. When increasing θ, Min1 wavelength blueshifts for helices with diameter and pitch close to the helical wire-diameter and redshifts for helices with larger diameter and pitch (Fig. 6.23A). At the same time, the reflectance value of Min1 increases when augmenting θ, following the experimentally observed trends as well. These observations agree with the fact that Min1 is determined by the Rayleigh-Debye scattering, whose range

of validity holds up to $\theta \sim 30°$ (see also **Appendix F**). In contrast, the experimental data for the Min2 wavelength and reflectance (Fig. 6.23B,D) is not well-described by the model used when increasing θ. Nevertheless, this behaviour is expected: the Maxwell-Garnett formalism holds only for isotropic systems or anisotropic systems at normal incidence (**Appendix F**). The measurements, however, do not meet these criteria when increasing θ.

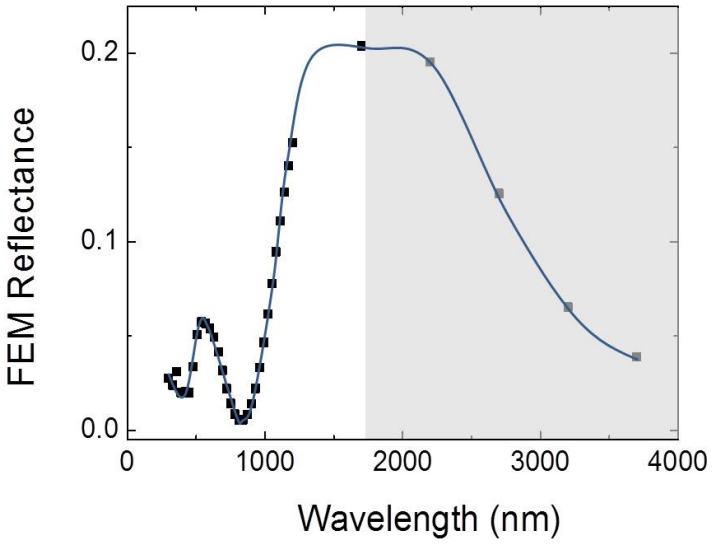

Fig. 6.24: FEM Calculated reflectance for a nano-helix with the structural parameters of sample S3 for normal incidence. The line is a cubic interpolation of the calculated points. The shaded area (> 1750 nm) indicates the wavelengths for which the FEM model is not valid due to restrictions in the numerical domain size.

To further confirm these conclusions, FEM simulations of the arrays of *Ni* nano-helices were undertaken (see **Section 3.1.6**) in collaboration with the group of Prof. J. Donegan at Trinity College Dublin. The reflectance is calculated at normal incidence as a function of the specular scattered power (P_{sca}) and the absorbed power (P_{abs}) as $R = P_{sca} - P_{abs}$ and is plotted in Fig. 6.24. It is similar to the experimentally measured reflectance for wavelengths below the effective medium threshold ∼2000 nm. Above 2000 nm the FEM domain height becomes too small compared to the wavelength and the Perfect Matched Layer (PML) region does not work properly. Min1 is however at the expected position, reproducing the experimental measurements at normal incidence in the four different nano-helix arrays.

The experimental and theoretical *far-field* results presented so far prove that the electromagnetic response of the *Ni* nano-helix forests is deliberately tunable by changing the nano-helix pitch, diameter, and the number of turns.

Next, the aim of the present study is to determine if this conclusion can be generalized to other metals, *i.e.* to evaluate the actual impact of the helical shape on the optical

properties of these nano-structures.

To do so, *Ag* was chosen to extend the investigation due to the noticeable differences in the bulk electronic properties of this material with respect to *Ni* [51, 52] such as higher electrical resistivity (Table 6.1). Initially, the reflectance of two samples of *Ag* nano-helix forests with different growth parameters (see Table 6.4) was measured at normal incidence from 350 nm to 1000 nm (thus, covering most of the individual particle range, the interesting regime for this evaluation). These measurements were performed in collaboration with the group of Prof. J. Donegan at Trinity College Dublin.

Tab. 6.4: Pitch p, diameter D, height h, number of turns N, and length of a single turn $l = \sqrt{(\pi D)^2 + p^2}$ of regular-shaped and free-standing fabricated *Ni* (S5) and *Ag* nano-helix forests (S6 and S7). The helix wire diameter is $2r_w \approx 70$ nm in all samples. The nano-helices are grown in a square lattice with a periodicity of $\delta = 150$ nm. S5 is a *Ni* sample fabricated to test the reproducibility of the reflectance measurements with the second *far-field* set-up used to obtain the reflectance at normal incidence (**Section 5.3.2**)

Sample	pitch, p [nm]	diameter, D [nm]	height, h [nm]	no. turns, N	lenth one turn, l [nm]
S5 (*Ni*)	128 ± 10	72 ± 7	275 ± 15	2.11	260 ± 13
S6 (*Ag*)	130 ± 9	75 ± 10	300 ± 16	2.3	258 ± 10
S7 (*Ag*)	140 ± 11	103 ± 9	301 ± 13	2.1	352 ± 8

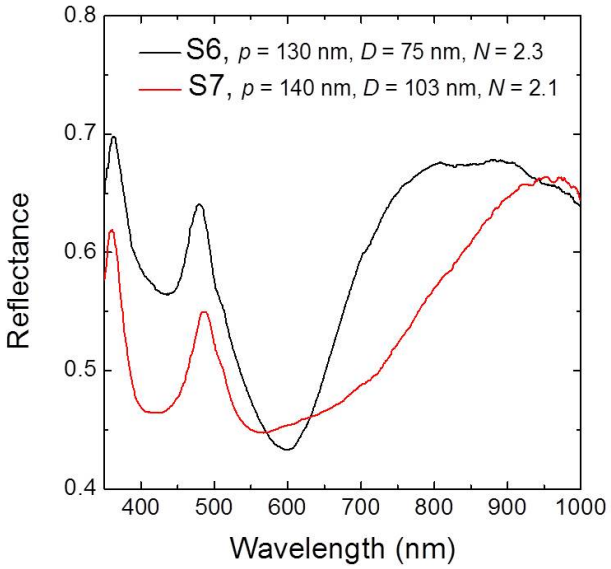

Fig. 6.25: Reflectance of *Ag nano-helices* in the range 350 nm to 1000 nm. The structural parameters of samples S6 and S7 are given.

Fig. 6.25 shows the reflectance of the samples S6 and S7 (*Ag* nano-helices). Their overall reflectance value is larger than for *Ni* nano-helices (Fig. 6.20). However, the reflectance shape looks similar in the measured range, showing two minima around ∼440 nm and ∼600 nm and two relative maxima at lower and higher wavelengths, respectively. The

minimum at lower wavelength stays constant for both types of *Ag* nano-helices (S6 and S7). Furthermore, although less noticeable (smaller difference between the minimum and the surrounding maxima), it also appears at the same wavelength in *Ni* nano-helices (Figs. 6.20 and 6.24). As it will be argued later in **Section 6.2.2**, this observation indicates that this minimum is due to the existence of a transverse localized plasmon mode in the metallic helices, similar to the case of straight nano-rods [118]. In contrast, the minimum at longer wavelengths (∼600 nm) changes for the different *Ag* nano-helices, as Min1 does in *Ni* nano-helix forests, *i.e.* this minimum in Fig. 6.25 has the same origin as Min1 in the *Ni* nano-helix case. The maximum at longer wavelengths (∼900 nm) is due to the scattering of the individual nano-helix and is placed between Min1 and Min2, in agreement with the *Ni* case, too. (Note that, in the normal incidence reflection set-up, the spectra was limited from 350 nm to 1000 nm thus although Min2 starts to develop, is not fully seen).

The possible presence of LSPR enriches and makes the evaluation of the optical data from the nano-helices more challenging. As aforementioned (**Section 3.3**), electromagnetic radiation is highly absorbed at a localized plasmon resonance. Afterwards, its decay (damping) can be radiative (*i.e.* increasing the scattering from the sample) or non-radiative depending on the wavelength in consideration and the material constituting the nano-structure [61]. The challenge is, then, to be able to isolate and prove individual plasmonic contributions existing in the optical spectra of arrays of nano-helices.

To properly evaluate LSPR, usually extinction (or equivalently transmission) measurements have to be undertaken [17, 118], since they represent the total light absorbed and scattered by the nano-structures[1] (see **Section 3.1.3**). In addition, transmission measurements are useful to complement and corroborate the information obtained in reflectance. This is the strategy which is followed in this thesis.

Transmission

Ni and *Ag* nano-helices were fabricated (Table 6.5) on transparent substrates (*cf.* **Section 5.1**) to measure their transmission spectra (**Section 5.3.2**) in the range from 350 nm to 1000 nm. In fact, for comparative purposes the first batch of nano-helices grown on transparent substrates (S8-S10) were fabricated simultaneously to their opaque substrates counterparts (S5-S7).

Ni nano-helices on transparent substrates show a low transmission ($< 12\%$) for the measured range, as shown in Fig. 6.26. Since they possess a low reflectance as well, it is confirmed that a high absorption is produced in these nano-structures. In addition, it is noticed that the position of the minimum Min1 is reproduced at the same wavelength either in transmission or reflection. *Ag* nano-helices on transparent substrates also show low transmission ($< 15\%$) within the measured range (Fig. 6.27) as well. Interestingly,

[1] Reflection measurements are only sensitive to the scattered light.

Tab. 6.5: Pitch p, diameter D, height h, number of turns N, and length of a single turn $l = \sqrt{(\pi D)^2 + p^2}$ of the regular-shaped and free-standing fabricated *Ni* (S8) and *Ag* (S9, S10) nano-helix forests. The helix wire diameter is $2r_w \approx 70$ nm in all samples. The nano-helices are grown in a square lattice with a periodicity of $\delta = 150$ nm. Note that samples S8-S10 grown on transparent substrates were fabricated during the same growth process as S5-S7 grown on Si/SiO_2, respectively.

Sample	pitch, p [nm]	diameter, D [nm]	height, h [nm]	no. turns, N	lenth one turn, l [nm]
S8 (*Ni*)	128 ± 10	72 ± 7	275 ± 11	2.11	260 ± 13
S9 (*Ag*)	130 ± 9	75 ± 10	300 ± 16	2.3	258 ± 10
S10 (*Ag*)	140 ± 11	103 ± 9	300 ± 13	2.1	352 ± 8

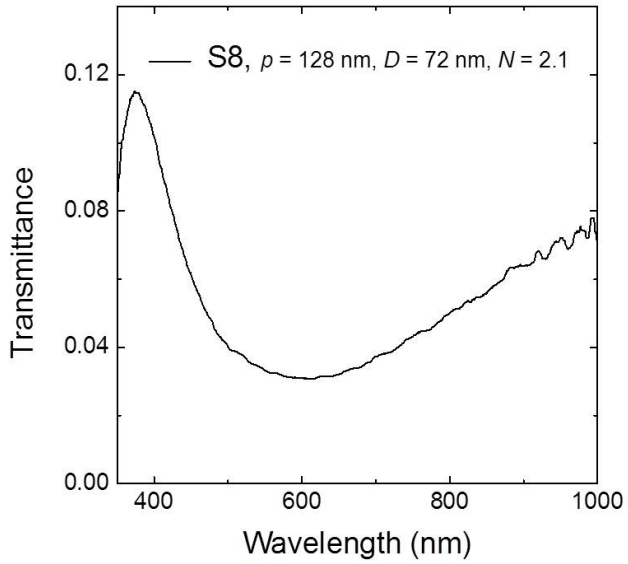

Fig. 6.26: Transmittance of *Ni* nano-helices in the range 350 nm to 1000 nm. The structural parameters of sample S8 are given.

in this case the 'position' of Min1 in transmission and reflection are not coincident (Figs. 6.27 and 6.25). As discussed in **Section 6.2.2**, Min1 is the wavelength of a longitudinal LSPR and the reported match (*Ni* nano-helices) and discrepancies (*Ag* nano-helices) between its position in reflectance and transmittance are a consequence of a non-radiative and radiative damping of this plasmon in *Ni* and *Ag* nano-helices, respectively.

6.2.2 Surface Plasmon Resonances

Both surface plasmon resonances (**Section 3.3**) are observed in the *far-field* measurements of *Ni* and *Ag* nano-helices: Surface Plasmon Polariton (SPP) and Localized Surface Plasmon Resonance (LSPR). In general, surface plasmons polaritons are electromagnetic waves coupled to charge fluctuations, and are pinned to the interface between a metal and a dielectric [119]. On a flat surface a surface plasmon has a greater momentum than an

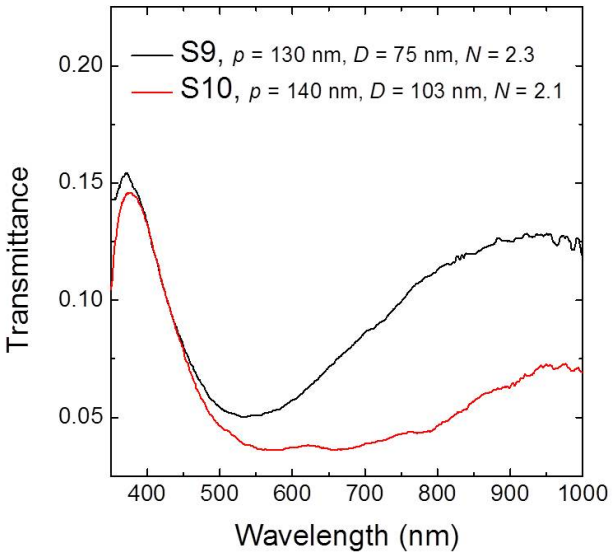

Fig. 6.27: Transmittance of *Ag* nano-helices in the range 350 nm to 1000 nm. The structural parameters of samples S9 and S10 are given.

optical field traversing above the surface, so no optical coupling is allowed [119]. However, on a patterned surface, the optical field can scatter to higher-momentum states and excite plasmons. This is why nano-patterned structures are ideal for studying both SPP and LSPR [104]. In more detail, SPP have energies that depend strongly on both incident angle and sample orientation [119]. Meanwhile LSPR have energies that are highly dependent on the nano-structured geometry, although they are independent of the incident angle of the excitation light and sample orientation [119]. These are the reasons why angle-resolved spectroscopy is the key to distinguishing the plasmons on nano-structured surfaces [104, 119]. Both plasmonic effects unveil the performance of the presented nano-structures as helical antennae at optical frequencies.

Surface Plasmon Polariton Resonance

In the *Ni* nano-helix case, the reflectance of Min1 is strongly modified for incident angles above 45° (*cf.* Fig. 6.20B). This effect is attributed to the appearance of delocalized surface-plasmon polaritons above that angle, reducing the absorption of the nano-structures [104]. There are further and stronger indicators of this possible plasmonic effect: Fig. 6.28 shows the reflectance spectra for sample S2 at 40°, 55° and 70°. At 55° the spectrum shows a strong modulation for visible wavelengths whereas at 40° and 70° it is weaker, which is a typical effect for surface-plasmon resonators [120]. In the case of a straight wire resonator, light only couples into the wire perpendicular to the wire-end planes [120]. In our sample S2, 55° is close to the growth helical angle (50°). At this angle light coupling into the structure would be highly increased suggesting more prominent

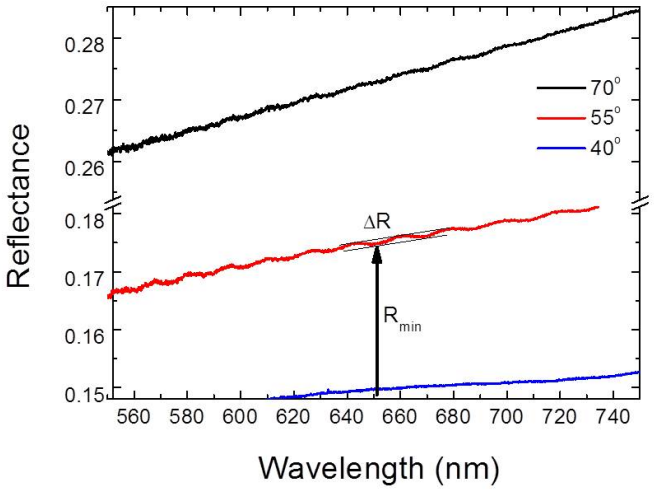

Fig. 6.28: Reflectance spectra from 550 nm to 750 nm of sample S2 showing a periodic modulation between a minimum value R_{min} and maximum value $R_{min} + \Delta R$. This modulation is suggested to be due to a surface-plasmon resonator [120], whose interference is detected specularly in the *far-field* due to a leackage radiation effect [121].

surface-plasmon effects. This statement is further underpinned by the observation that the spectra at 25° does not show any sign of modulation. Surface plasmon resonators are proved to behave as Fabry-Perot cavities [120], and the produced interference patterns can be detected in the specular and retroreflected *far-field* by observing their leakage radiation [121]. The plasmon coupling efficiency can be assessed by the relative modulation depth given by the reflectance ratio $\Delta R/R_{min}$ (see Fig. 6.28), which in the *Ni* nano-helix case is ∼1.5% at $\theta = 55°$. This value is much lower compared to the ∼ 15% reported in [120] due to the losses (damping) introduced in our nano-coils. The possible sources of surface plasmon polariton damping in the samples are: First, the structures are not mono-crystalline as the wires studied in [120]. Second, the nano-helices possess no well-defined and planar ends due to the *GLAD* fabrication method. And third, the coupling of the light into the wire forming the nano-helix is produced at the air-metal interface, whereas in [120] the coupling is realized with the aid of a higher permittivity medium.

To conclude this subsection, it is convenient to note that SPPs in *Ag* nano-helices were not detected due to two possible reasons: *i*) the lower sensitivity of the reflectance set-up at normal incidence and *ii*) (more likely) the fact that *Ag* nano-helices were not measured at different angles of incidence as the *Ni* case, thus, SPPs were not excited in the nano-helices made from this metal.

Localized Surface Plasmon Resonances

As previously introduced (**Section 6.2.1**), Localized Plasmon Resonances might considerably constitute the optical response of metallic nano-helices. Both, transverse and longitudinal LSPR exist in metallic nano-helices as demonstrated in this subsection.

The existance of a transverse plasmon resonance in metallic nano-helices is linked to the thickness of the wire composing the helix, similarly to what occurs in the case of nano-rods [118]. This is justified as follows: the minima appearing at lower wavelength (∼440 nm) in the reflectance of *Ag* nano-helices stays constant for samples with different diameter, D, and pitch p of the individual nano-helix (Fig. 6.26). Furthermore, although weaker, it also appears at the same wavelength in *Ni* nano-helices (Figs. 6.20 and 6.24). Transverse LSPR highly depend on the wire-diameter of the nano-structures [118], which in *GLAD* is determined by the dot spacing δ (see **Sections 5.1** and **6.1**). δ being constant (150 nm) in all the samples studied for the optical measurements, the wire-diameter of all the measured nano-helices is constant, too (∼70 nm). Hence, any transverse plasmon peak will appear at approximately the same wavelength in all the samples. The minimum in *Ni* nano-helices is less noticeable due to interband transitions at this wavelength in this metal [52]. This result needs to be further confirmed by growing helices with different wire thickness, *i.e.* changing δ. This additional study is not considered here since the present work is focused on the electromagnetic properties induced by the actual helical shape (in principle, any rod-like nano-structure with a different morphology would possess this transverse plasmon mode).

In contrast, the minimum at higher wavelengths, Min1, correspond to a longitudinal LSPR along the nano-helix. As demonstrated below, the resonant position and decay of this mode clearly depends on the helical structure and material constituting the nano-helices, respectively.

The Min1 position[2] in all *Ni* and *Ag* samples is at a wavelength approximately equal to the total length, lN, of the wire forming an individual nano-helix (l is the length of one turn). This apparent structural dependence suggests the presence of a longitudinal localized surface-plasmon resonance in the nano-helix at this associated wavelength. To confirm its existence, the *near-field* intensity of a nano-helix forest was simulated using FEM (see **Section 3.1.6** and **Appendix B**). When light is incident in the negative z-direction and linearly polarized in the y-direction (Fig. 6.29A), the surface charge is accumulated along the nano-helix at positions separated by $l/2 = \sqrt{(\pi D)^2 + p^2}/2$. This charge distribution is associated with a periodic appearance of dipoles with an effective length of $l/2$ (Fig. 6.29B). Around the Min1 position, the specular scattered power (P_{sca}) shows a minimum whereas the absorption power (P_{abs}) is maximal (Fig. 6.29C). This agrees with the fact that *Min1 occurs at the wavelength associated with the longitudinal*

[2] In the case of radiative plasmonic damping, the real position of Min1 is the one obtained in the extinction (*i.e.* transmission) measurements.

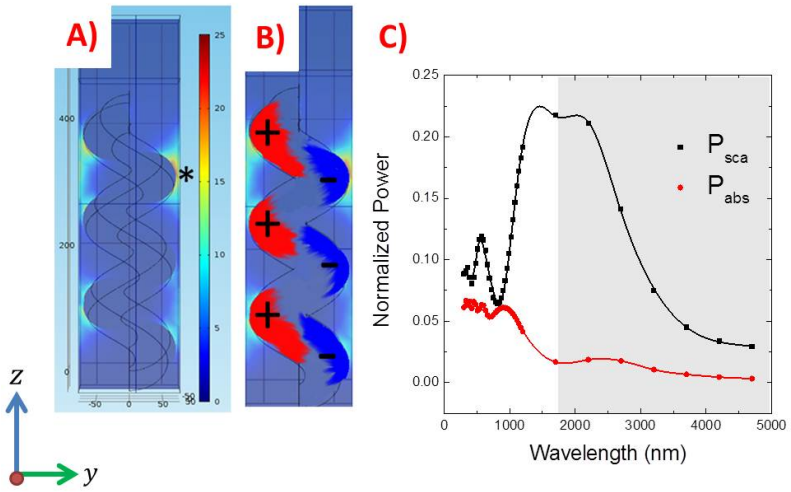

Fig. 6.29: Numerical simulation (FEM) of the near-field enhancement and dipoles. A) Enhancement in the zy-plane of a nano-helix at incident monochromatic light (900 nm). The field is enhanced at positions along the helical structure. B) Schematic showing the periodic dipole-appearance, each with the effective length $l/2$. C) Normalized absorbed power, P_{abs}, and specularly scattered power, P_{sca}, (lines are a cubic interpolation of the calculated points as guide to the eye).

plasmon resonance of the nano-helix: *Ni* nano-helices absorb most of the incoming light at this specific wavelength, resulting in a minimum in the *far-field* specular reflectance and transmission. In contrast, *Ag* nano-helices absorb and scatter most of the incoming light at this specific wavelength, resulting in a minimum in the *far-field* transmission.

The former reasoning agrees with the experimental fact that Min1 in *Ni* nano-helices is coincident in reflection and transmission measurements and non-coincident in the *Ag* case (Figs. 6.25 and 6.27). This indicates the presence of non-radiative and radiative decay of the longitudinal mode in both metals, respectively. The different decays in these two metals are due to their different interband activity [55].

In addition, for an arbitrary point (asterisk in Fig. 6.29A), the calculations undertaken using metals other than *Ni* and *Ag* but keeping the same nano-helix dimensions (Fig. 6.30) reveal that *Ni* and *Ag* show the lowest and highest intensity enhancement factor, respectively. The rest of the calculated metals present factors inbetween these two which are a consequence of their different electronic properties at optical frequencies [47]. The effects of the interband activity on the damping-mechanisms of the longitudinal LSPR in nano-helices are experimentally confirmed through an independent *near-field* study in **Section 6.2.4**.

According to the Gans-theory [122], the wavelength λ_p of this plasmon mode should scale linearly only with the effective length of the individual dipoles. Applying this theory to

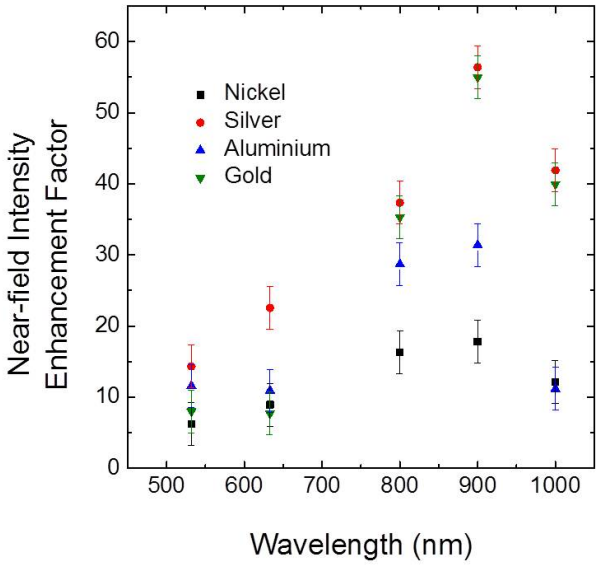

Fig. 6.30: Numerical simulation of the near-field enhancement factor for nano-helices made from different metals. The enhancement was obtained at an arbitrarily point marked with an asterisc in Fig. 6.29A.

our nano-helices, however, does not reveal a linear scaling (Fig. 6.31) indicating that the Gans-theory is not applicable for nano-sized metallic helices. Since the plasmon position was experimentally found to depend on the total length of the nano-helix, the following empirical scaling-law for λ_p is suggested:

$$\lambda_p \sim lN + \pi r_w \tag{6.2}$$

where r_w is the radius of the wire. The offset πr_w accounts for the nano-antenna tip approximated by a semi-spherical shape. To test this empirical scaling-law, the experimental Min1-positions against λ_p are plotted (Fig. 6.32) for the ten nano-helix samples (Tables 6.3, 6.4 and 6.5), for five more nano-helical forests grown for this purpose (Table 6.6) and ten additional numerically simulated samples (Table 6.7), all the sets being in the same structural parameter range. The data-points on the graph all lie on a straight line for each material, confirming that Eq. 6.2 correctly determines the longitudinal plasmon wavelength scaling of metallic nano-helices. The difference in slope for *Ni* and *Ag* nano-helices is due to different materials-parameters such as the bulk impedance, which in turn depend on the different electronic properties of the bulk material.

Therefore, the longitudinal plasmon mode in nano-helices is determined by both the effective dipole length ($l/2$) and the number of dipoles in the structure ($\sim 2N$), whose product equals the total length of the wire defining the nano-helix. This plasmon mode differs from the scaling of the axial operation-mode in a conventional helical antenna [6]: In macroscopic helical antenna the axial mode resonance is close to πD ($\sim l$ when $D >> p$)

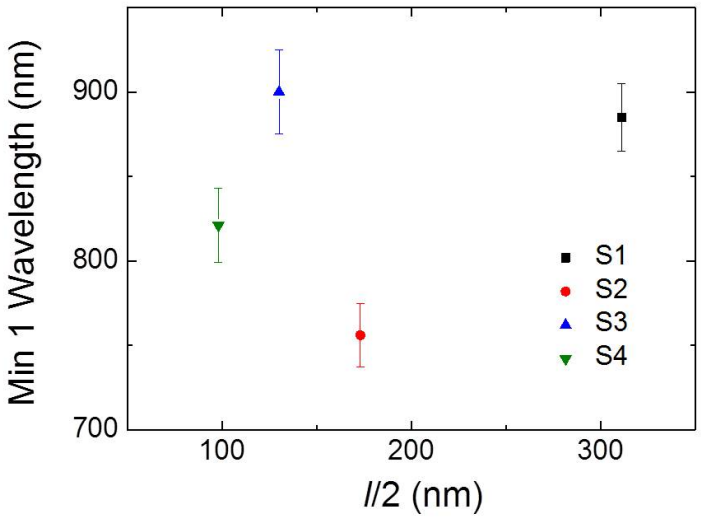

Fig. 6.31: Gans-Theory scaling of the longitudinal plasmon wavelength in nano-helices S1-S4. The scattered data indicate the non-applicability of this theory in the nano-helix case.

[6]. In contrast, in the present nano-helix case, the resonant wavelength of the longitudinal plasmon-mode is approximately N times larger due to the plasmon surface-charge-wave propagation along the entire helical structure.

Tab. 6.6: Pitch p, diameter D, height h, number of turns N, and length of a single turn $l = \sqrt{(\pi D)^2 + p^2}$ of the regular-shaped and free-standing Ag (S11- S14) and Ni (S15) nano-helix forests. The helix wire diameter is $2r_w \approx 70$ nm in all samples. The nano-helices are grown in a square lattice with a periodicity of $\delta = 150$ nm. All these samples are fabricated on transparent substrates.

Sample	pitch, p [nm]	diameter, D [nm]	height, h [nm]	no. turns, N	lenth one turn, l [nm]
S11 (Ag)	127 ± 9	71 ± 8	268 ± 12	2.11	256 ± 14
S12 (Ag)	127 ± 10	72 ± 9	238.7 ± 11	1.88	256 ± 14
S13 (Ag)	128 ± 11	72 ± 9	420 ± 15	3.28	256 ± 13
S14 (Ag)	131 ± 7	103 ± 7	227 ± 11	1.73	346 ± 9
S15 (Ni)	128 ± 7	71 ± 9	230.4 ± 12	1.80	256 ± 12

Note, that the Ag nano-helices reported in Table 6.7 were simulated in Ref. [122]. In this reference, the resonant wavelength of the longitudinal plasmon of hypothetical Ag nano-helices is calculated through numerical simulations using the discrete dipole approximation method (DDA). Under circularly polarized incident light, Ref. [122], the numerically obtained two close extinction peaks (with a maximum separation of ∼100 nm) located at λ_L and λ_R are associated with the longitudinal plasmon resonance. The number of dipoles in both peaks are $2int(N)+3$ and $2int(N)+2$ for the λ_L and λ_R peaks, respectively. For comparison purposes here, experimentally our samples are excited with unpolarized light

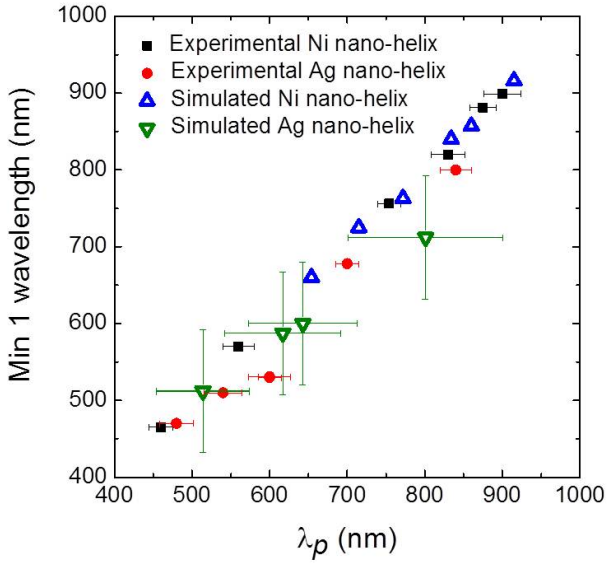

Fig. 6.32: Scaling of the longitudinal localized plasmon resonance wavelength λ_p of the metallic nano-helices. Dependence of Min1-position following Eq. 6.2 for experimentally measured and numerically simulated *Ni* and *Ag* nano-helix materials. A linear dependence is observed for all structures, proving unambiguously that the longitudinal localized surface-plasmon of the nano-helices scales with nano-helix total length lN.

Tab. 6.7: Pitch p, diameter D, height h, number of turns N, and length of a single turn $l = \sqrt{(\pi D)^2 + p^2}$ of the simulated *Ni*(Sim1 to Sim6) and *Ag* (Sim7 to Sim10) nano-helix forests . The helix wire-diameter is $2r_w \approx 70$ nm in all samples. The nano-structures are grown in a square lattice with a periodicity of $\delta = 150$ nm. The simulated *Ag* nano-helices are taken from Ref. [122]

Sample	pitch, p [nm]	diameter, D [nm]	height, h [nm]	no. turns, N	lenth one turn, l [nm]
Sim1 (*Ni*)	128	75	273	2.1	260
Sim2 (*Ni*)	128	75	299	2.3	260
Sim3 (*Ni*)	128	75	338	2.6	260
Sim4 (*Ni*)	128	75	364	2.8	260
Sim5 (*Ni*)	128	75	377	2.9	260
Sim6 (*Ni*)	128	75	403	3.1	260
Sim7 (*Ag*)	48	48	2.65	260	158.25
Sim8 (*Ag*)	48	80	2.65	290	255.87
Sim9 (*Ag*)	24	60	2.65	300	190
Sim10 (*Ag*)	60	60	2.65	355	198

and the theoretically predicted plasmon-resonances lie very close together, we consider an averaged peak composed of both, *i.e.*, $\lambda_{ave} \approx (\lambda_L + \lambda_R)/2$ and an average number of dipoles $\Delta_{ave} \approx (4int(N) + 5)/2$. In addition, the error of the simulations from Fig. 3 in Ref. [122] is assessed, which is produced from the electromagnetic behaviour of the helix when it varies from having d number of dipoles to $d + 1$, see Fig. 1B in Ref. [122].

Therefore, the error for λ_L and λ_R are $e_{\lambda_L}= \pm 70$ nm, $e_{\lambda_R}= \pm 150$ nm, respectively, and the error of the number of dipoles is $e_d= \pm 1$. Next, the effective wavelength of these simulated *Ag* structures can be calculated with the here proposed Eq. 6.2 as $\lambda_p = \lambda_{ave} \sim l/2\Delta_{ave}$. Note, that we do not include the offset term corresponding to the semi-spherical tip as the simulated structures in Ref. [122] do not possess this feature.
Thus, the proposed empirical linear scaling law for the longitudinal plasmon wavelength in metallic nano-helices is valid for all the cases and *generalizes* the one proposed in Ref. [122], in agreement with an observation we made before: the longitudinal plasmon resonance position of the metallic nano-helices is determined by the total length of the wire forming the nano-helix.

6.2.3 The optical helical antenna

Apart from the load impedance, there are three main parameters required to define any antenna: wavelength scaling, surface charge distribution and radiation pattern [20, 123]. In the present case (helical nano-antennae), two of these paremeters were already introduced in the previous section. The formerly introduced scaling-rule (Eq. 6.2) enables one to transfer the design rules for (conventional) helical antennae [6] into the optical (visible, plasmonic) wavelength-regime. Combined with the easy fabrication and the accuracy of the presented growing process (**Section 5.1**), the optical response of these metallic nano-structure can be tunable on demand for any electromagnetic application. In addition, FEM simulations (Fig. 6.29) demonstrate that the charge distribution associated to the longitudinal plasmon in metallic nano-helices is similar to the surface charge appearing in the resonant axial mode of the macroscopic helical antenna [6]. This charge distribution generates a characteristic radiation pattern of the macroscopic helical antenna mainly directed in the direction of the helical axis [6].
In consequence, to complete the here presented *far-field* study of the helical antennas in the optical range (*i.e.* the plasmonic helical antenna), the directivity of these metallic nano-structures needs to be assessed. Instead of using a conventional angle-dependent scattering set-up at a particular wavelength, this task was accomplished through standard transmission and reflection measurements in an optical microscope. The magnification of the objective lens used in the experiment was $\times 5$.
Fig. 6.33 shows the transmission and reflectance images of samples S12 and S15 made from *Ag* and *Ni* and with a total length of $\sim$480 and $\sim$460 nm, respectively. Therefore, Eq. 6.2 predicts that both samples have the longitudinal plasmon resonance situated in the blue color of the visible electromagnetic spectrum.
Several conclusions can be extracted from the analysis of these four images, confirming previous conclusions:

- The transmission spectra of both type of nano-helices show a red colour (square in the sample), as a consequence of the plasmon resonance being located at the blue

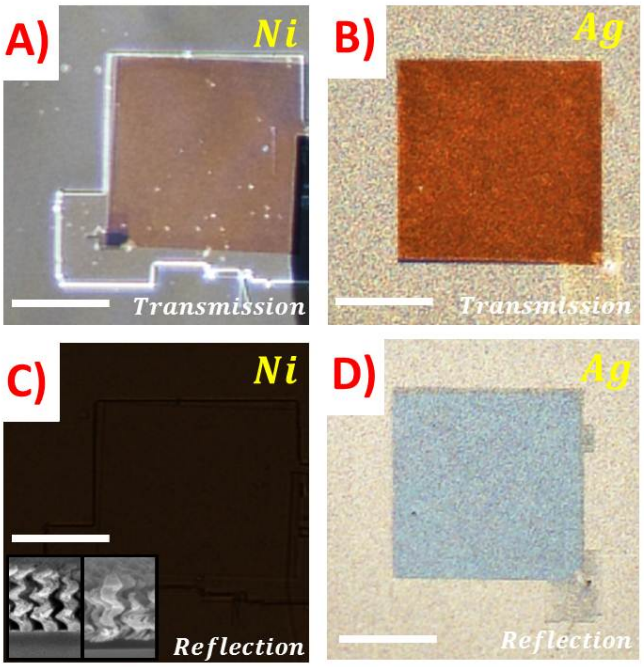

Fig. 6.33: Optical images in transmission and reflection of *Ni* A) and *Ag* B) nano-helix arrays in an square shape. Both *Ni* and *Ag* nano-helices show a reddish colour in transmission since their total length is ∼475 nm, *i.e.* the longitudinal LSPR situated in the blue colour of the visible spectrum. The reflectance of *Ni* nano-helices C) shows a dark colour due to absorption effects on this material (*i.e.* non-radiative plasmon decay). Instead, the reflectance of *Ag* nano-helices D) shows a blue colour due to the scattering effects on this material (*i.e.* radiative plasmon decay). Note that the sample area around the actual nano-helices are irregular nano-helices grown without the *heat-management* system. This is an optical proof of the superb quality of the nano-helices grown in this thesis (inset in C), left SEM image) and helically-shaped films (inset in C), right SEM image) reflecting prior art. The scale bars are 100 μm.

wavelenth. This spectrum is very different from that of helically-shaped films not grown with the presented growing method with the *heat-management* system (rest of the sample). The latter is an optical proof of the superb quality of the nano-helices presented in this study in comparison with prior art (for comparison purposes, the inset in Fig. 6.33C shows the morphological differences between regular nano-helices from this thesis and irregular helices grown on the same sample with no *heat-management*).

- The reflectance of regular *Ni* nano-helices is completely black, proving the non-resonant damping of the LSPR in this material through absorption.

- The reflectance of regular *Ag* nano-helices shows a blue colour, demonstrating the main scattering of the resonant plasmonic wavelength of the nano-helices along the direction of their axis. This result is further confirmed in Fig. 6.34, where the scattered light at an angle of ∼30° from regular *Ag* nano-helices starts to show a

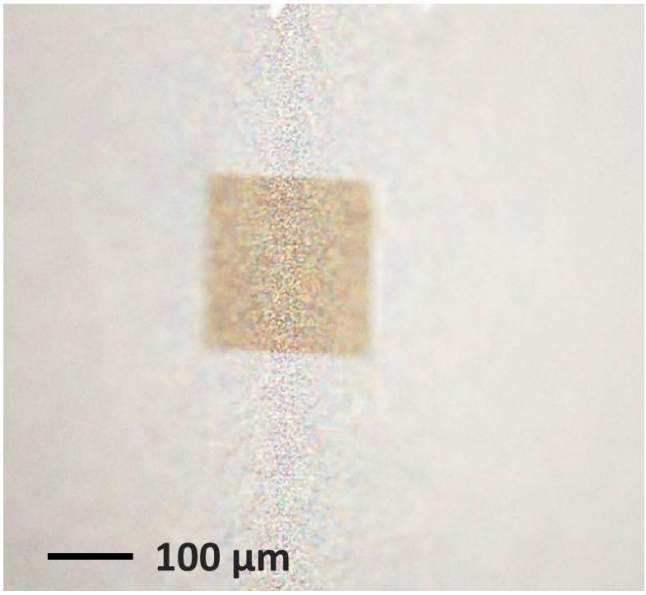

Fig. 6.34: Optical image of *Ag* nano-helix arrays taken in reflection at an angle different to the normal angle (note that only the centre of the image is at focus). The indicent light was indident along the helical axis and the microscope objective was placed at ∼30° respect this axis. The observed reddish colour indicate the absence of scattering of blue colour, the color at which the localized plasmon is situated.

reddish colour. These figures prove the potential usage of these nano-structures as colour filters.

6.2.4 Near-field regime

Surface Enhanced Raman Spectroscopy (*SERS*) was used in this study to investigate the plasmonic near-field distribution of structurally similar nano-helices made from *Ni*, *Co*, *Cu* and *Ag* (**Section 5.3.3**). The structural parameters of the nano-helices made from all four metals were those of sample S3 in Table 6.3. First, the near-field electromagnetic enhancement through *SERS* of graphene deposited on top of the nano-helical arrays was examined. Then, the maximum enhancement factor (*EF*) of these samples by using p-Mercaptoaniline (pMA) as a commonly used probing molecule (see **Section 5.3.3**) was determined. The experimental results agree qualitatively with the plasmonic *near-field* induced by the helical shape and the electronic activity of the selected metals and quantitatively with corresponding numerical simulations, demonstrating the controllability of the plasmonic near-field of the nano-helices.

SERS results: graphene

In this study, monolayer graphene is grown on Cu foil using the chemical vapour deposition technique (CVD) [124]. A thin layer of polymethyl methacrylate (*PMMA*) is spun on top of the graphene prior to the *Cu* etching. Graphene supported with *PMMA* is transferred

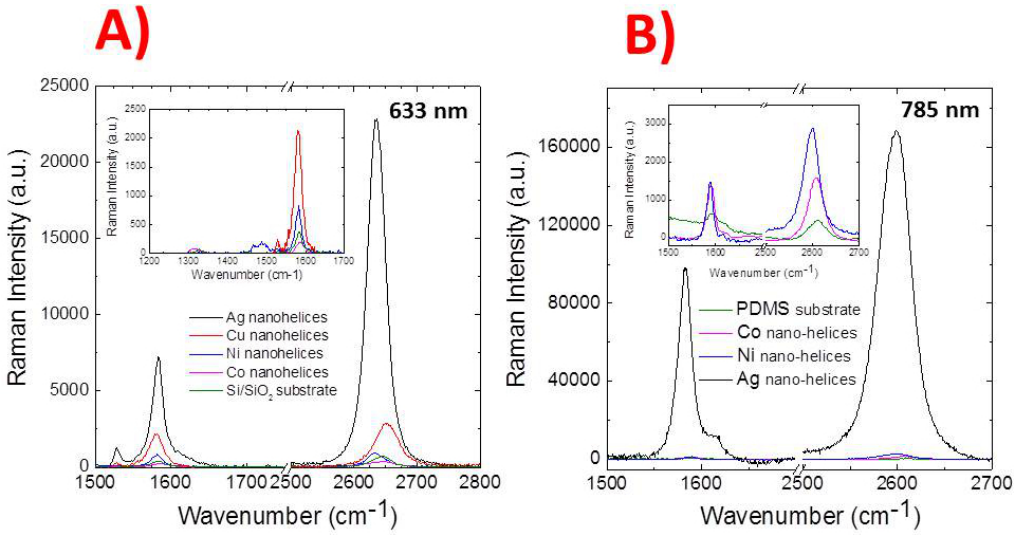

Fig. 6.35: *SERS* enhancement of graphene deposited on nano-helix arrays made from different metals. A) Raman spectra for an excitation wavelength of 633 nm. The inset shows only the *SERS* enhancement for the *Ni*, *Cu*, *Co* nano-helices and the Si/SiO_2 substrate. B) Raman spectra for an excitation wavelength of 785 nm. The inset shows only the *SERS* enhancement for the *Ni*, *Co* nano-helices and the polydimethylsiloxane (PDMS) substrate.

on the nano-helix arrays. Then, the *PMMA* is dissolved in acetone, samples are rinsed in isopropanol and dried with N_2 gas. The growth and transfer of graphene was done in collaboration with the group of Prof. Georg Düsberg in the School of Chemistry, Trinity College Dublin. Fig. 6.35A shows the G and 2D Raman peaks of graphene monolayer (633 nm excitation wavelength) on arrays of nano-helices made from *Ni*, *Co*, *Cu* and *Ag* and on a reference substrate consisting of 300 nm thermally grown SiO_2 on top of Si. The data demonstrate that the growth material has a significant impact on the *SERS* enhancement factor. More precisely, the metals with more enhanced *SERS* signal are (in decreasing order) *Ag*, *Cu*, *Ni* and *Co*. As will be explained below, these are real differences caused by the material constituting the nano-helices rather than intrinsic Raman inhomogeneities of graphene. A graphene monolayer has local inhomogeneities in their charge density which depend on the growing procedure, the interaction with the substrate and enviromental conditions [125, 126]. These charge fluctuations modify locally the graphene Raman spectra, particularly the ratio between the 2D and G peak intensity $I(2D)/I(G)$, however this ratio does generally not exceed the value 2 [126]. In contrast, first, Fig. 6.35 shows enhancements of the individual G and 2D peaks up to 40 (*Ag* nano-helix case). Second, to calculate accurately the *SERS* enhancement from the Raman measurements (Eq. 5.2), I_{SERS} and I_{REF} are compared from areas with the same I(2D)/I(G) ratio, thus, ensuring similar doping levels of the graphene flakes measured on the nano-helices and the reference substrate. In addition, two more considerations were

taken into account to select the graphene flakes for this experiment: *i*) graphene flakes with low structural disorder are selected (D peak is relatively small in comparison with the G-peak as previously stated), and *ii*) to minimize a possible mechanical stress in the samples [127], graphene flakes on each of the different types of metallic helices with the same G-peak position (Pos(G)) within our experimental accuracy (2 cm^{-1}) are selected[3]. Having excluded possible sources of error in the measurements, the *SERS* enhancement of graphene can be qualitatively explained through the electronic properties the materials used to grow the nano-helices: the wavelengths at which the main interband transitions of these metals appear are 309 nm (*Ag*) [51], 652 nm (*Cu*) [51, 52], 885 and 4132 nm (*Ni*) [52], and 1458 and 6199 nm (*Co*) [53]. Therefore, the 633 nm laser wavelength induces interband activity in all the metals except for *Ag*. Furthermore, at this excitation energy, *Cu* has only one main transition, whereas *Ni* and *Co* possess much stronger interband effects over a wide range of lower energies [52, 53]. The presence of a higher interband activity increases the damping of the plasmon resonance and concomitantly reduces the near-field and *SERS* enhancement, in agreement with our experimental results. Thus, for a given excitation wavelength, the *SERS EF* of *structurally* similar nano-helices is determined and controlled by the electronic properties of their constituting material.

As demonstrated in previous sections, the longitudinal plasmon resonance of the used metallic nano-helices is found around 850 to 900 nm (due to the structural properties of sample S3). Consequently, by measuring the Raman spectra of the nano-forests at a higher wavelength, an enhancement of the *SERS* signal should be observed for two reasons: *i*) the closer proximity to the LSPR wavelength, and *ii*) the smaller contribution of interband transitions for some of the metals of the study. Fig. 6.35B shows the G and 2D graphene Raman peaks at a 785 nm laser wavelength on three different forest of nano-helices and on a reference substrate made from polydimethylsiloxane. Note that this reference substrate was chosen not to be SiO_2/Si due to the broad fluorescence band of SiO_2 at this excitation wavelength, hindering the observation of graphenes G and 2D Raman modes [128]. In comparison with the 633 nm excitation wavelength (Figure 6.35A), the four nano-helix arrays show an enhanced *SERS* effect at 785 nm as was expected. This enhancement is not uniquely attributed to reduced interband transitions for *Cu*, *Co*, and *Ni* at 785 nm, since *Ag* does not present interband activity at either 785 nm or 633 nm. In consequence, since material-related properties cannot account for the observations of *Ag* nano-helices, the actual structure of the nano-helices has to play a role in the *EF* as well. Indeed, by changing the structural parameters (pitch, diameter and total length of the nano-helices) one would change the LSPR position, affecting the *EF* as aforementioned.

To confirm these measurements, the experimentally obtained near-field intensity enhancement at the top of the nano-helices is compared with the appropriate numerical near-field simulations (**Section 3.1.6**) using the finite-element method (FEM). Fig. 6.36 shows the

[3] Pos(G) is highly sensitive to uniaxial strain in graphene [127].

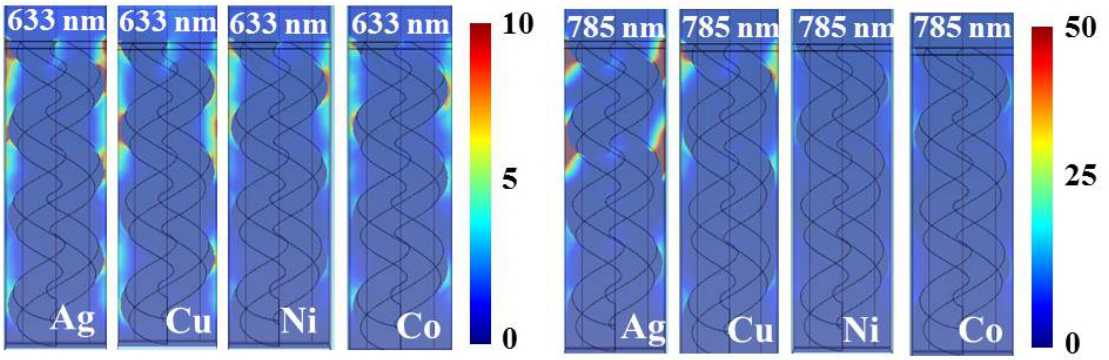

Fig. 6.36: Near-field *EF* simulation of nano-helices made from *Ag*, *Cu*, *Ni* and *Co* at 633 nm (left graphs) and 785 nm (right graphs). Note that in all the cases, the near-field distribution is not homogeneous from the top to the bottom of the nano-helices. This is due to scattering and absorption mechanisms occurring when the radiation penetrates through the nano-helix arrays.

calculated near-field intensity enhancement for nano-helices made from the four types of metals under study at 633 nm and 785 nm excitation wavelengths. Apart from the general intensity enhancement at 785 nm, for a given wavelength the materials with more intensity enhancement are in decreasing order *Ag*, *Cu*, *Ni* and *Co*, confirming the experimentally observed trends. Table 6.8 compares the experimental and numerically calculated near-field intensity enhancement $\frac{|E|^2}{|E_0|^2}$ for the two excitation wavelengths 633 nm and 785 nm. Both values agree to within less than 30% error for all the samples investigated at the two measured wavelengths. This is a strong demonstration of the actual distribution and controllability of the *near-field* distribution of the nano-helix. Apart from residual structural inhomogeneities in the samples, the mismatch with the experiments is attributed to granular effects [56] on the plasmonic near-field of the actual helical nano-structures which were not taken into account in the simulations.

Tab. 6.8: Experimental and theoretical values of the near-field enhancement $\frac{|E|^2}{|E_0|^2}$ for nano-helices made from different metals.

Metal	Experiment $\frac{\lvert E\rvert^2}{\lvert E_0\rvert^2}$ 633 nm	Theory $\frac{\lvert E\rvert^2}{\lvert E_0\rvert^2}$ 633 nm	Experiment $\frac{\lvert E\rvert^2}{\lvert E_0\rvert^2}$ 785 nm	Theory $\frac{\lvert E\rvert^2}{\lvert E_0\rvert^2}$ 785 nm
Ni	1.7	1.2	1.6	1.0
Co	1.1	1.2	1.1	0.9
Ag	6.5	8.5	15.8	12
Cu	3.6	4.3	-	7

SERS results: p-Mercaptoaniline (pMA)

Next, to extract the maximum *EF* which nano-helices are capable to generate, samples were covered entirely with pMA as probing molecule. For this, nano-helix arrays were exposed for ∼12 hours to an aqueous solution (10^{-5} M) of pMA, which lead to a uniform coating of the metallic surface by a monolayer of these molecules due to a chemisorption process [30]. *Ag* nano-helices were chosen as they exhibit the highest *near-field* intensity enhancement. Also, the experiments were carried out at 785 nm laser wavelength to be as close as possible to the localized plasmon resonance. Fig. 6.37 shows the Raman spectra of pMA covering the *Ag* nano-helix array, and two reference substrates consisting of bulk pMA and a monolayer of pMA on top of a flat thin *Ag* film.

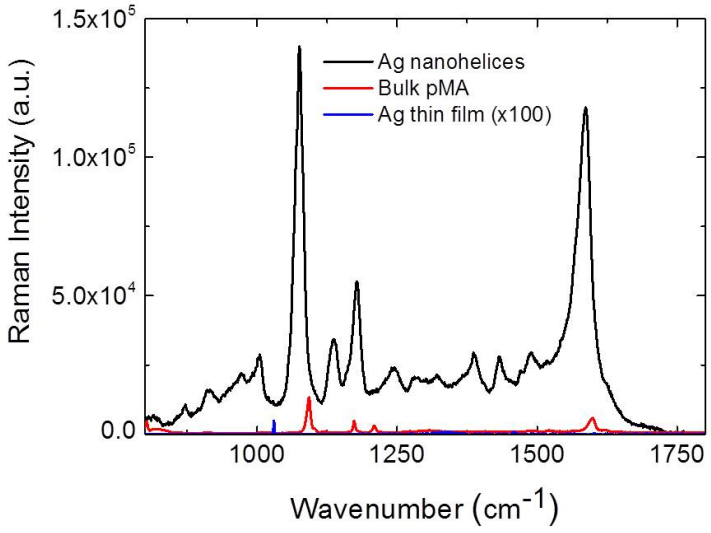

Fig. 6.37: SERS enhancement of bulk pMA, pMA deposited on *Ag* nano-helix arrays, and pMA on top of a thin *Ag* film (magnified by a factor of 100 for better visibility).

It is clearly observed how the *Ag* nano-helices considerably enhance the Raman signal of only a single monolayer of pMA molecules (the Raman intensity of the peak around 1600 cm^{-1} is $\sim 10^5$). Meanwhile, for the same laser power and integration time, a pMA monolayer on the thin *Ag* film has an enhancement factor of that peak less than 10 and bulk pMA has an enhancement of the peak of $\sim 10^3$. For comparison purposes with the *Ag* nano-helices there is a need to renormalize all these quantities with respect to the number of molecules involved in the *SERS* (*Ag* nano-helix) substrate and the reference (thin *Ag* film and bulk pMA) substrates, N_{SERS} and N_{REF}, respectively (see **Section 5.3.3**). Calculating the corresponding N_{SERS} and N_{REF} (see **Appendix E**) the maximum *EF* of the *Ag* nano-helix samples can be estimated to be at least $\sim 6 \times 10^6$. This value is a lower bound as the laser wavelength used is not fully coincident with the LSPR position (**Appendix E**). Furthermore, measuring the pMA spectra across the entire area of

nano-helices (100 μm $\times$ 1 mm), reproducible results with less than a 25% difference are observed. This good spatial reproducibility is due to the homogeneity of the nano-helical arrays and the uniformity of the individual nano-helices, making *Ag* nano-helices attractive from a practical standpoint [105]. The obtained *EF* is slightly higher than the one reported for metallic rods [105, 129] and other scalable nano-structures [130]. In contrast, it is much smaller than in other reported 'nano-gapped' antennas such as the Bow-Tie type [30]. Nevertheless, 'nano-gapped' antennas are not grown in general by a high-throughput, industrially scalable process and they lack of spatial homogeneity of the *SERS EF*, making them difficult to be efficiently used in practical applications [105].

6.3 Chiral properties of metallic nano-helices

In this section, the results of the chirality-related experiments are shown and discussed. They comprise optical, magneto-optical and magneto-electric measurements addresing optical activity and magnetochiral anisotropy in reflectance and magneto-transport, respectively.

6.3.1 Optical Activity

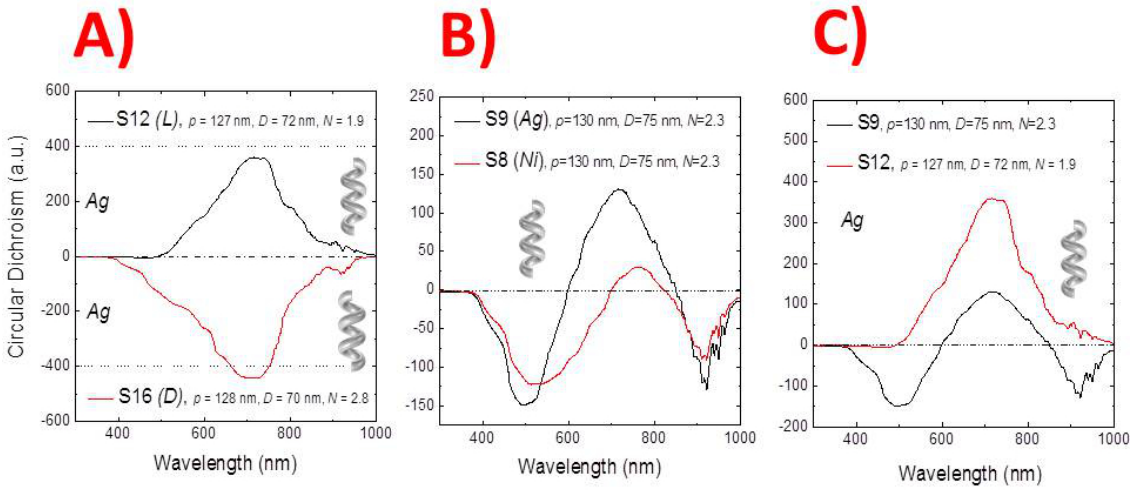

Fig. 6.38: Circular dichroism for arrays of *Ag* and *Ni* nano-helices. A) *Ag* nano-helices with similar p and D but different N and opposite helicity. B) *Ag* and *Ni* nano-helices with similar structural parameters and the same helicity (L). C) Comparing both graphs (*i.e.* Figs. A) and B)) show how the *CD* can be deliberately tuned by the growing metal and the actual helical structure.

Helically structured films exhibit optical activity *OA* effects also known as Circular Bragg or Cotton effects [62]. They tend to reflect circularly polarized light of same handdedness while transmitting circularly polarized light of opposite handedness [17, 131]. Optical activity effects were measured in the transmission spectra of nano-helix arrays (**Section 5.3.2**). In this particular case, the set-up had to be modified by introducing a linear polarizer and a Fresnel rhomb circular polarizer to produce circular right- or left-handed polarized light, RHC and LHC respectively. Fig. 6.38A represents the Circular Dichroism, *CD*, (RHC - LHC) of samples S12 and S16. They are *Ag* nano-helices with different helicity. Their structural parameters are $p = 127$ nm, $D = 72$ nm, $N = 1.88$ for S12 and $p = 128$ nm, $D = 70$ nm, $N = 2.8$ for S16. The spectral range was measured from 350 nm to 1000 nm, which correspond to the achromatic range of the quarter wavelength plate. It can be observed that the *CD* response is inverted due to the opposite helicity. A maximum *CD* difference can be observed at ∼720 nm for both samples. The latter is due to the fact that *OA* effects emerge at a wavelength related to the diameter of the

helix, which is approximately the same for S12 and S16 [8, 101]. Furthermore, the *CD* value of the maximum is larger in S16 than in S12 due to the larger number of turns in the former nano-structure [101]. Fig. 6.38B shows the *CD* of samples S8 (*Ni*) and S9 (*Ag*), both being L enantiomers. Their structural parameters are $p = 128$ nm, $D = 72$ nm, $N = 2.11$ for S8 and $p = 130$ nm, $D = 75$ nm, $N = 2.3$ for S9. Although they show a qualitatively similar dependence on the wavelength (*cf.* occuring minima and maxima in Fig. 6.38B), the *CD* effects are weaker in the *Ni* sample, which might be due to a stronger interband activity in *Ni* than in *Ag* for those wavelenghts [51,52]. The data here presented demonstrate how the chiroptic response of metallic nano-helices can be tailored by choice of the helix growth material, and by the helix structure and size.

6.3.2 Optical Magneto-Chiral Anisotropy

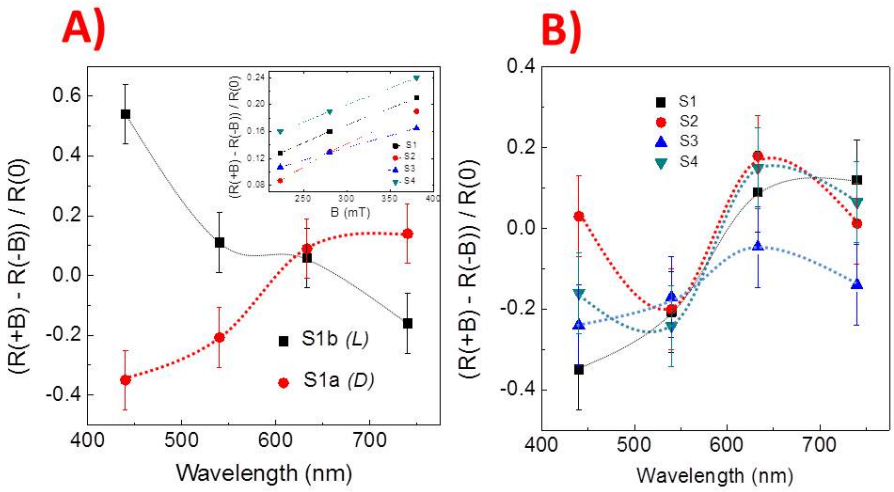

Fig. 6.39: *oMChD* signal in *Ni* nano-helices A) *oMChD* for samples S1 (L- and D-enantiomers). Inset: *oMChD* linear dependence for samples S1a, S2, S3, S4 on the external magnetic field for a 540 nm excitation. All the samples in the inset were D-enantiomers. B) *oMChD* for samples S1,S2, S3 and S4. All the samples were D-enantiomers. Dotted lines are a guide to the eye showing the tilted $'S'$ shape dependence of the *oMChD* with the wavelength.

Optical magneto-chiral effects were examined in *Ni* nano-helices due to the enhancement of chiral effects in ferromagnetic materials [70]. Samples were measured in the reflection set-up as described in **Section 5.5**. Fig. 6.39A shows the *oMChD* signal (ΔR/R=(R(+$\vec{B}$)-R(-$\vec{B}$))/R(0)) as a function of the laser wavelengths for the two (L- and D-) enantiomers of the sample type S1. Both enantiomers show opposite behaviour in their magneto-optical

response, which experimentally proves the existence of the *oMChD* in these samples. We would like to emphasize that this is the first *oMChD* measurement of a chiral medium made from a material with a non-chiral internal structure. Furthermore, as our selected growth method can efficiently modify the nano-helix parameters, *oMChA* effects on these types of nano-structured samples could be easily tuned. This is verified in Fig. 6.39B where the variation of the *oMChD* signals for the four different sample types are shown for the selected laser wavelengths. The *oMChD* effect shown in Fig. 6.39B shows a tilted $'S'$ shape dependence with the wavelength which is unlikely to be due to the longitudinal plasmon presented in the structures: the latter plasmonic effect occurs in these samples at wavelengths larger than 750 nm (Fig. 6.32). Finally, there is a need to point out that at ∼530 nm, the *oMChD* has similar values for all the measured samples. Although the latter effect is unexplained, it is convenient to point out that the only structural parameter which is similar in the measured samples is the wire thickness r_w. Therefore, there could be some link between the *oMChD* data at ∼530 nm and the transverse plasmon of the metallic nano-helices.

6.3.3 Electrical Magneto-Chiral Anisotropy

Electrical magneto-chiral effects were examined in *Ni* nano-helices due to the enhancement of chiral effects in ferromagnetic materials [70]. The two point resistance of the samples was measured in a set-up as described in **Section 5.5**. There are three hallmarks of the *eMChA* [7]: *i*) a linear increase of the resistance difference $\Delta R(\vec{I},\vec{B}) = R(+\vec{I},\vec{B}) - R(-\vec{I},\vec{B})$ as a function of the current $\vec{I}$ for a constant magnetic flux $\vec{B}$; *ii*) a linear increase of the resistance difference $\Delta R(\vec{I},\vec{B}) = R(\vec{I},+\vec{B}) - R(\vec{I},-\vec{B})$ as a function of $\vec{B}$ for a constant $\vec{I}$; and *iii*) the inversion of the resistance difference (change of sign) for the two former hallmarks when exchanging the enantiomer (L and D).

Initially, the *eMChA* effect was attempted to be measured in arrays of 100 μm × 100 μm containing nano-helices with the structural parameters similar to those of sample S3 (Table 6.3). The top contact of these samples was made from *Cu* using the capping technique explained in **Section 5.1**. The overall measured resistance of these nano-helix array and contacts was ∼4 Ω. This batch of samples show some of the *eMChA* hallmarks at 2K and 40K. The effect was vanishing at 140K, which indicates that the possible *eMChA* effect in *Ni* nano-helices is less affected by temperature variations than previous nano-scaled samples such as single-walled carbon nanotubes [78]. Fig. 6.40 shows the required graphs to examine each hallmark. Fig. 6.40A plots the variation of resistance for constant $\vec{B}$ when augmenting the current $\vec{I}$, showing the expected linear behaviour. More in detail, the first measurement (Fig. 6.40A, triangles) is undertaken for an external magnetic flux $\vec{B}_{ext} = \mu_0\vec{H} = 0$ T, showing no ΔR. Then, $\vec{B}_{ext}$ is ramped up to 4 and 7 T and a linear change of ΔR is measured. However, the change in ΔR with $\vec{B}_{ext}$ from 4 to 7 T should be noted, since it does not scale linearly with the magnitude of $\vec{B}_{ext}$. This effect

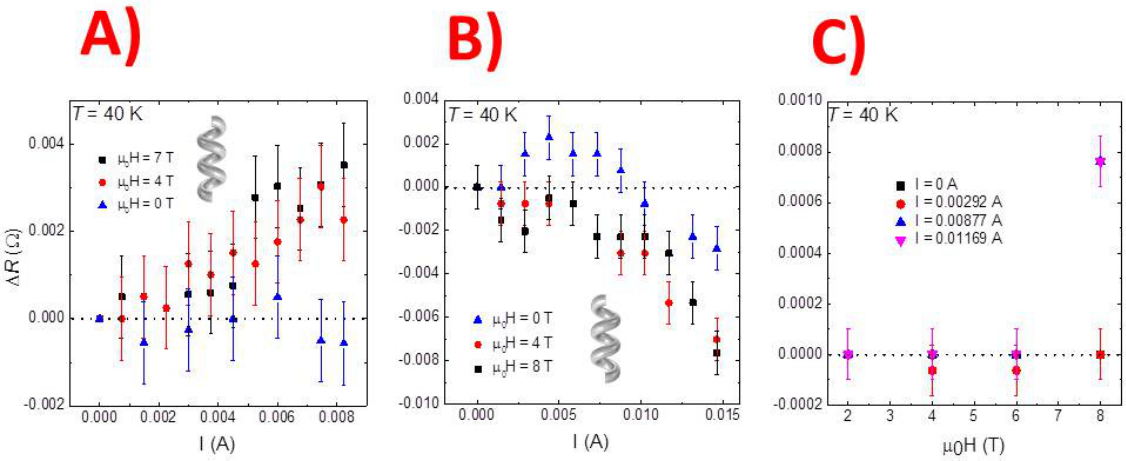

Fig. 6.40: *eMChA* effects in *Ni* nano-helices at 40 K. The array area was 100 μm × 100 μm. A) ΔR depending on the applied current for a constant magnetic field in a L-enantiomer. The first measurement was taken at $\mu_0\vec{H} = 0$ T, thus the sample is not pre-magnetized. B) ΔR depending on the applied current for a constant magnetic field in a D-enantiomer. The measurement taken at $\mu_0\vec{H} = 0$ T was not the first measurement, thus, this sample is pre-magnetized. C) ΔR depending on the external magnetic field for a constant current in a D-enantiomer. The lines are meant to be a guide for the eye.

might be due to the small contribution of the external applied magnetic flux $\vec{B}_{ext}$ to the total magnetic flux density $\vec{B}$ in the ferromagnetic nano-helices ($\vec{B} = \mu_0\vec{H} + \mu_0\vec{M} + \vec{B}_{coil}$ $= \vec{B}_{ext} + \vec{B}_{int} + \vec{B}_{coil}$). In the former expression $\vec{B}_{int}$ is the internal magnetic flux created in the nano-helix arrays due to their ferromagnetic growth material and $\vec{B}_{coil}$ is the magnetic flux generated in the nano-helix when a current $\vec{I}$ passes through the coiled nano-structure. The maximum value of ΔR ($\vec{I}, \vec{B} = const.$) ∼0.004 Ω measured in the 100 μm × 100 μm array of nano-helices, gives an estimation of the *eMChA* effect of one nano-helix of ∼2000 Ω at 7 T and a current passing through the helix of ∼18 μA. Fig. 6.40B shows the data collected for a sample with opposite helicity. The general behaviour is the same except for a sign inversion of ΔR, agreeing with the fact the enantiomers are different. However, it should be noted that in Fig. 6.40B the measurement taken at $\vec{B}_{ext}$ = 0 T was taken after exposing the sample to different external fields, *i.e.* the sample was pre-magnetized. This fact will produce $\Delta R \neq 0$ even at $\vec{B}_{ext} = 0$ T as shown in Fig. 6.40B. Fig. 6.40C plots the variation of resistance for constant $\vec{I}$ when augmenting the external magnetic flux for the same sample of Fig 6.40B. Surprisingly, it does not show the typical linear behaviour expected for these chiral samples [7]: in this case, at lower currents no ΔR at any magnetic field could be detected. Only at the higher currents for high external magnetic fields ($\mu_0\vec{H} > 6$ T) $\Delta R \neq 0$. Furthermore, the variation of $\Delta R(\vec{B}, \vec{I} = const.)$ ∼0.008 Ω is an order of magnitude smaller than $\Delta R(\vec{I}, \vec{B} = const.)$ (Fig. 6.40B). These two observations are in marked contrast to previously measured chiral systems at the nano- and macro-scale (Ref. [78] and [7], respectively) where both

variations of resistances (ΔR $(\vec{B}, \vec{I} = const.)$ and ΔR $(\vec{I}, \vec{B} = const.)$) have similar values. A possible explanation to this observation can be again given by looking at the total magnetic flux: $\vec{B}_{ext} + \vec{B}_{int} + \vec{B}_{coil}$. In ferromagnetic nano-helices, the contribution due to these three terms has to be comparable to produce a $\Delta R \neq 0$ [4]. Therefore only high external magnetic fields (> 6 T) will produce any resistance variation at constant $\vec{I}$, which agrees with Fig. 6.40C. For currents below 5 mA the experimental resolution does not seem to be sufficient to detect these trends. These novel effects appearing in *Ni* nano-helices have to be further investigated and prove the different behaviour of chiral and ferromagnetic samples at the nano-scale: on one hand, the pitch p in nano-helices[5] is closer to the electronic mean-free path of the metals in marked contrast with previously measured twisted *Bi* wires at the macro-scale [7]. On the other hand, ferromagnetic samples show stronger magneto-chiral effects below the Curie temperature, an effect which has been shown in the optical measurements of (electrically insulating) chiral molecular ferromagnetic crystals [70].

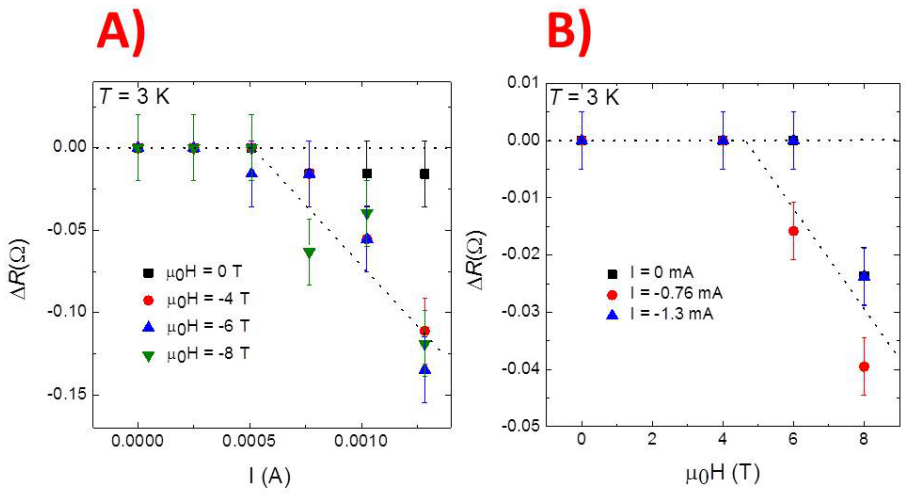

Fig. 6.41: eMChA effects in *Ni* nano-helices at 3 K. The array area was 20 μm $\times$ 20 μm A) ΔR depending on the applied current for a constant magnetic field in a L-enantiomer. B) ΔR depending on the external magnetic field for a constant current in a L-enantiomer. The lines are meant to be a guide for the eye.

A further measurement of the *eMChA* effect was undertaken in arrays of *Ni* nano-helices with a smaller area (20 μm $\times$ 20 μm). The overall measured resistance of these samples was $\sim$80 Ω. Fig. 6.41A shows the data containing the resistance variation depending on the current $\vec{I}$ for different constant magnetic flux densities at a temperature of 3 K: $\Delta R = (R(\vec{B}, +\vec{I}) - R(\vec{B}, -\vec{I}))$. Within the experimental error ΔR becomes sizeable for currents above 1 mA. The three currents measured above 1 mA show the expected linear behaviour. There was no initial magnetization of these nano-helices. The sample was not

[4] If one term is predominant, it will lead to a ΔR smaller than the experimental resolution.
[5] p is the chiral parameter of helices as previously discussed in **Section 4**

measured at higher currents due to problems in reproducibility: at these higher currents, the sample heats up considerably[6], and might cause movements of the domain walls. The latter will introduce changes in the magnetorresistance of the sample making these measurements not reproducible for high currents. As in the previous case, a small change in ΔR when changing the external magnetic flux from 4 to 8 T is observed. Furthermore, the value of ΔR ∼0.14 Ω measured in the 20 μm × 20 μm array of nano-helices, gives an estimation of the *eMChA* effect of one nano-helix of ∼ 2500 Ω at 8 T, which is of the same order of magnitude as for the 100 μm × 100 μm array of nano-helices. This confirms that the observed phenomenon is indeed related to the nano-helices and not to a spurious effect. However, further arrays with different sizes have to be measured to corroborate this nano-helix value by extrapolation. Fig. 6.41B plots the resistance variation depending on the applied magnetic flux $\vec{B}_{ext}$ for different constant currents at a temperature of 3 K: ΔR=$(R(+\vec{B},\vec{I}) - R(-\vec{B},\vec{I}))$. In agreement with the sample previously described, the variation of $\Delta R(\vec{B},\vec{I} = const.)$ is smaller than $\Delta R(\vec{I},\vec{B} = const.)$ and it is only present at the higher currents and magnetic fluxes (ΔR$(\vec{B},\vec{I} = const.)$ ∼0.04 Ω, meanwhile ΔR$(\vec{I},\vec{B} = const.)$ ∼0.12 Ω).

In summary, although not all the *eMChA* hallmarks have been observed neatly, this data presented is consistent and indicates the different impact of chirality on ferromagnetic samples at the nano-scale compared to non-ferromagnetic ones (both of them electrically conducting). One of this expected effects is the existance of an extraordinarily strong *eMChA* effect. The estimated values of the *eMChA* magnetoresistance of one helix (∼300 Ω/T) points towards that direction since such high resistance values were never detected in macroscopic twisted *Bi* wires (∼ 10^{-3} Ω/T [7]) nor non-ferromagnetic single-walled carbon nanotubes (∼ 10^{-1} Ω/T [78]). To comprehensively identify all mechanisms which give rise to the present observation, multiple arrays with different areas are needed to give an accurate value for the *eMChA* of one ferromagnetic nano-helix through extrapolation.

[6] The sensor measuring the sample temperature in the cryostat goes up 4 K when changing the current from 1 mA to 6 mA.

7. SUMMARY, FUTURE WORK AND POTENTIAL APPLICATIONS

The fabrication and electromagnetic properties of metallic three-dimesional (3D) helices at the nano-scale were addressed in the present thesis. Experimentally, a complete description and improvement of the chosen growth technique, the Glancing Angle Deposition (*GLAD*) is provided. The associated studied optical properties unveil the function of these structures as helical antennae in the optical range of the electromagnetic spectrum. In addition, the predicted magneto-chiral anisotropies in the optical and electrical resistance of these samples were proven. The presented experimental and theoretical *far-field* and *near-field* results confirm that the electromagnetic response of the nano-helix forests is deliberately tunable by changing the nano-helix pitch, diameter, the number of turns, diameter of the wire composing the helix and the growth material. These results agree with the fact that the optical response of these metallic nano-structures is mainly influenced by their plasmonic effects.

In more detail, the entire fabrication method proposed is able to produce large area arrays of regularly-shaped, nano-sized, aligned and freestanding metallic nano-helices. These results demonstrate a further development of the *GLAD* method to produce metallic nano-structures by using a straight-forward implementable *heat-management* technique. Four different metals were sucessfully investigated in this study: *Ag*, *Cu*, *Co* and *Ni*. These are four of the most difficult materials to engineer by *GLAD* on the nano-scale due to their high surface mobility. Futhermore, this work reports a systematic study describing key factors to optimize the growth parameters for general metallic nano-structures fabricated by *GLAD*.

The manufacturing precision of the here reported metallic helical nano-structures make these samples ideal for the identification of novel effects of metallic nano-helices not only at optical but also at low frequencies. More specifically, the optical reflectance properties of arrays of nano-helices are different from the thin-film behaviour: the tuneability of this optical response with the structural parameters of the individual nano-helices was proven, in agreement with the applied theoretical models. In addition, nano-helices exhibit a longitudinal localized-plasmon resonance which scales linearly with the total length of the structure. This scaling-law is in marked contrast to conventional micro- and macroscopic helical structures where the antenna operational mode scales with the length of a single turn only. This novel scaling law was neither predicted nor proposed by any theoretical or experimental work in the literature, reflecting the unique nature of 3D helical metal

nano-structures and their electromagnetic properties. At the plasmon wavelength, the surface charges along the nano-helix produce scattered radiation mainly directed parallel to the axis of the nano-helix. Moreover, the nano-helical structure combined with the electronic properties of the used metals, specifically the interband transtions, were proven to determine the intensity of the plasmonic *near-field* of these nano-structures. Optical and magneto-optical chirality-related effects are demonstrated for the first time in this study for metals with no internal chiral-structure, but being topologically formed into a chiral shape on the nano-scale. It was demonstrated also, that the here reported nano-structures present tuneable chirality-related properties over the entire optical range of the electromagnetic spectrum. These tunable chiral effects were further confirmed by magneto-transport measurements of arrays of nano-helices at different temperatures.

7.1 Future Work

Having a sample quality far exceeding prior art, the future work to be done on metallic nano-helices should be more focused on their optical, magneto-optical and magneto-transport properties.

Regarding the optical properties, the knowledge of the metallic nano-helices is at the stage where single photon sources can be coupled with the nano-antennae to investigate the antenna-load interactions at optical frequencies (impedance matching).

The magneto-optical properties can be measured in a transmission set-up with *Ag* and *Ni* nano-helices to examine how large the chiral optical pre-factor of ferromagnetic samples is with respect to non-ferromagnetic ones. This value of the Magneto-Chiral Dichroism measured in transmission can be also compared with previously measured molecular crystals [69, 70].

Finally, as indicated before, the magneto-electrical properties shown in this thesis are preliminary and further studies have to be undertaken mainly to obtain a reasonable value of the *eMChA* for a single ferromagnetic nano-helix. The latter can potentially be measured by dispersing the nano-helix arrays in solution and contacting it by standard electron beam lithography techniques.

7.2 Potential Applications

The highly spatial homogeneity and the fabrication accuracy of the presented metallic nano-helices enable the tuneability of the electromagnetic properties of these nano-structures. As a consequence, these metallic nano-helices can be potentially used in several applications. Particularly, the newly discovered scaling-rule enables us to transfer the design rules for (conventional) helical antennae [6] into the optical (visible, plasmonic) wavelength-regime. Combined with the easy tuneability and the fabrication accuracy of the production process, the use of such nano-antennae is foreseeable in a wide range of ap-

plications including optical chiral sensors, light-emitting devices, surface-enhanced spectroscopy, broadband visible-light polarisers, light filters, and photo-detectors in biotechnological applications. Furthermore, the highly directional scattering along the helical axis at the longitudinal plasmon wavelength make these metallic nano-helices particularly interesting to be used in optical communications.
Finally, the demonstrated topogically induced chiral effects enable the utilization of nano-helical forests in solid-state devices for multiple chirality-related applications such as enantiomeric selection, data storage or spin filters.

APPENDIX

A. ELECTROMAGNETIC EQUATIONS

A.1 Maxwell Equations. Time domain

The problem of determining the electromagnetic response of any material on a macroscopic level is the problem of solving Maxwell's equations subjected to certain boundary conditions. These equations state the relationships between fundamental electromagnetic quantities at a position $\vec{r}$ and time t: the electric field intensity $\vec{E}$, the electric flux density $\vec{D}$, the magnetic field intensity $\vec{H}$, the magnetic flux density $\vec{B}$, the current density $\vec{J}$ and the electric charge density ρ. For general time-varying fields, Maxwell's equations can be written as [9, 38]:

$$\nabla \times \vec{H}(\vec{r},t) = \vec{J}(\vec{r},t) + \frac{\partial \vec{D}(\vec{r},t)}{\partial t} \tag{A.1}$$

$$\nabla \times \vec{E}(\vec{r},t) = -\frac{\partial \vec{B}(\vec{r},t)}{\partial t} \tag{A.2}$$

$$\nabla \vec{D}(\vec{r},t) = \rho(\vec{r},t) \tag{A.3}$$

$$\nabla \vec{B}(\vec{r},t) = 0 \tag{A.4}$$

$$\tag{A.5}$$

The first two equations are also referred as *Maxwell-Ampere's law* and *Faraday's law* respectively. The remaining equations are two forms of the Gauss' laws. Another fundamental equation is the *equation of continuity*, which can be written as

$$\nabla \vec{J}(\vec{r},t) = -\frac{\partial \rho(\vec{r},t)}{\partial t} \tag{A.6}$$

$$\tag{A.7}$$

A.2 Constitutive Relations. Time domain

Out of the five equations mentioned, only three are independent [38]. The first two combined with either the electric from of Gauss' law or the equation of continuity form such an independent system. To obtain a solvable system, we need two more equations describing the macroscopic properties of the medium under study, the so called *constitutive relations*.

Determining the relationship between the auxiliary fields $\vec{D}(\vec{r},t)$ and $\vec{H}(\vec{r},t)$ and the $\vec{E}(\vec{r},t)$ and $\vec{B}(\vec{r},t)$ fields starts with the definition of the auxiliary fields themselves:

$$\vec{D}(\vec{r},t) = \epsilon_0 \vec{E}(\vec{r},t) + \vec{P}(\vec{r},t) \tag{A.8}$$

$$\vec{H}(\vec{r},t) = \mu_0^{-1} \vec{B}(\vec{r},t) - \vec{M}(\vec{r},t) \tag{A.9}$$

where $\vec{P}(\vec{r},t)$ is the polarization field and $\vec{M}(\vec{r},t)$ is the magnetization field which are defined in terms of microscopic bound charges and bound currents respectively. For real-world materials, the constitutive relations are, in general, not linear. Calculating the constitutive relations from first principles involves determining how $\vec{P}(\vec{r},t)$ and $\vec{M}(\vec{r},t)$ are created from a given $\vec{E}(\vec{r},t)$ and $\vec{B}(\vec{r},t)$. These relations may be empirical (based directly upon measurements), or theoretical (based upon statistical mechanics, transport theory or other tools of condensed matter physics).
Therefore, the constitutive relations may be naturally expressed in the general form [39]:

$$\vec{D}(\vec{r},t) = \mathcal{F}\{\vec{E}(\vec{r},t), \vec{B}(\vec{r},t)\} \tag{A.10}$$

$$\vec{H}(\vec{r},t) = \mathcal{G}\{\vec{E}(\vec{r},t), \vec{B}(\vec{r},t)\} \tag{A.11}$$

where $\mathcal{F}$ and $\mathcal{G}$ are in general non-linear functions of $\vec{E}(\vec{r},t)$ and $\vec{B}(\vec{r},t)$. The electromagnetic response of a medium is non-local respect to both space and time (spatial and temporal dispersion).
In the particular case of linear systems, the constitutive relations are stated as [39]:

$$\vec{D}(\vec{r},t) = \int_{t',r'} [\overline{\overline{\epsilon_{EB}}}(\vec{r'},t')\vec{E}(\vec{r}-\vec{r'},t-t') + \overline{\overline{\xi_{EB}}}(\vec{r'},t')\vec{B}(\vec{r}-\vec{r'},t-t')]d^3r'dt' \tag{A.12}$$

$$\vec{H}(\vec{r},t) = \int_{t',r'} [\overline{\overline{\zeta_{EB}}}(\vec{r'},t')\vec{E}(\vec{r}-\vec{r'},t-t') + \overline{\overline{\mu_{EB}}}(\vec{r'},t')\vec{B}(\vec{r}-\vec{r'},t-t')]d^3r'dt' \tag{A.13}$$

where $\overline{\overline{\epsilon_{EB}}}(\vec{r},t)$ is called permittivity, $\overline{\overline{\mu_{EB}}}(\vec{r},t)$ permeability and $\overline{\overline{\xi_{EB}}}(\vec{r},t)$, $\overline{\overline{\zeta_{EB}}}(\vec{r},t)$ are magneto-electric parameters of the medium. All of these elements are 3 x 3 constitutive dyadics (second-rank Cartesian tensors). The constitutive relations expressed in Eq. A.12, represent bianisotropic media: anisotropic systems with magnetoelectric coupling, and constitute the most general linear systems that can be studied.
In certain media such as metamaterials, spatial nonlocality play a minimal role since the wavelength is much larger than the feature size of the individual constituents and much smaller compared with any other characteristic length scale in the entire medium (length and width of the array), therefore the linear constitutive relations expressed in Eq. A.12 can be simplified to linear, spatially local, temporally nonlocal constitutive relations of

the form:

$$\vec{D}(\vec{r},t) = \int_{t'} [\overline{\overline{\epsilon_{EB}}}(\vec{r},t')\vec{E}(\vec{r},t-t') + \overline{\overline{\xi_{EB}}}(\vec{r},t')\vec{B}(\vec{r},t-t')]dt' \tag{A.14}$$

$$\vec{H}(\vec{r},t) = \int_{t'} [\overline{\overline{\zeta_{EB}}}(\vec{r},t')\vec{E}(\vec{r},t-t') + \overline{\overline{\mu_{EB}}}(\vec{r},t')\vec{B}(\vec{r},t-t')]dt' \tag{A.15}$$

A.3 Maxwell Equations and Constitutive Relations. Frequency domain

Some of the mathematical complexity appearing in the constitutive relations Eqs.A.14 come from a temporal convolution integral. In order to circumvent these difficulties, it is common practice to introduce temporal Fourier transforms in the temporal constitutive relations and Maxwell equations as

$$\mathcal{Z}(\vec{r},\omega) = \int_{-\infty}^{\infty} \vec{\mathcal{Z}}(\vec{r},t)e^{i\omega t}dt \tag{A.16}$$

with $\mathcal{Z}$ standing in for $\overline{\overline{\epsilon_{EB}}}$, $\overline{\overline{\xi_{EB}}}$, $\overline{\overline{\zeta_{EB}}}$, $\overline{\overline{\mu_{EB}}}$, $\vec{E}$, $\vec{D}$, $\vec{B}$ and $\vec{H}$; being ω the angular frequency.
The corresponding frequency-domain Maxwell postulates are then given by:

$$\nabla \times \vec{H}(\vec{r},\omega) = \vec{J}(\vec{r},\omega) + j\omega\vec{D}(\vec{r},\omega) \tag{A.17}$$

$$\nabla \times \vec{E}(\vec{r},\omega) = -j\omega\vec{B}(\vec{r},\omega) \tag{A.18}$$

$$\nabla\vec{D}(\vec{r},\omega) = \rho(\vec{r},\omega) \tag{A.19}$$

$$\nabla\vec{B}(\vec{r},\omega) = 0 \tag{A.20}$$

$$\tag{A.21}$$

Meanwhile, taking the temporal Fourier transform of Eqs.A.12 and having taken into account the convolution theorem, the frequency-domain constitutive relations for linear bianisotropic materials emerge as:

$$\vec{D}(\vec{r},\omega) = \overline{\overline{\epsilon_{EB}}}(\vec{r},\omega)\vec{E}(\vec{r},\omega) + \overline{\overline{\xi_{EB}}}(\vec{r},\omega)\vec{B}(\vec{r},\omega) \tag{A.22}$$

$$\vec{H}(\vec{r},\omega) = \overline{\overline{\zeta_{EB}}}(\vec{r},\omega)\vec{E}(\vec{r},\omega) + \overline{\overline{\mu_{EB}}}(\vec{r},\omega)\vec{B}(\vec{r},\omega) \tag{A.23}$$

A.4 Maxwell Equations and Constitutive Relations. Spatial nonlocality

In the case of dealing with an spatially nonlocal (homogeneous) system, the spatial convolution integral in Eqs. A.25 can be simplified by introducing the spatial Fourier transform:

$$\mathcal{Z}'(\vec{r},\omega) = \int_{-\infty}^{\infty} \vec{\mathcal{Z}}'(\vec{r},t) e^{-i\vec{k}\vec{r}} d\vec{r} \tag{A.24}$$

with $\mathcal{Z}'$ standing in for $\overline{\overline{\epsilon_{EB}}}$, $\overline{\overline{\xi_{EB}}}$, $\overline{\overline{\zeta_{EB}}}$, $\overline{\overline{\mu_{EB}}}$, $\vec{E}$, $\vec{D}$, $\vec{B}$ and $\vec{H}$; being $\vec{k}$ the wavevector. The corresponding spatial nonlocal frequency-domain Maxwell postulates are then given by:

$$\nabla \times \vec{H}(\vec{k},\omega) = \vec{J}(\vec{k},\omega) + j\omega\vec{D}(\vec{k},\omega) \tag{A.25}$$
$$\nabla \times \vec{E}(\vec{k},\omega) = -j\omega\vec{B}(\vec{k},\omega) \tag{A.26}$$
$$\nabla\vec{D}(\vec{k},\omega) = \rho(\vec{k},\omega) \tag{A.27}$$
$$\nabla\vec{B}(\vec{k},\omega) = 0 \tag{A.28}$$
$$\tag{A.29}$$

Meanwhile, the spatial nonlocal frequency-domain constitutive relations for linear bianisotropic materials are:

$$\vec{D}(\vec{k},\omega) = \overline{\overline{\epsilon_{EB}}}(\vec{k},\omega)\vec{E}(\vec{k},\omega) + \overline{\overline{\xi_{EB}}}(\vec{k},\omega)\vec{B}(\vec{k},\omega) \tag{A.30}$$
$$\vec{H}(\vec{k},\omega) = \overline{\overline{\zeta_{EB}}}(\vec{k},\omega)\vec{E}(\vec{k},\omega) + \overline{\overline{\mu_{EB}}}(\vec{k},\omega)\vec{B}(\vec{k},\omega) \tag{A.31}$$

A.5 Helmholtz equation. Vector wave equation

The Helmholtz equation is the partial differential equation

$$\nabla^2 A + |\vec{k}|^2 A = 0 \tag{A.32}$$

where ∇^2 is the Laplacian, $|\vec{k}|$ is the wavenumber module, and A is the field amplitude. It arises often in the study of physical problems involving partial differential equations (PDEs) in both space and time. For example, consider the space and time dependent wave equation:

$$\left(\nabla^2 - \frac{1}{c^2}\frac{\partial^2}{\partial t^2}\right) u(\vec{r},t) = 0 \tag{A.33}$$

The Helmholtz equation represents the time-independent form of the original wave equation and results from applying the technique of separation of variables to reduce the complexity of the analysis. Following this approach, the wave function $u(\vec{r},t)$ can be

expressed as

$$u(\vec{r},t) = A(\vec{r}) \cdot T(t) \tag{A.34}$$

substituying this form into the wave equation A.33:

$$\frac{\nabla^2 A}{A} = \frac{1}{c^2 T}\frac{d^2 T}{dt^2} \tag{A.35}$$

The left hand side of Eq. A.35 depends only on $\vec{r}$ and the right hand side on t. As a result, this equation is valid in the general case if and only if both sides of the equation are equal to a constant value. From this observation, it is possible to obtain two equations, one for $A(\vec{r})$ and other for $T(t)$:

$$\frac{\nabla^2 A}{A} = |\vec{k}|^2 \tag{A.36}$$

$$\frac{1}{c^2 T}\frac{d^2 T}{dt^2} = |\vec{k}|^2 \tag{A.37}$$

Rearranging Eq. A.36, the Helmholtz equation A.32 can be obtained.
The same reasoning applies in the case of the Maxwell equations. Taking the curl of the frequency dependent form of Maxwell equations (Eqs. A.25) and assuming a linear, isotropic and homogeneous medium, *LIH* ($\vec{D} = \epsilon\vec{E}$, $\vec{B} = \mu\vec{H}$):

$$\nabla \times (\nabla \times \vec{E}) = i\omega\mu(\nabla \times \vec{H}) = \omega^2\epsilon\mu\vec{E} \tag{A.38}$$

$$\nabla \times (\nabla \times \vec{H}) = -i\omega\mu(\nabla \times \vec{E}) = \omega^2\epsilon\mu\vec{H} \tag{A.39}$$

Using the vector identity $\nabla \times (\nabla \times \vec{A}) = \nabla(\nabla\vec{A}) - \nabla^2\vec{A}$, Eqs.A.38 are converted into a couple of Helmholz equations, one for each field $\vec{E}$ and $\vec{H}$:

$$\nabla^2\vec{E} + |\vec{k}|^2\vec{E} = 0 \tag{A.40}$$

$$\nabla^2\vec{H} + |\vec{k}|^2\vec{H} = 0 \tag{A.41}$$

where $|\vec{k}|^2 = \omega^2\epsilon\mu$. The solution of these equations are:

$$\vec{E} = E_0 e^{i(\vec{k}\cdot\vec{r})} \tag{A.42}$$

$$\vec{H} = H_0 e^{i(\vec{k}\cdot\vec{r})} \tag{A.43}$$

A similar reasoning can be applied to solve the time-independent wave equation of more complex medium such as chiral and/or anisotropic media [17, 39].

A.6 Boundary conditions

The set of differential Maxwell equations (Eqs.A.1) apply locally, at each position $\vec{r}$ and time t. Wherever the derivatives do not exist, boundary conditions must be specified in order to derive unique solutions. By using the Stokes and Gauss theorems for the curl and divergence, the Maxwell postulates can be recast in integral forms [39]:

$$\oint \vec{H} \cdot d\vec{l} = \int_S \vec{J} \cdot d\vec{S} + \int_S \frac{\partial \vec{D}}{\partial t} \cdot d\vec{S} \tag{A.44}$$

$$\oint \vec{E} \cdot d\vec{l} = -\int_S \frac{\partial \vec{B}}{\partial t} \cdot d\vec{S} \tag{A.45}$$

$$\oint \vec{D} \cdot d\vec{S} = \int_V \rho dV \tag{A.46}$$

$$\oint \vec{B} \cdot d\vec{S} = 0 \tag{A.47}$$

$$\tag{A.48}$$

and the boundary conditions may be established.

A.6.1 Boundary conditions for the Electric Field

Fig.A.1A illustrates how the electric field $\vec{E}$ may change at the interface between two different media 1 and 2. $\vec{E}$ can be decomposed into normal (perpendicular to the interface, E_n) and tangential (in the plane of the interface, E_t) components.

Normal component of $\vec{D}$

The boundary condition for the normal component of the electric field can be obtained by appying Gauss's flux law

$$\oint \vec{D} \cdot d\vec{S} = \int_V \rho dV \tag{A.49}$$

to a small cylinder, positioned such that the boundary sits between its 'upper' and 'lower' surfaces as shown in Fig.A.1B. If the side wall Δh is shrunk to zero, all electric flux enters or leaves the cylinder through the top and bottom surfaces, thus:

$$\oint \vec{D} \cdot d\vec{S} \to \vec{D}_1 \cdot \hat{n} \Delta s + \vec{D}_2 \cdot (-\hat{n}) \Delta s = D_{n1} \Delta s - D_{n2} \Delta s \tag{A.50}$$

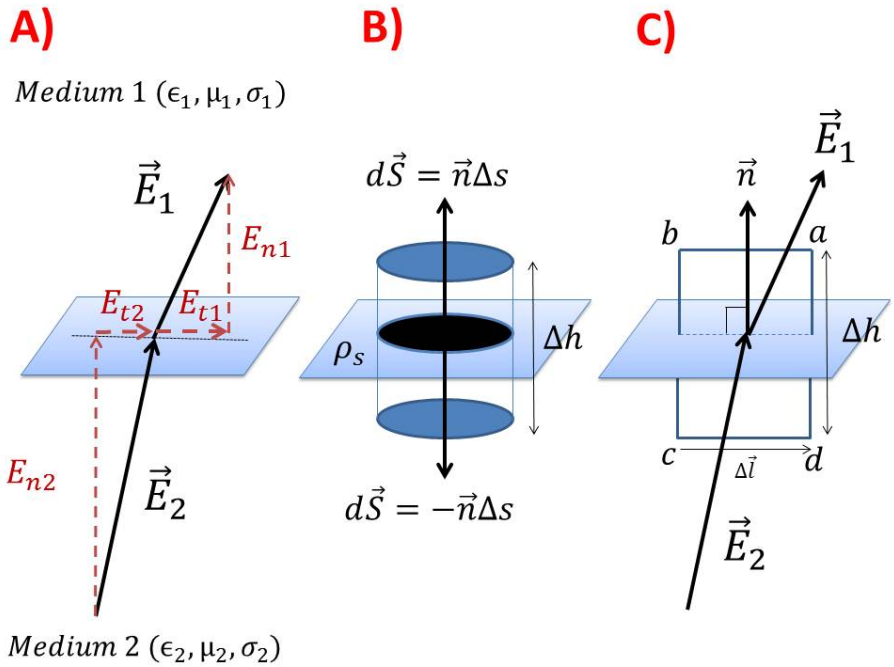

Fig. A.1: Boundary conditions for the Electric Field. A) Normal and tangential components of the $\vec{E}$ field on either side of the interface between two media. B) Gauss' law applied to a cylinder straddling the interface between two media. C)Faraday's law applied to a rectangular loop straddling the interface between the two media.

where D_{n1} and D_{n2} are the normal components of the flux density vector immediately on either side of the boundary in mediums 1 and 2, and Δs is the elemental surface area. The amount of charge enclosed as $\Delta h \to 0$ depends on whether there exists a surface charge ρ_s. In that case

$$\int_V \rho dV = \rho_s \Delta s \tag{A.51}$$

.

Inserting Eqs. A.50 and A.51 into Eq. A.49, one obtains:

$$D_{n1} - D_{n2} = \rho_s \tag{A.52}$$

.

Tangential Component of $\vec{E}$

Applying Faraday's law to a small rectangular loop of sides Δl and Δh and vertex a, b, c, d positioned across the boundary and in the plane of $\vec{E}_1$ and $\vec{E}_2$ (see Fig.A.1C), the tan-

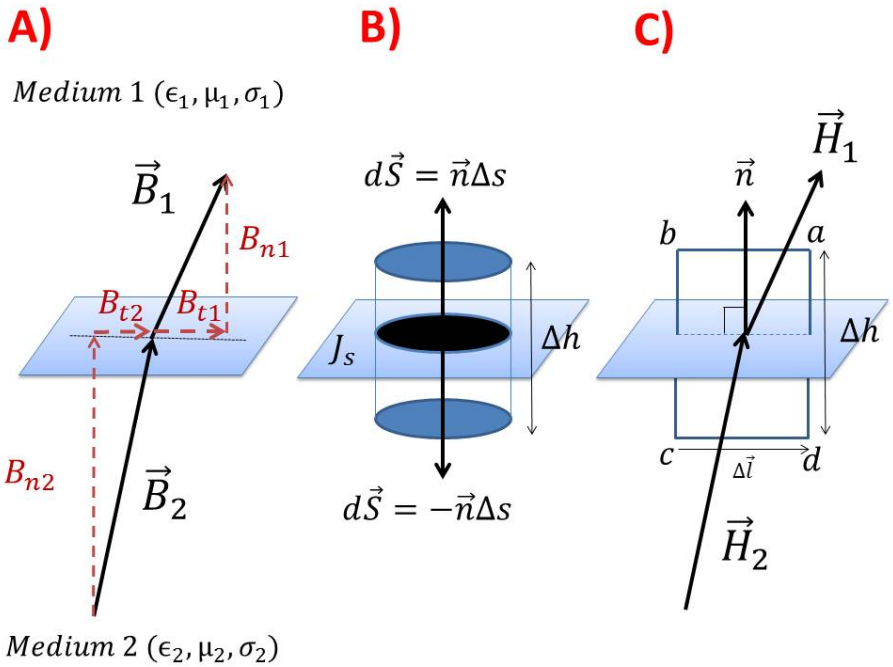

Fig. A.2: Boundary conditions for the Magnetic Field. A) Normal and tangential components of the $\vec{E}$ field on either side of the interface between two media. B) Gauss' flux law applied to a cylinder straddling the interface between two media. C)Ampere's law applied to a rectangular loop straddling the interface between the two media.

gential component of $\vec{E}$ across the boundary can be derived.

In the limit $\Delta h \to 0$, the magnetic flux threading the loop shrinks to zero, thus:

$$\oint \vec{E} \cdot d\vec{l} = \int_a^b \vec{E}_1 \cdot d\vec{l} + \int_c^d \vec{E}_2 \cdot d\vec{l} = 0 \tag{A.53}$$

$$\vec{E}_1 \cdot \Delta\vec{l} + \vec{E}_2 \cdot (-\Delta\vec{l}) = E_{t1}\Delta l - E_{t2}\Delta l = 0 \tag{A.54}$$

where the tangential components of $\vec{E}_1$ and $\vec{E}_2$ along the contour are E_{t1} and E_{t2}, respectively. From this, we can conclude that on either side of the boundary:

$$E_{t1} - E_{t2} = 0 \Rightarrow E_{t1} = E_{t2} \tag{A.55}$$

A.6.2 Boundary conditions for the Magnetic Field

The derivation of boundary conditions for the magnetic field, follows similar arguments to that of the electric field, but using the two remaining Maxwell equations. The normal and tangential components are again considered as illustrated in Fig.A.2A.

Normal component of $\vec{B}$

The boundary condition for the normal component of the electric field can be obtained by appying Gauss's flux law

$$\oint \vec{B} \cdot d\vec{S} = 0 \tag{A.56}$$

to a small cylinder, positioned such that the boundary sits between its 'upper' and 'lower' surfaces as shown in Fig.A.2B. If the side wall Δh is shrunk to zero, all magnetic flux enters or leaves the cylinder through the top and bottom surfaces, thus:

$$\oint \vec{B} \cdot d\vec{S} \rightarrow \vec{B}_1 \cdot \hat{n}\Delta s + \vec{B}_2 \cdot (-\hat{n})\Delta s = B_{n1}\Delta s - B_{n2}\Delta s \tag{A.57}$$

where B_{n1} and B_{n2} are the normal components of the flux density vector immediately on either side of the boundary in mediums 1 and 2. Equating to zero, one obtains:

$$B_{n1} - B_{n2} = 0 \tag{A.58}$$

.

Tangential Component of $\vec{H}$

Applying Ampere's law to a small rectangular loop of sides Δl and Δh and vertex a, b, c, d positioned across the boundary and in the plane of $\vec{H}_1$ and $\vec{H}_2$ (see Fig.A.2C), the tangential component of $\vec{H}$ across the boundary can be derived.

In the limit $\Delta h \rightarrow 0$, the magnetic flux threading the loop shrinks to zero. Thus, the left hand side of Ampere's law becomes:

$$\oint \vec{H} \cdot d\vec{l} = \int_a^b \vec{H}_1 \cdot d\vec{l} + \int_c^d \vec{H}_2 \cdot d\vec{l} \Rightarrow \tag{A.59}$$

$$\vec{H}_1 \cdot \Delta\vec{l} + \vec{H}_2 \cdot (-\Delta\vec{l}) \tag{A.60}$$

On the right hand side, the displacement current term $I_d = \int_S \frac{\partial \vec{D}}{\partial t} \cdot d\vec{S}$ tends towards zero. For physical media, the conductivity σ is finite, and $\vec{J}$ is also finite. Thus within the loop $\int \vec{J} \cdot d\vec{S}$ also tends to zero and

$$\vec{H}_1 \cdot \Delta\vec{l} + \vec{H}_2 \cdot (-\Delta\vec{l}) = 0 \tag{A.61}$$

$$H_{t1} - H_{t2} = 0. \tag{A.62}$$

For the special case of an idealised perfect conductor, $\sigma \to \infty$. Then, a surface current density of magnitude J_s may exist (i.e. current flowing perpendicularly to the rectangular loop within a vanishingly thin layer on the surface), and $\int \vec{J} \cdot d\vec{S} \to J_s \Delta l$.
In this case, it can be concluded that the boundary condition on the tangential component of $\vec{H}$ is therefore

$$H_{t1} - H_{t2} = J_s. \tag{A.63}$$

Summary of Boundary Conditions

The boundary conditions can be summarized in vectorial form as follows:

$$\hat{n} \cdot (\vec{D}_1 - \vec{D}_2) = \rho_s \tag{A.64}$$

$$\hat{n} \times (\vec{E}_1 - \vec{E}_2) = 0 \tag{A.65}$$

$$\hat{n} \cdot (\vec{B}_1 - \vec{B}_2) = 0 \tag{A.66}$$

$$\hat{n} \times (\vec{H}_1 - \vec{H}_2) = \vec{J}_s \tag{A.67}$$

A.6.3 Particular Cases of Boundary Conditions

Dielectric-Dielectric Interface

Dielectric materials are non-conducting, i.e. $\sigma \to 0$; no currents flow, and no unbound surface charges exist unless explicitly placed there (i.e. $\rho_s = 0$). Thus:

$$D_{n1} = D_{n2}; \epsilon_1 E_{n1} = \epsilon_2 E_{n2} \tag{A.68}$$

$$E_{t1} = E_{t2} \tag{A.69}$$

$$B_{n1} = B_{n2} \tag{A.70}$$

$$H_{t1} = H_{t2}; \frac{1}{\mu_1} B_{t1} = \frac{1}{\mu_2} B_{t2} \tag{A.71}$$

Dielectric-Perfect Conductor

If medium 2 is a perfect conductor $\sigma \to \infty$; then $E_{n2} = 0$ and $E_{t2} = 0$ inside the perfect conductor. Furthermore, for AC fields, no time-varying magnetic field exists in a perfect

conductor ($\nabla \times \vec{E} = 0 = -\frac{\partial \vec{B}}{\partial t}$). Therefore:

$$D_{n1} = \rho_s \tag{A.72}$$

$$E_{t1} = E_{t2} = 0 \tag{A.73}$$

$$B_{n1} = B_{n2} = 0 \tag{A.74}$$

$$H_{t1} = J_s \tag{A.75}$$

Conductor-Conductor (steady state current)

For the case of two conductors under static field conditions ($\frac{\partial \vec{E}}{\partial t} = 0$ and $\frac{\partial \vec{B}}{\partial t} = 0$), there can be no charge build up at the interface and hence $J_{n1} = J_{n2}$. Since $J_n = \sigma E_n$:

$$\sigma_1 E_{n1} = \sigma_2 E_{n2} \tag{A.76}$$

A.7 Propagation and attenuation of electromagnetic plane waves. Skin Depth

The propagation of an electromagnetic plane wave in a particular media (ϵ_1, μ_1) is given by Eqs. A.42. By replacing the complex wavevector $|\vec{k}| = \frac{\omega}{c}\sqrt{\epsilon_1 \mu_1}$ or $|\vec{k}| = \frac{\omega}{c}\tilde{n_1} = \frac{\omega}{c}(n_1 + ik_1)$ into the equation for the electric field:

$$\vec{E}(\vec{r}) = E_0 e^{i\omega \frac{\tilde{n}}{c}\vec{u}_k \cdot \vec{r}} = E_0 e^{i\omega \frac{n_1}{c}\vec{u}_k \cdot \vec{r}} e^{-\frac{\omega \tilde{k}}{c}\vec{u}_k \cdot \vec{r}} \tag{A.77}$$

It becomes obvious (see Fig.A.3) that the real part of the complex index of refraction $\tilde{n}$ expresses a travelling wave while the imaginary part takes into account the attenuation. The first exponent of Eq. A.78 describes the the reduction of the phase velocity of the wave to c/n_1. The second exponent gives the damping of the wave. We can define a characteristic length scale d_s for the attenuation of the electromagnetic radiation as the distance over which the field dereases by the factor $1/e$. d_s is called skin depth of the material and is given by:

$$d_s = \frac{c}{\omega k_1} \tag{A.78}$$

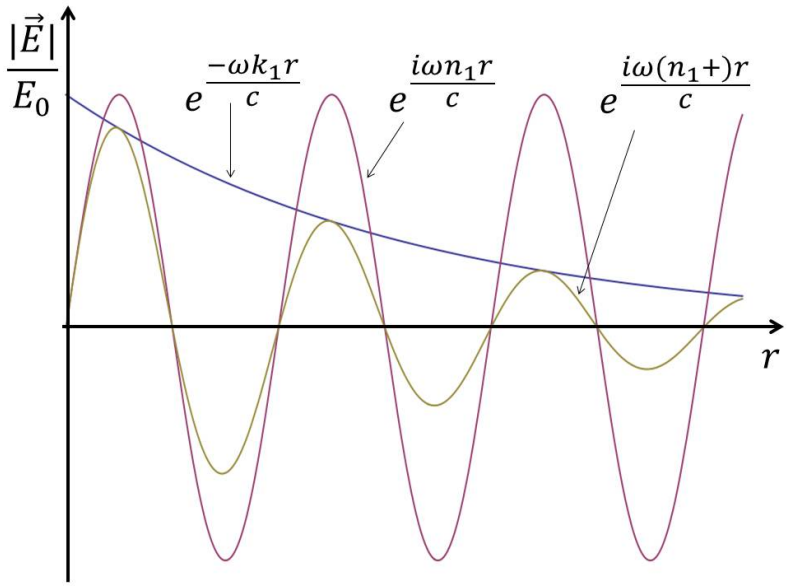

Fig. A.3: Propagation and attenuation of electromagnetic plane waves. Normalized amplitude of the electric field along the direction of propagation r.

B. SOLVING THE POISSONS' EQUATION THROUGH THE FINITE ELEMENT METHOD

The most expedient way to clarify FEM is through a simple two-dimensional example, taken from reference [26,27]. The Gauss' law for the divergence of the displacement vector $\vec{D}$ in the presence of a surface charge ρ (Eq. A.1) in linear, isotropic and homogeneous media is known as Poisson's equation and reads:

$$\nabla^2 V = \frac{\rho}{\epsilon} \tag{B.1}$$

where $\vec{E} = \nabla V$ as we are dealing with static electromagnetic fields. To solve Eq.B.1 using FEM, we take the four basic steps previously introduced in Section 3.1.6:

1. Discretizing the solution region into triangular finite elements;

2. Deriving the governing equations for a typical element;

3. Assembling all the elements in the solution region;

4. Solving the resulting system of equations by variational methods.

B.1 Finite Element Discretization

The solution region is divided into a finite number of non-overlapping elements and nodes as illustrated in Fig. B.1. We look for an approximation for the potential V_e and surface charge ρ_e within an element e and then interrelate the potential distributions in various elements such that the potential is continuous across interelement boundaries. The approximate solution for the entire region composed of N number of triangular elements is then:

$$V(x,y) \simeq \sum_{e=1}^{N} V_e(x,y) \tag{B.2}$$

$$\rho(x,y) \simeq \sum_{e=1}^{N} \rho_e(x,y) \tag{B.3}$$

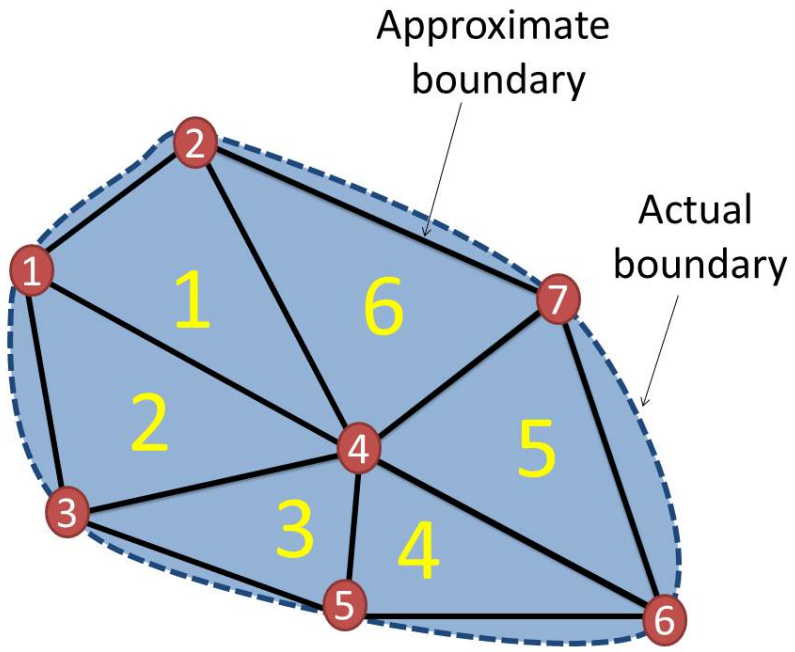

Fig. B.1: Typical finite element subdivision of an irregular domain. It consist of N non-overlapping elements and N+1 nodes.

Inside a triangular element e, V and ρ are approximated using a linear polynomial expression such as:

$$V_e(x,y) = a_V + b_V x + c_V y \tag{B.4}$$

$$\rho_e(x,y) = a_\rho + b_\rho x + c_\rho y \tag{B.5}$$

meanwhile, outside the element e, V and ρ are set to zero.

B.2 Deriving Element Govering Equations

After the solution region is devided into triangular elements, the potential distribution and the source term are approximated over each element by linear combinations of the local interpolation polynomials α_l. The governing equations for each element are:

$$V_e = \sum_{l=1}^{3} \alpha_l(x,y) V_{el} \tag{B.6}$$

$$\rho_e = \sum_{l=1}^{3} \alpha_l(x,y) \rho_{el} \tag{B.7}$$

$$\alpha_l = \frac{1}{2A}\Big[(x_m y_n - x_n y_m) + (y_m - y_n)x + (x_n - x_m)y\Big] \tag{B.8}$$

where l, m, n are permutations of the three nodes defining the triangular element, and A is the area of the element.

Note that B.4 gives the potential at any point (x, y) within the element provided that the potentials at the vertices are known. This is unlike finite difference analysis where the potential is known only at the grid points. The values of ρ_{el} are known since $\rho(x, y)$ is prescribed, while the values of V_{el} are to be determined.

Instead of directly solving Eqs.B.1 with the corresponding Dirichlet or Neumann boundary conditions, FEM works with an equivalent problem, namely an energy functional, whose minimum corresponds to the solution of the partial differential equation [25]. The equivalence between the PDE and the variational functional lies at the heart of the variational FEM approach. For Eq.B.1, a suitable functional is:

$$W(V) = \frac{1}{2}\int_S \left[\epsilon|\nabla V|^2 - 2\rho V\right] dS \tag{B.9}$$

The proof that the extremal point of this variational functional corresponds to the solution of the Poisson equation can be found in [25] and is beyond the scope of this Appendix. Note that this functional corresponds to the electromagnetic energy. The first term under the integral sign $\frac{1}{2}\vec{D}\vec{E} = \frac{1}{2}\epsilon|\nabla V|^2$ is the energy density in the electrostatic system, while the second term $2\rho V dS$ is the work done in moving the charge $2\rho dS$ to its locaton at potential V.

From these equations, we can write the energy associated with each element as:

$$W_e(V) = \frac{1}{2}\int_S \left[\epsilon|\nabla V_e|^2 - 2\rho_e V_e\right] dS \tag{B.10}$$

writing

$$\nabla V_e = \sum_{l=1}^{3} V_{el}\nabla\alpha_i \tag{B.11}$$

$$\nabla \rho_e = \sum_{l=1}^{3} \rho_{el}\nabla\alpha_l(x, y) \tag{B.12}$$

we have

$$W_e = \frac{1}{2}\sum_{l=1}^{3}\sum_{j=1}^{3} \epsilon V_{el}\left[\int_S \nabla\alpha_l \cdot \nabla\alpha_j dS\right] V_{ej} - \sum_{l=1}^{3}\sum_{j=1}^{3} V_{el}\left[\int_S \alpha_l\alpha_j dS\right]\rho_{ej} \tag{B.13}$$

Defining the term in brackets as

$$C_{lj}^{(e)} = \int \nabla\alpha_l \cdot \nabla\alpha_j dS \tag{B.14}$$

$$T_{lj}^{(e)} = \int \alpha_l \cdot \alpha_j dS \tag{B.15}$$

Eq. B.13 can be written in a matrix form as

$$W_e = \frac{1}{2}\epsilon \left[V_e\right]^T \left[C^{(e)}\right] \left[V_e\right] - \left[V_e\right]^T \left[T^{(e)}\right] \left[\rho_e\right] \tag{B.16}$$

The matrices $\left[C^{(e)}\right]$ and $\left[T^{(e)}\right]$ are called two element coefficient matrices (the so-called'stiffness matrix' and 'mass matrix' respectively, from the structural mechanics origin). Each composing element $\left[C_{lj}^{(e)}\right]$, $\left[T_{lj}^{(e)}\right]$ describe the coupling between nodes l and j.

B.3 Connecting the Elements

Up to this stage, we have worked in isolation, considering each element on its own. The next step is to assemble all such elements in the solution region. The energy associated with the assembly of elements is

$$W = \sum_{e=1}^{N} W_e = \frac{1}{2}\epsilon \left[V\right]^T \left[C\right] \left[V\right] \left[V\right]^T \left[T\right] \left[\rho\right] \tag{B.17}$$

B.4 Solving the Resulting Equations

As stated before, we can solve Poisson's equation at a free node k minimizing the energy by applying:

$$\frac{\partial W}{\partial V_k} = 0, k = 1, 2, ..., n \tag{B.18}$$

where the mesh has a total number of nodes n. Not all of the nodes's potential are unknown. Some of them are set according to the boundary conditions of the problem. To find the potential at a free node k, start with the known potentials and set the remaining unknown node potentials to zero. Then, iteratively solve Eq. B.19 for the free unknown potentials until the change between iterations is smaller than a prescribed error tolerance.

$$V_k = -\frac{1}{C_{kk}} \sum_{l=1, l\neq k}^{n} V_l C_{kl} + \frac{1}{\epsilon C_{kk}} \sum_{l=1,}^{n} T_{kl}\rho_l \tag{B.19}$$

B.5 Boundary Conditions in FEM

Boundary conditions must be specified for FEM as part of solving PDEs. For a second order PDE as in this case, the following boundary conditions are necessary and suficient for a unique solution:

- A value of a V is specified (Dirichlet boundary condition). If $V = 0$, this is called homogeneous boundary condition. In FEM these conditions are essential and must be explicitly set.
- A value of the normal derivative $\frac{\partial V}{\partial n}$ is specified (Neumann boundary condition). If $\frac{\partial V}{\partial n} = 0$, this is called homogeneous Neumann boundary condition. In FEM these conditions are natural and are implicitly enforced.
- A linear combination of the above is specified (Cauchy boundary condition)

Note that these may be mixed in any ratio along the boundary, however, they must be disjoint, i.e. more than one may not be simultaneously specified along the same part of the boundary. Furthermore, an unset boundary condition is not an error in the FEM process: it is a natural homogeneous Nuemann boundary condition.
FEM provides simple handling of inhomogeneous regions (material interfaces). The boundary conditions on the electrostatic potential at the interface between two regions with dielectric constants ϵ_1 and ϵ_2 are:

$$V_1 = V_2 \tag{B.20}$$

$$\epsilon_{r1}\frac{\partial V_1}{\partial n} = \epsilon_{r2}\frac{\partial V_2}{\partial n} \tag{B.21}$$

They come from the requirement of tangential electric field continuity and normal electric flux contituity, respectively (Apendix A).

B.5.1 Treatment of open boundaries in FEM

One of the challenges in finite element modeling is how to treat open boundaries in radiation problems, i.e. how to terminate the mesh. In many scattering and antenna-modeling problems, you cannot describe the incident radiation as a plane wave with a well-known direction of propagation. In such situations, consider using perfectly matched layers (PMLs). A PML is strictly speaking not a boundary condition but an additional domain that absorbs the incident radiation of all polarizations, at all frequencies and all angles of incidence without producing reflections [25]. It is not particularly sensitive to the shape of the wave fronts. The PML formulation can be deduced from Maxwells equations by introducing a complex-valued coordinate transformation under the additional requirement that the wave impedance should remain unaffected as in Ref. [132].

Finally, in the particular case that the material to be simulated is composed of individual components arranged in a periodic fashion (as is the case of metamaterial), periodic boundary conditions (PBC) set up a periodicity between the selected boundaries. In more detail, PBC are a set of boundary conditions that are used to simulate a large system by modelling a small part that is far from its edge. A *unit cell* or *simulation box* of a geometry suitable for perfect three-dimensional tiling is defined, and when radiation passes through one face of the unit cell, it reappears on the opposite face with the same characteristics. The simulation is of an infinite perfect tiling of the system. In topological terms, the space can be thought of as being mapped onto a torus. The tiled copies of the unit cell are called images, of which there are infinitely many. During the simulation, only the properties of the unit cell need be recorded and propagated. For more details about the practical implementation of PML and PBC conditions in COMSOL, the reader is referred to the corresponding manual of the program [133].

C. ENGINEERING THE NANO-HELIX MORPHOLOGY THROUGH GLAD

C.1 GLAD growing parameters and nano-helix morphology

As introduced in section **Section 2**, GLAD film structures predominantly grow due to geometrical shadowing, therefore, Zone 1 and T of the Structured Zone Model are the preferred zones for this deposition technique. Then, depending on the thermal and crystalline properties of the evaporant, the produced films are amorphous, polycrystalline or single crystalline [95]. In addition, the film crystallinity considerably affects the shape of the growth nano-structure. In particular, single-crystal nano-helices cannot be created through GLAD.

The *GLAD* growing parameters (**Section 5.1.2**): angle γ, rotational speed Ω and deposition rate r, can be related with the main parameters of the helical morphology: pitch p and diameter D. In this section, a set of simple equations which relate both sets of parameters are derived. The equations are a positive proof of the controlability offered by the GLAD technique when designing nano-structures. The analysis assumes to be under conditions of geometrical shadowing and low surface atom mobility (zone 1 of the Structure Zone Model).

The helical growth angle β (figure A1) can be linked to the incident flux angle γ through the relation [12]:

$$\beta = \gamma - \arcsin\left(\frac{1-\cos(\gamma)}{2}\right) \tag{C.1}$$

Eq.C.1 states that the columns are oriented at an angle closer to the substrate normal than the vapour flux. Several explanations have been found in literature [97], being the self-shadowing or the conservation of parallel momentum. By construction, in the standard *GLAD* method, the total angle ϕ turned at an specific time t is:

$$\phi(t) = \Omega \cdot t \tag{C.2}$$

The flux arriving to the substrate can be separated into two components: parallel ($F_{\parallel}$) and perpendicular ($F_{\perp}$) to the substrate (see Fig. C.1). These components are related with the depostion rate r and the tilted angle γ:

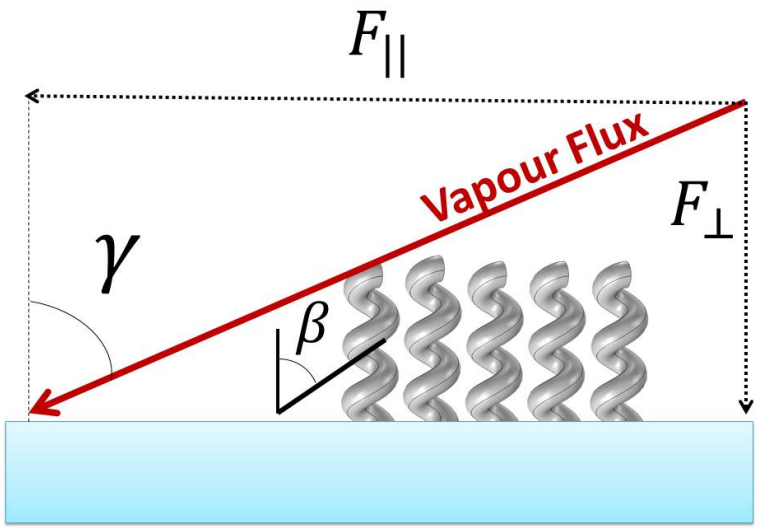

Fig. C.1: Flux components in an oblique PVD: parallel ($F_{\parallel}$) and perpendicular ($F_{\perp}$) to de substrate.

$$F_{\parallel} = S \cdot r \cdot \sin(\gamma) \tag{C.3}$$

$$F_{\perp} = S \cdot r \cdot \cos(\gamma) \tag{C.4}$$

where S is the sticking parameter (ratio between adsorbed adatoms and the total number of adatoms arriving within the same period of time). This parameter is close to the unity on GLAD evaporations performed within electron beam evaporators [9].

Considering the equations C.1 and C.3, the height of the helix z at any time t can be related with $F_{\perp}$ through the relation:

$$z(t) = F_{\perp} \cdot t = S \cdot r \cdot \cos(\beta) \cdot t \tag{C.5}$$

Meanwhile, the diameter of the helix D can be linked to the ratio $\frac{F_{\parallel}}{\Omega}$ as follows:

$$D = 2\frac{F_{\parallel}}{2\pi\Omega} = 2Sr\frac{\sin(\beta)}{2\pi\Omega} \tag{C.6}$$

From equations C.5 and C.6 it is easy to derive the pitch p of the helix as:

$$p = z\left(\frac{1}{\Omega}\right) \tag{C.7}$$

These equations relate the dependence of p and D on the growing conditions and reflect the experimental growth behaviour for conditions with controlled surface diffusion as it is our case.

C.2 Controlling the ad-atom mobility: selection of growth parameters

An appropiate selection of growth parameters for each evaporating material is highly desirable in *GLAD* processes in order to minimize the adatom diffusion and create high areal density of uniform nano-structures. No systematic study in literature has been reported on the *GLAD* technique in this respect and this is why we describe here a convenient way to choose these linked growth parameters: dot-array separation (δ), deposition rate (r), temperature of the film during growth (T), deposition angle (γ), rotation speed (Ω) and diffusion length (Λ).

In the first approximation, r and Ω are closely related as the pitch and diameter of the helix depend on them (see section C.1). γ mainly determines the porosity in non-dot-patterned substrates and the helical growth angle [80,134]. Having a pre-patterned substrate as it is in our case (section 5.1.3), the porosity is less dependent on this parameter and we set for every material γ to $\sim 87^\circ$ to obtain a nano-structure inclination angle of $\sim 55^\circ$ (Eq. C.1). δ closely depends on Λ and is chosen as small as possible to produce the thinnest possible wire diameter of the helix. δ will be experimentally determined for every material. Λ has to receive a special consideration: in general, Λ=$\Lambda(T,r)$ and can be calculated for any material [97, 99] via

$$\begin{aligned} \Lambda &= \sqrt{D\tau_m} \\ D &= D_0 e^{\frac{-E_h}{k_B T}} \\ D_0 &= \frac{a_0^2}{4} f \\ \tau_m &= \frac{a_0}{r} \\ E_h &= \frac{\Delta_h}{5} \end{aligned} \tag{C.8}$$

where k_B is the Boltzmann constant and the following are parameters of the incoming atoms (material): τ_m is the mobility lifetime, D_0 is the intrinsic diffusivity, E_h is the energy required for site hopping, f is the lattice vibration frequency, Δ_h is the activation energy for an atom to escape out of the structure, and a_0 is the atomic radius. In this

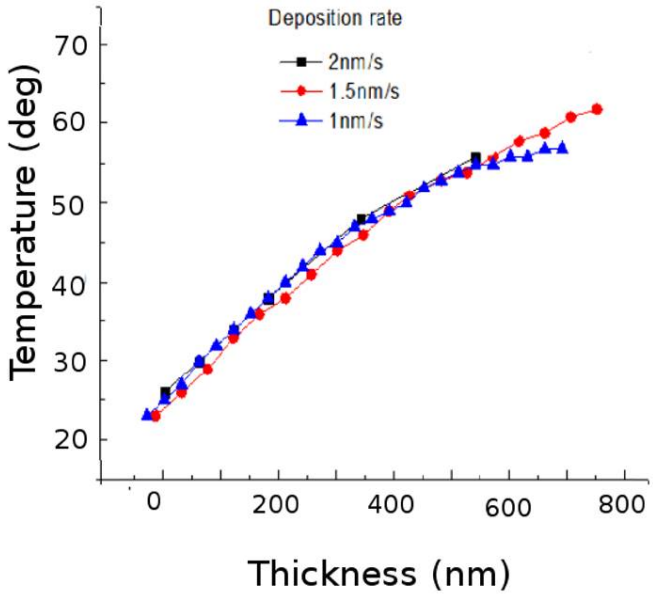

Fig. C.2: Measured temperature depending on the sample height for different deposition rates.

work, f is calculated following the Lennard-Jones estimations of a one-dimensional chain of surface atoms of mass m and spring constant K [97, 111]: $f = \sqrt{\frac{K}{m}}$
By limiting Λ according with our fabrication accuracy requirements, it is possible to have an initial idea of the range of optimum r and Ω to be used for a particular material. Once r and Ω are selected, δ is easily obtained experimentally by growing and imaging helices on dotted arrays with different separations.
Finally, in this work, T and r are considered independent parameters. This fact is confirmed by inserting a thermo-couple within the evaporator[1] during the growth at different depostion rates. The graph represented in Fig. C.2 shows that T rises equally for growing rates between 1 nm/s and 2 nm/s at least up to $\sim$ 800 nm film thickness. Therefore the consideration of independency of T and r is valid at least for the growth parameter variation within this project.

[1] Note the temperature given by the thermo-couple is not the actual temperature of the film.

D. FOURIER TRANSFORM SPECTROSCOPY

The principle of Fourier transform spectroscopy (FTS) relies on a Michelson-Morley interferometer, depicted in Fig. D.1. The radiation emitted from a light source is collected by the mirror MR1 and directed onto a 50% beam splitter BS. The two generated beams are reflected by the flat mirrors M1 and M2 and recombine on the mirror MR2, which focuses them onto a detector. Both beams produce interference at the detector due to their different optical paths.

Consider a monochromatic plane wave of wave number $|\vec{k}| = 1/\lambda$ emmited by the light source along a certain direction z. The electromagnetic field can then be written as:

$$\vec{E}(\vec{k}, z) = E_0(\vec{k}) e^{i(\omega t - 2\pi \vec{k} z)} \tag{D.1}$$

If z_1 and z_2 are the optical paths of the beams incident onto M1 and M2 respectively, the electric field in the detector is:

$$\vec{E}(\vec{k}, z_1, z_2) = F_r F_t E_0(\vec{k}) [e^{i(\omega t - 2\pi \vec{k} z_1)} + e^{i(\omega t - 2\pi \vec{k} z_2)}] \tag{D.2}$$

where F_r and F_t are the Fresnel reflection and transmission coeficients of the beamsplitter. The average radiation intensity measured by the detector per unit time and surface is given by:

$$S_r(\vec{k}, z_1, z_2) = \frac{c}{8\pi} \vec{E}(\vec{k}, z_1, z_2) \vec{E}^*(\vec{k}, z_1, z_2) \tag{D.3}$$

Inserting Eq.D.2 in Eq.D.4 and introducing the path difference $\delta = z_2 - z_1$ between the two beams, one obtains:

$$S_r(\vec{k}, \delta) = \frac{c}{4\pi} |F_r F_t|^2 E_0^2(\vec{k}) [1 + \cos(2\pi \vec{k} \delta)] \tag{D.4}$$

For the general case of a non monochromatic light source, the intensity measured by the detector is obatined summing over all $\vec{k}$:

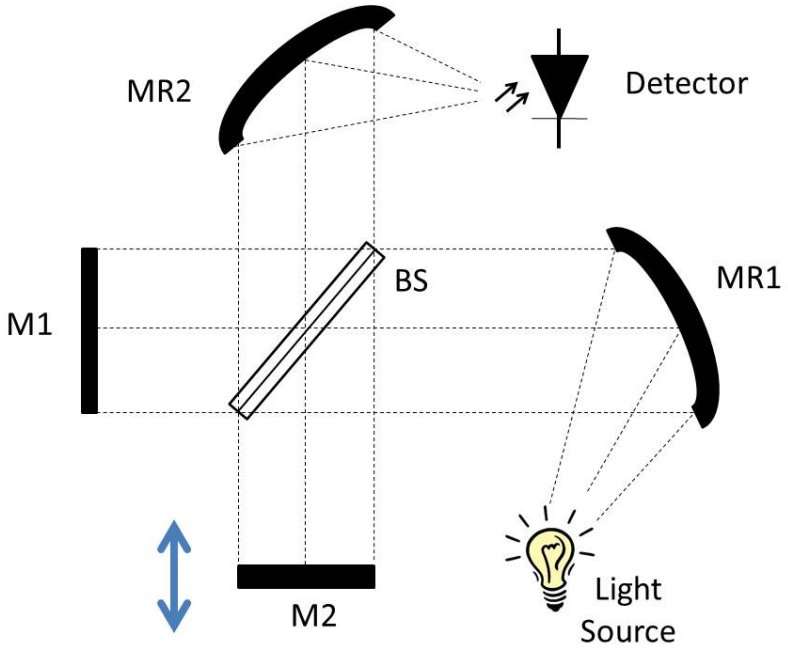

Fig. D.1: Michelson-Morley Interferometer. The two generated beams reflected by the flat mirrors M1 and M2 recombine on the mirror MR2, which focuses them onto a detector.

$$I = \int_0^\infty S_r(\vec{k},\delta)d\vec{k} = \frac{c}{4\pi}|F_r F_t|^2 \int_0^\infty E_0^2(\vec{k})[1+\cos(2\pi\vec{k}\delta)]d\vec{k} \tag{D.5}$$

I is composed of a constant and a variable part on δ. The interferogram F is defined as the variable part of the light intensity:

$$F = \frac{c}{4\pi}|F_r F_t|^2 \int_0^\infty E_0^2(\vec{k})\cos(2\pi\vec{k}\delta)d\vec{k} = 2|F_r F_t|^2 \int_0^\infty S(\vec{k})\cos(2\pi\vec{k}\delta)d\vec{k} \tag{D.6}$$

where the intensity of the source has been taken into account $S(\vec{k}) = cE_0^2(\vec{k})/(8\pi)$
Since $\vec{E}(\vec{k})$ is hermitian, $S(\vec{k}) = S(-\vec{k})$, therefore Eq.D.7 can be re-written in complex notation:

$$F(\delta) \propto \int_{-\infty}^{+\infty} S(\vec{k})e^{i(2\pi\vec{k}\delta)}d\vec{k} \tag{D.7}$$

The latter relation states that the interferogram is the Fourier transform of the spectrum $S(\vec{k})$ emitted by the light source. Furthermore, the source spectrum is the inverse Fourier transform of the interferogram:

$$S(\vec{k}) \propto \int_{-\infty}^{+\infty} F(\delta) e^{-i(2\pi\vec{k}\delta)} d\delta \tag{D.8}$$

Through Eq. D.8, the measurement of the interferogram provide information on the spectral response of the sample. Experimentally, the interferogram can be obtained by scanning the position of the mirror M2 and recording the light intensity as a function of δ.

FTS offers two major advantages over dispersive spectroscopy:

- the spectral resolution is inversely proportional to the maximum difference of the optical paths. It is thus improved by just increasing the scanning rate of the moving mirror, since it does not depend on the dimension of the spectrometer slit;
- the whole spectrum is acquired within a single scan of the moving mirror.

E. TECHNICALITIES OF THE SERS EXPERIMENT

E.1 Graphene fabrication, transfer and characterization on top of the metallic nano-helices

In this study, monolayer graphene is grown on *Cu* foil using the chemical vapour deposition technique (CVD) [124]. A thin layer of polymethyl methacrylate (*PMMA*) is spun on top of the graphene prior to the *Cu* etching. Graphene supported with PMMA is transferred on the helical nano-arrays. Then, the *PMMA* is dissolved in acetone, samples are rinsed in isopropanol and dried with N_2 gas. The roughness of graphene deposited on nano-helices is examined through atomic force microscopy (AFM). The measured graphene roughness is smaller than 20 nm in all the samples under study. This small value of roughness ensures the condition $N_{SERS} \approx N_{REF}$ for this monolayer material. This value of 20 nm is used the numerical theoretical simulations to calculate the *near-field* enhancement factor *EF* (see below).

The possible amount of disorder introduced when depositing graphene on top of the nanohelices is evaluated through the changes in the Raman D mode of graphene [107] which appears around $\sim$1300 cm^{-1}. Fig. E.1 shows the D and G Raman peaks of the samples under study. For all the used helical substrates the D band is much smaller than the G band which indicates a small amount of residual disorder present or introduced in graphene during its CVD growth or transfer on to the nano-structured substrates. Note the appearance of two small peaks at $\sim$1450 cm^{-1} and $\sim$1530 cm^{-1} in the *Cu* and specially *Ag* nano-helix substrates. They can be attributed to *SERS* enhancement of small residues from substances associated with the graphene production and transfer such as PMMA.

E.2 SERS EF measurements and estimations

Apart from unavoidable residual structural differences within the SERS helical substrates, the way the measurements are taken and evaluated could lead to misestimating the *SERS* Enhancement Factor. We report here the precautions we undertook when measuring the Raman *SERS* spectra of graphene and pMA, respectively. Graphene samples present local inhomogeneities in their charge density which depend on the growing procedure, the interaction with the substrate and enviromental conditions [125, 126]. These charge fluctuations modify locally the graphene Raman spectra, particularly the ratio between the 2D and G peak intensity I(2D)/I(G) usually varies from 1 to 2 [126]. This effects

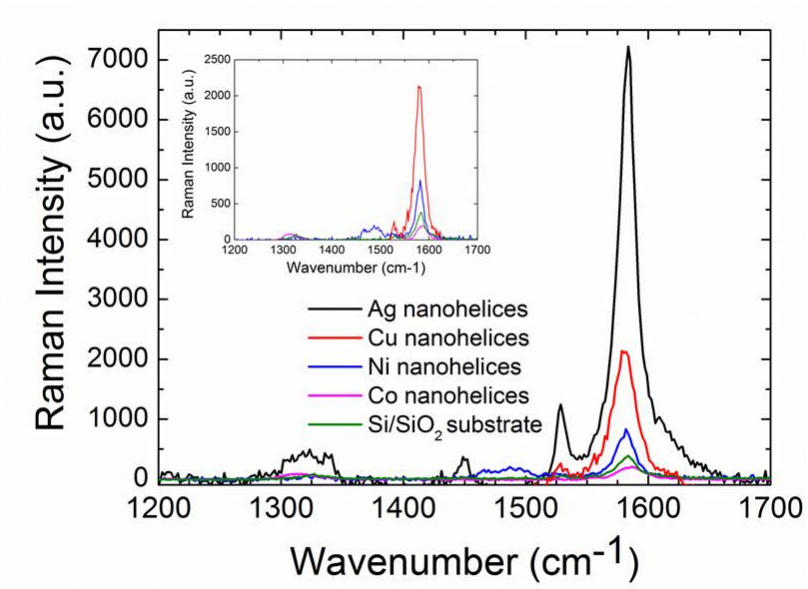

Fig. E.1: SERS of graphene on metallic nano-helices in the range 1200 cm^{-1} to 1700 cm^{-1}, thus showing any possible D peak and the G peak of graphene. The small I(D)/I(G) ratio , shows no signifficant deffects introduced when depositing graphene on metallic nano-helices. The inset does not show the *Ag* spectrum for a better visualization of the rest of the effect in the other metals.

are unlikely to affect the experimental observations here presented since enhancements up to 40 times are observed in the measurements. However, to precisely calculate the SERS enhancement from the Raman measurements (Eq.5.2) I take this into account and compare I_{SERS} and I_{REF} from areas with the same I(2D)/I(G) ratio, thus, ensuring similar doping levels of the graphene flakes measured on the nano-helices and the reference substrate. Furthermore, I selected graphene flakes with almost no structural disorder (D peak is relatively small in comparison with the G peak as previously stated). In addition, given a certain doping level, a residual mechanical stress could cause shifts of the G peak position (Pos(G)) [127]. To minimize this possible effect, I selected graphene flakes on the each metallic helices with the same Pos(G) within our experimental accuracy ($2cm^{-1}$).

In the case of pMA, the estimation of N_{REF} and N_{SERS} is the main source of possible error. Although pMA widely used in SERS [30,135], sometimes the method itself can lead to incorrect EF estimations. Fig. E.2 shows the Raman spectra of a pMA monolayer on *Ag* nano-helices and of bulk pMA. It is clearly shown how the Raman peaks are shifted and the relative intensity between some of them is different in both samples. Rather than being due to the actual nano-helices, these effects could be due to, first, the solution of pMA in water (concentration 10^{-5} M) or second, the posterior chemisorption process [135]

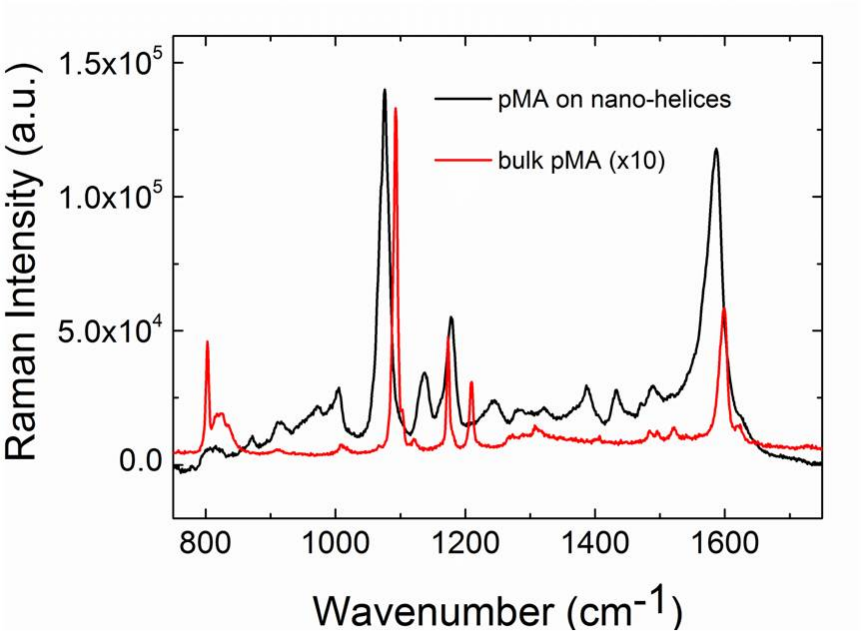

Fig. E.2: SERS of pMA molecule in bulk and on *Ag* nano-helices.

which occur in between these molecules and the silver surface of the nanohelices. To avoid these experimental sources of error, the reference substrates should pass through the same processing steps. For our purpose, pMA absorbed on evaporated smooth silver films seems a more convenient reference substrate rather than bulk pMA. Nevertheless, for comparison purposes we calculate the EF using bulk pMA as well:

Reference substrate: Ag film

$$N_{REF} = A_{LASER}\sigma \tag{E.1}$$

where A_{LASER} is the area of the focal spot of the laser and $\sigma \sim 5\text{nm}^{-2}$ is the surface density of absorbed pMA molecules [135].

$$N_{SERS} = \delta_{HELIX} A_{LASER} A_N \sigma \tag{E.2}$$

where δ_{HELIX} is the density of nano-helices and $A_N \sim \pi D^2/4$ is the nano-helix footprint area. Using this reference substrate, the ratio $N_{REF}/N_{SERS} = 1/(\delta_{HELIX} A_N)$ is independent of A_{LASER} and σ. I_{SERS} is obtained through the integration of the Raman pMA peak at ~ 1590 cm^{-1} and I_{REF} is taken to be equal to the spectral noise as within our set-up we did not appreciate any Raman peak of the pMA molecule (Fig. 6.37 in **Section**

6.2.4). The estimated EF (Eq.5.2) is then $\sim 6 \times 10^6$ which is a lower bound restricted to our experimental set-up. Note that, in addition, this method provides only the EF of the helical nano-structures, not accounting for any possible chemical enhancement [135].

Reference substrate: Bulk pMA

$$N_{REF} = \varrho \xi A_{LASER} \tag{E.3}$$

where ξ is the focal depth of the laser spot and ϱ 5.1×10^{21} m^{-3} is the density of pMA molecules. Note that in this case there is a need to further estimate variables such as A_{LASER} and ξ. I_{REF} is obtained through the integration of the Raman pMA peak of the bulk material at ~ 1590 cm^{-1} , giving the overall result an EF $\sim 0.8 \times 10^6$.
Although both methods provide an EF $\sim 10^6$, the first estimate is a more reliable EF lower bound as it reflects the EF of the actual nano-helices and does not need extra estimates. Finally, for both SERS probing molecules, graphene and pMA, the homogeneity and reproducibility of the spectra was checked by measuring 16 different spectra across the entire surface of the samples (100μm $\times$ 1mm). All the measured spectra fall within an intensity difference of 25% which is a good proof of the homogeneity of the helical substrate and the uniform deposition or cover of the nano-helices by graphene or pMA monolayers, respectively.

F. REFLECTANCE CALCULATION FOR ARRAYS OF NI NANO-HELICES

In this Appendix, the application of the Rayleigh-Debye and Maxwell-Garnett formalism is firstly assessed for our samples. Then the reflectance is calculated as the summation of both contributions.

F.1 Rayleigh-Debye scattering

The so-called Rayleigh-Debye scattering (see **Section 3.1.4**) was initialy formulated assuming two conditions which limit the application of the model :

- The refractive index relative to the surrounding medium $m = \frac{n_1}{n_2}$ is close to 1: $|m-1| << 1$. This condition results in a small reflection of the incident wave at the interface.

- Small change of phase and amplitude of an incident wave: $2ka|m-1| << 1$, where a represents any feature size of the particles.

Despite these restricting conditions, it has been recently demonstrated that the theory's applicability can be considerably extended. In particular, if the dimensionless quantity $x_p = \frac{\pi}{\lambda}a$ is smaller than 0.4, the Rayleigh-Debye theory yield predictions within 30% of error for $|m-1| \sim 2$ or more [31]. In the *Ni* nano-helix samples, at normal incidence, a is given by the diameter of the helix D and the condition $x_p < 0.4$ is fulfilled in samples S3 and S4 when the incident wavelength is larger than 700 nm. The model will be less accurate for the samples S1 and S2 where $x_p \sim 0.7$ and 0.5 at 700 nm, respectively. When increasing the incident angle θ, a will be dependent on θ as $a \sim h\sin\theta + D\cos\theta$, where h is the height of the nano-helix. Since $h > D$, for our samples we expect our model to match less well with the experimental data when increasing the incident angle [136]. Taking the *Ni* optical constants from [137], I have confirmed that the Rayleigh-Debye method is applicable in the samples S3 and S4 for incident wavelengths in the range 650 nm to 2000 nm and for $\theta < 30°$. The upper wavelength limit of 2000 nm comes from the fact that at larger wavelengths $|m-1|$ considerably increases for Ni [137]. In the present case, the range from 650 nm to 2000 nm is sufficient to determine the effective medium threshold and to demonstrate that the changes in the electromagnetic response of the nano-helices depend on the helical structural parameters and dimensions. Sample

S1 is modeled using this method as well, however, it provides less accurate results when compared with the experimental data.
Within the Rayleigh-Debye formalism, the scattering from a sample in the case of unpolarized light is proportional to [17]:

$$S_{RD} = S_2 S_2^* + S_1 S_1^* \tag{F.1}$$

where S_1 and S_2 are described in Eqs3.30.

F.2 Maxwell-Garnett formalism

The reflection of a plane wave incident at an angle θ to a reciprocal, chiral and isotropic medium is calculated as [138].

$$R_{MG} = R_{11}R_{11}^* + 2R_{12}R_{12}^* + R_{22}R_{22}^* \tag{F.2}$$

The coefficients R_{ij} are given by:

$$R_{11} = \frac{\cos(\theta)(1-g^2)(\cos(\theta_1)+\cos(\theta_2)+2g(\cos(\theta)\cos(\theta)-\cos(\theta_1)\cos(\theta_2))}{\cos(\theta)(1-g^2)(\cos(\theta_1)+\cos(\theta_2)+2g(\cos(\theta)\cos(\theta)+\cos(\theta_1)\cos(\theta_2))} \tag{F.3}$$

$$R_{12} = \frac{-2ig\cos(\theta)(\cos(\theta_1)-\cos(\theta_2)}{\cos(\theta)(1-g^2)(\cos(\theta_1)+\cos(\theta_2)+2g(\cos(\theta)\cos(\theta)+\cos(\theta_1)\cos(\theta_2))} \tag{F.4}$$

$$R_{22} = \frac{\cos(\theta)(1-g^2)(\cos(\theta_1)+\cos(\theta_2)-2g(\cos(\theta)\cos(\theta)-\cos(\theta_1)\cos(\theta_2))}{\cos(\theta)(1-g^2)(\cos(\theta_1)+\cos(\theta_2)+2g(\cos(\theta)\cos(\theta)+\cos(\theta_1)\cos(\theta_2))} \tag{F.5}$$

where $g = \sqrt{\frac{\mu_0}{\epsilon_0}\gamma^2 + \frac{\mu_0\epsilon}{\epsilon_0\mu}}$. The angles of the transmitted waves θ_1 and θ_2 are given by:

$$\theta_1 = sin^{-1}\left(\frac{k\sin\theta}{\omega\mu\gamma + \sqrt{\omega^2\mu^2\gamma^2+\omega^2\mu\epsilon}}\right) \tag{F.6}$$

$$\theta_2 = sin^{-1}\left(\frac{k\sin\theta}{-\omega\mu\gamma + \sqrt{\omega^2\mu^2\gamma^2+\omega^2\mu\epsilon}}\right) \tag{F.7}$$

For Eqs F.3-F.6, $\omega = k/\sqrt{\mu\epsilon}$, μ, ϵ and γ are the effective-medium parameters (permeability, permittivity and chirality parameter) of the chiral medium and ϵ_0, μ_0 are the permittivity and permeability of the vacuum. Note that although our nano-helix forests are uniaxial chiral media, we still can use the isotropic chiral media approximation for normal incidence: when the incident wave is propagating in the same direction as the optical axis, the waves see the medium as isotropic [139]. Thus, the effective-medium model will decrease in accuracy when increasing the incident angle θ. I calculated the

effective-medium parameters through the chiral Maxwell-Garnett equations showed in Section 3.68 [44].
Note that the effective medium parameters from references [44] $(\epsilon_H, \mu_H, \xi_H)$ and [138] (ϵ, μ, γ) come from a different way of writing the constitutive relations of the medium; their equivalence being:

$$\epsilon_H = \epsilon + \mu\gamma^2 \tag{F.8}$$

$$\mu_H = \mu \tag{F.9}$$

$$\xi_H = -\mu\gamma \tag{F.10}$$

F.3 Overall Reflectance Calculation

The total reflectance is given by the summation of Eq.F.1 and Eq. F.2:

$$R_{tot} = \mathcal{A}S_{RD}(\theta = \phi) + \mathcal{B}R_{MG} \tag{F.11}$$

$\mathcal{A}$ can be determined at a wavelength of 800 nm where the Maxwell-Garnett contribution is negligible, $R_{MG} = 0$, therefore the experimental reflectance at that wavelength R_{exp}(800 nm) = $\mathcal{A}S_{RG}$(800 nm). $\mathcal{B}$ is extracted at a wavelength of 5000 nm where the Rayleigh-Debye contribution is negligible, $S_{RG} = 0$, therefore R_{exp}(5000 nm) = $\mathcal{B}R_{MG}$(5000 nm).

BIBLIOGRAPHY

[1] N. C. et al, "Helices," *PNAS, vol 103, 9398*, 2005.

[2] A. P. V.Y. Prinz, V.A. Seleznev and A. Kopylov, "3d heterostructures and systems for novel mems/nems," *Sci. Technol. Adv. Mater., vol 10, 034502*, 2009.

[3] S. Kennedy and M. Brett, "Fabrication of tetragonal square spiral photonic crystals," *Nano Lett. vol 2, no 1, 59*, 2002.

[4] A. K. M. B. M.A. Summers, K. Tabunshcyk, "Fabrication of 2d-3d photonic crystal heterostructures by glacing angle deposition," *Photon. and Nanostructures, vol 7, 76*, 2009.

[5] M. R. M. D. K. V. S. G. v. F. S. L. J.K. Gansel, M. Thiel and M. Wegener, "Gold helix photonic metamaterial as broadband circular polarizer," *Science, vol 325, 1513*, 2009.

[6] C. Balanis, *Antenna Theory - Analysis and Design.* London: Wiley & Sons, 2005.

[7] J. F. G.L.J.A. Rikken and P. Wyder, "Electrical magnetochiral anisotropy," *Phys. Rev. Lett, vol 87, 23, 236602*, 2001.

[8] G. Wagniere and G. Rikken, "Chirality and magnetism: Free electron on an infinite helix, ncd, mcd and magnetochiral dichroism.," *Chem.Phys.Lett. 481, 166-168*, 2009.

[9] A. Lakhtaria and R. Messier, *Sculptured Thin Films: Nanoengineered Morphology and Optics.* Washington: SPIE, 2005.

[10] P. Martin, *Handbook of Deposition Technologies for Films and Coatings.* Oxford, United Kingdom: Elsevier, 2005.

[11] S. Mukherjee and D. Gall, "Structure zone model for extreme shadowing conditions," *Thin Solid Films, vol.527, 158*, 2009.

[12] T. R.N. Tait and M. Brett, "Modelling and characterization of columnar growth in evaporated films," *Thin solid films, vol.226, 196*, 1993.

[13] D. H. B. Z. R. Liu, T. J. Cui and D. R. Smith, "Description and explanation of electromagnetic behaviors in artificial metamaterials based on effective medium theory," *Phys. Rev. E 76, 026606*, 2007.

[14] D. S. T. Driscoll and D. Basov, "Spectroscopic investigation of metamaterials across the effectivemedium threshold," *Metamaterials 4, 175*, 2010.

[15] J. H. M.I. Mishchenko and L. Travis, *Light Scattering by Nonspherical Particles.* New York, United States: Academic Press, 2000.

[16] A. P. B. G. R. Abdeddaim, G. Guida and J. Rivory, "Negative permittivity and permeability of gold square nanospirals," *Appl. Phys. Lett., vol 94, 081907*, 2009.

[17] C. Bohren and D. Huffman, *Absorption and Light scattering by small particles.* New York: John Wiley & Sons, 1983.

[18] L. Novotny and B. Hercht, *Principles of Nano-Optics.* Cambridge: Cambridge University Press, 2006.

[19] L. Novotny, "Effective wavelength scaling for optical antennas," *Phys.Rev.Lett vol. 98, 266802*, 2007.

[20] B. P.Bjaradwaj and L. Novotny, "Optical antennas," *Adv. Optics and Photon., vol.1, 438*, 2009.

[21] H. van de Hulst, *Light scattering by small particles.* New York: Cover Publications, Inc, 1981.

[22] R. Schiffer and K. O. Thielheim, "Light scattering by dielectric needles and disks," *J. Appl. Phys. 50, 2476*, 1979.

[23] R. H. L. D. M. LeVine, R. Meneghini and S. S. Seker, "Scattering from arbitrarily oriented dielectric disks in the physical optics regime," *J. Opt. Soc. Am. 73, 1255*, 1983.

[24] B.T.Draine and P. Flatau, "Discrete-dipole approximation for scattering calculations," *J.Opt. Soc. Am. A 11, 1491*, 1994.

[25] D. Davidson, *Computational Electromagnetics for RF and microwave engineering.* Cambridge, U.K.: Cambridge, 2005.

[26] M. Sadiku, "A simple introduction to finite element analysis of electromagnetic problems," *IEEE Trans. Edu. 32, 85*, 1989.

[27] A. M. M.N.O. Sadiku and L. Agba, "A further introduction to finite element analysis of electromagnetic problems," *IEEE Trans. Edu. 34, 332*, 1991.

[28] A. C. J. L. Volakis and L. C. Kempel, "Review of the finite-element method for three-dimensional electromagnetic scattering," *J. Opt. Soc. Am. A 11, 1422*, 1994.

[29] M. S. J. C. F. H. A. G.-E. F. C. F. G. L. A. L. H. J. A. P. Alonso-González, P. Albella and R. eenbrand, "Resolving the electromagnetic mechanism of surface-enhanced light scattering at single hot spots," *Nat. Comm. 3, 684*, 2012.

[30] A. G. S. R. J. L. G. E. Z. Z. N.A. Hatab, C.H. Hsueh and B. Gu, "Free-standing optical gold bowtie nanoantenna with variable gap size for enhanced raman spectroscopy," *NanoLett. 10, 4952*, 2010.

[31] U. K. T.L. Farias and M. Carvalho, "Range of validity of the rayleighdebyegans theory for optics of fractal aggregates," *J.Appl. Opctics 35, 6560*, 1996.

[32] A. Patitsas, "Scattering from a helical coil of circular cross section in the rayleigh-debye theory," *Can. J. Phys 58, 1357*, 1980.

[33] J. A. Stratton and L. J. Chu, "Diffraction theory of electromagnetic waves," *Phys. Rev. 56, 99*, 1939.

[34] C. Raman, "A new radiation," *Indian J. Phys. 2: 387*, 1928.

[35] A. Smekal, "Zur quantentheorie der dispersion," *Die Naturwissenschaften, 11, 43, 873*, 1923.

[36] D. Harris and M. Bertolucci, *Symmetry and Spectroscopy: An Introduction to Vibrational and Electronic Spectroscopy.* New York: Dover Publications, 1989.

[37] M. O. et al., "Charge transfer resonance raman process in surface-enhanced raman scattering from p-aminothiophenol adsorbed on silver: Herzberg-teller contribution," *J. Phys. Chem., 98, 12702*, 1994.

[38] W. Weiglhofer and A. Lakhtakia, *Introduction to Complex Mediums for Optics and Electromagnetics.* Washington, United States: SPIE, 2003.

[39] T. Mackay and A. Lakhtakia, *Electromagnetic Anisotropy and Bianisotropy.* New Jersey, United States: World Scientific, 2009.

[40] F. Capolino, *Theory and Phenomena of Metamaterials.* London, UK: CRC Press, 2009.

[41] C. Simovski, "On the electromagnetic characterization and homogenization of nanostructured metamaterials," *J. Opt. 13, 013001*, 2011.

[42] D. Schmidt and J. Pendry, "Homogeneization of metamaterials by field averaging," *J. Opt. Soc. Am. B, 23, 3, 391*, 2006.

[43] S. T. A. Serdyukov, I. Semchenko and A. Shivlola, *Electromagnetics of Bi-anisotropic Materials*. France: Gordon and Breach, 2001.

[44] C. Brewitt-Taylor, "Modeling of helix-loaded chiral radar-absorbing layers," *PIER, 9, 289*, 1923.

[45] C. R. S. T. G. K. S.A. Tretyakov, F. Mariotte and J. Heliot, "Analytical antenna model for chiral scatterers: Comparison with numerical and experimental data," *IEEE Trans. on Antenas and Propagation, 44, 7, 1006*, 1996.

[46] G. Grandi and M. Kazimierczuk, "Stray capacitances of single-layered solenoid air-core inductros," *IEEE Trans. Indust. Appl. 35, 5, 1162*, 1999.

[47] M. Dressel and G. Gruner, *Electrodynamics of Solids*. Cambridge, United Kingdom: Cambridge, 2002.

[48] J. P. et al., "Theory of surface plasmons and surface-plasmon polaritons," *Rep.Prog.Phys, 70, 1*, 2007.

[49] T. E. J.M. Luther, P.K. Jain and A. Alivisatos, "Localized surface plasmon resonances arising from free carriers in doped quantum dots," *Nat. Mat. 10, 361*, 2011.

[50] G. A. W. B. A. M. M. W. L. Z. Z. Z. M. T. G. D. M. F. A. C.-N. C. L. F. K. Z. Fei, A.S. Rodin and D. Basov, "Gate-tuning of graphene plasmons revealed by infrared nano-imaging," *Nature 487, 82*, 2012.

[51] H. Ehrenreich and H. Philipp, "Optical properties of ag and cu," *Phys. Rev. 128, 4, 1622*, 1962.

[52] H. P. H. Ehrenreich and D. Olechna, "Optical properties and fermi surface of nickel," *Phys. Rev. 131, 6, 2469*, 1963.

[53] L. M. E.A. Ganshina, G.S. Krinchik and A. Tablin, "Anisotropy of the magneto-optical properties of cobalt single crystals," *Sov. Phys. JETP, 51, 369*, 1980.

[54] B. K. I. Zorić, M. Zäch and C. Langhammer, "Gold, platinum and aluminum nanodisk plasmons: Material independence, subradiande and damping," *ACS Nano, 4, 2535*, 2011.

[55] J. C. et al., "Plasmonic nickel nanoantennas," *Small 7, 2341*, 2011.

[56] J. B. M. B. M. D. S. B. A. K. O. M. A. T. K. T. P. Dawson, J.A. Duenas and W. Milne, "Combined antenna and localized plasmon resonance in raman scattering from random arrayis of silver-coated, vertically alligned multiwalled carbon nanotubes," *NanoLett, 11, 365*, 2011.

[57] J. Sekhon and S. Verma, "Rational selectoin of nanorod plasmons: material, size, and shape dependence mechanism for optical sensors," *Plasmonics, 7, 453*, 2012.

[58] R. M. L. K. T.H. Taminiau, F.B. Segerink and N. van Hulst, "Near-field driving of a optical monopole antenna," *J.Opt. A: Pure Appl. Opt., 9, 315*, 20107.

[59] T. Fischer and O. Martin, "Engineering the optical response of plasmonic nanoantennas," *Opt. Expr. 16, 9144*, 2008.

[60] Y. K. T. Kosako and H. Hofmann, "Directional control of light by a nano-optical yagi-uda antenna," *Nat. Phot. 4, 312*, 2010.

[61] C. S. et al., "Drastic reduction of plasmon damping in gold nanorods," *Phys. Rev. Lett. 88, 7, 077402*, 2002.

[62] L. Barron, *Molecular light scattering and optical activity.* Cambridge, United Kingdom: Cambridge University Press, 2004.

[63] V. Krstić, *Charge transport in one-dimensional molecular nanostructures: single-walled carbon nanotubes.* Switzeland: E.P.F Laussane, 2002.

[64] J. Stone, *Radiation and Optics.* New York, San Francisco Toronto,London: McGraw-Hill Book Company, 1963.

[65] N. B. Nakanishi and R. Woody, *Circular dichroism. Principles and applications, p. 473.* New York: VCH Publishers, 1994.

[66] G. S. A.T. Wecksler and T. Holman, "Kinetic and spectroscopic studies of n694c lipoxygenase: A probe of the substrate activation mechanism of a nonheme ferric enzyme," *JACS, vol 129, 7531*, 2007.

[67] E. Solomon and A. Lever, *Inorganic Electronic Structure and Spectroscopy, Volume I: Methodology, p.78.* San Francisco: Wiley, 2006.

[68] P. Kleindienst and G. Wagniere, "Interferometric detection of magnetochiral birefringence," *Chem.Phys. Lett. vol 288, 89*, 1998.

[69] G. Rikken and E. Raupach, "Observation of magneto-chiral dichroism," *Nature, vol 390, 493*, 1997.

[70] V. K. L. C. N. O. G. R. M. G. C. Train, R. Gheorghe and M. Verdaguer, "Strong magneto-chiral dichroism in enantiopure chiral ferromagnets," *Nature materials, vol 7, 729*, 2008.

[71] G. Rikken and E. Raupach, "Pure and cascaded magnetochiral anisotropy in optical absorption," *Phys. Rev. E, vol 58, 5081*, 1998.

[72] M. V. et al., "Observation of magnetochiral birefringence," *Phys. Rev. Lett. vol 87, 183003*, 2001.

[73] H. C. P. H. G. S. A. V.A. Sautenkov, Y. V. Rostovtsev and M. Scully, "Electromagnetically induced magnetochiral anisotropy in a resonant medium," *Phys. Rev. Lett. vol 94, 233601*, 2005.

[74] G. Rikken and E. Raupach, "Enantioselective magnetochiral photochemistry," *Nature vol 405, 932*, 2000.

[75] D. Lide, *CRC Handbook of Chemistry and Physics*. Boca Raton: CRC Press, 1997.

[76] S. K. K. S. H. S. K. Akagi, G. Piao and M. Kyotani, "Helical polyacetylene synthesized with a chiral nematic reaction field," *Science, vol 282, 1683*, 1998.

[77] D. W. K. Ray, S.P. Ananthavel and R. Naaman, "Asymmetric scattering of polarized electrons by organized organic films of chiral molecules," *Science, vol 283, 814*, 1999.

[78] M. B. K. K. V. Krstić, S. Roth and G. Rikken, "Magneto-chiral anisotropy in charge transport through single-walled carbon nanotubes," *J. Chem. Phys, vol 117, 24, 11315*, 2002.

[79] K. Robbie and M. Brett, "Chiral sculputed thin films," *Nature, vol 384, 616*, 1996.

[80] K. Robbie and M. Brett, "Sculptured thin films and glancing angle deposition: Growth mechanics and applications," *J. Vac. Sci. Technol. A, vol.15, 1460*, 1997.

[81] Z. F. G. P. E. R. A. F. S. A. G. A. Kuzyk, R. Schreiber and T. Liedl, "Dna-based self-assembly of chiral plasmonic nanostructures with tailored optical response," *Nature vol. 483, 311*, 2012.

[82] M. D. D. Zhang, J. Jasinski and M. Badal, "Synthesis and characterization of silica nanosprings by a low temperature chemical vapor deposition," *Appl. Phys. A, vol. 92, 595*, 2008.

[83] Y. K. D.N. McIlroy, D. Zhang and M. Norton, "Nanosprings," *Appl. Phys. Lett, vol. 79, no. 10, 1540*, 2001.

[84] X. Chen and R. Ruoff, "Simple and catalyst-free synthesis of silicon oxide nanowires and nanocoils," *NANO: Brief Reports and Reviews. vol 2, no 2, 91*, 2007.

[85] B. Korgel, "Nanosprings take shape," *Science, vol 309, 1683*, 2005.

[86] D. A. D. W. D. X. Chen, S. Zhang and R. Ruoff, "Mechanics of a carbon nanocoil," *Nano Lett. vol 3, no 9, 1299*, 2003.

[87] P. P. D. Z. M. N. L. Wang, D. Major and D. McIlroy, "High yield synthesis and lithography of silica-based nanospring mats," *Nanotechnol., vol. 17, S238*, 2006.

[88] M. Jensen and M. Brett, "Periodically structured glacing angle deposition thin films," *IEEE Trans. on Nanotech., vol.4, no.2, 269*, 2005.

[89] D. Y. R. P. T. L. J. P. Singh, D.L. Liu and G. Wang, "Metal-coated si springs: Nanoelectromechanical actuators," *Appl. Phys. Lett., vol. 84, no 18, 3657*, 2004.

[90] J. S. K.D. Harris and M. Brett, "Fabrication and optical characterization of template-constructed thin films with chiral nanostructure," *IEEE Trans. on Nanotech., vol 1, no.3, 122*, 2002.

[91] K. H. A.L. Elias and M. Brett, "Fabrication aof hellically perforated gold, nickel, and polystyrene thin films," *J. of Micromech. Systems, vol 13, no.5, 808*, 2002.

[92] T. S. M. F. M. M. B. Dick, M.J. Brett and R. Egerton, "Periodic magnetic microstructures by glacing angle deposition," *J. Vac. Sci. Technol. A, vol 18, 1838*, 2002.

[93] T. R. S. E. S. D. Schmidt, A.C. Kjerstad and M. Schubert, "Optical, structural and magnetic properties of cobalt nanostructure thin films," *J. Appl. Phys, vol 105, 113508*, 2009.

[94] R. A. G. G. J. Y. J. R. B. Gallas, K. Robbie and A. Priou, "Silver square nanospirals mimic optical properties of u-shaped metamaterials," *Optics Express, vol. 18, no. 16, 16335*, 2010.

[95] M. Jensen and M. Brett, "Porosity engineering in glancing angle deposition thin films," *Appl. Phys. A., vol.80, 763*, 2005.

[96] L. Z. L. D. B. N. D. G. D.J. Bell, Y. Sun, "Three-dimensional nanosprings for electromechanical sensors," *Sensors and Actuators A, vol 130131, 54*, 2006.

[97] L. Abelmann and C. Lodder, "Oblique evaporation and surface diffusion," *Thin Solid Films, vol.305, 1*, 1997.

[98] D. Thornburg and C. Wayman, "Temperature changes in thin films during growth by physical vapor deposition. i. theoretical," *J. App. Phys., vol.42, no.10, 4063*, 1971.

[99] S. D. M. B. K. R. M. S. D. Vick, L.J. Fiedrich and T. Smy, "Self-shadowing and surface diffusion effects in obliquely deposited thin films," *Thin Solid Films, vol.339, 88*, 1999.

[100] T. B. C. D. J. A. K. Robbie, G. Beydaghyan, "Ultrahigh vacuum glancing angle deposition system for thin films with controlled three-dimensional nanoscale structure," *Rev. Scientific Instruments, vol. 75, no.4, 1098*, 2004.

[101] A. M. et al., "Hybrid nanocolloids with programmed three-dimensional shape and material composition," *Nat. Mat. DOI: 10.1038/NMAT3685*, 2013.

[102] J. Bozzola, *Electron Microscopy*. New York: John Wiley & Sons, 2001.

[103] P. Potts, *A Handbook of Silicate Rock Analysis*. Cambridge, United Kingdom: Blackie, 1987.

[104] T. T. et al., "Omnidirectional absorption in nanostructured metal surfaces," *Nat. Photon. 2, 299*, 2008.

[105] S. S. H. Ko and V. Tsukruk, "Nanostructured surfaces and assemblies as sers media," *Small, 4, 10, 1576*, 2008.

[106] A. L. V. K. A. G. A. N. G. K. N. F. Schedin, E. Lidorikis and A. Ferrari, "Surface-enhanced raman spectroscopy of graphene," *ACS Nano, 4, 10, 5617*, 2010.

[107] V. S. C. C. M. L. F. M. S. P. D. J. K. N. A.C. Ferrari, J.C. Meyer and A. Geim, "The raman spectrum of graphene and graphene layers," *Phys. Rev. Lett. 97, 18, 187401*, 2006.

[108] V. Krstić and G. Rikken, "Magneto-chiral anisotropy of the free electron on a helix," *Chem. Phys. Lett., vol 364, 51*, 2002.

[109] R. T. Y.S. Touloukian, R.K. Kirby and P. Desai, *Thermophysical Properties of Matter - the TPRC Data Series. Volume 1. Thermal Conductivity-Metallic Elements and Alloys*. New York, United States: IFI Plenum, 1970.

[110] D. Giancoli, *Physics*. New York, United States: Prentice Hall, 1995.

[111] J. Lennard-Jones, "The interaction of atoms and molecules with solid surfaces xi: The disperlas of energy from an activated link," *Proc. Phys. Soc. London A163, 127*, 1937.

[112] I. B. J. Fan and C. Shelton, "Monte carlo modeling of electron physical vapor deposition of yttrium," *J. Vac. Sci. Technol. A, 18, 2937*, 20100.

[113] M. Malac and R. Egerton, "Thin-film regular-array structures with 10-100nm repeat distance," *Nanotech., vol 12, 11*, 2000.

[114] M. Malac and R. Egerton, "Observations of the microscopic growth mechanism of pillars and helices formed by glancing-angle thin-film deposition," *J.Vac.Sci.Technol. A 19, 158*, 2000.

[115] V. S. G.V. Naik and A. Boltasseva, "Alternative plasmonic materials: Beyond gold and silver," *Adv. Mater., 25, 3264*, 2013.

[116] M. P. L. B. T. P. S. D. L. M. H.C. Yuan, V.E. Yost and H. Branz, "Efficient black silicon solar cells with nanoporous anti-reflection mada in a single-step liquid etch," *IEEE Photovoltaics Conference*, 2009.

[117] A. Vorobyev and C. Guo, "Metallic light absorbers produced by femtosecond laser pulses," *Advances in Mech. Engineering, 2010*, 2009.

[118] J.-J. et al., "Electric-field-directed growth of gold nanorod in aqueous surfactant solutions," *Adv.Funct.Mater., 14, 6, 571*, 2004.

[119] T. K. et al., "Localized and delocalized plasmons in metallic nanovoids," *Phys. Rev. B, 74, 245415*, 2006.

[120] D. W. U. K. M. R. F. H. F. A. H. Ditlbacher, A. Hohenau and J. Krenn, "Silver nanowires as surface plasmon resonators," *Phys.Rev.Lett vol. 95, 257403*, 2005.

[121] M. C. A. Arca and M. Somekh, "Surface plasmon resonator: Design, construction, and observation in the farfield," *J. Appl. Phys. 108, 103109*, 2010.

[122] Z. Zhang and Y. Zhao, "The visible extinction peaks of ag nanohelices: A periodic effective dipole model," *Appl. Phys. Lett. 98, 083102*, 2011.

[123] R. O. et al., "Antenna-load interactions at optical frequencies: impedance matching to quantum systems," *Nanotechnol. 23, 444001*, 2012.

[124] N. K. T. H. N. McEvoy, H. Nolan and G. Duesberg, "Functionalisation of graphene surfaces with downstream plasma treatments," *Carbon, 54, 283*, 2013.

[125] C. G. A. Z. Y. Zhang, V.W. Brar and M. Crommiel, "Origin of spatial charge inhomogeneity in graphene," *Nat. Phys., 5, 722*, 2009.

[126] V. B. M. M. M. P. J.M. Caridad, F. Rossella and E. Díez, "Effects of particle contamination and substrate interaction on the raman response of unintentionally doped graphene," *J. Appl. Phys., 108, 084321*, 2010.

[127] M. et al., "Uniaxial strain in graphene by raman spectroscopy: G peak splitting, grneisen parameters, and sample orientation," *Phys. Rev. B, 79, 205433*, 2009.

[128] L. Z. P. Wang, D. Zhang and Y. Fang, "The sers study of graphene deposited by gold nanoparticles with 785 nm excitation," *Chem. Phys. Lett., 556, 146-150*, 2013.

[129] T. H. M.A. Khan and B. Shanker, "Metallic nanorods synthesis and application in surface enhanced raman spectroscopy," *J. NanoSyst. & Tech. 1, 1*, 2009.

[130] J. S. T. Qiu, X.L. Wua and K. Chu, "Silver nanocrystal superlattice coating for molecular sensing by surface-enhanced raman spectroscopy," *Appl. Phys. Lett., 89, 13 1914*, 2006.

[131] J. S. J.B. Sorge, A.C. van Popta and M. Brett, "Circular birefringence dependence on chiral film porosity," *Optics Express vol. 14, 22, 10550*, 2006.

[132] J. Jin, *The Finite Element Method in Electromagnetics*. New York, United States: Wiley-IEEE Press, 2002.

[133] COMSOL08, *RF Module. Comsol User Guide*. London, United Kingdom: COMSOL AB, 2008.

[134] J. S. K. Robbie and M. Brett, "Advanced techniques for glancing angle deposition," *J. Vac. Sci. Technol. B, vol. 16, 1115*, 1998.

[135] L. W. X. Hu, T. Wang and S. Dong, "Surface-enhanded raman scattering of 4-aminothiophenol self-assembled monolayers in sandwich structure with nanoparticle shape dependence: Off-surface plasmon resonance condition.," *J. Phys. Chem. C, 111, 6962*, 2007.

[136] P. Barber and D. Wang, "Rayleigh-gans-debye applicability to scattering by non-spherical particles," *Appl. Optics 17,797*, 1978.

[137] E. Palik, *Handbook of optical constants of solids*. London: Academic Press, 1997.

[138] C. P. S. Bassiri and N. Engheta, "Electromagnetic wave propagation through a dielectric-chiral interface and through a chiral slab," *J. Opt. Soc. Am. A 5, 1450*, 1988.

[139] I. Lindell and A. Viitanen, "Uniaxial chiral quarter-wave polarization transformer," *Elect. Lett. 29, 1074*, 1993.

INDEX